PORTUGALIAE PHYSICA

VOLUME 19
FASCÍCULO 1-2
1988

SOCIEDADE PORTUGUESA DE FÍSICA

PORTUGALIAE PHYSICA

Fundada em 1943 por A. Cyrillo Soares, M. Telles Antunes, A. Marques da Silva e M. Valadares

Publicação subsidiada pelo INSTITUTO NACIONAL DE INVESTIGAÇÃO CIENTÍFICA

ISSN 0048 - 4903

PORTUGALIAE PHYSICA

117

VOLUME 19
FASCÍCULO 1-2
1988

PROCEEDINGS
OF
SAGAMORE IX

Conference on Charge, Spin and Momentum Densities

Luso (Coimbra) - Portugal

26 June - 2 July 1988

Part I — Invited Lectures

DEFECT STRUCTURE STUDIES OF TRANSITION METAL COMPOUNDS

D. E. ELLIS

Department of Physics and Astronomy
Northwestern University
Evanston, IL 60208
and
Argonne National Laboratory
Argonne, IL 60439

ABSTRACT — Self consistent field local density theory has been applied to study the electronic structure of transition metal compounds. Single-particle wavefunctions, spectral densities, and charge and spin densities have been determined using a variational LCAO method. Finite clusters are treated by embedding techniques to include interactions with the infinite host crystal. Cohesive energies are calculated to explore relative stability of different defect structures and lattice distortions. Properties of oxide compounds ranging from rock salt structures to spinels and superconducting perovskites are presented in detail.

I — INTRODUCTION

The electronic, magnetic, and structural properties of transition metal compounds are often controlled by defect and impurity structures. Nonstoichiometric compositions are frequently thermodynamically more stable than the perfect lattice, even at low temperature. In view of the numerous practical applications or potential uses in structural ceramics, magnetic recording media, optical storage and computing elements, communication devices, superconducting compositions – among others – it is clear that a fundamental understanding of the operative electronic mechanisms is required. As a result of more than twenty years of fairly intense experimental and theoretical effort, many general features and useful techniques have emerged. However, it is fair to say that we have only begun to understand the simplest transition metal (TM) oxides, and the «real» materials and their properties at finite temperature still present a formidable challenge.

In this report we will concentrate mainly on results obtained by the self consistent field local density (LD) theory. The band structure approach to LD models for TM compounds is presented in another article of this volume [1]; here we examine possibilities of the embedded cluster-finite fragment treatment of an infinite system. The linear combination of atomic orbital (LCAO) representation will be used to develop chemical interpretations of the electronic charge and spin distributions. The spectral functions $N_i(\varepsilon)$ and $n(\varepsilon, \mathbf{r})$ representing the energy distribution of a particular AO or the energy density distribution of the ensemble of occupied states

Portgal. Phys. — Vol. 19, fasc. 1-2, pp. 1-20, 1988

respectively provide insight into the bonding mechanisms and changes which take place when the ideal crystal is perturbed by introduction of defects. Within the LD spin unrestricted formalism [2], the spin density components

$$\rho_\sigma (\mathbf{r}) = \sum_i n_{i\sigma} \mid \psi_{i\sigma} (\mathbf{r}) \mid^2 \qquad (1)$$

are defined in terms of the single particle eigenfunctions $\psi_{i\sigma}$ of the effective Hamiltonian, and the Fermi-Dirac accupation numbers $n_{i\sigma}$ with spin index $\sigma = \uparrow, \downarrow$. The charge density is thus $\rho_c = \rho\uparrow + \rho\downarrow$ and the net spin density is

$$\rho_s = \rho\uparrow - \rho\downarrow \qquad (2)$$

A number of effective computational schemes have been developed to approximately solve the self consistent field problem. As a result, efforts have begun to be concentrated on extraction of derived physical properties. It is worthwhile making a distinction between experimental (and calculated) properties which depend upon the *ground state* electronic distribution and those which depend essentially upon *electronic excitations*. X-ray diffraction data fall in the first category; X-ray absorption cross-sections belong to the second, for example. Whereas the LD theory is on a firm footing for generating the ground distribution and its properties [3], the basic principles for treating excitations generally are in a state of evolution. When we compare experiment and theory for ground state properties we may seek to learn about the effects of correlation which have been crudely averaged in the single particle effective potential, and perhaps build a more rigorous model, starting from the LD orbitals. In the case of excitations, we must bear in mind that the orbitals generated and the distributions and properties predicted are of a tentative nature, based upon a pseudoparticle picture such as the transition state scheme [2] which can certainly be improved both conceptually and computationally.

II — SELF-CONSISTENT EMBEDDING: POTENTIAL AND BOUNDARY CONDITIONS

The construction of an embedding scheme to be used in treating a fragment of an extended solid or molecule presents interesting problems, independent of the electronic structure theory in use. Some properties, such as charge density and local densities of states, converge rather rapidly as a function of cluster size, while others such as details of the DOS around the Fermi energy may require unmanageably large numbers of atoms. The use of an *embedding potential* which approximates contributions to the Hamiltonian of «host» atoms exterior to the cluster helps removing surface states and surface chemical shifts which obscure the bulk structure of interest [4]. The application of appropriate *boundary conditions* serves to drive the cluster wavefunctions toward the physical states we wish to characterize [5, 6].

There are a number of schools of thought about practical methods for embedding, ranging from complete omission of any environment, to detailed matching to the host potential and wavefunctions via the Green's function method [7]. The scheme used in the present work is a compromise between accuracy and computational cost, which permits self consistent modelling of a complex environment and extraction of a set of parameters which compactly describe the chemical state of the system. The iteration scheme used in our LD calculations goes as follows:

i. Given an approximate potential, solve the Schrödinger (or Dirac) equation $(h - \varepsilon_i)\ \psi_i = 0$ for the discrete cluster energy levels ε_i and eigenfunctions ψ_i.

ii. With an estimate of the number of electrons in the cluster, N, and a rule for generating occupation numbers n_i (such as Fermi-Dirac) calculate the charge and spin densities according to Eq. 1 to obtain ρ_σ (cluster).

iii. Partition the cluster density into a sum of «atomic» contributions,

$$\rho\ (\text{cluster}) \simeq \sum_{\nu=1}^{M} \rho_\nu\ (\mathbf{r}_\nu)$$

In the Self Consistent Charge (SCC) scheme Mulliken atomic orbital population analysis is used to carry out the partitioning [8]; in the Self Consistent Multipolar (SCM) procedure a global least squares fitting to a set of localized functions is performed [9]. Constraints are applied; e. g., to maintain neutrality of the crystal unit cell. Geometrical partitioning by cellular muffin-tin «cuts» of the density is equally feasible.

iv. Synthesize the charge and spin density of the entire system – host plus cluster – by summation, as in Eq. 3. In LD theories, the Coulomb and exchange-correlation potentials can be constructed directly from a given ρ_σ (total), thus redefining the effective Hamiltonian. Include some form of (Pauli exclusion principle) repulsion potential to prevent cluster electrons from occupying states on host atom sites.

v. Compare input and output charge densities and potential; redetermine N, and return to step (i) until both *host* and *cluster* have converged.

Imposition of boundary conditions (BC) offers a second «chance» to optimize the simulation of the extended solid by a cluster. In the Multiple Scattering (MS-Xα) or Green's function method [10] this is most easily accomplished by matching the wavefunctions ψ_i at an outer spherical boundary of radius R_0 to functions of predetermined simple form. In an LCAO representation the basis functions generated analytically or by solution of atomic bound-state problems already satisfy decaying-wave BC and are generally used without modification. The use of BC matching the localized cluster wavefunctions to an exterior wave, provides a convenient and physically understandable means of broadening cluster levels into bands resembling more nearly the continuous band structures of metals as well as semiconductors [6].

Another kind of BC useful in practical calculations is a bit more subtle, depending upon an idea of graduated levels of approximation. To be concrete, let us consider a kind of shell model of the physical system, consisting of:

i. An inner set of «fully bonded» atoms, i. e., atoms whose neighbours all reside in the cluster, and are hence described variationally.

ii. An intermediate set of «boundary» atoms, which participate in the cluster wavefunction, but have some neighbours belonging to the host.

iii. The remaining set of «host» atoms, which together form an effective medium for the cluster.

These three types may be considered to form a set of sequentially less accurate representations, in which correspondingly less computational effort needs to be placed. For example, one may wish to treat all states of type (i), including core levels, with a very flexible basis and a highly accurate numerical integration of Hamiltonian matrix elements. At the same time one may treat type (ii) in the frozen core approximation with a modest basis, and represent type (iii) as a «frozen atom». The properties of interest, and in particular, the parameters of the self-consistent potential, can be extracted by a state-by-state local DOS analysis of type (i) contributions. This strategy permits the calculation of rather accurate site-specific quantities for cluster sizes of 20-50 atoms in complex crystal structures [11].

III — COHESIVE ENERGY

The cohesive energy is the *difference* in total energy between the assembled molecule or solid and its isolated constituents. The resulting experimental values of a few eV per atom are, from a theoretical point of view, difficult to compute, since the total energy itself is very large and subject to many types of error. At the LD level of theory some years of intensive effort have led to algorithms capable of giving the necessary precision. However, serious questions about systematic errors due to the exchange-correlation approximations, imperfect solution of the Poisson equation, inadequate basis sets, etc. remain to be resolved practically on a case by case basis. Nevertheless, at the present stage it is possible to obtain data which is helpful in understanding and interpreting defect stabilization mechanisms [9, 12].

For the purpose of identifying the source of different contributions to cohesion we require an energy density function, ρ_ε (r), with volume contributions to the energy defined as:

$$E_\Omega = \int_\Omega \rho_\varepsilon (\mathbf{r})\, d^3r \text{ and total energy } \quad E_{tot} = \sum_\Omega E_\Omega \qquad (4)$$

One could as well carry out an orbital analysis or a pair by pair density analysis of E_{tot}, as has been successfully done in molecular calculations [13]. However, in the present context, a volume partitioning seems most convenient.

Using the simple LD expressions for total energy we may obtain a useful form for ρ_ε :

$$\begin{aligned} \rho_\varepsilon (\mathbf{r}) = {} & \sum_{i\sigma} n_{i\sigma}\, \varepsilon_{i\sigma} \left| \psi_i (\mathbf{r}) \right|^2 \\ & - \frac{1}{2} V_C (\mathbf{r}) \cdot \Big(\sum_\sigma \rho_\sigma (\mathbf{r}) + \rho_{nuc} (\mathbf{r}) \Big) \\ & + \sum_\sigma \rho_\sigma (\mathbf{r}) \cdot \big(E_{xc,\sigma} (\mathbf{r}) - V_{xc,\sigma} (\mathbf{r}) \big) \end{aligned} \qquad (5)$$

Here V_C is the total Coulomb potential, $E_{xc,\sigma}$ and $V_{xc,\sigma}$ are the exchange-correlation energy and potential function for spin σ respectively, and ρ_{nuc} is the nuclear charge distribution. This formulation has the merit that over an arbitrarily chosen volume, single particle Coulomb and exchange-correlation contributions are clearly displayed and arranged to balance each other in a manner similar to that of the integrated total.

Finally, the cohesive energy is calculated by a point by point numerical integration of the difference-energy density,

$$E_{\mathrm{coh},\,\Omega} = \int_{\Omega} (\rho_{\varepsilon} - \rho_{\varepsilon}^{0})\ d^{3}r \qquad (6)$$

where ρ_{ε}^{0} is the energy density of the reference system. The reference system is usually (but not necessarily) taken as an ensemble of noninteracting atoms or ions placed at the lattice sites.

IV — MONOXIDES WITH ROCK SALT STRUCTURE

Superficially, the rock-salt structure monoxides with chemical formula MO appear to be quite simple. However, the facile interconversion of M^{2+} and M^{3+} valence states and the mixed ionic-covalent bonding structure of the TM oxides offers ample possibilities to lower the crystal total energy by creating defects. Thus at the beginning of the 3d series, TiO_x with $x \simeq 1$ is observed to contain ~15 % vacancies at *both* metal and oxygen sites. This means that the average coordination is more nearly 5 than 6, and the beautiful octahedra environment suggested by the lattice geometry is far from the real one. From the middle towards the heavy side of the 3d series, the formation of metal interstitials and associated defect clusters appears to be dominant. Wustite, $Fe_{1-x}O$, is a well studied case and is found to be a small gap semiconducting antiferromagnet which is unstable with respect to decomposition into magnetite, Fe_3O_4, and metallic iron. Indeed, the mixed valence, Fe^{2+}, Fe^{3+} and simultaneous existence of tetrahedral and octahedral coordination metal sites inferred from X-ray, Mössbauer and transport measurements on $Fe_{1-x}O$, reveal a close relationship between the two oxide structures [14-16]. If we start with the rock salt lattice and $x < 0.25$, we can imagine a sequence of steps in which Fe is eliminated from the lattice, Fe^{2+} (octahedral) $\rightarrow Fe^{3+}$ (octahedral, tetrahedral), and the relatively stable $x = 0.25$ magnetite phase is formed.

One of the principal goals of the present work is to try the calculation of the energy gain/loss associated with microscopic steps in formation of lattice defects, making use of first principles theory. We wish to understand how certain defects stabilize one lattice, as in TiO_x, and different defects stabilize other isomorphic structures such as $Fe_{1-x}O$. Here we discuss electronic energetic properties at zero temperature; clearly, a real description of the thermodynamical and transport properties requires an investigation of the free energy including entropy contributions for $T > 0\,K$. Fortunately classical and semiclassical methods for simulating dynamical and thermodynamical properties already exist — what is lacking are reliable electronic energies and related interatomic potentials. The data presented here represent a small step in that direction.

Local density self consistent field calculations have been carried out on embedded clusters representing both ideal lattice and defected TiO, MnO, FeO, and CoO [12, 17, 18]. Clusters as small as M_4O_4 and as large as $M_{14}O_{13}$ have been treated in order to explore sensitivity of predicted properties to cluster size. A typical result for

FeO gives an equilibrium lattice constant within 2-3 % of experiment; a near minimal LCAO numerical basis generates ~50 % of the experimental cohesive energy and a modestly extended basis yields more than 80 % of E_{coh}. It is worth noting that in systems where highly accurate LD energies can be calculated, it is common to observe a slight *overbinding* with respect to experiment. In the present context, by maintaining the same level of computational and theoretical approximations throughout, we are able to determine *differences* in binding energies between different complexes to a higher accuracy than for the individual components. Thus, with a typical E_{coh} ~20 eV/formula unit we are able to discriminate differences in ΔE_{coh} of the order of 0.1 eV.

Certain qualitative features of defect electronic structure can be usefully verified. For example, Mössbauer isomer shift measurements indicate that the dominant iron species presumably occuring in 4:1 (metal vacancy: interstitial ratio) defect clusters is in the trivalent state [15]. LD calculations on the 4:1 defect in FeO show a clear minimum in E_{coh} for an electron count N corresponding to Fe^{3+}. The Fe^{2+} configuration is found to be ~2.4 eV higher, and it costs more than 9 eV to reach the Fe^{4+} state. While it is thus clearly possible to identify the ground state with a particular «Fe^{3+}» configuration, a detailed charge density analysis shows that iron is not in the classical $d^5s^0p^0$ valence state; overlap of diffuse oxygen 2p and metal 4sp states produces significant sp occupancy around the metal valence region. In addition, covalent mixing of metal 3d into the «oxygen 2p» valence band leads to fractional occupation of the Fe d state in addition to the d^5 «crystal field» levels. These features are familiar from studies on ideal crystal structures of TM compounds.

A comparison of calculated energies for m:n (vacancy:interstitial) defects is presented on Table I, on the basis of energy per vacancy created, relative to the ideal lattice. The reader should see the original literature [12, 18] for diagrams of the geometric structure used; in general, edge and vertex shared clusters of the 4:1 tetrahedral interstitial are found to be relatively more stable than close-packed structures. The 4:1 cluster has T_d symmetry, the interstitial Fe having four Fe and four Fe vacancy nearest neighbours at the vertices of a cube. The greater stability of

TABLE I — Binding energy per net vacancy (eV) in metal vacancy, vacancy complexes and interstitial, relative to ideal lattice.

Compound:	TiO	MnO	FeO	CoO
Defect (Vacancy: Interstitial)				
0:1	−1.1	−1.0	—	−1.3
1:1	—	—	—	+0.2
2:1	−1.8	−1.2	−1.8	−0.2
3:1	+1.0	−0.2	−2.0	−0.7
4:1	+3.6	+1.2	−2.7	−1.7
2:2	—	+3.8	—	—
3:2	−0.2	+1.5	—	—
4:2	+1.6	+0.9	—	—
5:2	+1.3	+0.2	—	—
6:2	+1.0	−0.6	−2.4	−1.5
7:2	+1.1	−0.2	−3.9 (b)	−1.0
8:2	—	—	−3.2	—
8:3	—	—	−1.2	—
13:4 (a)	—	—	−1.1	—

(a) Close packed Koch-Cohen cluster; Ref. 14.
(b) Vertex shared < 111 > pair of 4:1 defects; edge shared < 110 > energy is −3.6 eV; Ref. 12.

the open structures such as 7:2 in FeO can be explained simply in terms of the close approach and resulting electrostatic energy of Fe^{3+} ions on lattice sites required for overall electroneutrality. The high mobility of Fe^{3+} on octahedral sites, or equivalently the facile $Fe^{2+} \longleftrightarrow Fe^{3+}$ interconversion plays an important role in models of charge transport properties of this and related semiconductors [19].

As can be seen from the Table, the 2:1 defect is predicted to be energetically most favoured for TiO with the single metal vacancy 0:1 lying ~0.7 eV higher. This is in contradiction with experiment, and indicates the likely importance of multiple vacancy clusters in stabilizing the lattice. This has not yet been investigated by cluster methods, but band structure calculations on ordered and disordered vacancy lattices have been carried out. The disordered lattice calculations yielded no stabilization for TiO [20] while LAPW calculations on ordered lattices and vacancies (e. g., 25 % of metal and oxygen sites empty in NbO) have been discussed qualitatively in terms of the densities of states [21].

For MnO the 2:1 interstitial is also predicted to be favoured [18], stabilizing the lattice by -1.2 eV/vacancy, although the difference between this and the single metal vacancy is now only 0.2 eV. Recent thermopower and conductivity measurements on well characterized MnO samples fit well into a small polaron transport model based on the 2:1 defect [22]. The defect clusters begin to be energetically favourable, with the 6:2 double interstitial appearing at -0.6 eV.

In FeO the m:1 single interstitial is energetically favoured [18], with 4:1 falling at -2.7 eV. However, the 7:2 vertex and edge shared double interstitial is clearly most favoured, at -3.9 eV and -3.6 eV respectively. The compact cubic 13:4 cluster proposed by Koch and Cohen [14] on the basis of fits to X-ray data is found to be relatively unattractive, due to the inability of Fe^{3+} counter-ions to get close to all the vacancy sites and minimize the Coulomb energy.

In CoO the 4:1 complex (-1.7 eV) is followed closely by the 6:2 structure (-1.5 eV); surprisingly, the 7:2 double interstitial is even less favoured than an isolated vacancy. Considering the close similarity between valence states of Fe and Co and their compounds, the notable difference in defect energies predicted is interesting. Experimental studies now underway with controlled defect concentrations will provide data for further comparison with these values.

In concluding this section, it may be worth recalling the numerous approximations which were made, and noting possible future improvements. At the fundamental level, the LD approximation makes an average over the interelectronic correlations; the resulting E_{coh} functional of the density is not necessarily a very good representation of the $d^n s^x p^y$ metal configuration in the environment of the solid. At the model level, we are using lusters of modest size, embedded in a physically appealing but approximate scheme in the infinite solid. At the computational level, LCAO variational bases of merely «acceptable» quality have been employed and numerical integrations of limited precision have been carried out. In general, very little effort was made to optimize bond distances in defect clusters; as a rule, experimental bulk lattice constants were used.

Beyond the obvious extensions which could improve the present model results, we believe that it is especially important to begin a systematic treatment of local lattice relaxation. It seems likely that the energy gained by local geometry relaxation is of the same order of magnitude as the defect-defect interactions which stabilize complexes like 7:2 and are perhaps responsible for the large vacancy concentration in TiO. This theme is further pursued in the following section.

V — SAPPHIRE AND RUBY

As a second example we consider the electronic structure of α-Al_2O_3 corundum (or sapphire) and the chromium impurity in sapphire which is called ruby. Because of its large insulating band gap (> 8 eV), thermal stability and mechanical strength, artificial sapphire is widely used as a substrate. Beyond its use as a gem stone, ruby is famous for its applications as a laser material. In contrast to the monoxides discussed in the previous section, the lattice structure of α-Al_2O_3, Cr:Al_2O_3 and Cr_2O_3 is of rather low symmetry with distorted octahedral coordination of oxygen around metal sites.

Optical properties in general, and laser frequencies in particular, depend strongly upon effects of local geometry on the electronic configuration. Frequency shifts due to external pressure are observable, but are not as large as desired. Thus the use of Ti and other transition metal dopants is considered for the development of new materials. Clearly a good understanding of the atomic cohesive structure, as well as the electronic states available for excitation, is necessary for the design of improved properties.

The crystalline unit cell of α-alumina contains two formula units; i. e., ten atoms. Band structure models provide a useful picture of the «O 2p» valence band and «Al 3sp» conduction band regions which can be compared with photoemission and X-ray emission data [23]. However, for an understanding of defect and impurity levels cluster models offer many advantages. In order to explore the sensitivity of predicted properties to cluster size and shape, a number of fragments were iterated to self-consistency in the potential field of a «frozen» Al^{+3}, O^{2-} ionic crystal. With cluster sizes ranging from Al_2O_3 to $Al_{10}O_{15}$ it was found that the insulating gap varied between ~8 and ~10 eV while the occupied valence band widths remained quite stable [24]. The band gap and valence band widths derived from the larger clusters are internally consistent and agree fairly well with the LCAO tight binding band structure results of Batra et al. [23].

We do notice a sensitivity of results, particularly of the atomic configurations derived from Mulliken population analysis, to basis set composition. Basis sets were generated numerically for both ions and free atoms placed in a potential well. It was found that for small clusters or clusters of open structure (which are hard to avoid with α-Al_2O_3) diffuse basis functions often developed large weights in the occupied states which were strongly dependent on the embedding parameters. In order to minimize problems of interpretation and influence of boundary conditions on energetics of atomic displacements, we eventually selected a near-minimal basis of compact functions.

To a good approximation one may consider the lattice spacing of α-Al_2O_3 to be determined by oxygen-oxygen contacts. A charge density map of the LD results shows the Al ions as isolated and localized, very nearly in the $3s^0 3p^0$ trivalent configuration (see Table II). On the other hand, when one plots the corresponding result for Cr substituted at an Al site, one immediately sees that the Cr^{3+} d^3 configuration must exert considerable pressure on neighbouring oxygen ions for expansion and rearrangement. Further evidence of the importance of local lattice relaxation can be derived by comparison of theoretical d → d «crystal-field» optical transitions with experiment [25, 26]. Reasonable agreement between theory and experiment can be obtained only by repositioning the six nearest neighbour O to nearly octahedral coordination *and* by moving the next-neighbour Al to maintain approximately the lattice Al-O bond length [24]. The value $R\ (Cr - O) = 1.9$ Å gives a good match to the $t_{2g}\uparrow - e_g\uparrow$ transition at $\sim 18{,}000\ cm^{-1}$ in comparison with the unperturbed $R\ (Al - O) = 1.86,\ 1.97$ Å. Minimization of the total energy leads to a predicted bond length $R\ (Cr - O) = 2.0$ Å in good agreement with the value inferred from the optical transition, considering the computational approximations which were made [27]. The self-consistent configurations for both Cr and Ti impurities near the equilibrium geometry are given in Table II.

TABLE II — Mulliken atomic orbital populations for Al and for Cr and Ti impurities in α-Al_2O_3.

	Al	3s	0.08	Cr	3d	3.13	Ti	3d	0.84
		3p	0.02		4s	0.01		4s	0.01
					4p	0.02		4p	0.04
Q_{net}			2.90			2.84			3.12

Spin-polarized calculations on the Cr impurity give a value of the spin moment of $\sim 1.8\ \mu_B$ and an estimate of the $t_{2g}\uparrow - t_{2g}\downarrow$ spin flip transition at $\sim 9000\ cm^{-1}$ again in reasonable agreement with experiment. However, to gain a quantitative model of the optical bands of ruby or Ti-substituted alumina it will be desirable to carry out more rigorous multiplet structure calculations. The LD cluster orbitals are likely to serve very well as a basis for such a many-electron model.

VI — COPPER OXIDE COMPOUNDS

A. *Reference Compounds and Cu Valency*

As a final example let us consider the very interesting bonding structures of copper oxide compounds, beginning with the question of valency. If one assumes that oxygen is divalent, then the series Cu_2O, CuO, and $KCuO_2$ can be considered as providing examples of $Cu^{I}3d^{10}$, $Cu^{II}3d^9 4s^0$ and $Cu^{III}3d^8 4s^0$ respectively. However, the large electronic polarizability observed for many Cu compounds and the tendency to form complex structures dominated by planar four-fold or even linear two-fold coordination immediately raises serious doubts about simple ionic models. The critical role of oxygen stoichiometry in conductivity and superconductivity in more complex compounds like $YBa_2Cu_3O_{7-y}$ points to the necessity of including oxygen vacancies in any realistic model [28-31].

The potential commercial applications of Cu-based high T_c superconducting materials have resulted in very intense scrutiny of these and related Cu compounds recently. While the *fundamental mechanism* of superconductive pair formation is still in disput, it is plausible to claim that the normal electronic properties of these materials are as well (or better) characterized as those of the other transition metals.

In the Cu_2O «monovalent» copper compound, Cu has a local two-fold coordination with two oxygen ions at a distance of 1.85 Å forming a (CuO_2) linear complex [32]. The second neighbour value of R (Cu − O) is already 3.54 Å. The LD cluster calculations give an effective configuration Cu 3d(0.54)4s(0.69)4p(0.11) with a net charge of +0.66 e, showing immediately that the formal d^{10} state is not achieved, and significant mixing with O 2sp states occurs via the diffuse Cu 4sp levels [33]. In CuO, a quasitetrahedral local geometry is found with distances R(Cu − O) = 1.88 and 1.96 Å. In attaining a net charge of +1.56 e, the Cu ion adopts the self-consistent configuration 3d(9.25)4s (0.16)4p(0.03) which is similar to that found in other «divalent» compounds. In $KCuO_2$, the «trivalent» state is far from being attained, the calculated configuration being 3d(8.98)4s(0.13)4p(0.04) and the net charge +1.85 e, corresponding to the planar four-fold coordination with R(Cu − O) = 1.84 Å.

X-ray absorption near edge spectra (XANES) measurements on the Cu K− edge reveal a shift of the threshold and a variation of spectral features in comparing these three «reference compounds» and the superconducting (SC) materials such as $La_{2-x}Sr_xCuO_4$ and $YBa_2Cu_3O_{7-y}$ [34, 35]. In general «divalent» Cu features appear to be dominant in the superconducting compounds, with «monovalent» structure appearing in oxygen deficient specimens. Features of the «trivalent» species sometimes invoked in SC pairing models do not appear with any prominence in the XANES data. An extensive series of calculations of the Cu K-edge cross-section were carried out, to see if the LD theory is adequate to interpret these data [36].

Before describing these results it will be useful to review data from a complementary spectroscopy, X-ray photoemission spectra (XPS). Ultra-violet photoemission spectra and XPS of the O2p valence band region show a band of 5-6 eV width with poorly resolved features in a material like La_2CuO_4 [37]. These features are in fair agreement with densities of states obtained from band calculations [38, 39]. The XPS of the Cu L_{II}, L_{III} region are more informative [40]:

i. In Cu_2O a weak satellite structure is seen to the high binding energy side of the $2p_{1/2}$ and $2p_{3/2}$ main lines.
ii. The satellite structure is much stronger in CuO, with intensity comparable to that of the main lines.
iii. The features of $La_{1.85}Sr_{0.15}CuO_4$ and $YBa_2Cu_3O_7$, appear to be very similar to those of CuO.

In a model previously applied to satellite structures in TM compounds such as $FeCl_2$ [41], the main line is interpreted as due to transitions into the fully relaxed $d^n \rightarrow d^{n+1}$ localized final state, while the satellites are calculated as transitions into metastable $d^n \rightarrow d^n \chi^1$ diffuse states. Here χ is a mixture of TM sp and ligand sp character which provides a weaker screening of the core hole than the d^{n+1} configuration. A key point here is that such transitions are characteristic of rather localized ionic configurations and not of metallic species.

In the simplest single particle model and in the dipole approximation the X-ray K-absorption cross-section is given by [42]:

$$\sigma(\omega) = 4\pi^2\alpha \hbar \omega \sum_f | < \Psi_f | \hat{\varepsilon} \cdot \mathbf{r} | \Phi_{1s} > |^2 \qquad (7)$$

$$\delta \; (E_{1s} + \hbar \omega - E_f)$$

Here Φ is the initial state, Ψ_f is a bound or continuum (energy normalized) final state, and $\hat{\varepsilon}$ is the polarization vector of the photon with energy $\hbar\omega$. Within this approximation questions arise about the most appropriate potential and final state relaxation effects. Furthermore, it is clear that two-electron and perhaps many-body excitations will also contribute to the observed absorption profile. There exists an extensive literature on unresolved issues in X-ray cross-sections; here we limit ourselves to the question: What does the LD cluster model predict in the lowest order of approximation?

To answer this question we have used the LD self-consistent *ground state* and *transition state* (core hole) potentials to generate the final states Ψ_f. On physical grounds it is clear that Ψ_f states localized near the Cu 1s hole will suffer an energy shift and a corresponding shift of $\sigma(\omega)$ contributions, in comparison with more delocalized final states. Such features of specific final state «channels» can be easily examined with the aid of *trapping time* diagrams analogous to the DOS used in analyzing discrete levels [36]. Here

$$T_{\nu l}(E) = h \sum_f \int d^3r \; P_{\nu l} \; | \Psi_f \; (E, \mathbf{r}) |^2 \qquad (8)$$

uses a projection operator $P_{\nu l}$ to select the l-wave amplitude of atom ν of each final state at a specified energy. If the dipole transition matrix element is slowly varying with energy, as is often the case, then $T_{\nu l} \sim \sigma_{\nu l}$ and a very direct interpretation of observed spectral features is possible.

The Multiple-Scattering (MS) [10] method was used to generate final states with the correct oscillatory boundary conditions. The cross-section was evaluated using the methods developed by Natoli et al. [43]. To accomodate the MS procedure, a muffin-tin spherical truncation of the LD potential was made. To generate ionic final states, the cluster potential was matched to a 1/r Coulomb tail at a radius R_0 outside the cluster. The use of the truncated potential introduces shifts in the position of the continuum edge and other features relative to the bound states. These shifts were minimized by recalculating valence band levels in the MS method and aligning valence structures with those obtained by the DV method. In this way we are able to obtain a quantitative measure of the position of the edge and determine shifts of one compound relative to another.

The position of the Cu K-edge is of course correlated with the metal oxidation state; experimentally, $E\,(Cu_2O) < E\,(CuO) < E\,(KCuO_2)$ with ~2 eV difference between Cu^{I}-Cu^{II} and Cu^{II}-Cu^{III}. According to the LD calculations the effective d-electron population is a better measure of the screening, with a derived value of 6.3 ± 0.5 eV shift per unit change in d-electron occupation accounting well for the experimental values. Both the edge position and principal features of the peaks in $\sigma(\omega)$ for Cu_2O, CuO, $KCuO_2$ and the layered perovskite structure La_2CuO_4 are well reproduced by the LD model [34, 35, 44]. The theoretical $\sigma(\omega)$ given in Fig. 1 shows the following structures:

i. Weak features near the edge, associated with admixture of oxigen p character into nominal Cu-d states. Although dipole allowed, transitions are weak due to their two--center nature.

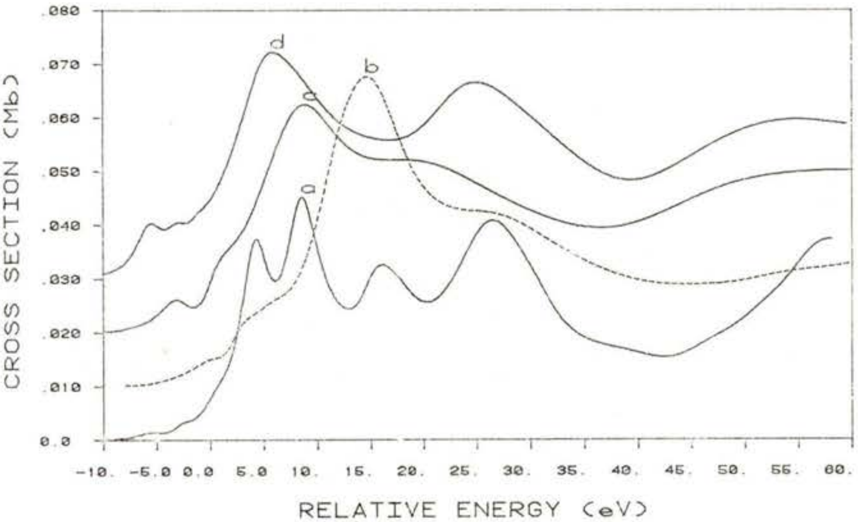

Fig. 1 — Theoretical Cu K-edge absorption spectra of (a) La_2CuO_4, (b) $KCuO_2$, (c) CuO, (d) Cu_2O.

ii. A prominant peak known as the «white line» dominated by transitions into the Cu 4p, the position of the maximum being shifted according to the oxidation state. In La_2CuO_4 the distorted octahedral symmetry results in a separation of the σ- and π- components which appears in the experimental results as a broadened peak and shoulder.

iii. Modulations in σ seen from about 15 eV above the edge and higher are due to back-scattering of the outgoing photoelectron from neighbouring atom potentials. The broad bump ranging from ~20 to ~30 eV is dominated by nearest neighbour oxyxen. In La_2CuO_4, the peak seen at ~17 eV was initially identified as due to Cu^{III}, since the main peak in $KCuO_2$ occurs at the same energy. However, it is now known that *interference* between first and second neighbour oxygen scattering is responsible for this peak; Cu^{III}, if present, must contribute little to the observed amplitude.

B. *$YBa_2Cu_3O_{7-y}$: Chains versus Planes*

The famous superconducting compound $YBa_2Cu_3O_{7-y}$ belongs to the perovskite structural family with two types of copper sites. In site 1, one finds Cu ions in the (a, b) plane; for $y = 0$, $a \neq b$; i. e., the lattice is orthorhombic and there exist -O-Cu-O-Cu- chains along the b axis. Oxygen ions above and below along the c axis complete the coordination of site 1, which ranges from two-fold to four-fold, depending on *y*. For $y = 1$, the oxygen sites are all vacant in the (a, b) plane, and $a = b$, i. e., the lattice is tetragonal. For intermediate values, $6.5 < y < 7$, partial occupancy with partial disorder of oxygen sites along the *a* and *b* axes is inferred from neutron scattering [45, 63, 65], Cu nuclear quadrupole resonance [46] and other experiments. The oxygen stoichiometry and the arrangement of vacancies in the (a, b) plane are found to be strongly correlated with the superconducting transition temperature T_c. Site 2 Cu ions also form a square network, displaced along the c stacking axis. These Cu sites are approximately fivefold coordinated with four oxygens in the (a, b) plane and the fifth (axial) oxygen located on the c axis. These five oxygen sites appear to be nearly completely occupied, and the axial oxygen plays an important role in coupling site 1 and site 2 Cu to each other. One of the main tasks of theory and experi-

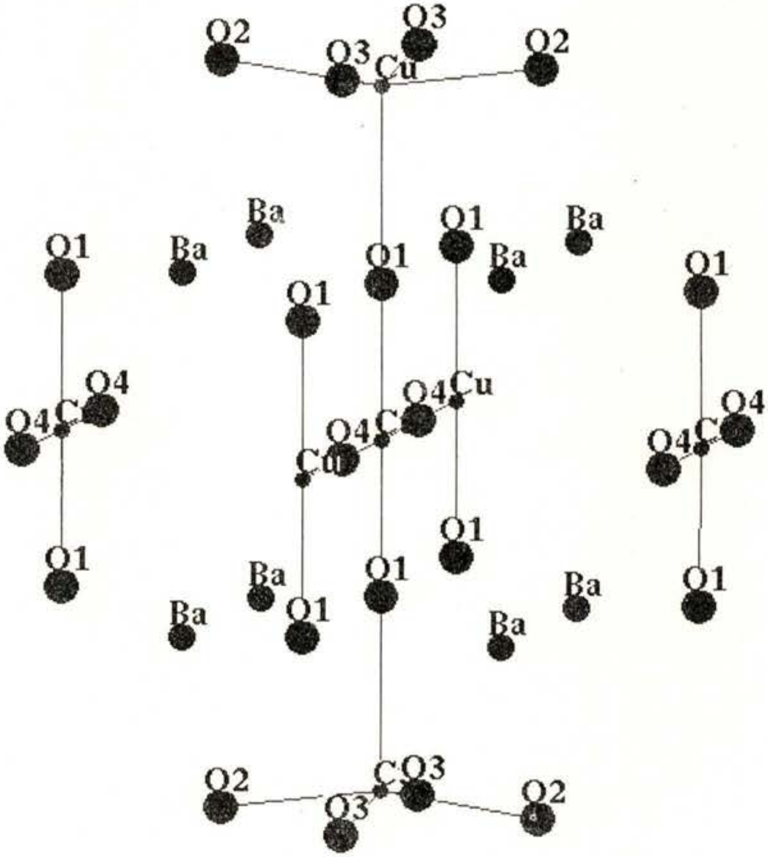

Fig. 2 — Scheme of cluster used in $YBa_2Cu_3O_7$ calculations.

ment is to understand how the electronic structure depends upon oxygen stoichiometry and vacancy distributions, and how this in turn affects superconductivity mechanisms.

Measurements of T_c versus y show [47] a decrease from the maximum (~95 K) at $y \simeq 0.05$ reaching zero for $y \simeq 0.65$ with an interesting plateau for $0.3<y<0.4$. In the non-superconducting region $0.65<y<1.0$ muon spin resonance data [48] reveal a local antiferromagnetic order with Néel temperature varying from ~400 K at $y = 1$ down to zero for $y \simeq 0.5$. One can thus construct a phase diagram in which the oxygen composition, varying primarily in the (a, b) plane, takes the system from superconducting to magnetic phases, with a small coexistence region [49]. Experiments in which Cu is substituted by another transition metal throw additional light on the relationship between oxygen stoichiometry and electronic properties. The iron-substituted case $YBa_2(Cu_{3-x}Fe_x)O_{7-y}$ is especially interesting: first, it is surprising that significant amounts of the magnetic ion, up to $x = 0.15$, can be introduced causing only a gradual reduction in T_c [50]. One possible explanation is that Fe substitutes preferentially at site 1, while the superconducting pairs are associated with site 2 — this is a presently popular speculation. Secondly, additional oxygen enters the lattice with iron, presumably because of its propensity to form tetrahedral four-fold and octahedral six-fold coordination. Mössbauer spectroscopy experiments on ^{57}Fe reveal electric field

TABLE III — Self-consistent atomic orbital populations and ionic charges for reference compounds and superconductors as calculated by the embedded cluster method.

	Cu_2O	CuO	$KCuO_2$	La_2CuO_4	$YBa_2Cu_3O_7$	
Cu 3d	9.54	9.24	8.98	9.18	9.03	plane
4s	0.69	0.16	0.13	0.05	0.30	
4p	0.11	0.03	0.04	0.06	0.19	
charge	0.66	1.57	1.85	1.72	1.48	
O 2s	1.91	1.97	1.97	1.99	1.94	axial
2p	5.42	5.60	5.45	5.85	5.35	
charge	− 1.34	− 1.57	− 1.42	− 1.84	− 1.30	
				Cu d3	9.23	chain
				4s	0.23	
				4p	0.21	
				charge	1.33	
				O 2s	1.96	b axis
				2p	5.54	
				charge	− 1.50	
				O 2s	1.96	plane
				2p	5.61	
				charge	− 1.56	

gradients and isomer shift characteristics of three or more sites [51]. A convincing interpretation and assignment of sites would be very useful in resolving questions concerning the role of oxygen-site occupancy in charge transport processes.

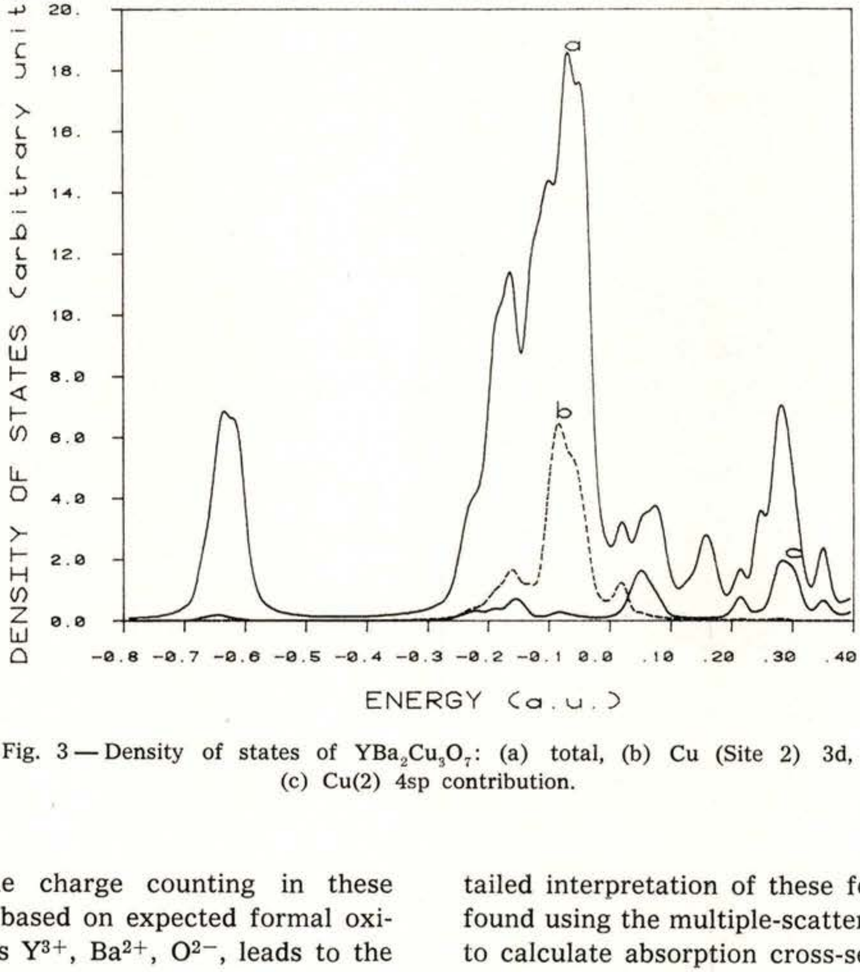

Fig. 3 — Density of states of $YBa_2Cu_3O_7$: (a) total, (b) Cu (Site 2) 3d, (c) Cu(2) 4sp contribution.

A simple charge counting in these compounds based on expected formal oxidation states Y^{3+}, Ba^{2+}, O^{2-}, leads to the notion that copper is present in either multivalent (Cu^{2+}, Cu^{3+}) or mixed valence states Cu^q. In either case the average valence of Cu would be $q = (7-2y)/3$; e. g., $2\frac{1}{3}$ for $y = 0$. We have already mentioned that in La_2CuO_4 the Cu K-edge absorption spectra strongly resemble those of «divalent» CuO. Remarkably, the Cu K-edge of $YBa_2Cu_3O_{7-y}$ also appears essentially similar for $0 < y \lesssim 0.5$, with low energy features associated with the reduced Cu^I species appearing in oxygen deficient compounds, $0.5 \lesssim y \lesssim 1$. A detailed interpretation of these features was found using the multiple-scattering method to calculate absorption cross-sections, and is reported elsewhere [34, 35, 44].

Here we wish to concentrate on simple features of the self consistent variational charge density obtained by the embedded cluster method described in Sec. II. A sketch of the 39 atom cluster, which was treated explicitly, is given on Fig. 2.

Ewald summations of the Coulomb potential and direct space summation of the atomic densities were carried out to embed the cluster in the crystalline environment. The self consistent Mulliken atomic orbital populations and net charges for mono-, di-, and trivalent compounds as well as La_2CuO_4 and $YBa_2Cu_3O_7$ are given on Table III. One sees here that in the 1-2-3 compound, Cu in site 1 (chains) does have a different, more electropositive configuration than that of Cu on site 2 (planes). The difference is, however, considerably less than the $Cu^{II} \rightarrow Cu^{III}$ variation seen in CuO versus $KCuO_2$, which is in turn much less than the formal $d^9s^0 \rightarrow d^8s^0$ ionic configuration change. A notable feature of both site 1 and site 2 is the ~0.5 *e* occupancy of 4sp diffuse states which are mixed into the «oxygen 2p» valence band. Density of states (DOS) diagrams (Figs. 3 and 4) show that the Cu 4sp character is spread across the entire valence band, while the 3d structure is more localized with a peak centered 1-2 eV below the Fermi energy. The main features of DOS obtained in cluster calculations are seen to be rather similar to those found in periodic band structure studies. A charge density map on a (100) plane passing both through Cu(1) and Cu(2) sites is given on Fig. 5. The charge distribution between Cu(1)

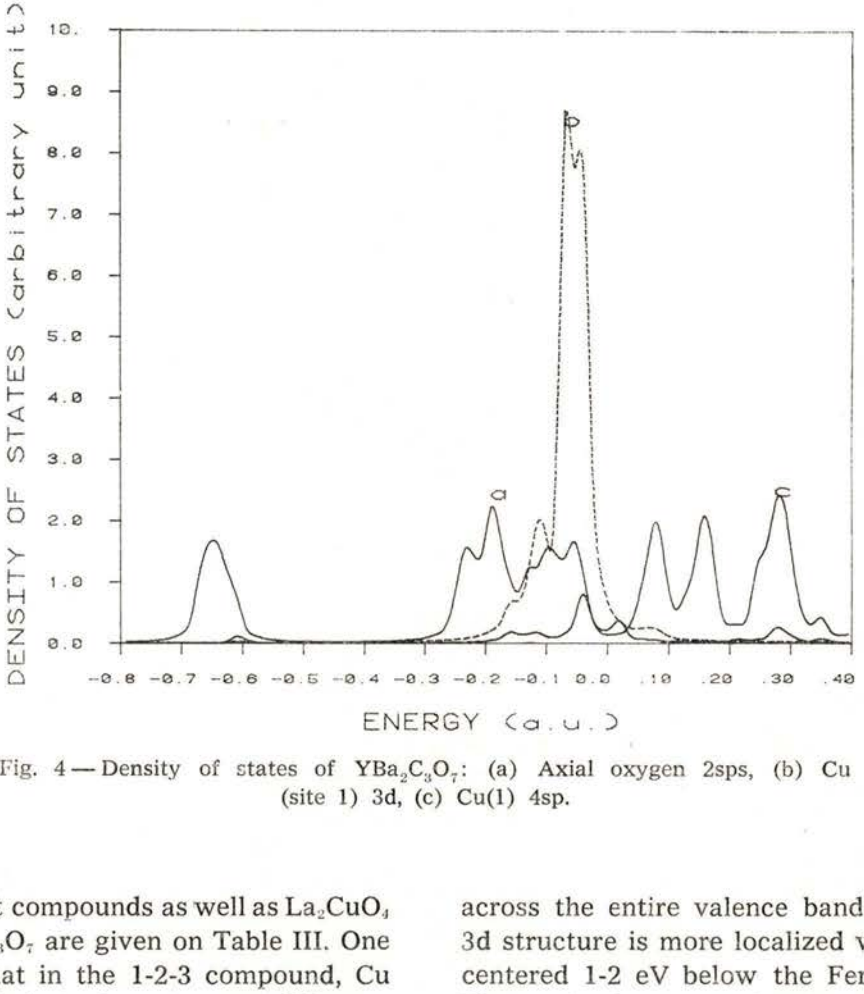

Fig. 4 — Density of states of $YBa_2C_3O_7$: (a) Axial oxygen 2sps, (b) Cu (site 1) 3d, (c) Cu(1) 4sp.

and O(1) on the chains along the crystal b axis is found to be very similar to the Cu(1)-O(4) c-axis distribution. The shorter c axis bond length (1.85 Å vs. 1.94 Å) leads to greater orbital mixing and smaller effective charge, as measured by atomic populations (see Table III). The zig-zag bonding pattern between Cu(2) and its nearest neighbour oxygen has about the same overlap density as Cu(1)-O(4), while the long bond Cu(2)-O(4) shows the lowest density, as would be expected. The variation of this bonding structure, particularly the Cu(1)-O(4)-Cu(2) axial coupling between Cu chains and planes, is expected to be a strong function of oxygen stoichiometry and substitution at metal sites. Theoretical calculations which take into account the observed displacements of O(4) should be very helpful in interpreting measured changes in electronic (and possibly vibrational) properties.

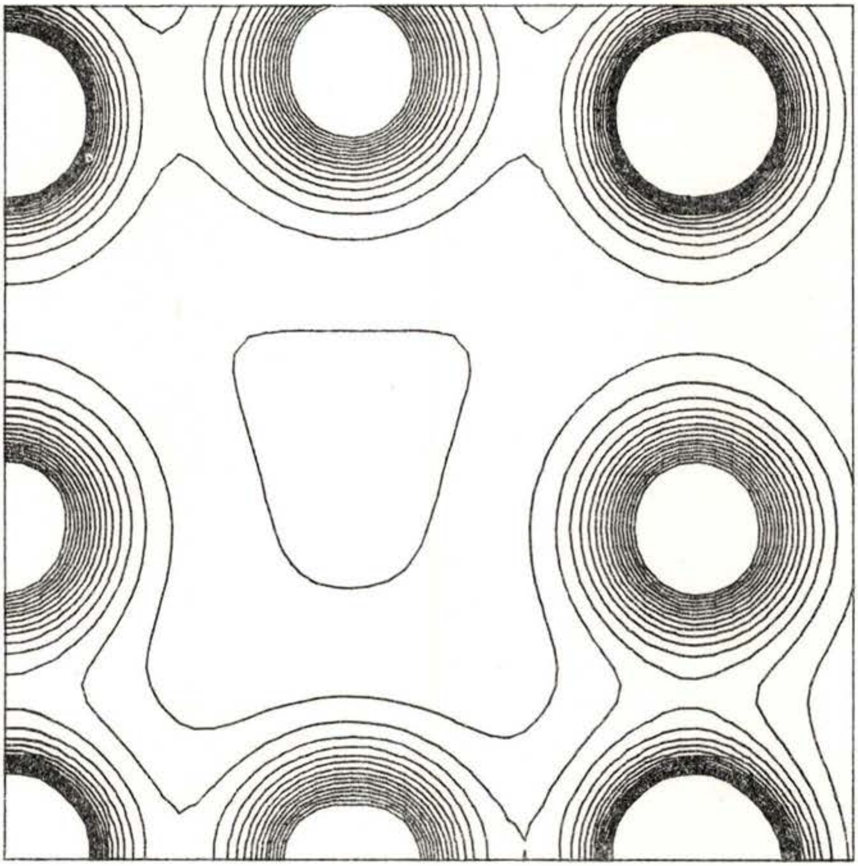

Fig. 5 — Valence charge density contour map of $YBa_2Cu_3O_7$ on a (100) plane containing both Cu(1) and Cu(2) sites. Contour interval = 0.1 e/a_0^3. The lower right corner represents the center of the cluster.

Finally, let us return to the question of the evidence for the elusive Cu^{3+} state. There exists a very successful empirical *theory* of charge conduction in oxides which has been *small polaron* used in explaining thermal and oxygen stoichiometry variation of conductivity and thermopower. According to Mason and others [19, 52] it has been possible to extract the relative concentrations $[Cu^{2+}]$, $[Cu^{3+}]$ as a function of T and y. These data indicate that the site fraction of Cu^{3+} should be of the order or 60 % (at site 1), at 700°C and 1 atm pressure of oxygen corresponding to $y \simeq 0.75$ [53]. Under these conditions Cu^{+1} is predicted to be present at less than 10 % on site 1. So, if Cu^{+3} is present at such a large concentration at 700°C, why is there little or no evidence for its existence in spectroscopy at room temperature and below? One interesting possibility is that the thermal activation energy for $Cu^{2+} \rightarrow Cu^{3+}$ is small in these crystal lattices, due to the slight charge redistributions inferred from calculations on CuO vs. $KCuO_2$ and to the slight differences seen between Cu(1) and Cu(2) in the 1-2-3 compounds. The ground state calculations and X-ray absorption excitations which have been studied have given no clear evidence for this state. However, with the imposition of suitable boundary conditions the transition state scheme can be used to generate and measure the energy of these valence excitations. The results of such «theoretical experiments» would depend somewhat upon the assumed boundary conditions, but should lead to new insights as well.

Thanks are due to G. L. Goodman, E. E. Alp, J. Guo, B. W. Veal, D. J. Lam and T. O. Mason for discussions, ideas and access to data, some of which has not yet been published. This work was supported in part by the U. S. Department of Energy (Grant No. DE-FG02-86-56097A01).

REFERENCES

[1] K. SCHWARZ, P. BLAHA et al., this volume.

[2] J. C. SLATER, *The Self-Consistent Field for Molecules and Solids*, (McGraw-Hill, New York, 1974).

[3] U. VON BARTH and L. HEDIN, J. Phys. **C5**, 1629 (1972).

[4] D. E. ELLIS, G. A. BENESH and E. BYROM, Phys. Rev. **B16**, 3308 (1977); *ibid*, **B20**, 1198 (1979).

[5] V. I. ANISIMOV, V. A. GUBANOV, D. E. ELLIS and E. Z. KURMAEV, J. Phys. **F11**, 405 (1981).

[6] B. LINDGREN and D. E. ELLIS, Phys. Rev. **B26**, 636 (1982).

[7] P. H. DEDERICHS, R. ZELLER, H. AKAI, S. BLÜGEL and A. OSWALK, Phil. Mag. **B51**, 137 (1985).

[8] A. ROSEN, D. E. ELLIS, H. ADACHI and F. W. AVERILL, J. Chem. Phys. **65**, 3629 (1976).

[9] B. DELLEY and D. E. ELLIS, J. Chem. Phys. **76**, 1949 (1982).

[10] K. H. JOHNSON, Adv. Quantum Chem. **7**, 143 (1973).

[11] G. L. GOODMAN and D. E. ELLIS, (submitted).

[12] M. PRESS and D. E. ELLIS, Phys, Rev. **B35**, 4438 (1987).

[13] T. ZIEGLER, J. G. SNIJDERS and E. J. BAERENDS, J. Chem. Phys. **74**, 1271 (1981).

[14] F. KOCH and J. B. COHEN, *Acta Crystallog.* **B25**, 295 (1969).

[15] N. N. GREENWOOD and A. T. HOWE, J. Chem. Soc. (Dalton Trans.) **1**, 110 (1972); **1**, 116 (1972); **1**, 122 (1972).

[16] E. GARTSTEIN and T. O. MASON, J. Am. Ceram. Soc. **65**, C24-26 (1982).

[17] D. E. ELLIS, Phys. Chem. Minerals **14**, 303 (1987).

[18] P. K. KHOWASH and D. E. ELLIS, Phys. Rev. **B36**, 3394 (1987); *ibid*, to be published.

[19] M.-Y. SU, D. E. DORRI: and T. O. MASON, J. Sol. Sta. Chem. **75**, 381 (1988).

[20] L. M. HUISMAN, A. E. CARLSSON, C. D. GELATT, Jr. and H. EHREUREICH, Phys. Rev. **B22**, 991 (1980).

[21] A. NECKEL, P. RASTL, R. EIBLER, P. WEINBERGER and K. SCHWARZ, J. Phys. **C9**, 579 (1976); P. Blaha and K Schwarz, Int. J. Quantum Chem. **23**, 1535 (1983).

[22] T. O. MASON (private communication).

[23] I. P. BATRA, J. Phys. **C15**, 5398 (1982).

[24] S. XIA, C.-X. GUO, L. LIN and D. E. ELLIS, Phys. Rev. **B35**, 7671 (1987).

[25] S. SUGANO and Y. TANAKE, J. Phys. Soc. Jpn. **13**, 880 (1958).

[26] S. OHNISHI and S. SUGANO, Jap. J. Appl. Phys. **21**, L309 (1982).

[27] P. K. KHOWASH and D. E. ELLIS (submitted).

[28] J. D. JORGENSEN, M. A. BENO, D. G. HINKS, L. SODERHOLM, K. J. VOLIN, R. L. HITTERMAN, J. D. GRARE, I. K. SCHULLER, C. U. SEGRE, ZHANG and M. S. KLEEFISCH, Phys. Rev. **B36**, 3608 (1987).

[29] J. D. JORGENSEN, B. W. VEAL, W. K. KWOK, G. W. CRABTREE, A. UMEZAWA, L. J. NOWICKI and A. P. PAULIKAS, Phys. Rev, **B36**, 5731 (1987).

[30] J. D. JORGENSEN, H. SHAKED, D. G. HINKS, B. DABROWSKI, B. W. VEAL, A. P. PAULIKIS, L. J. NOWICKI, G. W. CRABTREE, W. K. KWOK and L. H. NUNEZ, Physica **C153-155**, 578 (1988).

[31] M. A. BENO, L. SODERHOLM, D. W. CAPONE, D. G. HINKS, J. D. JORGENSEN, J. D. GRACE, I. K. SCHULLER, C. U. SEGRE and K. ZHANG, Appl. Phys. Lett. **51**, 57 (1987).

[32] R. W. G. WYCKOFF, Crystal Structures, (Interscience, N. Y., 1964) Vol. 2.

[33] G. L. GOODMAN, D. E. ELLIS, L. SODERHOLM and E. E. ALP (in preparation).

[34] E. E. ALP, G. K. SHENOY, D. G. HINKS, D. W. CAPONE, L. SODERHOLM, H. B. SCHUTTLER, J. GUO, D. E. ELLIS, P. A. MONTANO and M. RAMANATHAN, Phys. Rev. **B35**, 7199.

[35] E. E. ALP, G. K. SHENOY, L. SODERHOLM, G. L. GOODMAN, D. G. HINKS, B. W. VEAL and D. E. ELLIS, Mat. Res. Soc. Symp. Proc. **99**, 177 (1988).

[36] J. GUO and D. E. ELLIS (unpublished).

[37] P. STEINER, V. KINSINGER, I. SANDER, B. SIEGWART, S. HUFNER, C. POLITIS, T. HOPPE and H. P. MULLER, Z. Phys. **B67**, 497 (1987).

[38] L. F. MATTHEISS and D. R. HAMANN, Sol. Sta. Comm. **63**, 395 (1987).

[39] S. MASSIDA, J. YU, A. J. FREEMAN and D. D. KOELLING, Phys. Lett. **A122**, 198 (1987); **A122**, 203 (1987).

[40] H. BIANCHI, A. C. CASTELLANO, HM. DE SANTIS, P. DELOGU, A. GARGANO and R. GIORGI, Sol. St. Comm. **63**, 1135 (1987).

[41] B. W. VEAL, D. E. ELLIS and D. J. LAM, Phys. Rev. **B32**, 5391 (1985).

[42] L. HEDIN, in «X-Ray Spectroscopy», ed. by L. V. AZAIROFF, (McGraw-Hill, N. Y. 1974), p. 226.

[43] C. R. NATOLI, F. W. KUTZLER, O. K. MISEMER and S. DONIACH, Phys. Rev. **A22**, 1104 (1980).

[44] J. GUO, E. E. ALP, G. L. GOODMAN, D. E. ELLIS and L. SODERHOLM, (in preparation).

[45] Y. KUBO, Y. NAKABAYASKI, J. TABUCHI, T. YOSHITAKE, A. OCHI, K. UTSUMI, H. IGARASHI and M. YOUEZAWA, Jpn. J. Appl. Phys. **26**, B1888 (1987).

[46] H. RIESEMEIER, Ch. GRABOW, E. W. SCHEIDT, V. MÜLLER, K. LÜDERS and D. RIEGEL, Sol. Sta. Commun. **64**, 309 (1987).

[47] H. YASUOKA, T. SHIMIZU, T. IMAI, S. SASAKI, Y. UEDA, K. KOSUGE, Hyperfine Inter (to be published).

[48] J. H. BREWER, E. J. ANSALDO, J. F. CAROLAN, A. C. D. CHAKLADER, W. N. HARDY, D. R. HARSHMAN, M. E. HAYDEN, M. ISHIKAWA, N. KAPLAN, R. KEITEL, J. KEMPTON, R. F. KIEFL, W. J. KOSSLER, S. R. KRIETZMAN, A. KULPA, Y. KUMO, G. M. LUKE, H. MIYATAKE, K. NAGAMINE, Y. NAKAZAWA, N. NISHIDA, K. NISHIYAMA, S. OHKUMA, T. M. RISEMAN, G. ROEHMER, P. SCHLEGER, D. SHIMADA, C. E. STRONACH, T. TAKABATAKE, Y. J. UEMURA, Y. WATANABE, D. Ll. WILLIAMS, T. YMAZAKI and B. YANG, Phys. Rev. Lett. **60**, 1073 (1988).

[49] B. W. VEAL, A. P. PAULIHIS, D. J. LAM and J. W. DOWNEY (unpublished).

[50] B. D. DUNLAP, J. D. JORGENSEN, W. K. KWOK, C. W. KIMBALL, J. L. MATYHIEWICZ, H. LEE and C. U. SEGRE, Interlaken Conf. on Supercond. (to be published).

[51] E. BAGGIO-SAITOVITCH, I. SOUZA AZAVEDO, R. B. SCORZELLI, H. SAITOVITHC, S. D. DE CUNHA, A. P. GUIMARÃES, P. R. SILVA and A. Y. TAKEUCHI, Phys. Rev. **B37**, 7969 (1988).

[52] M.-Y. SU, K SUJGTG and T. O. MASON, in *Ceramic Superconductors II*, ed. by M. F. YAN, (Amer. Cer. Soc., Westerville, OH, 1988).

[53] K. FUEK(, K. KITAZAWA, K. KISHIO, T. HASEGAWA, S.-I. ICHIDA, H. TAkAGA(and S. TANAKA, in «Chemistry of High Temperature Superconductors» (Amer. Chem. Soc. Washington, D. C., 1987), p. 38.

CHARGE DENSITY AND CHEMICAL BONDING

DIRK FEIL
Chemical Physics Laboratory
University of Twente
P.O.B. 217
7500 AE Enschede
Netherlands

ABSTRACT — Madelungs theory of bonding in ionic crystals constituted the first quantitative theory of chemical bonding. The simplest model of charge distribution gave highly accurate results for a limited number of cases. Quantum theory suggests that in general the full wave function has to be known, but Hohenberg and Kohn showed the electron density distribution to contain all information necessary to calculate chemical bonds: *density functional theory*. Kohn and Sham suggested a computational procedure, quite similar to the Hartree-Fock-Slater method, containing the local density approximation. This and a number of other approximations are tested by comparing the results of calculations with experiment. The following properties are considered: the effect of correlation on the dissociation energy of diatomic molecules, the electron density distribution in atoms, and the structure factors of crystalline silicon, using $Si_n H_{2n+2}$ clusters in the calculation. The method seems to yield excellent electron density distributions.

Covalent bonding may cause strong electric fields to occur in the environment of the molecule. The effect of external electric fields on the charge distribution of molecules is discussed. These electric fields play a major role in hydrogen bonding. As a result the electron density distribution in hydrogen bonded complexes differs from the one in the monomers. The calculated effect is in excellent agreement with the one observed by X-ray diffraction in oxalic acid dihydrate. Substantial reductions in the R-factor occur when the theoretical model is increasingly refined so as to account for covalent bonding, hydrogen bonding, and the effects of electric fields subtended by surrounding molecules. This agreement testifies of the sensitivity of X-ray diffraction and the reliability of the electron density distribution calculated by the Hartree-Fock-Slater method.

INTRODUCTION

When Demokritus postulated the existence of atoms to reconcile his notion of the basic invariability of matter with the observation that everything changes in the course of time, he implicitly introduced the problem of chemical bonding: how do atoms and molecules stick together? It is clear that on basis of fundamental philosophical notions not much could be said about the character of the bonds between atoms. When during the Renaissance the concept of atoms was revived, it played a large role in the thinking of people like Boyle and Newton and soon the emerging chemistry was formulated in terms of atoms. This provided an empirical basis to chemical bonding and at the end of the previous century much could be said about strength and directionality of the bonds between atoms. Neither physicists nor chemists, however, could explain the nature of the bonds in terms of existing physics.

At the turn of the century it became clear that atoms consisted of more-elementary, charged particles and that charge transfer between atoms was possible. In 1909 Madelung [1] calculated the energy of an ionic crystal. The calculation was based on Coulomb forces between the ions constituing the crystal. This work established the first relation between the charge distribution and chemical bonding. Kossel (1916) [2] explained the bonding in the methane molecule by the same method in which he assumed the C-atom to be positive and the H-atoms to be negative. At the same time Lewis used the new ideas about the structure of atoms to explain the bonding in homonuclear compounds. His model became widely used and can still be found in textbooks on Organic Chemistry. Although it lacks foundation in fundamental physics, the basic idea can be found in the present quantumchemical theories. The Lewis model again relates chemical bonding to the charge distribution.

In 1927 Heitler and London explained the bonding in the hydrogen molecule in terms of the newly developed quantum theory. Later calculations show perfect agreement between theory and experiment. In quantum theory the state of a system such as a molecule is described by the wave function and, knowing the wave function, one can calculate the energy of the system. The value of the wave function depends on the value of 4n variables, in which n is the sum of the number of electrons and of nuclei in the molecule.

In 1964 Hohenberg and Kohn [3] showed in their innovative paper that the energy of the ground state of a system of electrons is a functional of the electron density distribution (EDD). Unfortunately the relation between the EDD and the energy is unknown, except for a few special systems. In a subsequent paper Kohn and Sham [4] used the variational principle to derive a Fock-like one-particle equation. The resulting M.O.'s yield the EDD.

The first half of the present paper, titled *from the Electron Density Distribution to the Cremical Bond*, discusses how one proceeds from the EDD to bonding. An almost trivial example is the ionic bond, with its simple assumptions and its excellent results. Then follows the Hohenberg--Kohn-Sham theory, together with some of its results.

When atoms combine to form a covalent bond, redistribution of the electron density takes place. The resulting EDD is open for inspection by X-ray diffraction. Provided the experiment is accurate enough, the results offer a severe test for the quality of the quantumchemical calculations [5]. The inhomogeneous charge distribution in molecules create an electric field that, depending on the moments of the molecular charge distribution, can extend quite far beyond the region of the molecule. The interaction between this field and the charge distribution in other molecules is one of the main contributors to hydrogen bonding and may play a considerable role in other intermolecular interactions. The molecular electric field polarizes surrounding molecules, an effect that recently has been observed by X-ray diffraction and calculated by quantumchemical methods [6]. These effects are discussed in the second half of the paper: *from Chemical Bonding to the Electron Density Distribution.*

FROM ELECTRON DENSITY DISTRIBUTION TO CHEMICAL BONDING

Ionic Bonding

The simplest model of charge distribution is to replace the atoms in a molecule or crystal by point charges. This model was used by Madelung (1909) to calculate the cohesive energy of a crystal [1]. Without repulsive forces between atoms, crystals would collapse. Born introduced a simple term to account for the repulsive forces between ions, containing the parameters n and b, which can be obtained from compressibility data and from $\partial E / \partial V = 0$. The energy is written as:

$$E = \frac{1}{2} \sum \frac{Q_i Q_j}{R_{ij}} + \sum \frac{b}{R_{ij}^n} \quad (1)$$

in which Q_i and Q_j are the charges on the ions and R_{ij} is the interionic distance. The first summation extends over all the ions and the second one only over nearest neighbours.

Using the model Sherman calculated in 1932 the cohesive energy of a number of crystals [7]. Some results are reported in table 1. The agreement with experiment is seen to be excellent. But from the beginning it was clear that the model fits only a limited number of crystals.

TABLE 1 — Comparison of the experimental and calculated values of the cohesion energy of some ionic compounds (kcal/mol).

Substance	U_{exp}	U_{theor}	Difference (%)
MgF_2	688	697	1.3
Li_2O	693	695	0.3
NiO	966	968	0.2
Al_2O_3	3617	3708	2.5

Density functional theory

Schrodenberg:	Let's start from the beginning — first, every electron has a wave function.
Alice	: Is it worn like clothing?
Schrodenberg:	Not quite.
Alice	: How do we know?
Schrodenberg:	Well to be perfectly truthful — we humans give it to them.
Alice	: Perhaps they'd be better off without one.

From Richard Weiss, the Magic of Physics, MACMILLAN, London (1987).

Quantum theory provides a valid basis for chemical bonding. In those cases where full calculations have been carried out the dissociation energy of molecules is in complete agreement with experiment. Unfortunately full calculations are found to be very cumbersome with the result that they are limited to very small systems. The main reason for the unwieldiness of the calculations is that the computation of the energy requires knowledge of the electronic wave function, a function with the space and spin coordinates of the electrons as variables. To handle systems of practical value, such as chemically interesting molecules and crystals, one has to introduce several approximations, some of which are doubtful in character.

Hohenberg and Kohn [3] showed that it was not necessary to know the full wave function, but that knowledge of the electron density distribution (EDD) was enough. More precisely: the energy of the electrons in a molecule in the ground state is a functional of the EDD: $E[\rho(\mathbf{r})]$. Unfortunately the relation between $\rho(\mathbf{r})$ and the energy is unknown. Kohn and Sham [4] showed in a subsequent paper how several good approximations could be made and turned the method into the widely used basis for computational solid state physics. Only recently the method gained acceptance in theoretical chemistry.

The Hohenberg-Kohn-Sham (HKS) approach will be briefly outlined to understand its possibilities and limitations. The energy of the electrons in a molecule is written as:

$$E = T' + E_{ne} + E_{ee}' \qquad (2)$$

in which T' is the kinetic energy, E_{ne} represents the interaction between the nuclei and the electrons and E_{ee}' stands for the mutual interaction between the electrons. We write

$$E_{ne} = \int V_n(r) \ \rho(r) \, d^3r \qquad (3)$$

in which $V_n(r)$ is the potential extended by the nuclei.

Writing the interaction between the electrons as follows

$$E_{ee} = \frac{e^2}{2} \int \frac{\rho(r)\, \rho(r')}{|r-r'|} d^3(r) d^3(r') \quad (4)$$

we include self-interaction of the electrons. Furthermore by considering the interelectronic interaction as the interaction between two charge clouds we neglect exchange and correlation between the electrons. For reasons that soon will be clear, we replace T' by T, the kinetic energy of a system of non-interacting electrons with the same EDD. Again we make an error. Both errors are accounted for by adding the term E_{xc}. The expression for the energy becomes:

$$E = T + E_{ne} + E_{ee} + E_{xc} \qquad (5)$$

Kohn and Sham showed with the help of the variational principle that a system of non-interacting electrons in the field V(r) will yield the same EDD as the system under consideration, provided V(r) is given by:

$$V(r) = V_n(r) + V_e + V_{xc} \qquad (6)$$

in which

$$V_e(r) \equiv -e \int \{ \rho(r') / |r-r'| \} d^3r' \quad (7)$$

and the exchange correlation potential is defined by:

$$V_{xc}(r) \equiv \partial E_{xc} / \partial \rho(r) \qquad (8)$$

Non-interacting electrons obey a simple Fock-equation:

$$\{ -\frac{1}{2} \nabla^2 + V(r) \} \, \phi_n(r) = \varepsilon_n \phi_n(r) \quad (9)$$

and the EDD is given by

$$\rho(r) = \sum_n |\phi_n(r)|^2 \qquad (10)$$

Since the orbitals and the orbital energies refer to the system of non-interacting electrons their physical significance remained obscure for a long time. The eigenvalues should not be identified with excitation energies, with the exception of the one corresponding with the highest occupied orbital, which equals the ionization potential [8]. The EDD's of the interacting electrons in the nuclear field $V_n(r)$ and of the non-interacting electrons in the field V(r), however, are the same by definition.

Several authors have suggested expressions relating E_{xc} to the EDD, based on the relation for a homogenous electron gas [9].

Often one writes:

$$E_{xc} = E_x + E_c \tag{11}$$

adding the contributions for exchange and correlation respectively. Hartree-Fock calculations take full account of the exchange energy and the self interaction, the major contributions to E_{xc}.

Following Slater, Kohn and Sham wrote:

$$V_x(r) \equiv \delta E_x / \delta \rho(r) = -(1/\pi)\,[3\pi^2 \rho(r)]^{1/3} \tag{12}$$

the value $V_x(r)$ being for a homogeneous electron gas. The assumption that the potential at a certain position is a function of the electron density at that point is known as the local density approximation (LDA).

To include the effects of the correlation as well we write:

$$V_{xc}(r) = -(3\alpha/2\pi)\,[3\pi^2 \rho(r)]^{1/3} \tag{13}$$

with the empirical parameter, $\alpha = 0.7$ yielding good results. The resulting Fock-equation is identical to the one used in the Hartree-Fock-Slater method (HFS). In a refined version of the method the exchange-correlation energy is written as a

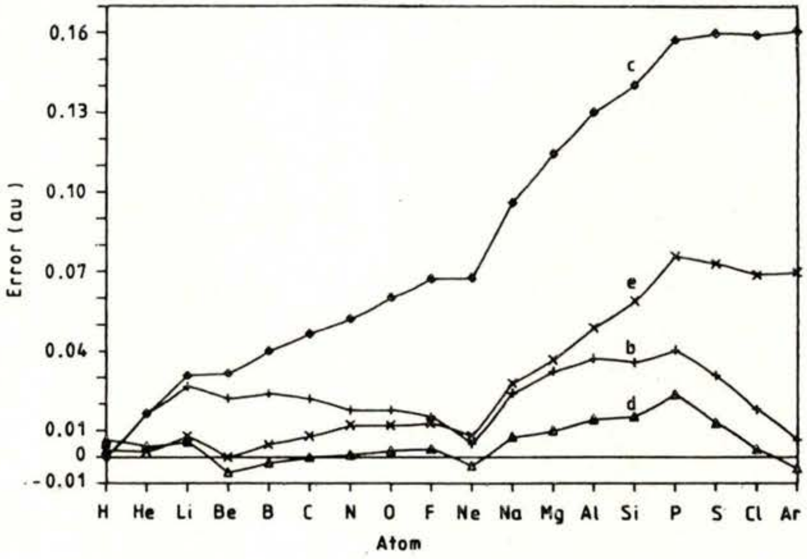

Fig. 1 — Error in the atomic correlation energy for hydrogen to argon. The approximations used are:
a : Kohn and Sham's local density approximation (LDA), not shown
b, c: LDA, corrected for self-interaction
d, e: gradient-corrected functionals.
(From M. T. Carroll, R. F. W. Bader and S. H. Vosko, J. Phys. B: At. Mol. Phys. (1987), 20, 3599).

functional of the spin densities and the local spin density approximation is used (LSDA).

We shall now test the quality of the various approximations in Density Functional Theory by comparing calculated molecular properties with experimental results.

By adding the correlation energy to the Hartree-Fock energy they obtained total energies and were able to compare the values obtained for the dissociation energy of a large number of diatomic molecules with experimental values. The results for a number of diatomic oxides is shown in Fig. 2.

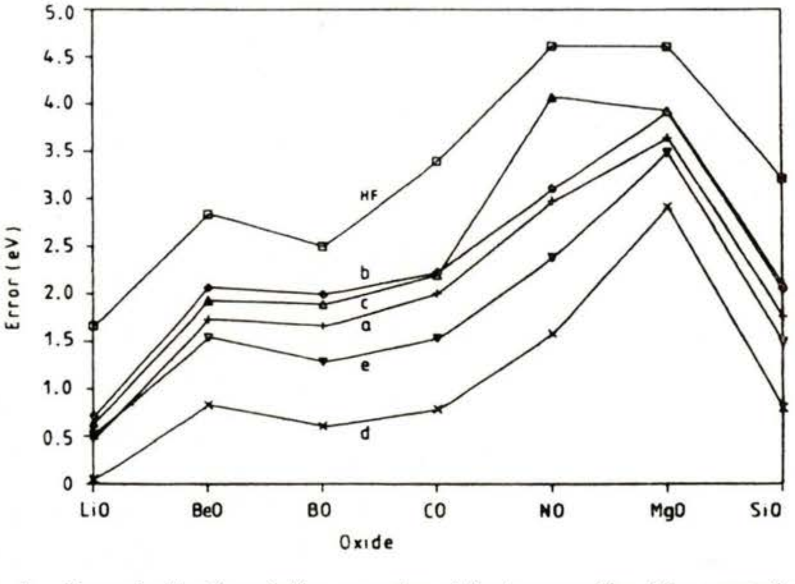

Fig. 2 — Error in the dissociation energies of first-row oxides. The approximations used are:
HF: Hartree-Fock
a : Kohn and Sham's local density approximation (LDA)
b, c: LDA, corrected for self-interaction
d, e: gradient-corrected functionals.
(From M. T. Carroll, R. F. W. Bader and S. H. Vosko, J. Phys. B: At. Mol. Phys. (1987), 20, 3599).

In recent work by Carroll *et al.* various proposals for the correlation energy are tested [10]. The authors consider application of the LSDA approximation (a), this approximation corrected for self-interaction (b, c), and the use of gradient-corrected functionals for the correlation energy (d, e). Fig. 1 shows the error in the correlation energy for a number of atoms.

Although all schemes yield an improvement over the Hartree-Fock results, there is no clear preference for anyone. The agreement with experiment is not quite satisfactory.

The next comparison concerns the EDD in simple atoms [11]). Fig. 3 shows that for the Be-atom the HFS-method in which the orbitals are expanded in a quadruple-ζ

basis set yields virtually the same EDD as the Hartree-Fock method. In Fig. 4a various expressions for V_x are tested by comparing the resulting EDD for the Ne-atom with the Hartree-Fock value. Fig. 4b shows the difference between the EDD's, obtained with different expressions for E_{xc}, with the EDD calculated with the Configuration Interaction method [12], which is considered to yield very accurate results.

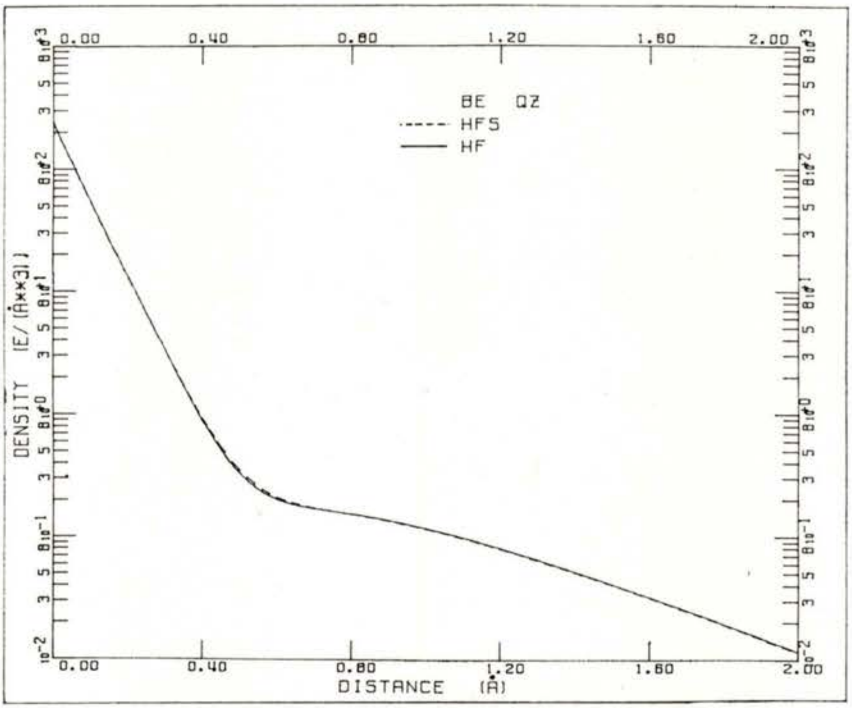

Fig. 3 — The electron density distribution in the Be-atom.
broken line: HFS - calculation.
solid line : CI - calculation

Nearly all calculations of the electron energy in solids are based on the local density approximation. The translational symmetry is accounted for by the use of Bloch orbitals. Various approximations are used to describe the translation-invariant part of these orbitals. Velders and Feil recently calculated the EDD of a number of Si_nH_m-clusters using the LDA-approximation [13]. The orbitals were expanded in a large basis set of atomic orbitals. Fig. 5 shows the EDD in the central region of the Si_8H_{18} cluster. The EDD of the most central atom of the cluster was used to construct the EDD of an infinite crystal. Accurate measurements of the structure factors of perfect crystals by the Pendellösung method [14] allow judgement of the quality of the results of the computations. Table 2 shows the measured and the calculated values of a number of structure factors. The present method is seen to yield highly accurate structure factors, superior to the results of band structure

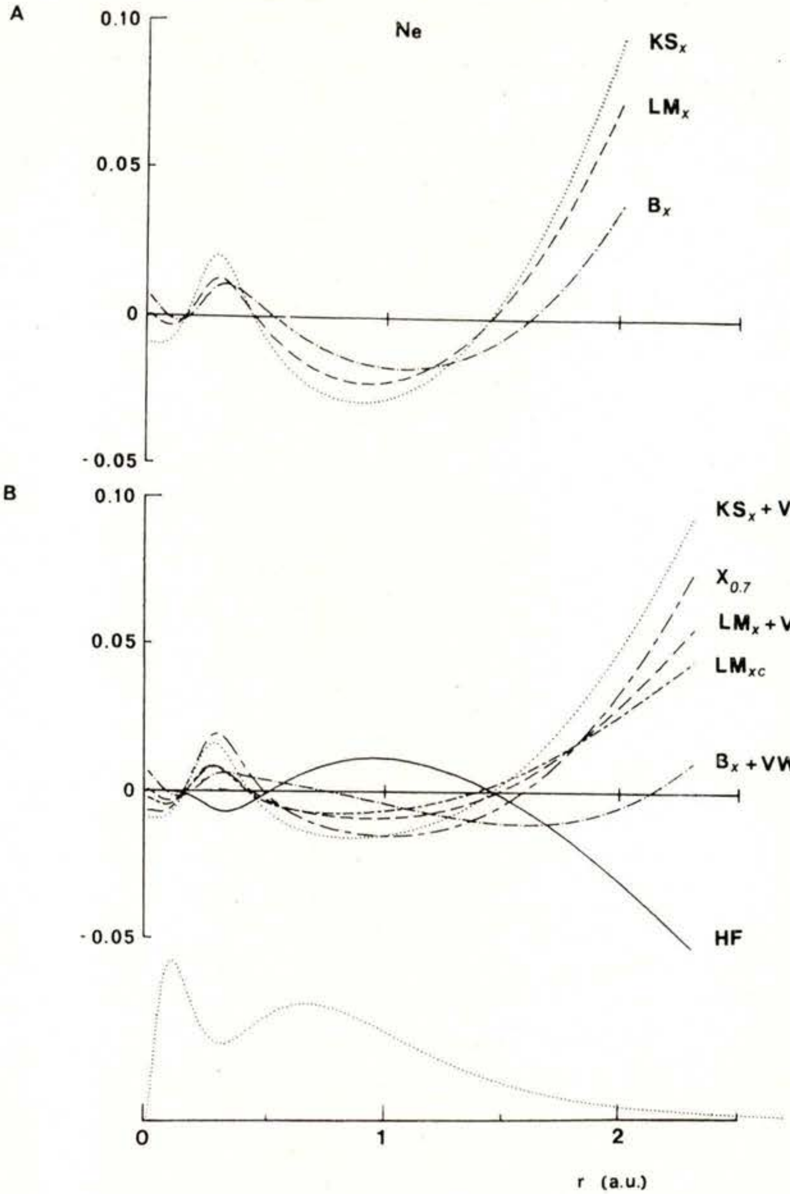

Fig. 4 — The relative deviation from HF and exact results of the EDD in Ne, obtained for various exchange-correlation potentials. The radial electron density $4 \pi r^2 \rho$ is given for comparison.

(a) $(\rho-\rho_{\mathrm{HF}}) / \rho_{\mathrm{HF}}$, (b) $(\rho-\rho_{\mathrm{exact}}) / \rho_{\mathrm{exact}}$

The approximations used are (see [7] for details):

KS_x : Kohn and Sham, exchange only
LM_x : non-local exchange only functional
B_x : semi-empirical potential
VWN_c: local correlation potential, corrected for self-correlation
$\mathrm{X}_{0.7}$: Semi-empirical LDA exchange-correlation potential
LM_{xc} : non-local exchange-correlation potential
HF : Hartree-Fock

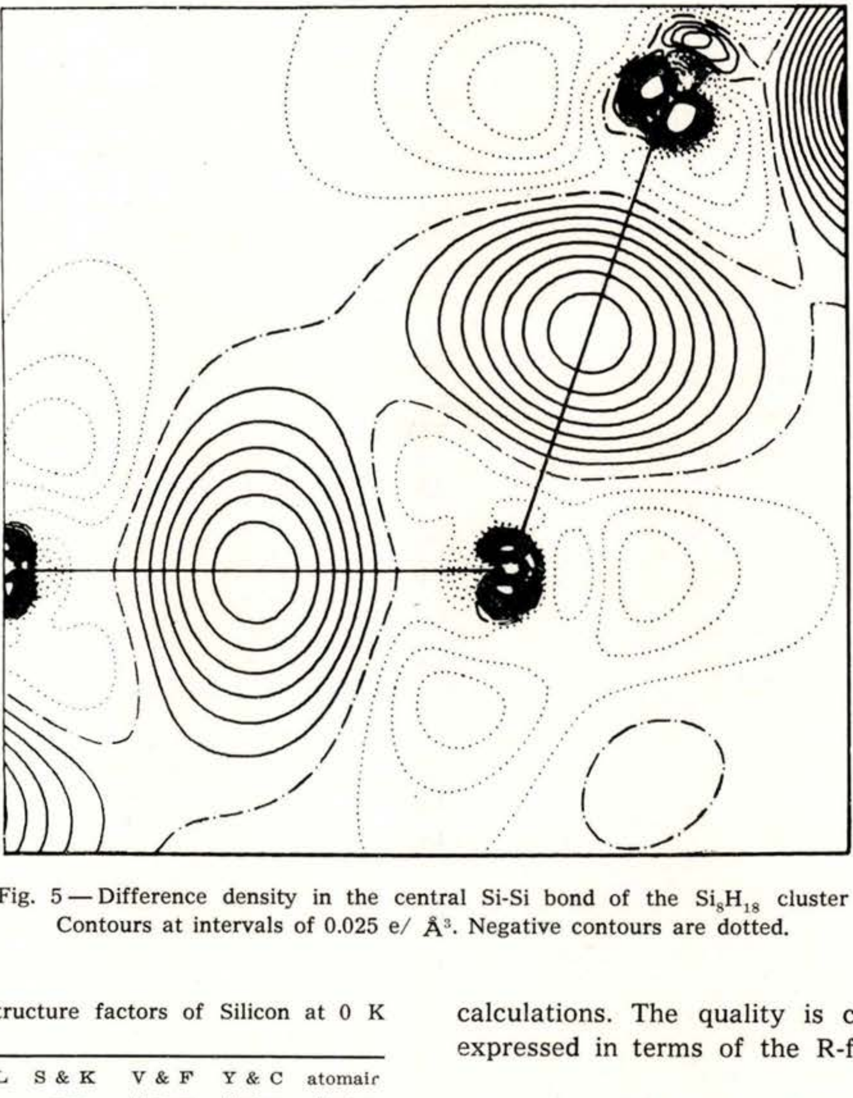

Fig. 5 — Difference density in the central Si-Si bond of the Si_8H_{18} cluster Contours at intervals of 0.025 e/ Å³. Negative contours are dotted.

TABLE 2 — Structure factors of Silicon at 0 K

h k l	sinO/L	S & K	V & F	Y & C	atomair
		exp	theory	theory	theory
1 1 1	0,159	10,724	10,659	10,699	10,529
2 2 0	0,260	8,655	8,659	8,615	8,710
3 1 1	0,305	8,023	8,039	7,976	8,164
4 0 0	0,368	7,454	7,464	7,381	7,508
3 3 1	0,401	7,250	7,234	7,149	7,183
4 2 2	0,451	6,715	6,716	6,611	6,702
3 3 3	0,478	6,423	6,422	6,307	6,439
5 1 1	0,478	6,445	6,454	6,336	6,439
4 4 0	0,521	6,049	6,056	5,941	6,035
R — factor (%).			0,19	1,07	0,83

S & K: T. Saka and N. Kato [14].
V & F: G. Velders and D. Feil [13].
Y & C: M. T. Yin and M. L. Cohen [15].

calculations. The quality is conveniently expressed in terms of the R-factor:

$$R = \frac{\Sigma_H \mid F_H^{obs} - F_H^{calc} \mid}{\Sigma_H F_H^{obs}} \tag{14}$$

FROM BONDING TO CHARGE DENSITY

In the first part we have seen how bonding can be derived from the atomic or molecular EDD. Since covalent bonding between atoms leads to intra- and inter--atomic charge transfer, electric fields are surrounding the molecules. In this part we shall show how these electric fields affect the EDD in neighbouring molecules, an effect that can be calculated by quantum chemistry and verified by X-ray diffaction.

The electric field of a molecule

As an example we consider the water molecule. Defining the deformation or difference density distribution, $\Delta\rho$ (r), by the

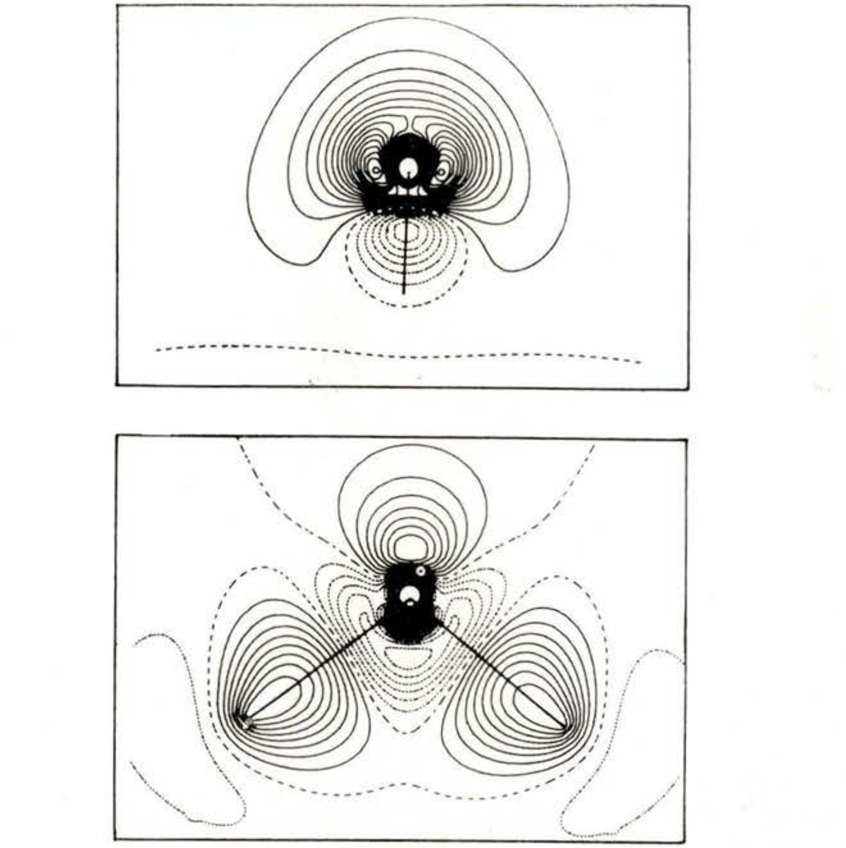

Fig. 6 — Difference density in the water molecule. Contours at intervals of 0.015 au (~0.1 e/ Å^3). The triple-ζ basis set was augmented with Slater-type d- and f-functions on the oxygen and p- and d-functions on the hydrogen. The dipole moment is given in au's.

difference between the molecular EDD and the sum of the atomic EDD's with the nuclei on the molecular positions, this distribution shows the extent to which molecule formation leads to electron transfer within the atomic regions and between the atoms (Fig. 6). A more detailed analysis [16] shows that dipole moment of the water molecule is as much due to charge transfer between atoms as to atomic dipole moments. Rosenberg and Shavitt [17] showed that large basis sets and CI are necessary to obtain the proper dipole moment of water. In Fig. 6b the results of various quantumchemical methods with respect to the dipole moment are compared. The results of the Hartree-Fock-Slater calculation, employing a large basis set are seen to be excellent.

Effect of electric fields on the EDD in atoms

The first type of bonding discussed was *electrostatic bonding* between ions. It was assumed that the ions were spherically symmetric about the nucleus. It is clear that this can only be a first approximation since the electric field will affect the EDD. To illustrate the effect we place a closed shell atom such as Ne in a weak extern electric field, E_{ex}, in the z-direction. The resulting electron density distribution, $\rho^E(r)$, shows a complex pattern. To bring out the details, the original electron density distribution, $\rho^{\circ}(r)$, is subtracted and the difference, the so called polarization density, is shown in Fig. 7. We might have expected a shift of the electron cloud in the direction opposite to the field. The polarization density, however shows alternating regions of depletion and accumulation.

The calculations were carried out with the Hartree-Fock-Slater method, using Slater-type orbitals as basis set. The method is described by Krijn and Feil [16].

The pattern of the polarization density can easily be understood as follows: the total electron density is the sum of the densities of the occupied orbitals:

$$\rho^{E}(r) = 2 \Sigma \mid \phi^{E}(r) \mid^{2} \qquad (15)$$

in which double occupancy is assumed. The atomic orbitals of the polarized atom differ slightly from the ones in the free atom, and can be obtained by mixing in unoccupied orbitals ϕ_j^O of the proper symmetry.

$$\phi_i^{E}(r) = \phi_i^{O}(r) + + \sum_j c_{ij}\, \phi_i^{O}(r) \qquad (16)$$

Mixing in of occupied orbitals does not change the Slater determinant.

Since the effect of the electric field is small, the coefficients c_{ij} can be calculated by second order perturbation theory:

$$c_{ij} = \frac{E_{cx} < \phi_j^O \mid z \mid \phi_i^O >}{\varepsilon_i - \varepsilon_j} \qquad (17)$$

in which ε_i and ε_j are orbital energies.

For qualitative purposes we can restrict the summation to the coupling of the highest occupied atomic orbital with the lowest unoccupied one with the proper symmetry. In case of a field in the z-direction, the $2p_z$ orbital of Ne is coupled with the 3s-orbital. The energy difference in the denominator of (17) makes other contributions less significant.

The contribution to the total electron density distribution by the polarized orbital $2p_z^E$ is given by

$$\begin{aligned} 2 \times \mid 2p_z^E \mid^2 &= 2 \times \mid 2p_z^O \mid^2 + \\ &+ 4 \times c \times 2p_z^O \times 3s^O + \ldots \qquad (18) \end{aligned}$$

Consequently the contribution to the polarization density is

$$\Delta\rho\ (r) = 4 \times c \times 2p_z^O(r) \times 3s^O(r) \quad (19)$$

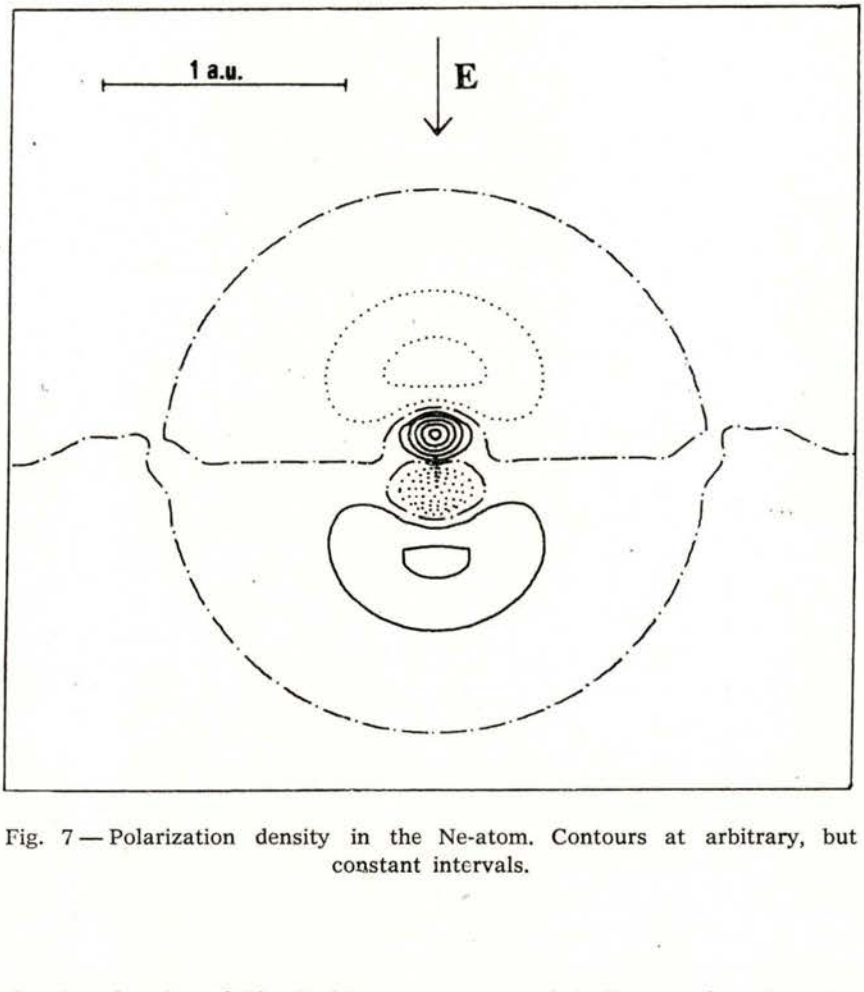

Fig. 7 — Polarization density in the Ne-atom. Contours at arbitrary, but constant intervals.

The polarization density of Fig. 7 shows the topology of the product of the 2p and the 3s orbitals. Since these orbitals are hydrogenic in character, the product can easily be visualized: the number of nodal points on the z-axis is the sum of the number of nodes of the individual orbitals, i. e. one for the 2p and four for the 3s-orbital, making a total of five, one of which is on the origin.

The dipole moment, calculated from the polarization density, might appear to be a good indicator for the strength of the electric frield. Indeed, the polarizabilities along the different axes of the water molecule, calculated with the HFS-method, closely correspond to the experimental values. Where the fields are due to neighbouring atoms problems arise. In Fig. 8a we see the polarization density distribution of a water molecule in the field of a proton. The oxyxen atom shows the familiar features of a polarized atom. Subsequently the proton is replaced by a potassium ion. The K...O distance is chosen so as to be the same as the K...O

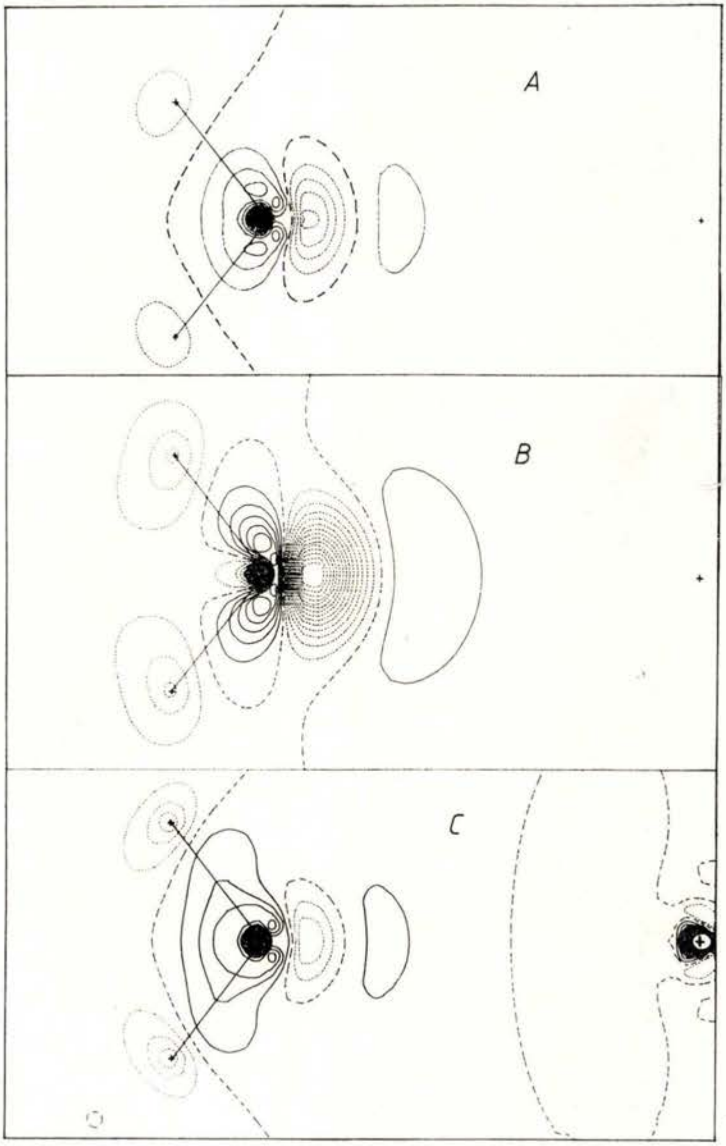

Fig. 8 — Polarization density of the water molecule in the field of:
a) a proton
b) a potassium ion.
c) Interaction density in the $H_2O...K^+$ complex.
Contours at .005 a. u. intervals.

distance in the 18-crown-6 ...K^+ complex. First we calculate the electric field in and around the K^+-ion. Then the water molecule is placed in this ionic field and the polarization density is calculated. Fig. 8b shows the polarization to be much larger than in the proton case. The difference can be explained by considering the electric field in the region of the K^+-ion. Penetrating the ion the nucleus becomes less shielded and the electric field increases, leading to increased polarization (Fig. 8b). A HFS-calculation of the $K^+ \ldots H_2O$ complex, however, yields a different polarization density distribution (Fig. 8c). The difference can be explained by taking exchange repulsion into consideration: the Pauli principle forbids extension of the electron cloud of the water molecule into the K^+-region.

The electron density distribution in the hydrogen bond

The forces between molecules consist of many contributions. We distinguish: the electrostatic interaction between the undisturbed charge distributions of the monomers, the effect of charge transfer and mutual polarization, the repulsive exchange forces, and the London forces, due to the correlation between the electrons in different molecules.

Bonding in complexes is difficult to calculate. For all but the simplest monomers like He, the system is large. However calculation of electrostatic interaction requires the use of large basis sets in LCAO-calculations in order to obtain the proper EDD. Few calculations satisfy this requirement.

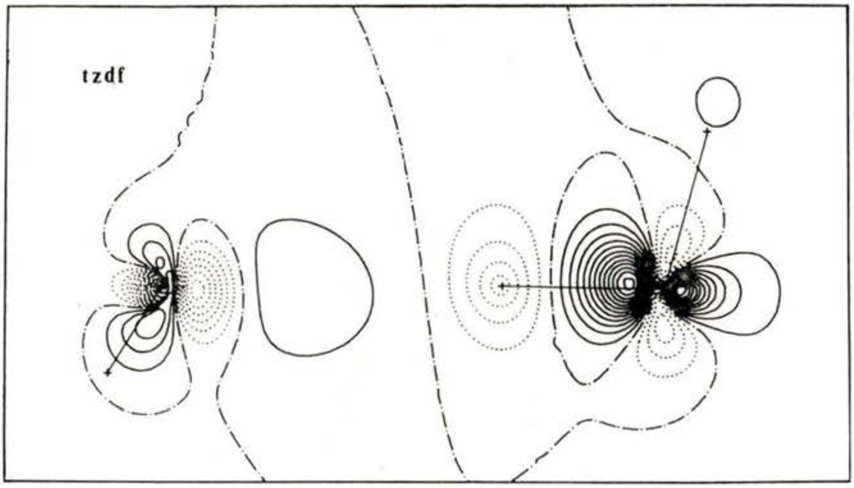

Fig. 9 — Interaction density in the water dimer in the equilibrium configuration: O...O distante 5.63 au., corrected for basis set superposition error. Contours at 0.002 au.

We shall now apply the results of the two previous sections in studying the EDD in the hydrogen bond in the water dimer. Since the interaction effects are small, we shall consider the interaction density, defined as the difference between the EDD of the dimer and the sum of the EDD's of the monomers placed at the proper position.

Fig. 9 shows the interaction density distribution of the dimer in the equilibrium configuration. Comparison with Fig. 7 suggests that most of the interaction density is due to polarization of one monomer

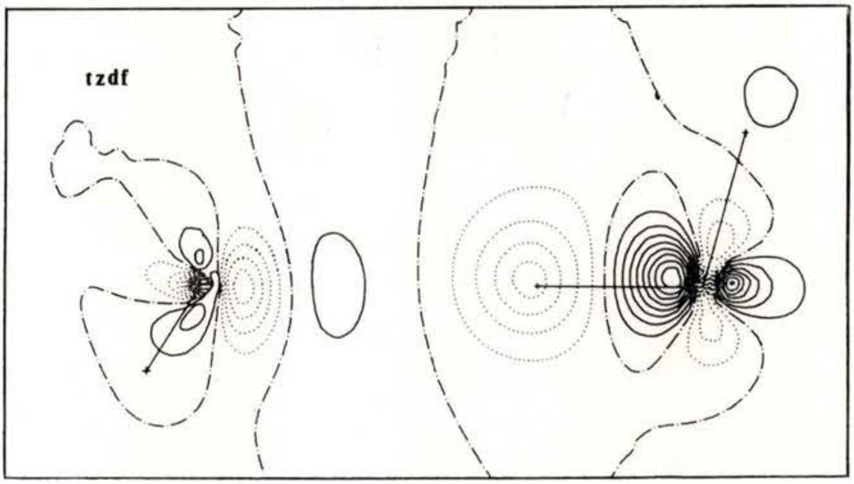

Fig. 10 — Polarization density in water molecules placed in the field of the dimer partner at the equilibrium distance. Contours at 0.002 au.

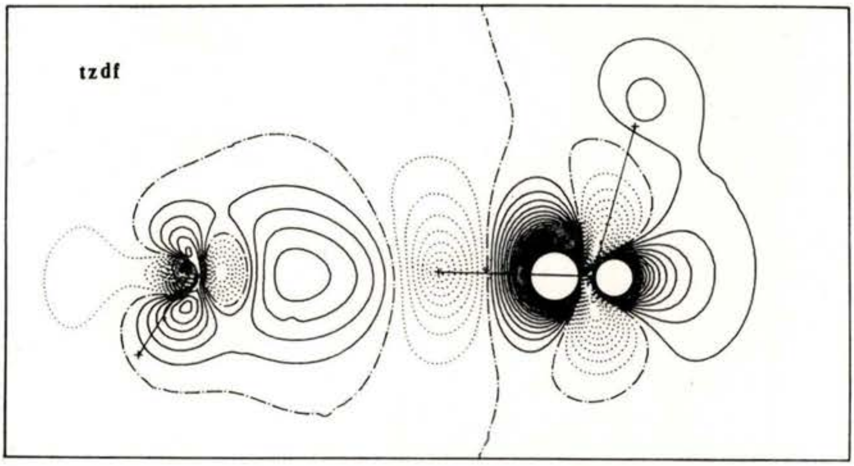

Fig. 11 — Interaction density in the water dimer at reduced distance. The O..O distance of 4.70 au. is the same as found in the oxalic acid/water complex. Contours at intervals of 0.002 au.

by the field of the other. To confirm this we placed each molecule of the dimer in the field of the other one and calculated the polarization density distribution [18]. The

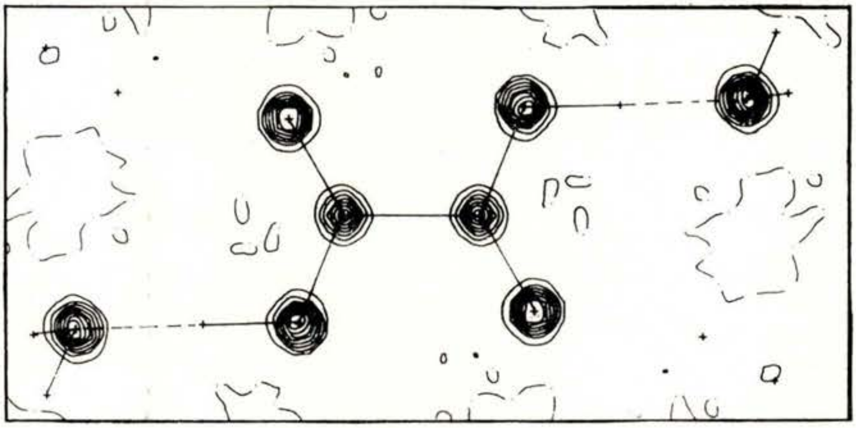

Fig. 12 — The electron density distribution in the oxalic acid/water complex. Contours at arbitrary intervals.

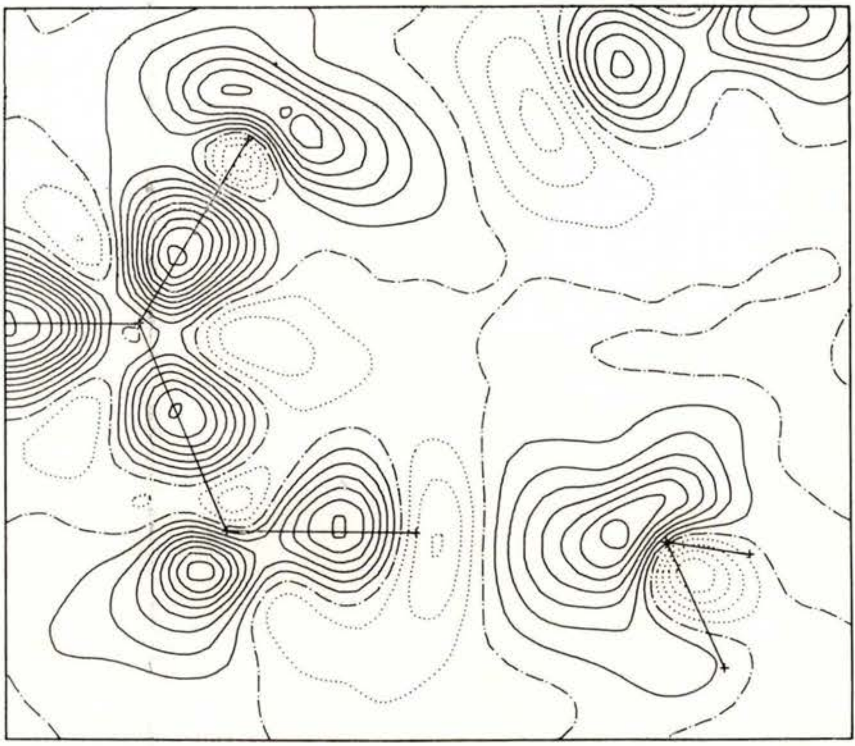

Fig. 13 — The difference between the experimental EDD and the superposition of the atomic EDD's in the oxalic acid/water complex. Contours at intervals of 0.05 e/Å^3.

result is shown in Fig. 10. The close correspondence between this figure and the previous one proves the point.

When the monomers are placed closer together other effects occur. The polarizing fields are much stronger, but exchange repulsion prevents polarization proportional to the electric field [19]. Fig. 11 shows the result. The strongest effect of hydrogen bonding is seen to occur in the O-H bond of the donor, where the interaction density is large in volume and magnitude. The donor hydrogen is further depleted and electrons accumulate in the lone pair region of the acceptor atom.

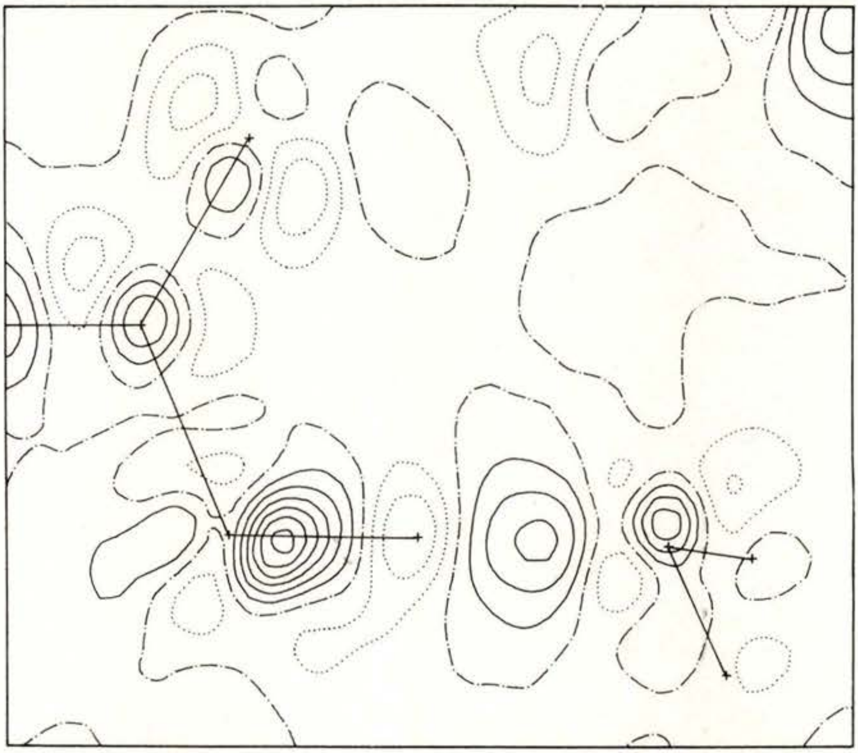

Fig. 14 — The difference between the experimental EDD and the superposition of the molecular EDD's in the oxalic acid/water complex. Contours at intervals of 0.05 e/Å^3.

The typical polarization features of the acceptor atom are easily recognized. The effect of the polarization density distribution on the electrostatic interaction between molecules is responsible for the breakdown of the calculation of electrostatic interaction as sum of two-monomer interactions [19].

Experimental verification: X-ray diffraction

The features of the hydrogen bond in the O-H...O region are the result of the subtle interplay of many effects. Consequently the outcome of calculations using different quantumchemical methods and applying different approximations varies considerably. In their study of the hydrogen bond in oxalic acid dihydrate Breitenstein *et al.* [20] find the lone pair density to be decreased, contrary to the result reported above. Lunell [21], studying sodium hydrogen oxalate monohydrate, does not observe an increase of the lone pair density either. It should be noted, however, that the polarization density in the lone pair region is very diffuse, with hardly any contours as witness. In fact, depletion in the region close to the nucleus is a better indicator of polarization.

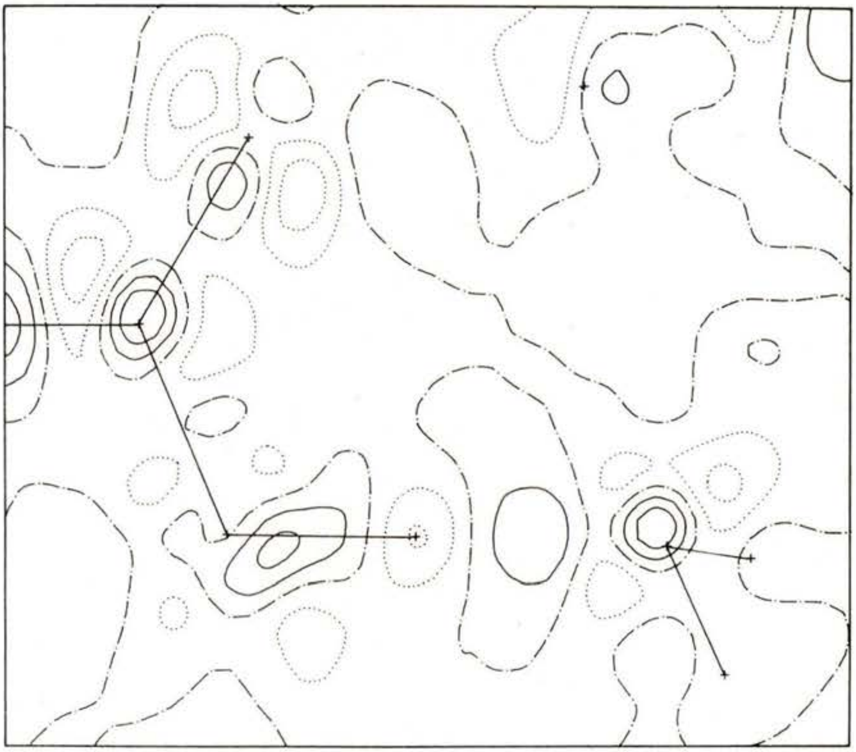

Fig. 15 — The difference between the experimental EDD and the EDD of the oxalic acid/water dimer. Contours at intervals of 0.05 e/Å^3.

Fortunately, a number of careful X-ray and neutron diffraction experiments on oxalic acid dihydrate have been carried out, together with elaborate analyses [22]. Fig. 12 shows the EDD in the plane of the oxalic acid molecule. The X-ray results of Stevens *et al.* [23] and of Dam *et al.* [24] agree quite well, both showing the effect of hydrogen bonding. Fig. 13 shows the difference density in the plane of the complex. The smooth features of this density distribution are due to the fact that the difference density was expanded in a limited number of functions centred on the atoms of the crystal. The flexibility of the basis was tested by comparing a theoretical density distribution after expansion with the original one. The coefficients are chosen in such a way that the difference between the structure factors based on the fitted density distribution and the experimental ones is minimal in the least squares sense. In this way experimental noise is removed from the difference maps.

Stevens [25] showed these experimental results to be similar to the outcome of Hartree-Fock calculations on the molecules constituting the oxalic-acid water complexes in the crystals. The differences between theory and experiment could be attributed to the fact that the basis set used was not large and that the hydrogen bond was not taken into account.

Recently Krijn *et al.* [6] carried out HFS-calculations on the oxalic-acid water complex, using a large basis set of Slater functions. To see the effect of the various contributions the authors first compared the experimental EDD with the EDD based on the wave functions of the individual molecules. Fig. 14 shows the result. We notice that the covalent bonds are well taken care of in the model, but the features characteristic for the hydrogen bond remain. The next theoretical model was

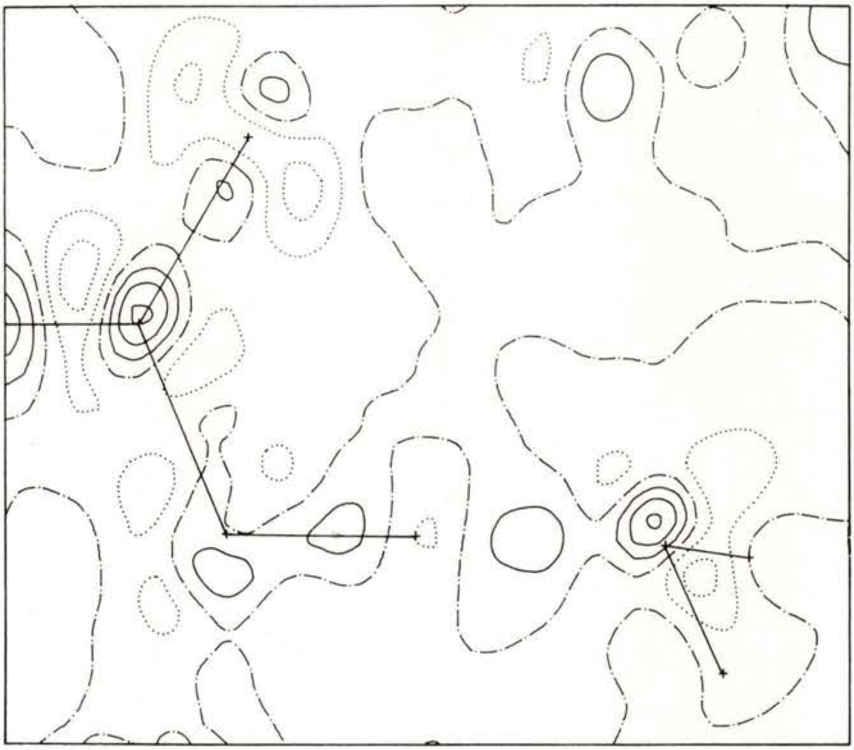

Fig. 16 — The difference between the experimental EDD and the EDD computed for the oxalic acid/water dimer placed in the field of the surrounding molecules. Contours at intervals of 0.05 e/Å^3.

based on the wave function of the oxalic-acid water complex. Fig. 15 shows the difference between the model density and the one obtained by experiment. Only weak features remain. A further improvement of the theoretical model was based on the consideration that only the strongest hydrogen bond was taken care of. Although other hydrogen bonds are weaker, they have some influence on the EDD. From the work on the water dimer we learned that the effect of weak hydrogen bonds is due to the electric fields of the monomers. In a further calculation the complex was placed in the electric fields subtended by the surrounding molecules. A few iterations were enough to make the final EDD self consistent. Fig. 16 shows the

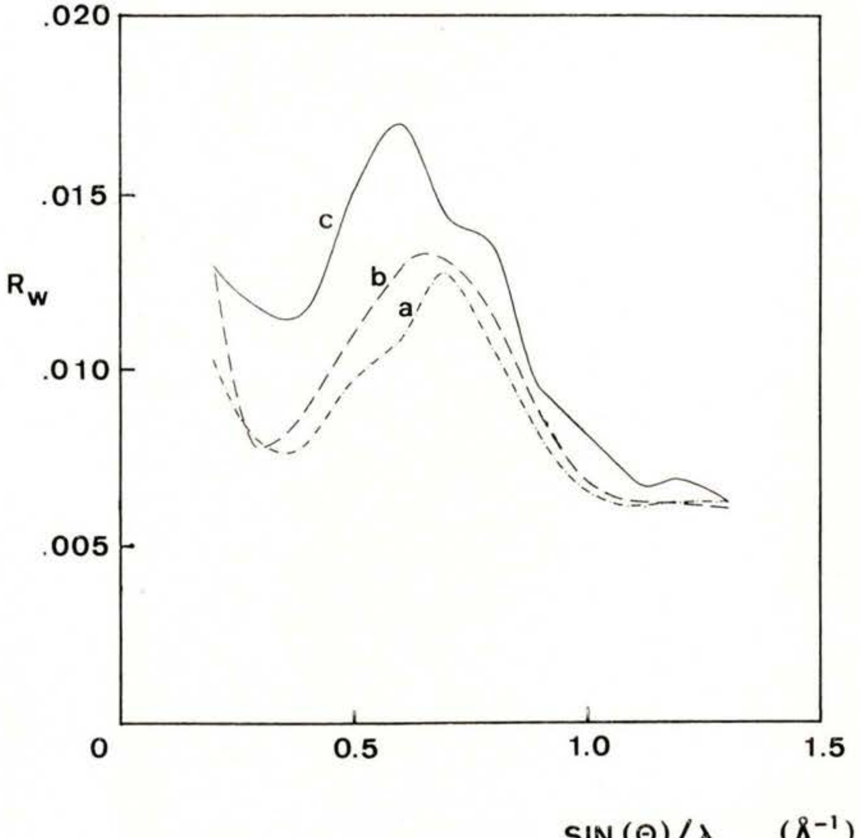

Fig. 17 — The R-factor as function of the scattering angle for the different models of the EDD used for calculating the structure factor.

Models: *a*) superposition of molecular EDD's

- b) oxalic acid/water dimer
- *c*) oxalic acid/water dimer placed in the electrostatic field of the surrounding molecules.

final result. The remaining differences are centred on the atoms, where the standard deviations in the EDD are large. The differences at the carbonyl oxygen atom suggest that the harmonic model does not suffice to account for the thermal motion.

It is interesting to see that the environment seems to enforce the effect of the central hydrogen bond.

The close correspondence between an *ab initio* model containing only the scale factor as variable and the experimental EDD is very satisfying. Since the observations of the X-ray experiment are closely related to the magnitude of the structure factors, a quantitative measure of the correspondence between model and experiment is given by the R-factor, defined in eq. (14), in which F_H^{calc} are the structure factors based on the model used. The final R-factor is well below 1 %: 0.0095.

The structure factors can be grouped according to their $\sin\Theta/\lambda$ value and for each interval in $\sin\Theta/\lambda$ a partial R-factor can be calculated. In Fig. 17 a smooth curve is drawn through the different partial R-factors corresponding to the same model. We see that the intensity of the high order reflections does note depend on the model. The curves facilitate the selection of intervals in reciprocal space that are most sensitive to the effects of intermolecular interaction.

CONCLUSIONS

The excellent agreement between theory and experiment, witnessed by Figs. 16 and 17 shows that the X-ray experiment is sensitive to details of the effects of interaction between molecules.

This sensitivity makes it possible to use X-ray difraction to test the quality of quantumchemical models, i. e. to test the various approximations that are inherent in the models.

The Hartree-Fock-Slater method, using large basis sets to expand the molecular orbitals, is seen to yield good results. This implies that the Kohn-Sham equations, applying the local density approximation, are well suited for calculating properties that depend on the electron density distribution.

The calculation of the polarization density in the Ne-atom by H. Bruning is gratefully acknowledged.

Much of the work is based on the calculations of M. Krijn.

REFERENCES

[1] E. MADELUNG, Gött. Nach. (1909), 100.

[2] W. KOSSEL, Ann. Phys. (1916), **49**, 229.

[3] P. HOHENBERG and W. KOHN, Phys. Rev. (1964), **136**, B864.

[4] W. KOHN and L. SHAM, Phys. Rev. (1965), **140**, A1133.

[5] D. FEIL, Chemica Scripta (1986), **26**, 395.

[6] M. KRIJN, Thesis University of Twente (1988).
M. KRIJN and D. FEIL, J. Chem. Phys. (1988), **89**, 4199.
M. KRIJN, H. GRAAFSMA and D. FEIL, Acta Cryst. (1988), **B44**, 609.

[7] J. SHERMAN, Chem. Rev. (1932), **11**, 93.

[8] A. R. WILLIAMS and U. von BARTH, in «Theory of the Inhomogeneous Electron Gas», S. Lundqvist and N. H. March, ed. Plenum Press, New York (1983).

[9] See e. g. W. KOHN and P. VASHISTA in «Theory of the Inhomogeneous Electron Gas», S. Lundqvist and N. H. March, ed. Plenum Press, New York (1983).

[10] M. T. CARROL, R. F. W. BADER and S. H. VOSKO, J. Phys. B: At. Mol. Phys. (1987), **20**, 3599.

[11] M. KRIJN and D. FEIL, Chem. Phys. L. (1988), **150**, 45.

[12] R. O. ESQUIVEL and A. V. BUNGE, Int. J. Quantum Chem. (1987), **32**, 295.
A. V. BUNGE and R. O. ESQUIVEL, Phys. Rev. (1986), **A34**, 853.

[13] G. VELDERS and D. FEIL, Acta Cryst. (1989), **B45**, 359.

[14] T. SAKA & N. KATO, Acta Cryst. (1986), **A42**, 469.
S. CUMMINGS & M. HART, Aust. J. Phys. (1988), **41**, 423 have reanalyzed S & K's data. The corrected values are used in the present study.

[15] M. T. YIN & M. L. COHEN, Phys. Rev. B (1982), **26**, 5668.

[16] M. KRIJN and D. FEIL, J. Chem. Phys. (1986), **85**, 319, J. Phys. Chem. (1987), **91**, 540.

[17] B. J. ROSENBERG and I. SHAVITT, J. Chem. Phys. (1975), **63**, 2162.

[18] M. KRIJN and D. FEIL, J. Chem. Phys. (1988), **89**, 5787.

[19] KERSTI HERMANSSON, Thesis, University of Uppsala, Sweden (1984).

[20] M. BREITENSTEIN, H. DANNÖHL, H. MEYER, A. SCHWEIG and W. ZITTLAU, in «Electron Distributions and the Chemical Bond», ed by P. Coppens and M. B. Hall (Plenum Press, New York, 1982), pp. 255.

[21] S. LUNELL, J. Chem. Phys. (1984), **80**, 6185.

[22] P. COPPENS, J. DAM, S. HARKEMA, D. FEIL, M. S. LEHMANN, R. GODDARD, C. KRÜGER, E. HELLNER, H. JOHANSEN, F. K. LARSEN, T. F. KOETZLE, R. K. MCMULLAN, E. N. MASLEN and E. D. STEVENS, Act. Cryst. (1984), **A40**, 184.

[23] E. D. STEVENS and P. COPPENS, Acta Cryst. (1980), **B36**, 1876.

[24] J. DAM, S. HARKEMA and D. FEIL, Acta Cryst. (1983), **B39**, 760.

[25] E. D. STEVENS, Acta Cryst. (1980), **B36**, 1876.

MAGNETIC X-RAY SCATTERING

MALCOLM J. COOPER

Department of Physics
University of Warwick
Coventry CV4 7AL, UK.

ABSTRACT — The existence of spin-dependent terms in the X-ray scattering cross-section was established, both theoretically and experimentally, many years ago but these effects remain unexploited. This was because of the small cross-sections involved and the general need to use polarised beams or employ polarisation analysis of the scattered beam. Now, with the advent of the present generation of high brightness, high flux synchrotrons there is an opportunity for change. In this review the magnetic cross-section for both elastic and inelastic scattering will be described, the interference terms leading to the first order contributions discussed and illustrated by the key experiments that have been performed so far. The possibility of separating spin and orbital contributions to the magnetisation exists and the feasibility of achieving this will be considered.

1 — INTRODUCTION — HISTORICAL AND PHYSICAL ORIGINS

There is nothing new in the notion that X-rays are scattered not only from the electron charge distribution but also from the magnetisation density. The theory was presented some fifty years ago [1], and definitive papers published some thirty years ago when the polarisation of the gamma radiation emitted by nuclei was of considerable interest [2, 3]. Indeed a polarimeter for the analysis of the degree of circular polarisation of gamma rays was based upon the magnetic Compton scattering effect [4], its most fundamental application being in the determination of the neutrino helicity [5]. The close connections within the physics community are well illustrated by the fact that Professor Berko, who provides the keynote address on positron annihilation at this meeting [6] was acknowledged in the definitive work of Lipps and Tolhoek [2, 3] more years ago than he may care to remember!

Seminal papers in the historical development of magnetic X-ray scattering are listed in Table 1. Despite the time that has passed most of the experiments have been demonstrations rather than exploitations of effects. The subject remains one having great potential rather than a proven track record. This should change rapidly but for the moment there remains the danger that the number of enthusiastic review papers exceeds that of real research publications in the current lliterature! I only hope that, although I am adding to the imbalance, this review will provide a brief but useful introduction to those involved in conventional X-ray scattering and point them in the direction of more serious and satisfying texts.

TABLE 1 — Magnetic X-ray scattering — a chronological summary

Date	Event
1938	The first derivation of an expression for the scattering of polarised radiation by oriented electrons — Franz [1].
1955	Development of a magnetic Compton polarimeter for measuring the degree of circular polarisation of gamma rays — Wheatley *et al.* [4].
1970	First suggestion that magnetisation density, in positon and momentum space could be studied with X-rays — Platzman and Tzoar [24].
1972	First X-ray measurement of antiferromagnetic superlattice diffraction peaks — de Bergevin and Brunel [13].
1976	First Compton line shape measurement with circularly polarised gamma radiation — Sakai and Ono [25].
1985	First synchrotron study of an antiferromagnet (Ho) — Gibbs *et al.* [17].
1986	Magnetic Compton profile measurements with circularly polarised synchrotron radiation established — Cooper *et al.* [28].
1987	First magnetic photoabsorption measurements with circularly polarised synchrotron radiation — Schütz *et al.* [34].
1987/8	Detailed accounts of the polarisation dependence of magnetic diffraction occur — Lovesey [8], Blume and Gibbs [9].

The appropriate terms for the scattering cross-section appear in standard texts [7], albeit not in a readly interpretable form, but several «interpretations» have now appeared, which translate the obscure quantum-mechanical formulae into simpler expressions involving the polarisation of the beam and the angle of scattering [8 & 9].

Despite the complicated algebra en route there is a simple classical origin to these effects which was pointed out by two of the pioneers in this field, de Bergevin and Brunel [10, 11]. Figure 1 is taken from their work. The Thomson term, for example, corresponds to electric dipole re-radiation of the E-field of the incident electromagnetic wave; there is no change in the plane of polarisation. The higher order «magnetic» effects arise because of the H-field of the wave and the magnetic moment (spin and orbital) of the electron.

The interaction is richer than that between neutron and electron because of the involvement of the charge, spin and the orbital momentum of the electron with both the electrical and magnetic fields of the radiation. Classically all these effects produce secondary elastic scattering that is scaled down in amplitude by the factor (photon energy/mc^2) and its plane of polarisation changed from that of the incident electromagnetic wave, furthermore spin and orbital scattering are different. In contrast a neutron is scattered solely by virtue of its magnetic moment and therefore it measures the total (i. e. spin plus orbital) magnetisation density. The comparison with neutron scattering and the detailed derivation of the photon cross-section for magnetic scattering is the subject of another review at this conference [12] and results will be merely quoted here. In general terms a neutron source delivering 10^8 ns^{-1} and a photon source of 10^{12} ps^{-1}, produce comparable magnetic scattering and both figures are realistic for high flux reactors and high brightness storage rings. The balance can be tipped in favour of the photon source by using the interference effects described below.

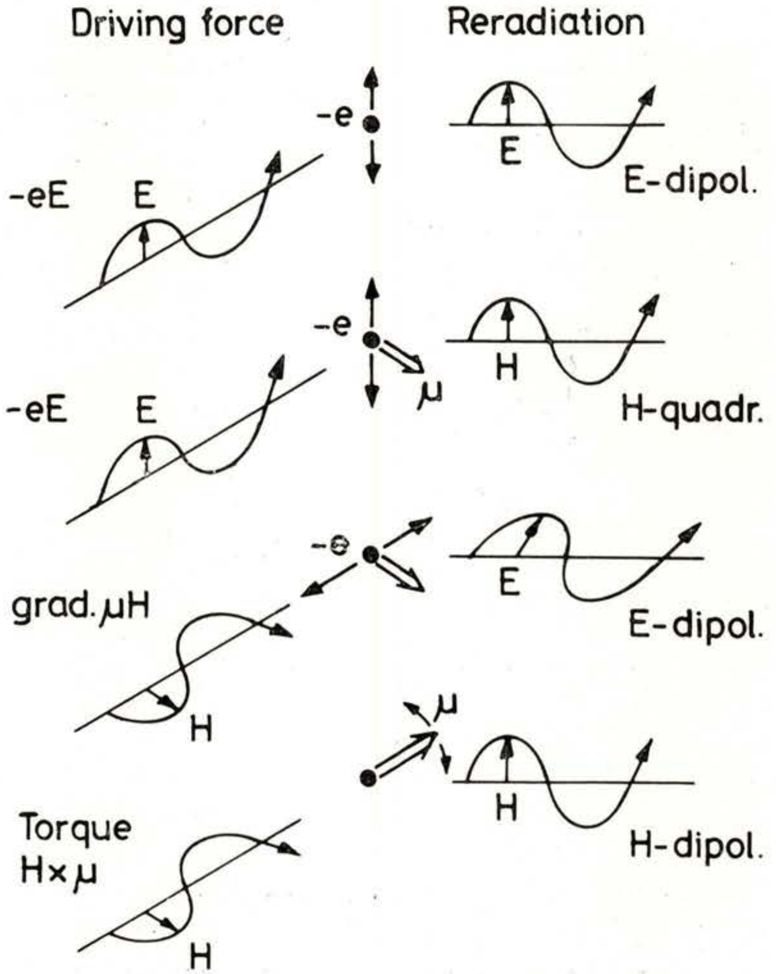

Fig. 1 — Classical X-ray scattering. The top diagram shows Thomson scattering and the lower diagrams describe quadrupolar and dipolar magnetic interactions which lead to a change in the plane of polarisation of the electromagnetic wave. (Reproduced from [10], copyright International Union of Crystallography).

2 — THE SCATTERING CROSS-SECTION

The classical terms persist in the quantum derivation which now allows the possibility of inelastic (Compton) scattering effects. The expression for the elastic scattering cross-section has the general form

$$\frac{d\sigma}{d\Omega} = \left(\frac{e^2}{mc^2}\right)\Big\{ < i \,|\, \sum_j e^{i\mathbf{K}\,.\,\mathbf{r}_j} \,|\, i > \mathbf{A} - \frac{i\hbar\omega}{mc^2}\,[< i \,|\, \sum_j e^{i\mathbf{K}\,.\,\mathbf{r}_j}\, \mathbf{S}_j\,.\,\mathbf{B} \,|\, i > + < i \,|\, \sum_j e^{i\mathbf{K}\,.\,\mathbf{r}_j}\, \frac{\mathbf{K}\,.\,\mathbf{p}}{\hbar^2 K^2}\,.\,\mathbf{C} \,|\, i >] \Big\}$$

where **A**, **B**, **C**, are polarisation vectors, **K** is the X-ray scattering vector and the sums are over the j target electrons; **A** leads to the familiar Thomson term whereas the second and third terms, which are in quadrature with it, contribute in their own right in second order only (i. e. $\simeq \left[\frac{\hbar\omega}{mc^2}\right]^2$). At conventional X-ray energies this represents an alarming reduction, especially when it is remembered that only 10 % of the atomic electrons give a net magnetic contribution. In antiferromagnets, where the magnetic superlattice reflections can be separated from

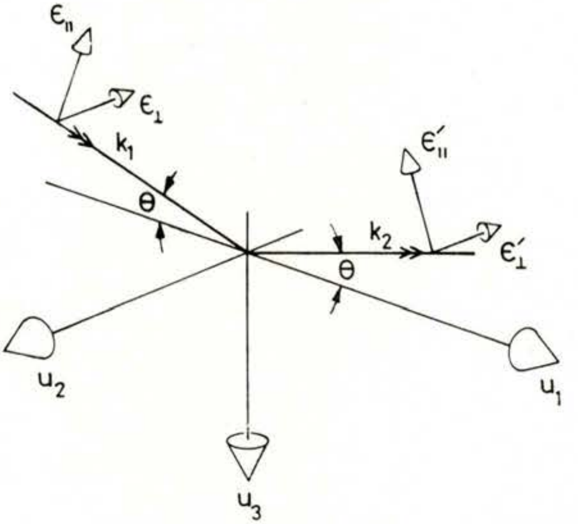

CHARGE

$$\begin{array}{c|cc} & \epsilon'_{\perp} & \epsilon'_{\parallel} \\ \hline \epsilon_{\perp} & 1 & 0 \\ \epsilon_{\parallel} & 0 & \cos 2\theta \end{array}$$

MAGNETISATION

$$\begin{array}{c|cc} & \epsilon'_{\perp} & \epsilon'_{\parallel} \\ \hline \epsilon_{\perp} & S_2 \sin 2\theta & -2\sin^2\theta[(L_1+S_1)\cos\theta - S_3\sin\theta] \\ \epsilon_{\parallel} & +2\sin^2\theta[(L_1+S_1)\cos\theta - S_3\sin\theta] & (L_2+S_2)4\sin^3\theta\cos\theta \end{array}$$

Fig. 2 — The diagram defines the wavevectors, $\mathbf{k}_1$ and $\mathbf{k}_2$ and the unit polarisation vectors, $\underline{\epsilon}\parallel$, $\underline{\epsilon}_{\perp}$, $\underline{\epsilon}'\parallel$, $\underline{\epsilon}'_{\perp}$ for the incident and diffracted beams. The diffraction plane is defined by the $\mathbf{u}_1$, $\mathbf{u}_3$ axes and the Bragg angle is Θ. The polarisation matrices show how the incident and scattered beam amplitudes depend upon the components of spin (S_1, S_2 and S_3) and orbital (L_1, L_2, L_3) magnetisation resolved along the $\mathbf{u}_1$, $\mathbf{u}_2$, $\mathbf{u}_3$ axes.

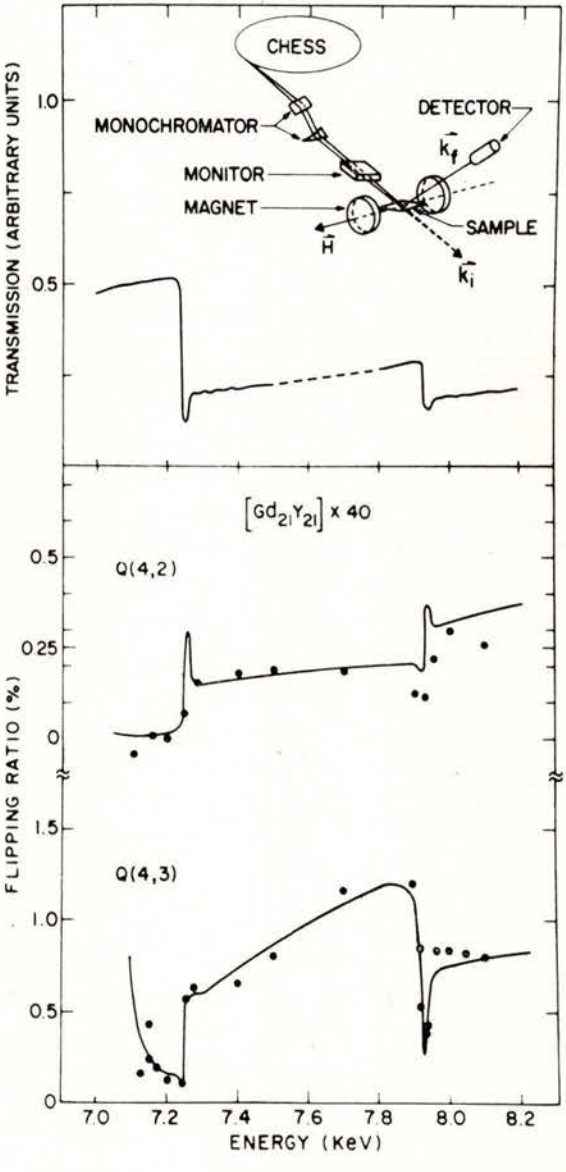

Fig. 3 — Magnetic X-ray scattering from a 40-layer $Gd_{21}Y_{21}$ superlattice interface. The upper diagram shows the schematic experimental arrangement whereby the monochromated synchrotron radiation can be tuned through the L_2 and L_3 Gd absorption edges, coupling the magnetic scattering to the charge scattering to produce a first order magnetic contribution from the magnetisation density perpendicular to the diffraction plane. The lower diagrams show the flipping ratio (change of intensity upon reversal of the field) for two reflections from the layer. (Taken from [16], copyright American Physical Society.)

the Bragg peaks, such small signals can be measured even with modest laboratory X-ray power. The first measurements on NiO [13] were done with a 1 kW CuKα tube and recent work on the discommensurate spiral spin structure of antiferromagnetic holmium has been pursued with rotating anode X-ray systems as well as synchrotron radiation [14]. Incoherent scattering experiments such as Compton scattering simply sum the magnetisation density and therefore provide no information about antiferromagnetism. In ferromagnets, however, there is a net contribution to the Compton profile as well as the Bragg peaks from the summed magnetic moments. Unfortunately in the diffraction experiment the magnetisation and charge Bragg peaks are coincident and the measurement of weak second order effects is highly problematical.

The separation of spin and orbital magnetisation can be appreciated by inspection of the polarisation matrices which are shown, together with the defining axes, in figure 2 [10]; when incident and scattered beam polarisations are perpendicular to the diffraction plane the spin component **S** alone produces the scattering whereas **L** and **S** contribute to the parallel component pair and produce the polarisation switching from one plane to another.

2.1 — *Interference Terms and Anomalous Effects*

The weakness of these second order terms renders them of little practical interest especially in ferromagnets. However, a real first order contribution can arise if the overlap with the Thomson term produces a further 90 degrees phase-shift. There are various ways in a diffraction experiment in which that might arise, for example the leading term will be complex if the structure is non-centrosymmetric or if anomalous scattering occurs. As yet there are no examples in the literature of the former, although many magnetic structures fall into that category. On the other hand anomalous dispersion has been used in the early synchrotron studies of ferromagnets, helped by the fortuitous proximity of the CuKα X-ray energy and the Fe K shell binding edge [15]. More recently the tuneability of synchrotron radiation has been exploited, for example in the study of the magnetisation in Gd-Y superlattice layers [16]. Flipping ratios of the order of 1 % were found upon reversal of the spin direction in the 40 layer interface as shown in figure 3.

Surprising enhancements of the magnetic scattering have also been observed in antiferromagnetic holmium, where synchrotron data first showed up the complex spin-slip discommensurations in the magnetic structure [17]. The new data show a resonant enhancement at the L_3 edge of a factor of 50 [18]! There is already an explanation of this effects in terms of electric multipole transitions to unoccupied orbitals producing an interaction that is sensitive to the f and d-band magnetisation [19]. This is clearly a very interesting phenomenon; it will facilitate the measurement of magnetic effects and prompt further development of the theory.

3 — DIFFRACTION PROSPECTS

The first synchrotron results on antiferromagnetic holmium [17] were heralded as representing an advance over neutron data, which was true for that particular case but current neutron experiments are capable of similar wave vector resolution and indeed the spin-slip structure has been confirmed in that way [20]. Contrasting the depth of experience in neutron diffraction with the immaturity of synchrotron studies it will be a long time before the new method «challenges» rather than «complements» the established technique. If it does it will be as a consequence of one of the following three real advantages of synchrotron studies.

Firstly the brightness of the beam, which has not yet reached theoretical limits imposed by the thermal load on the optical elements, facilitates the study of smaller crystals than are practicable with neutrons, where fluxes are much closer to the practical limits. This is an important factor because large crystals may simply be unobtainable.

Secondly there is a range of materials for which neutron absorption or isotopic impurity pose formidable problems. Those materials may be easier to probe with synchrotron radiation. (Of course there is another set of materials which have prohibitive X-ray absorption, but it is, in general, a different set.)

Thirdly X-ray scattering can provide different information because spin and orbital contributions are separable, albeit with difficulty. It is quite clear from the polarisation matrices shown in figure 2 how this separation can be achieved by the polarisation analysis of an initially polarised beam and Blume and Gibbs [9] have comprehensively treated this problem. At an experimental level polarisation analysis can simply be used to enhance the «signal to noise» of the magnetic scattering as was done in the holmium study [17] but in compounds that contain substantial contributions to the magnetisation from both **S** and **L** the separation may be of real physical interest.

This is not so in transition metal systems where the orbital moment is quenched or in the lantanides where the orbital moment is large but predictable. On the other hand in the actinides the orbital moment is unknown, it is calculated to be large and opposed to the spin moment. Data on some of the compounds are given in Table 2. The separation of **L** from **S** is of great importance in guiding ab initio calculations in these materials [21, 22].

TABLE 2 — Magnetic properties of some uranium compounds. All have the NaCl structure and are ferromagnetic (F) or antiferromagnetic (AF), μ_N is the total moment determined in neutron studies whereas M_L and μ_S refer to calculated values [21, 22]; all moments are expressed in Bohr magnetons.

Compound	Magnetic Ordering Temperature (°K)	μ_N	μ_L	μ_S
UN	53 (AF)	0.75	1.5	− 1.0
US	177 (AF)	1.7	4.0	− 2.2
U Se	160 (F)	2.0	4.3	− 2.4
U Te	104 (F)	2.2	4.6	− 2.6

In ferromagnetic actinide compounds the use of circularly polarised radiation offers one route to the separation of **L** and **S** and it is instructive to see how this might work in practice. The cross-section quoted by Lovesey [8] can be written

$$\frac{d\Omega}{d\sigma} = \frac{1}{2}\left(\frac{e^2}{mc^2}\right)^2 f(\mathbf{K}) \{f(\mathbf{K}) ([1 + \cos^2 2\Theta] - 2gP_c(1 - \cos 2\Theta) \; [\mathbf{S}(\mathbf{K}) . (\mathbf{k}_1 \cos 2\Theta + \mathbf{k}_2) + \cos^2\Theta \; \mathbf{L}(\mathbf{K}) . (\mathbf{k}_1 + \mathbf{k}_2)]\} \qquad (2)$$

where P_c represents the degree of circular polarisation (± 1), $g = \frac{\hbar\omega}{mc^2}$ and 2Θ the scattering angle is now related to the photon wavelength by the Bragg equation; $f(\mathbf{K})$, $\mathbf{S}(\mathbf{K})$ and $\mathbf{L}(\mathbf{K})$ are the form factors for charge, spin and orbital moment scattering and $\mathbf{k}_1$, $\mathbf{k}_2$ unit vectors along incident and scattering beam directions, respectively. It is obvious that spin and orbital contributions are distinguished by angular terms that differ most when $2\Theta \rightarrow 90°$. This means that long wavelengths ($\lambda > 1$Å) must be used if the magnetic form factors are to be non-negligible (i. e. $(\sin\Theta)/\lambda$ remains small). Clearly other factors such as photoelectric absorption are important and any experiment designed to maximise the flipping ratio must also take into consideration the signal level in the measurement.

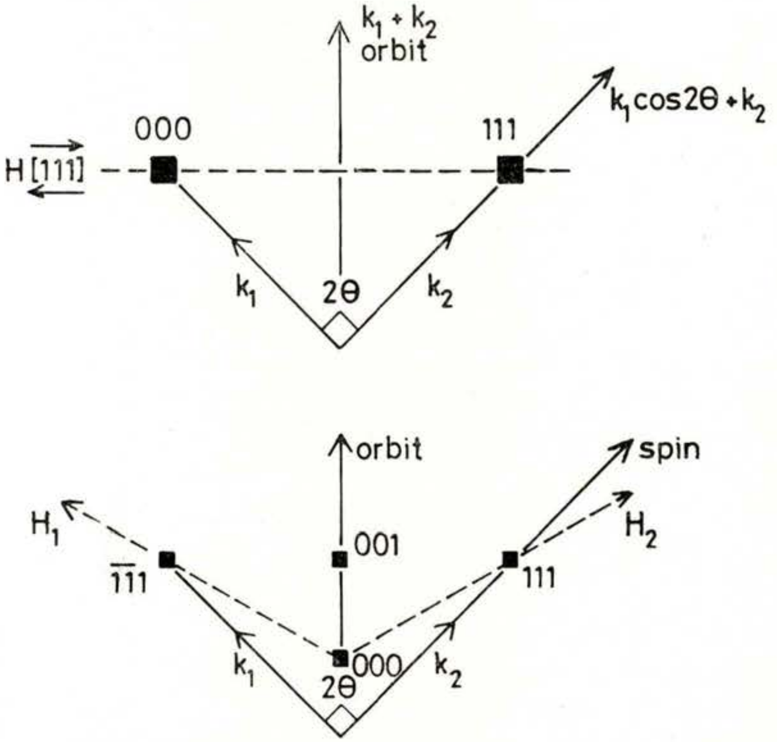

Fig. 4 — Possible geometries for separating spin and orbital contributions to the magnetisation. A Bragg angle of 45°, obtained by tuning the synchrotron beam, has been assumed in both cases. In the upper diagram the orbital term, $\propto(\mathbf{k}_1 + \mathbf{k}_2)$, is perpendicular to the field direction and is therefore unmeasured; the flipping ratio relates to the spin contribution, $\propto\mathbf{k}_1\cos2\Theta + \mathbf{k}_2)$ alone. The geometry depicted in the lower diagram involves switching from one «easy» direction to another, thereby varying the contribution from spin and orbital terms. [Lander — private communication].

Figure 4 shows two possible geometries for the separation of **L** and **S** where reversing the field between the easy directions either eliminates one contribution (Fig. 4a) or alters their relative value (Fig. 4b). It appears that even in favourable situations the flipping ratio is unlikely to exceed $\sim 10^{-3}$ [Lander, Private communication].

4 — COMPTON SCATTERING

In the high energy, high momentum transfer regime of the impulse approximation the double-differential inelastic scattering cross-section can be directly related to the Compton profile, $J(p_z)$, which is the projection of the total electron momentum distribution, $n(\mathbf{p})$ along the scattering vector, i. e.

$$J(p_z) = \int_{p_x} \int_{p_y} n(\mathbf{p}) dp_x dp_y \tag{3}$$

Compton studies are reviewed in another paper in the volume [23]; all that need be emphasised here is the difficulty of separating information about the conduction electrons from those in the core which are in any case well described by free atom models. This is done for example by constructing the difference between line shapes measured in different directions (the core will be spherically symmetric). The asphericities only amount to a few percent of the total but are nonetheless interpretable.

The magnetic interaction allows the core to be eliminated directly. Platzman and Tzoar [24] pointed out in 1970 that the spin-dependent contribution could be isolated in a Compton experiment where the magnetisation direction is reversed. Their observation is equally valid for any orbital component and the result of such an experiment is a magnetic Compton spectrum given as

$$\Delta \left(\frac{d^2\sigma}{d\Omega d_\omega} \right)^2 = 4 \frac{e^2}{mc^2} g (1 - \cos 2\Theta) [\mathbf{S} . \tag{4}$$

$$(\mathbf{k}_1 \cos 2\Theta + \mathbf{k}_2) + \mathbf{L} . (\mathbf{k}_1 + \mathbf{k}_2)] J_{mag} (P_z)$$

where

$$J_{mag}(p_z) = \iint [\sum_i n_i \uparrow (\mathbf{p}) - n_i \downarrow (\mathbf{p})] \, dp_x dp_y \tag{5}$$

and the sum is over all the bands.

As far as the spin term in equation 4 is concerned, there is a maximum for $2\Theta = 180^\circ$ and **S** parallel to $\mathbf{k}_1$.

Although the small band of Compton scatterers is dwarfed by the cohorts of diffractionists the development of magnetic inelastic studies has kept pace with its coherent counterpart. The pioneering experiment of de Bergevin and Brunel on NiO [13] was matched by an equally heroic magnetic Compton measurement, using the circularly polarised gamma emission from cooled oriented nuclei, by Sakai and Ono [25]. Although that technique has been developed with great skill and patience [26, 27] it is closer to its natural limit than the synchrotron-based studies which take advantage of the polarisation properties of synchrotron radiation to produce circularly polarised flux [28]; a method whose feasibility was pointed out by Holt and Cooper [29].

Table 3 summarises the work to date which has concentrated on the most obvious ferromagnet, iron. The development of quarter wave plates [30] seems

TABLE 3 — Magnetic Compton studies of iron. The numerical data for the degree of circular polarisation, P_c; integrated magnetic counts, T_M and elapsed time T are only approximate, being inferred from the publications referenced.

Method	P_C	I_M	T hours	Notes/reference
Oriented ^{57}Co radioisotope 122 keV	0.6	8×10^4	139	Repeated cooling by adiabatic demagnetisation, polycrystalline iron [25]
Oriented ^{129m}Ir I - radioisotope 129 keV emission	0.8	6×10^5	165	Cooling by ^{3}He/^{4}He [26] dilution refrigerator
		2×10^6	600	polycrystalline iron [27]
Synchrotron radiation (SR) $\lambda/4$ plate at 40 keV	?	$< 10^4$	14	Cornell, CHESS bending [30] magnet, polycrystalline iron
SR - 'Inclined view method' at 46 keV	0.8	4×10^5	24	Daresbury SRS Wiggler [28], polycrystalline iron
SR - 'Inclined view method' at 60 keV	0.7	2×10^5	24 hrs per direction	Daresbury SRS Wiggler after installation of high brightness lattice, single crystal samples [32]

logical but X-ray birefringences are very small and conversion efficiencies from linear to circular polarisation correspondingly low. They have restricted tuneability, which is no problem for Compton studies, but places a real limitation on diffraction work where the Bragg angle needs to be tuned as described earlier. The published magnetic Compton study by the quarter wave plate method [31] does not rival data obtained by the «inclined view» technique. The latter takes advantage of the elliptical polarisation of the emission at a small angle (typically a fraction of a milliradian) to the orbital plane of the bending magnet. There is no circularly polarised flux from a symmetric multipole wiggler, but an asymmetric wiggler does produce a net hand of polarisation above/below the orbital plane at high energies.

Since the emission is strongly peaked in the orbital plane the optimisation of these experiments is extremely important. It depends on the operating parameters of the storage ring: at the Daresbury SRS wiggler, where the author's group have worked, a photon energy around 60 keV produces the best ratio of magnetic to charge scattering at angles ~1/10 mrad with a loss of flux of less than one order of magnitude compared with the same aperture straddling the orbital plane [Laundy and Collins — private communication]. The compromise between flux and polarisation is illustrated in Figure 5.

The importance of high flux cannot be overemphasised, at 25 keV for example the magnetic intensity from iron is only ~1 % of the total scattering. This means that over 10^6 counts must be accumulated to yield 10 % accuracy in the magnetic difference profile which is clearly inadequate. At 50 keV 1 % accuracy requires 10^8 counts. Current achievements fall far short of this (see Table 3). Figure 6 shows the current best that has been achieved in single crystal studies of the magnetic anisotropy in iron [32]. At this stage the

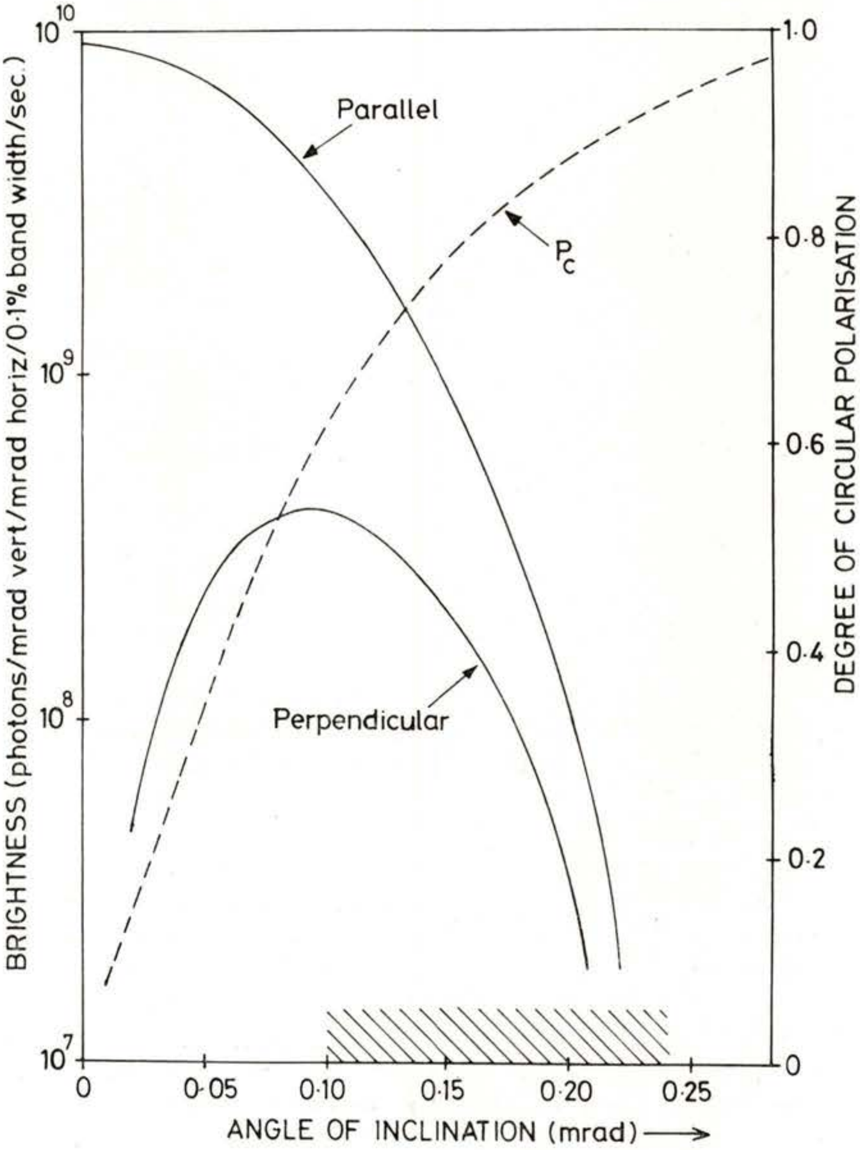

Fig. 5 — The brightness of the SRS wiggler source at 60 keV as a function of the angle of inclination to the orbital plane (left hand axis). The right hand ordinate shows how P_c, the degree of circular polarisation, increases out of the orbital plane and the hatched area outlines the typical angular range.

establishment of the anisotropy, which is not in complete agreement with theory, is seen as a useful step forward. Improvements in the statistical accuracy will arise with the implementation of focussing optics and the installation of tailor-made insertion devices, some of which have been discussed at this conference [33].

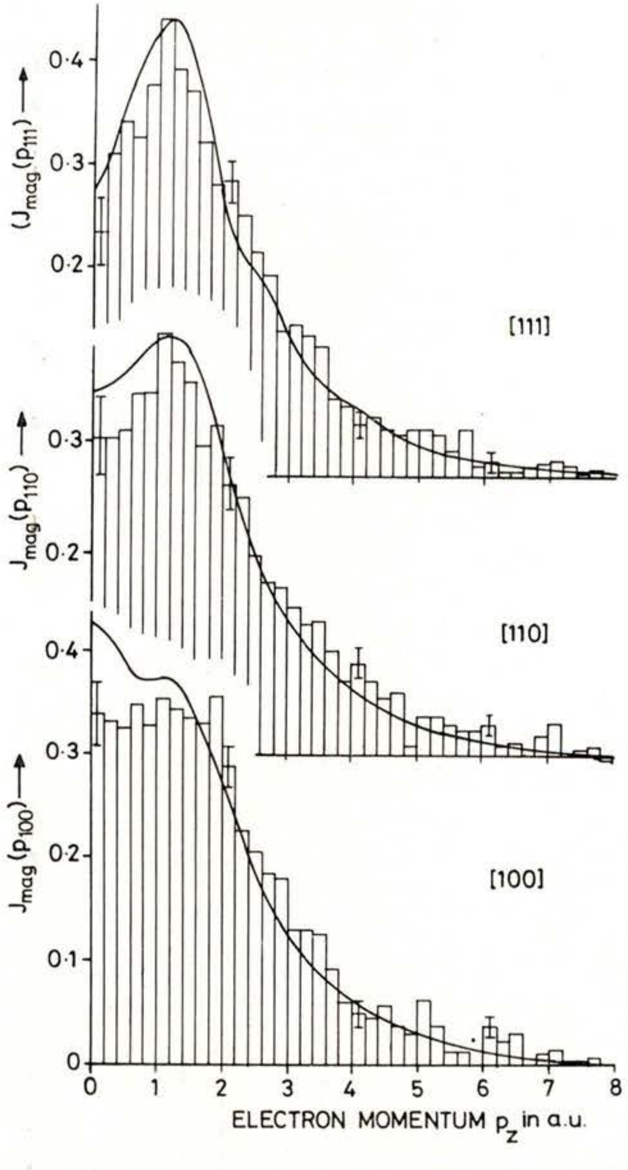

Fig. 6 — The directional magnetic Compton profiles of iron, shown at intervals of 0.20 a. u. obtained from data taken at 60 keV on the Daresbury wiggler line. The solid line represents an APW prediction. Magnetic anisotropy is evident in both experiment and theory which disagree significantly for the [100] orientation. [Taken from 31 — copyright Nature.]

5 — SPIN DEPENDENT PHOTOABSORPTION

This review would not be complete without some mention of the recent absorption studies with circularly polarised synchrotron radiation made by Schutz *et al.* at DESY who also use the inclined view method [34, 35]. Briefly the photon polarisation induces a net electron spin

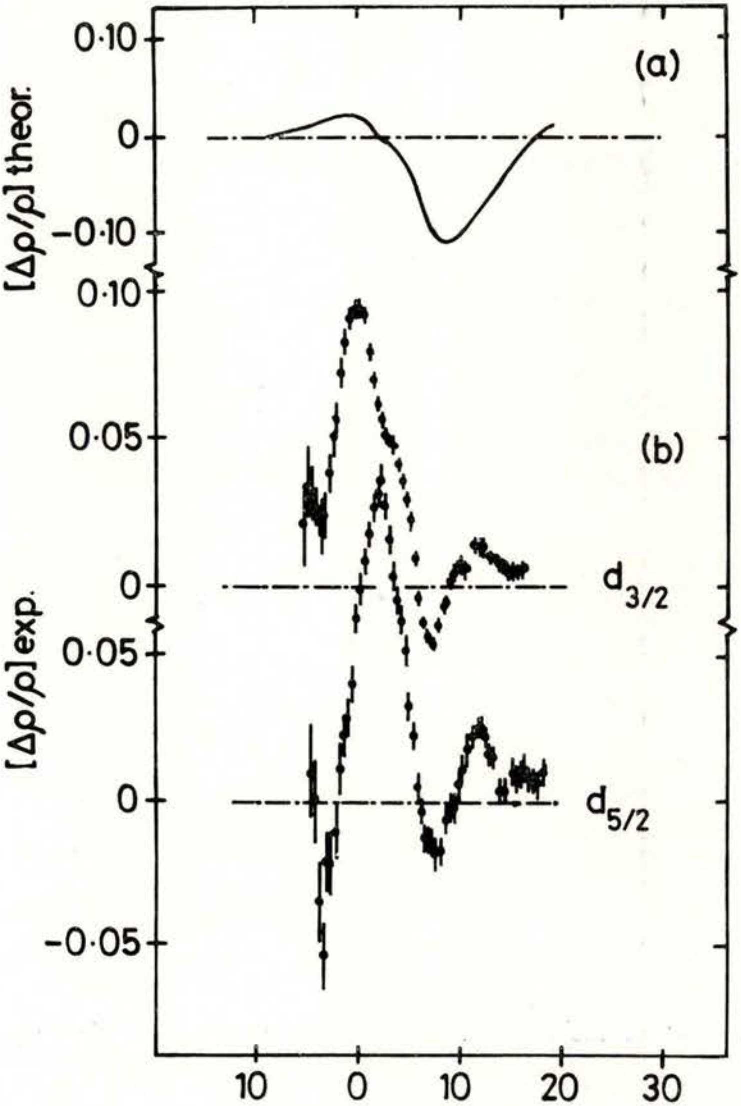

Fig. 7 — Theoretical (upper) difference densities of states $\Delta \rho / \rho$ for the unoccupied d-states in gadolinium compared with those deduced from the spin-dependent near edge structure measured in photoabsorption experiments with circularly polarised synchrotron radiation. [Taken from [34] copyright Z. Phys.]

polarisation parallel to it and there is then a difference transition probability into «up» and «down» final states. The electron polarisation is greater for transitions from p than s states and therefore although the first experiments were performed at the K edge of iron subsequent work at L_2 an L_3 edges have shown larger and more interesting effects.

Both XANES and EXAFS can be studied and as in the Compton scattering work the selection of the spin dependent part greatly enhances the physical interpretability of the results. Figure 7 shows results obtained at the Gd L and L edges, the theoretical curve, taken from a local spin density functional ground state calculation, shows rather poor agreement which the authors suggest is due to the influence of the polarised core hole. In other materials they have found magnetic effects as large as 25 % suggesting that an absorption polarimeter for circularly polarised X-rays may be feasible. There is no doubt that magnetic absorption edge spectroscopy can provide profound information about ferro or ferri- magnetic systems in which both spin orbit coupling and exchange splitting are large.

6 — CONCLUSIONS

Magnetic photon scattering is not an established subject. The theory is not fully explored and the experiments have hardly started. It will be some time before the diffraction experiments complement, let alone challenge neutron work, but it is equally clear that synchrotron based experiments will eventually add a new dimension to our evergreen studies of magnetism. This paper is too brief to have done justice to all the contributions in the field, but it may from a modest starting point for further reading.

I am grateful to the organisers of the conference for inviting me to present this review. I should like to thank my colleagues at Warwick and elsewhere who have provided the subject matter for this talk and the SERC who have supported our endeavours. My understanding of this topic owes much to the patient help of Stephen Lovesey whose presentation of the theory at this meeting should be read in conjunction with this experimental survey. The data for Table 2 and the geometries in Figure 4 were devised by Gerry Lander to whom I am indebted, together with those other authors whose results are reproduced with their kind permission in Figures 1, 3 and 7.

REFERENCES

[1] FRANZ, W., Ann der Physik **33**, 689 (1938).

[2] LIPPS, F. W. and TOLHOEK, H. A., Physica, **20**, 89 (1954) ibid **20**, 395 (1954).

[3] TOLHOEK, H. A., Rev. Mod. Phys. **28**, 277 (1956).

[4] WHEATLEY, J. C., HUISKAMP, W. J., DIDDENS, A. N., STEENLAND, M. J. and TOLHOEK, H. A., Physica, **21**, 841 (1955).

[5] GOLDHABER, M., GRODZINS, L. and SUNYAR, A. W., Phys. Rev. **109**, 1015 (1958).

[6] BERKO, S., Communication at the Sagamore IX Conference, Luso, Portugal (1988).

[7] LANDAU, L. D. and LIFSHITZ, E. M., Course of Theoretical Physics vol. 4; 2nd edn. by Berestetskii, V. B., Lifshitz, E. M. and Pitaevskii, L. P., Oxford: Pergamon.

[8] LOVESEY, S. W., J. Phys. C., **20**, 5625 (1987).

[9] BLUME, M. and GIBBS, D., Phys. Rev. **B37**, 1779 (1988).

[10] DE BERGEVIN, F. and BRUNEL, M., Acta Cryst. **A37**, 314 (1981).

[11] DE BERGEVIN, F. and BRUNEL, M., Studies of Magnetic Structures by X-ray Diffraction in Structures and Dynamics of Molecular Systems II, ed. by Daudel, R., publ. Reidel (1986).

[12] LOVESEY, S. W., Portgal. Phys. **19**, 81 (1988).

[13] DE BERGEVIN, F. and BRUNEL, M., Phys. Letts. **A39**, 141 (1972).

[14] GIBBS, D., MONCTON, D. E. and D'AMICO, K. L., J. Appl. Phys. **57**, 3619 (1985).

[15] BRUNEL, M. and DE BERGEVIN, F., Acta Cryst. **A37**, 324 (1981).

[16] VETTIER, C., MCWHAN, D. B., GYORGY, E. M., KWO, T., BUNTSCHUH, B. M. and BATTERMAN, B. W., Phys. Rev. Letts. **56**, 757 (1986).

[17] GIBBS, D., MONCTON, D. E., D'AMICO, K. L., BOHR, J. and GRIER, B. H., Phys. Rev. Letts. **55**, 234 (1985).

[18] GIBBS, D., HARSHMAN, D. R., ISAACS, E. D., MCWHAN, D. B., MILLS, D., VETTIER, C., submitted to Phys. Rev. Letts.

[19] HANNON, J. P., TRAMMELL, G. T., BLUME, M. and GIBBS, D., Phys. Rev. Letts. **61**, 1245 (1988).

[20] COWLEY, R. A. and BATES, S., to be published.

[21] BROOKS, M. S. S., Physica **130B**, 6 (1985).

[22] BROOKS, M. S. S. and KELLY, P. J., Phys. Rev. Letts. **51**, 1708 (1983).

[23] MANNINEN, S. O., Portgal. Phys. **19**, 91 (1988).

[24] PLATZMAN, P. M. and TZOAR, N., Phys. Rev. **B2**, 3356 (1970).

[25] SAKAI, N. and ONO, K., Phys. Rev. Letts. **37**, 351 (1976).

[26] SAKAI, N., TERASHIMA, O. and SEKIZAWA, H., Nucl. Instr. and Meths **221**, 419 (1984).

[27] SAKAI, N. and SEKIZAWA, H., Phys. Rev. **B36**, 2164, (1987).

[28] COOPER, M. J., LAUNDY, D., CARDWELL, D. A., TIMMS, D. N., HOLT, R. S. and CLARK, G., Phys. Rev. **B34**, 5984 (1986).

[29] HOLT, R. S. and COOPER, M., Nucl. Instr. & Meths **213**, 44 (1983).

[30] GOLOVCHENKO, J. A., KINCAID, B. M., LEVESQUE, R. A., MEXNER, A. E. and KAPLAN, D. R., Phys. Rev. Letts. **57**, 202 (1986).

[31] MILLS, D. M., Phys. Rev. **B36**, 6178 (1988).

[32] COOPER, M. J., COLLINS, S. P., TIMMS, D. N., BRAHMIA, A., KANE, P. P., HOLT, R. S. and LAUNDY, D., Nature **333**, 151 (1988).

[33] SAKAI, N., SHIOTANI, N., ITO, M., ITO, H. F., SAKURAI, M., SUGAWA, T., KAWATA, H., AMEMIYA, Y., and ANDO, M., these proceedings, Portgal. Phys. **19** (1988), in press.

[34] SCHUTZ, G., WAGNER, W., WILHELM, W., KIENLE, P., ZELLER, R., FRAHM, R. and MATERLIK, G., Phys. Rev. Letts. **58**, 737, (1987).

[35] SCHUTZ, G., KNULLE, M., WIENKE, R., WILHELM, W., WAGNER, W., KIENLE and FRAHM, R., Z. Phys. **B73**, 67 (1989).

NEW FRONTIERS IN MAGNETIZATION DENSITIES

J. B. FORSYTH

Rutherford Appleton Laboratory, Chilton Oxon OX11 OQX UK

ABSTRACT — Experimental studies of magnetization densities in crystalline solids have traditionally been centred on the diffraction of polarized neutrons by a magnetized sample. The polarization dependent cross-section provides a sensitive means of determining magnetic scattering amplitudes and the technique continues to provide the majority of the experimental data which has led to more or less detailed descriptions of the wavefunctions of the electrons involved.

Precise measurement of the magnetic scattering by antiferromagnets is more difficult, since it is generally based on polarization-independent integrated intensities in which the magnetic contribution becomes very weak at high momentum transfer due to the fall off in the magnetic form factor. Nevertheless, in many cases the improved accuracy of modern diffractometry justifies a magnetic model in which the orientations and amplitudes of the moments are associated with a more sophisticated description of the magnetization than that implied by the use of spherically-symmetric form factors based on free-atom wavefunctions.

Recent magnetization studies using both the above techniques are reviewed. The change in polarization of a beam of polarized neutrons on scattering by a magnetic crystal may provide a direct measure of both the amplitude and the orientation of the magnetic interation vector. The latter information is of importance in describing the magnetization density in crystal for which the orientation of the moments is anything but trivial. A new method for general polarization analysis is described.

1 — OPENING REMARKS

Sagamore conferences are about electrons. This paper is concerned with the measurement of the spatial distribution of magnetization in crystalline solids and will be confined to its determination by neutron scattering. In a companion paper [1], Stephen Lovesey draws together the dual threads of photon and neutron scattering and demonstrates that, contrary to the simple ideas presented in most undergraduate courses, photons also exhibit magnetic scattering and neutrons are sensitive to the distribution of charge. The scattering potentials for both of these processes are very weak, however, and their experimental exploitation has only recently begun.

I begin with a short and simple discussion of magnetic neutron diffraction before illustrating recent progress on the experimental front by examples drawn from some of the major areas of current interest: covalency in inorganic salts, ground state determinations in actinide materials, form factors in heavy fermion intermetallics and the magnetization distribution in a cluster compound. Time and space prevent me from mentioning all the good work that has appeared in the last three years, nor have all the frontiers continued to advance — for example, I am not aware of any new studies of aligned paramagnetism in the elementary metals.

2 — INTRODUCTION TO MAGNETIC NEUTRON DIFFRACTION

With the exception of the electrostatic interaction, elastic scattering cross sections in the first Born approximation may be written in terms of the Fourier transform of the interaction potential, thus:

$$d\sigma/d\Omega \ \propto \int \Psi^{*} V(\mathbf{r}) \exp(i\mathbf{k}\,.\,\mathbf{r})\, \Psi\,.\, dr^{3}$$

where **k** denotes the scattering vector. The interaction potential for neutron magnetic scattering, V(**r**), is related directly to the magnetic flux density, **B**, in the scatterer and through that to the magnetization, **M**(**r**), defined as the magnetic moment per unit volume.

The vector magnetic structure factor, **M**(**k**), can be defined such that

$$\mathbf{M}(\mathbf{k}) = \int \mathbf{M}(\mathbf{r}) \exp(i\mathbf{k}\,.\,\mathbf{r})\,.\, dr^{3}$$

but, unlike the scattering of X-rays by electrons or neutrons by nuclei, the structure factor for magnetic scattering cannot in general be related directly to the square root of the observed Bragg scattering after suitable correction for the instrumental geometry. Only those components of the magnetization, or of the magnetic structure factor, which lie in the plane perpendicular to the scattering vector, **k**, are effective in scattering neutrons and we may define this generalized magnetic interaction vector as:

$$\mathbf{Q} = \mathbf{k} \times [\mathbf{M}(\mathbf{k}) \times \mathbf{k}]$$

The magnetic elastic scattering cross section for unpolarized neutrons is

$$d\sigma/d\Omega \propto |\,\mathbf{Q}(\mathbf{k})\,|^{2}$$

and it is this quantity (which must be measured in the presence of the nuclear scattering from a crystal) which contains information about the magnetic structure and, in more detail, about the spatial distribution of its magnetization.

The magnetization in a crystal may arise from the intrinsic magnetic moment of the electrons (their spin) or from their motion (orbital magnetization). The magnetic moments of nuclei are smaller by the ratio of the nuclear to the Bohr magneton ($m_e/m_n = 1/1836$) and are disordered at temperatures above 1 K, giving rise to incoherent scattering which will not be discussed. In most materials, paired electrons generate equal and opposite magnetic moments so that the net magnetization is everywhere zero, but in magnetic or magnetized matter some electrons are unpaired. In such cases the magnetization due to spin reflects the spatial distribution of these electrons, but that due to their orbital motion is less simply interpreted.

Model calculations of magnetic scattering are simplified if the total magnetization is considered as the sum of distributions from individual atoms or ions. It is then useful to define a magnetic from factor, f(**k**), such that:

$$f(\mathbf{k}) = \left(\int m(\mathbf{r}) \exp(i\mathbf{k}\,.\,\mathbf{r})\,.\, dr^{3}\right) / \left(\int m(\mathbf{r})\,.\, dr^{3}\right)$$

where m(**r**) is the magnetization associated with the atom. The magnetic structure factor can then be readily expressed in terms of these form factors as:

$$\mathbf{M}(\mathbf{k}) = \Sigma f_n(\mathbf{k}) \mathbf{M}_n \exp(i\mathbf{k} \cdot \mathbf{r}_n)$$

where the summation is taken over the n magnetic centre at distance $\mathbf{r}_n$ from the origin with moment $\mathbf{M}_n$ and form factor $f_n(\mathbf{k})$.

The form factor for magnetization due to electrons in a single unfilled shell may be written as a sum of radial integrals, $< j_l(k) >$, in a manner formally equivalent to the methods used by X-ray crystallographers to express charge densities:

$$f(\mathbf{k}) = \Sigma\ A_l(\mathbf{k}) < j_l(k) >$$

$$\text{where } < j_l(k) > = \int U^2(r) j_l(kr) \cdot dr$$

Here, $j_l(kr)$ is the spherical Bessel function of order l and $U^2(r)$ the radial distribution function of the electrons in the open shell. The $A_l(\mathbf{k})$ are coefficients that depend both on the direction of the scattering vector, **k**, and on the magnetic configuration. For spherically symmetric, spin-only configurations only A_0 is finite.

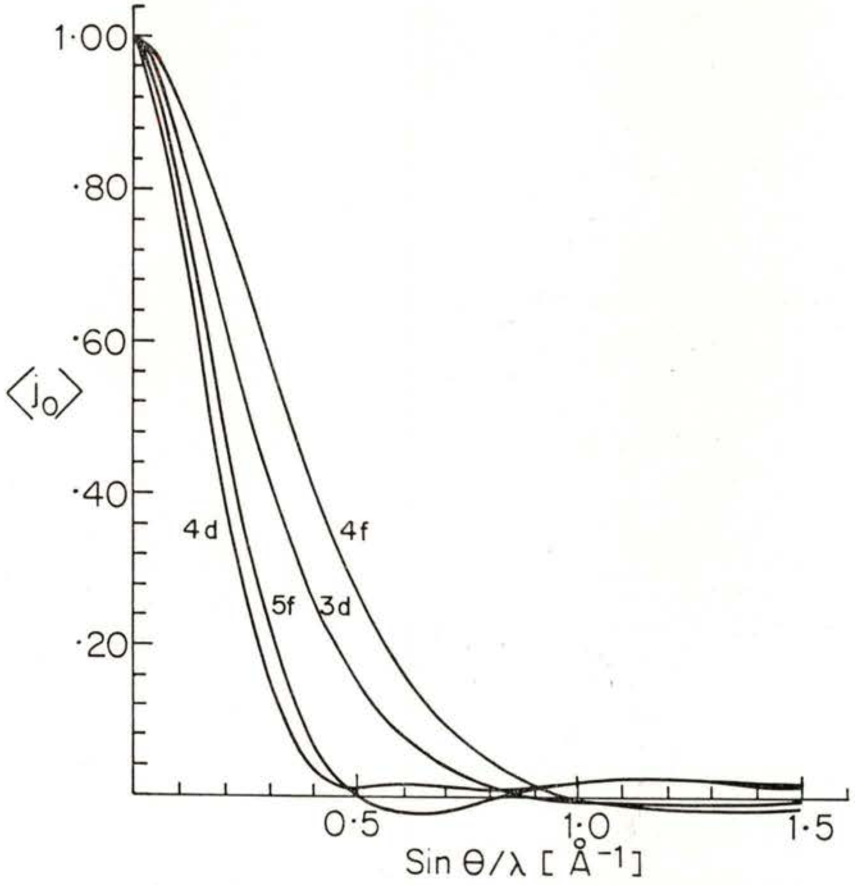

Fig. 1 — The sinθ/λ dependence of $<j_0>$ for some magnetic electron shells computed from free atom wavefunctions.

Figure 1 illustrates the k dependence of $<j_0>$ for the electron shells of magnetic interest. For the general spin-only case with d electrons, A_0, A_2 and A_4 are non-zero. An approximation to the spherical form factor valid for small k when orbital moment is present is given by the dipole approximation:

$$f(k) = 2S<j_0(k)> + \\ + L\{<j_0(k)> + <j_2(k)>\}$$

Figure 2 shows the k dependence of the three integrals $<j_0>$, $<j_2>$ and $<j_4>$ for 3d electrons in the Fe^{2+} free ion. The X-ray form factor for Fe^{2+}, to which all the electrons contribute, is also shown; the presence of the core electrons makes this form factor larger than the magnetic one at high k. The absolute magnitudes of the spherical form factors for X-rays and for the spin-only magnetic and nuclear scattering of neutrons are 5.18, 0.60 and 0.951×10^{-12} cm respectively at $\sin\theta/\lambda = 0.25$ Å^{-1}.

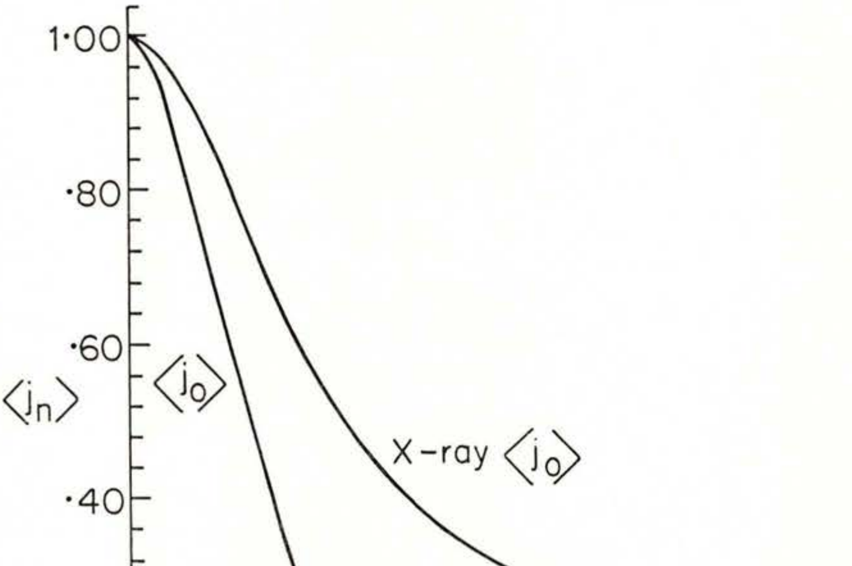

Fig. 2 — The radial integrals $<j_0>$, $<j_2>$ and $<j_4>$ for the 3d electrons of an Fe^{2+} free ion. Also shown is the X-ray form factor to which all electrons contribute.

3 — SCATTERING OF POLARIZED NEUTRONS

The magnetic scattering cross section is the sum of two partial cross sections that correspond to scattering with and without change of neutron spin direction and there can be interference between nuclear and magnetic scattering in the latter case:

$$d\sigma/d\Omega(++) \;\propto\; |N(\mathbf{k}) + \mathbf{P}\,.\,\mathbf{Q}(\mathbf{k})|^2$$

Here N is the nuclear structure factor and **P** is the neutron polarization vector. In the absence of nuclear polarization, only magnetic scattering can change the neutron spin direction and the spin flip cross section is

$$d\sigma/d\Omega(+-) \;\propto\; |\mathbf{P} \times \mathbf{Q}(\mathbf{k})|^2$$

The requirement for a Bragg reflection to have a polarization dependent cross section is that both its nuclear and magnetic components should exist and that they should not be in phase quadrature. This is always true for magnetized ferromagnets, ferrimagnets and, most importantly, for paramagnets whose moments have been aligned by an external magnetic field.

Short wavelength monochromatic polarized neutron beams for diffractometry are typically produced by Bragg reflection of unpolarized neutrons from a reactor by a magnetized singe crystal. If $N(\mathbf{k}) = |Q(\mathbf{k})|$ for the reflection, a high degree of polarization is obtained. Further experimental details are given in section 3.

The flipping ratio, R, between the intensity of Bragg scattering for neutrons polarized parallel and antiparallel to a magnetized sample is

$$\begin{aligned} R = \{\, & |N(\mathbf{k})|^2 + [N(\mathbf{k})\mathbf{P}\,.\,\mathbf{Q}^*(\mathbf{k}) + \\ & + N^*(\mathbf{k})\mathbf{P}\,.\,\mathbf{Q}(\mathbf{k})] + |\mathbf{Q}(\mathbf{k})|^2 \,\}\,/ \\ /\,\{\, & |N(\mathbf{k})|^2 - [N(\mathbf{k})\mathbf{P}\,.\,\mathbf{Q}^*(\mathbf{k}) + \\ & + N^*(\mathbf{k})\mathbf{P}\,.\,\mathbf{Q}(\mathbf{k})] + |\mathbf{Q}(\mathbf{k})|^2 \,\} \end{aligned}$$

In the case of centrosymmetric crystals, both $N(\mathbf{k})$ and $\mathbf{Q}(\mathbf{k})$ are real; if in addition the polarization is parallel to the magnetization and perpendicular to the scattering vector **k**, the ratio becomes:

$$\begin{aligned} R &= \{\, N(\mathbf{k})^2 + 2\,[N(\mathbf{k})M(\mathbf{k})] + N(\mathbf{k})^2 \,\}\,/ \\ &/\,\{\, N(\mathbf{k})^2 - 2\,[N(\mathbf{k})M(\mathbf{k})] + N(\mathbf{k})^2 \,\} = \\ &= (1+\gamma)^2\,/\,(1-\gamma^2) \end{aligned}$$

where $\gamma = M(\mathbf{k})\,/\,N(\mathbf{k})$ and $Q(\mathbf{k}) = M(\mathbf{k})$ The solution to the quadratic equation for γ assuming perfect beam polarization and reversal is:

$$\gamma = \{R + 1 \pm \sqrt{(4R)}\}/(R-1)$$

The choice of root depends on whether the $M(\mathbf{k})$ is greater or less than $N(\mathbf{k})$ and the sign of γ depends on whether R is greater or less than unity. This means that the phase of $M(\mathbf{k})$ is determined relative to the phase of $N(\mathbf{k})$. It should be noted that γ is not well determined by R when γ is close to unity and, in this region, integrated intensity measurements give better accuracy. However, integrated intensities are not needed for the polarized technique and the counting rates in the peak need only be corrected for the background rates measured at ω positions on either side of the reflection.

In most cases magnetic scattering is much weaker than nuclear scattering and $|\gamma|$ is significantly less than one. For small γ, the expression for R can be simplified as:

$$R = 1 + 4\gamma$$

The enhanced sensitivity of the technique for measurement of weak magnetic scattering is easily seen by comparison with fraction of the integrated intensity due to the magnetic scattering of an unpolarized beam:

$$\Delta I/I = 1 + \gamma^2$$

Typically, the peak count rate in a strong reflection from a simple crystal some tens of cubic millimetres in volume will not exceed $10^4\ s^{-1}$. A 5 % error in γ would then require two minutes of measurement for $\gamma = 0.01$; three hours for $\gamma = 0.001$ and some 12 days if $\gamma = 0.0001$.

4 — STEADY STATE AND PULSED NEUTRON SOURCES

The study of magnetization densities rests on single crystal diffractometry. The techniques are well developed at conventional steady state reactor sources: four-circle diffractometers for integrated intensity measurements are equiped with two-stage Joule-Thompson coolers which can provide an accurately controlled specimen temperature down to some 10 K. Materials which order magnetically at even lower temperatures require some form of liquid helium cryostat or dilution refrigerator: these are less manoeuverable so are normally mounted about a vertical, ω, axis and the detector is mounted on a lifting arm, ν, so that data can be collected in normal-beam, zero- and higher-layer geometry. Neutron wavelengths between 0.8 and 1.1 Å are usually used, but access to shorter wavelengths down to some 0.35 Å is desirable to establish extinction parameters. Sizeable fluxes of these shorter wavelengths from a reactor requires the use of a hot source, such as that found at the ILL, Grenoble. Polarized beam diffractometers use the latter geometry with the provision of split-coil superconducting magnets to provide the high fields for aligning paramagnets as well as ferri-and ferromagnets not oriented along their easy axis of magnetization. Polarizing monochromators are normally $Co_{0.92}Fe_{0.08}$ or a Heusler alloy. Flipping is by Larmour precession in an RF field, by Mezei coils or by Tasset's Meissner-Majorana CRYO-FLIPPER. The major advantage of the latter system is its relative insensitivity to stray and possibly varying magnetic fields originating from the magnet at the sample position. All these devices are well described by Williams [2]. A new technique for general polarization analysis, also due to Tasset, is covered in section 8.

Single crystal diffractometry is less well developed at the pulsed neutron sources, ISIS, IPNS, KENS and LANSCE. The major difficulty is the need to use area position-sensitive detectors, which must subtend a large solid angle at the specimen in order to compete effectively with the data collection rates achieved at the best conventional sources. Integrated intensities are obtained using white-beam Laue geometry, the integration being over wavelength (time-of-flight) rather than crystal angle, as in a monochromatic incident beam diffractometry. One advantage of this type of source is the abundance of short wavelength neutrons which render special provisions for extinction unnecessary. The provision of a polarized white neutron beam is another technical problem which has yet to be completely overcome for wavelengths in the range 0.3-1.0 Å: filters based on selective absorption by magnetically aligned ^{149}Sm nuclei at 12 mK, or on selective scattering by aligned protons are both being developed [2]. It is to be hoped that, by SAGAMORE X, pulsed neutron sources will have made the sort of major contribution to the field of magnetization densities that they have already made in other areas of neutron science.

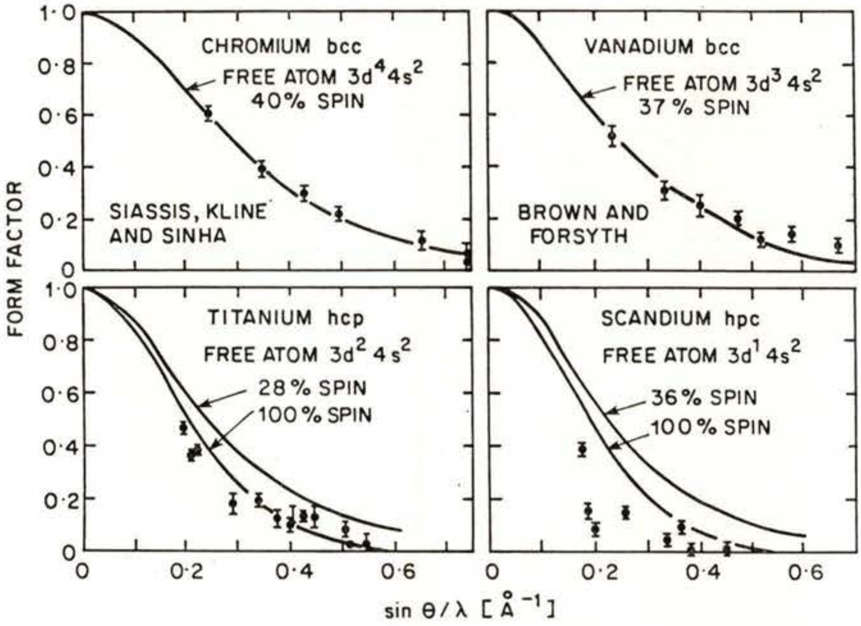

Fig. 3 — Form factors for the aligned paramagnetic scattering from some first group transition elements.

5 — WEAKLY MAGNETIC SYSTEMS

We have seen that counting statistics alone place limitations on the smallness of γ that can reasonable be measured, even if all sources of systematic error could be removed. For this reason, no recent addition has been made to our knowledge of the form factors of paramagnetic elements in an applied external field, examples of which are shown in Figure 3. In making this sort of measurement, corrections must be made for other effects which contribut to the polarization dependent cross-section such as

(i) any slight degree of nuclear polarization

(ii) charge scattering by the nuclei and all electrons (Schwinger scattering)

(iii) the diamagnetism of all electrons, including those in the core before the data can be interpreted in terms of the spatial distribution of the magnetization of unpaired electrons. (i) and (ii) above are susceptible to measurement, but (iii) must be calculated.

Above all, extinction remains the severest source of error in most neutron diffraction measurements and this remains true for the polarized beam method, even when the magnetic contribution to the reflection is small. This is because the slope of the curve relating the observed structure factor to its true value is no longer constant (see Figure 4).

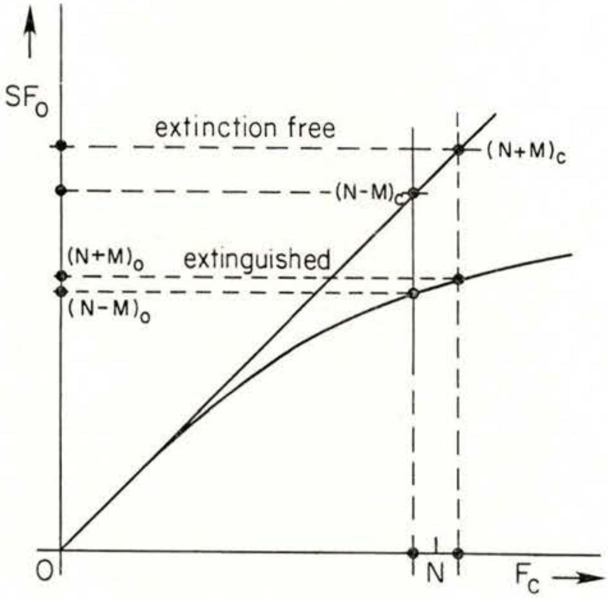

Fig. 4 — The effect of extinction on an observed flipping ratio in a polarized beam experiment, showing that even the ratios close to unity are affected due to the change in the slope of observed, F_0, to calculated structure factor, F_c, when extinction is present.

5.1 — *Magnetic Form Factors in Heavy Fermion Materials*

Heavy fermion superconductors such as UBe_{13}, UPt_3, $CeCu_2Si_2$ and $CeCu_6$ have magnetic susceptibilities which exhibit local-moment behaviour at high temperatures but approach large finite values at low temperature. The properties of these systems are typical of intermetallics with localized f electrons at high temperatures but, at low temperatures, are characteristic of a highly correlated electronic Fermi liquid. Stassis and coworkers [3-5] have measured the induced magnetic form factors in a number of these materials at temperatures characteristic of the different electronic regimes to see if any changes are observable.

In CeCu$_6$, which does not exhibit superconductivity down to 10 mK, measurements [3] were made at 4.2 K and 92 mK, spanning the temperature of 0.5 K below which the material behaves as a Kondo lattice. Figure 5 shows the results which, at both temperatures, agree quite well with the ionic Ce^{3+} free atom form factor and the bulk susceptibility. Thus the generalized susceptibility $\chi(\mathbf{k})$ is Pauli-like in this temperature region and the authors conclude that the suggested transition to the Kondo lattice regime does not affect the induced magnetization. The difference between the form factor extrapolated to zero momentum transfer and the value of χH is atributed to s or p contributions to the induced magnetization.

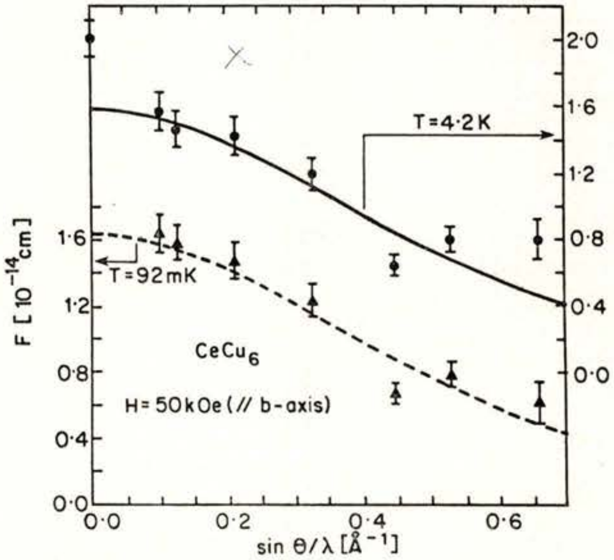

Fig. 5 — The aligned paramagnetic scattering in CeCu$_6$ at 4.2 K and 92 mK [3].

Similar conclusions were reached in the studies of UBe$_{13}$ [4], UPt$_3$ [4] and CeCu$_2$Si$_2$ [4, 5]. The latter material becomes superconducting below 1 K, but the form factor was measured at 4.2 K, in the region of high electronic specific heat. In this case, however, the measured form factor agreed well with the induced magnetization derived from susceptibility.

5.2 — *Magnetization in the Cluster Compound Nb$_6$I$_{11}$*

Transition metal cluster compounds have been the subject of considerable interest over the last two decades. They are characterised by clusters of metal atoms with distances between them close to that found in the pure metals, the clusters being linked together through non-metal atoms by predominantly covalent bonds. Nb$_6$I$_{11}$ is one such cluster compound which is of particular interest because of its magnetic properties: the temperature dependence of the inverse susceptibility (Figure 6) shows four different regions. In regions II and IV the susceptibility follows Curie-Weiss laws with effective moments indicating a low-temperature doublet state ($S = {}^1/_2$) in region II and a high-temperature quartet state ($S = {}^3/_2$) in the region IV. At 274 K the compound undergoes a structural phase transition in which the symmetry drops from Pccn to $P2_1cn$.

The structures of both the high and low temperature phases are characterised by units of six Nb atoms arranged as a distorted octahedron surrounded by eight iodine atoms in a distorted cube, one over each face of the octahedron: the units are connected by six additional bridging iodine atoms. The occurence of the Nb_6I_8 cluster is rather surprising since only 19 electrons are available for 12 metal-metal bonding orbitals and the odd number of electrons is the source of the paramagnetism. Figure 7 shows the geometry of the Nb octahedron in the low and high temperature phases; the symmetry debasement in the former leads to an acentric arrangement.

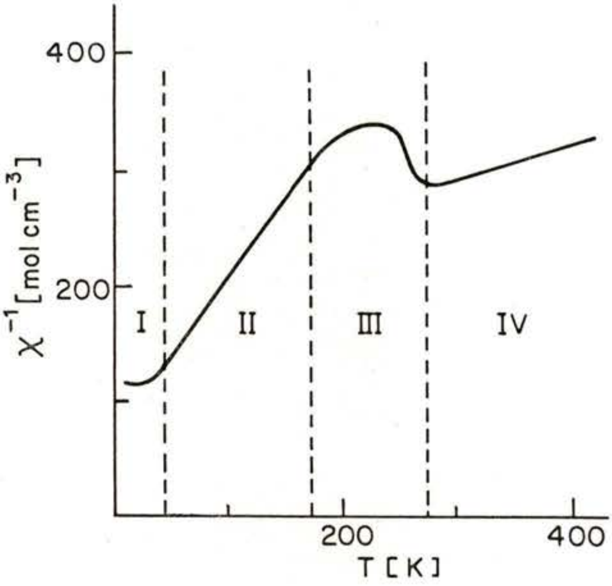

Fig. 6 — The inverse susceptibility of the cluster compound Nb_6I_{11} as a function of temperature. Regions II and IV show Curie-Weiss behaviour corresponding to $S = 1/2$ and $S = 3/2$, respectively.

Nohl and Andersen [6] have made a molecular orbital calculation which identifies the lowest unoccupied and the highest occupied one-electron levels amongst the five bonding d states of highest energy as a function of the distortion of the octahedron which takes place as the temperature is lowered. At 298 K, the range of Nb-Nb distances is small (Figure 7) and the calculations show that the upper four bonding d states are close to one another in energy, and the corresponding electron density is evenly distributed over the octahedron. At 110 K the range of metal-metal distances is greater and the MO model suggests that the states associated with the two shortest bonds (2-3A and 1A-3) lie lowest in energy and are doubly occupied; the next lowest state associated with the 1-2A bond is singly occupied and the remainder are empty.

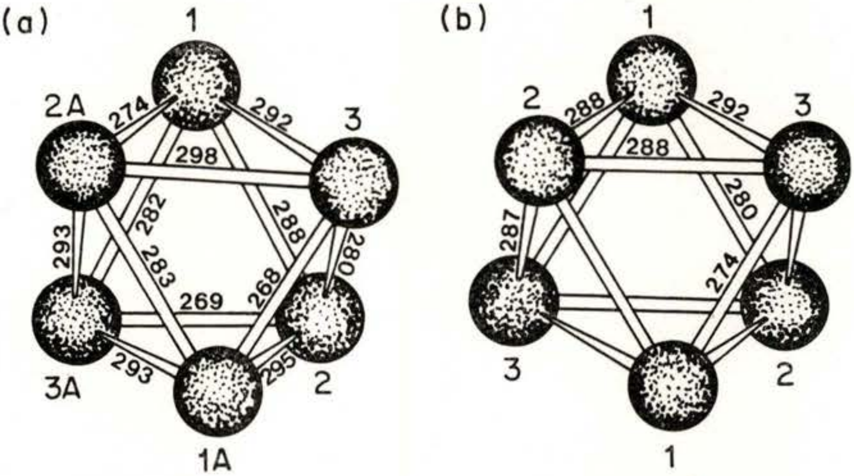

Fig. 7 — The Nb_6I_8 octahedron in Nb_6I_{11} at (a) 110 K, where it is centrosymmetric and (b) at 298 K [7]. The interatomic distances are given in pm.

The consequences of this MO model for the spin density distribution are quite dramatic. In the high temperature phase the spin density should be shared evenly amongst the niobium atoms, whereas in the low temperature phase the spin should be confined to just two of the six Nb atoms. A neutron diffraction experiment to locate the aligned paramagnetism must rely on the sensitivity of the polarized beam technique, since the largest value to be expected for $|\gamma|$ is ~0.005. However Brown, Ziebeck, Simon and Sägebarth [7] were able to obtain sufficient accuracy in γ for 15 reflections at both 40 and 285 K to enable them to assign moments to each Nb site which could then be compared with the predictions of the MO model.

For the low temperature phase, a least squares fit suggests that the majority of the moment is associated with the Nb(1) site, which was predicted to form the polarized bond with Nb(2). The latter atom also has significant moment, but the experiment shows that there may in addition be some moment on other neighbours of Nb(1), such as Nb(3A) and this may in turn indicate that the energy associated with the Nb(1)-Nb(3) bond is sufficiently close to that of Nb(1)-Nb(2) so that the higher state is still partially occupied at 40 K. In the high temperature phase, the observations indicate that most of the moment is associated with the pair of Nb(2) atoms. The authors [7] argue that this may be understood if the lowest lying states are still associated with the shortest bonds, even at 285 K, and the higher energy ones with the long bonds. Since the two longest and the two shortest bonds are between Nb(1) and Nb(3), the intermediate bonds which should be singly occupied all involve Nb(2). Figure 8 illustrates the moment distribution obtained using the best fit models.

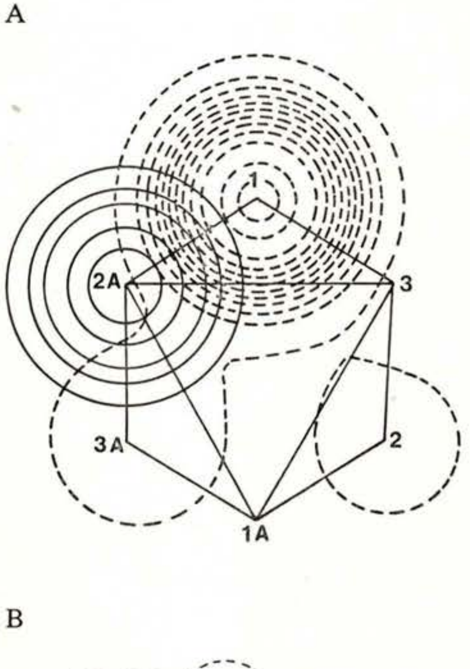

Fig. 8 — The moment distributions found in Nb_6I_{11} at (a) 40 K and (b) 285 K [7]. The solid contours are drawn in the plane of Nb atoms 1A, 2A and 3; the dashed contours are in the parallel plane through Nb(2). In (a) the contours are at equal intervals of 5×10^{-4} μ_B $\AA^{-3}$ and in (b) the interval is halved.

This study of Nb_6I_{11} demonstrates the application of polarized neutron diffractometry to provide a critical test of chemical modelling which will hopefully lead to refinements in the model and further experiments on other cluster compounds.

6 — COVALENCY IN TRANSITION METAL COMPOUNDS

The polarized beam technique continues to provide the valuable information on covalency which modifies the spatial distribution of magnetization from that to be expected in purely ionic salts. The effects are more pronounced in transition metal and actinide rather than rare earth compounds, since the magnetic electrons in the first two take part more fully in the bonding. Many salts of interest remain paramagnetic to liquid helium temperature and a high degree of paramagnetic alignment may be obtained by the application of a magnetic field of some 5 T produced by a split coil superconducting magnet. The measurements then proceed as if the sample were ferromagnetic, the magnetic structure factor of every reflection being accessible at least in principle. In practice, structures of chemical interest are relatively complex and their weaker nuclear structure factors uncertain, even when a companion low temperature neutron structure refinement has been completed. This fact, coupled with the greater sensitivity of weak reflections to the effects of multiple scattering and the difficulty in obtaining good statistical accuracy, renders them unsuitable for inclusion in an accurate study. The availability of experimental beam time places a further constraint on the number of magnetic structure factors which may be measured and, hence, on the use of Fourier methods in their analysis.

More magnetically concentrated salts usually become antiferromagnetic at relatively high temperatures and have small susceptibilities in the paramagnetic region. In some cases the antiferromagnetic structure has the same unit cell as the chemical structure and a symmetry which allows interference between magnetic and nuclear scattering in certain reflections. Polarization-dependent intensities may then be measured if one magnetic domain predominates in the single crystal. This effect was first demonstrated in a study of MnF_2 [8] and measurements on FeF_2, which is isostructural both chemically and magnetically, have just been reported [9]. In this structure, certain reflections are entirely magnetic and their structure factors must therefore be measured by classical integrated intensity methods.

In the majority of instances, long-range antiferromagnetic order is described by a propagation vector which has one or more fractional components or is incommensurate. The magnetic reflections are then completely separated from the nuclear and the polarized beam flipping ratio technique cannot be applied.

6.1 — *First Group Transition Metal(II) Hexaaquacationic Compounds*

An illustration of recent polarized beam studies of covalency in transition metal compounds is provided by the results obtained by Figgis and coworkers [10, 11, 12] for a series of Tutton salts. The materials contained the $[M(II)(H_2O)_6]^{2+}$ complex in the ammonium salt $(NH_4)_2M(SO_4)_2 . 6H_2O$ and crystallize in space group $P2_1/a$, $Z = 2$ with $a = 9$, $b = 12$ and $c = 6$ Å, $\beta = 107°$. In some cases, deuterated crystals were used to reduce the background from the hydrogen incoherent scattering. The M(II) ion is located at (000) and (½½0) so that reflections with $h + k$ odd contain no contribution from moment which is centrosymmetic and centred on these positions. The fact that small but measurable flipping ratios are observed provides direct evidence that the moment distribution of the free ion is perturbed in the solid and that some spin delocalization occurs.

Results are now available for V(II), V(II)0.45(Zn)0.55, Mn(II) and Ni(II): the measurements on Fe(II) are being analysed. The measurements were carried out on the D3 diffractometer at the ILL in a field of 4.6 T and at temperatures in the range 2-4.2 K. All data have recently been reanalysed [12] using the same nine parameter model to describe the magnetic density:

(*a*) 3d, 4s and '4d' orbitals on the transition metal ion
(*b*) (sp^2) hybrid orbitals on oxygen (3 parameters)
(*c*) a 1s orbital on H or D atoms
(*d*) a Gaussian function to represent the M-O overlap density
(*e*) the possibility of radial expansion of the 3d form factor

The most recent results are for V(II), which is nominally spin-only $3d^3$ occupying the octahedral t_{2g} states. Here the experiment finds:

$3d^3$-t_{2g} 2.84(6) $3d^3$-e_g $-0.03(4)$

together with a substantial difuse 4d-t_{2g} like population and a relatively large spin population on H (D). There is evidence for π covalence in the plane of the water molecule, with spin donation from 3d-t_{2g} into diffuse metal and O-D(H) bond regions. Negative spin elsewhere in the σ framework suggests that there is appreciable spin polarization and hence electron correlation.

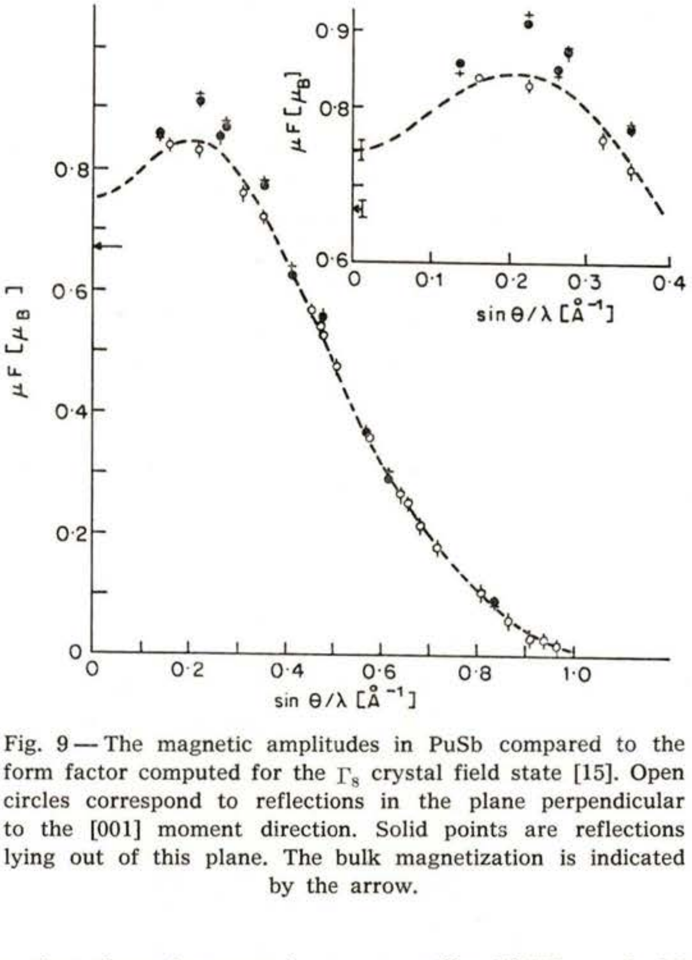

Fig. 9 — The magnetic amplitudes in PuSb compared to the form factor computed for the Γ_8 crystal field state [15]. Open circles correspond to reflections in the plane perpendicular to the [001] moment direction. Solid points are reflections lying out of this plane. The bulk magnetization is indicated by the arrow.

Most importantly, the comparison with the previous studies on Mn(II) and Ni(II) show a consistent qualitative picture in accord with the varying 3d-t_{2g} and -e_g configurations and the covalence in all cases is small, but measurable:

- (i) V(II) and Mn(II) have 3d t_{2g} populations and substantial in-plane π spin delocalisation leading to spin transfer to diffuse metal and O-D orbitals
- (ii) Ni(II) and Mn(II) have 3d e_g populations, but σ transfer of spin in an antibonding orbital. The occupation of diffuse metal and O lone-pairs is less.
- (iii) for all ions, the out-of-plane π interaction is negligible.

6.2 — *An Actinide Salt*

Similar techniques to those described in 5.1 above have been used to study the distribution of bonding in UCl_4 [13] and this is referred to in more detail in this Volume by Lander [14]. Sufficient to say that, although no transferred spin density is found on the Cl sites, the observations can be qualitatively accounted for by electron transfer from the uranium 5f orbital to the 6d antibonding orbital formed through the covalent interaction between the U 6d and the Cl p states. This is the first direct observation of covalency in systems involving 5f and 6d electrons and its positive outcome encourages further experimentation.

7 — ACTINIDE INTERMETALLICS

Light actinide (U, Np and Pu) intermetallic compounds provide many interesting examples in which long range order is established between localised 5f electron moments. The last three years have seen an expansion in the number of studies devoted to these materials and I have chosen to illustrate this section of my review with

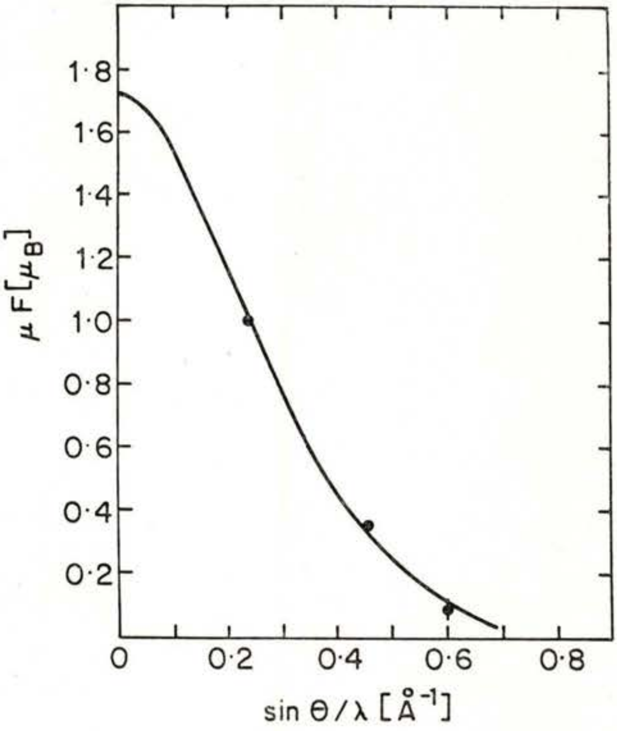

Fig. 10 — The k dependence of the iron form factor in $PuFe_2$ compared to that found in the element (solid curve) [16].

some of the results obtained by Lander and co- workers on the plutonium compounds PuSb [15], $PuFe_2$ [16] and PuTe [17]. The first two of these are ferromagnets below 67 and 564 K, respectively, so polarised beam flipping ratio measurements could be made to determine the moments and form factors of the magnetic constituents.

form factor computed for the Γ_8 crystal field state in intermediate coupling with the spin-orbit parameter $\xi = 2241$ cm^{-1}, in which the **k** dependence of the scattering amplitude can be expressed as:

$$\begin{aligned} \mu f(\mathbf{k}) = \mu[< j_0(k) + \\ + (C_2 + \Delta C_2 \sin^2\Phi) < j_2(k) > + \\ + C_4 < j_4(k) >] \end{aligned} \qquad 7.1$$

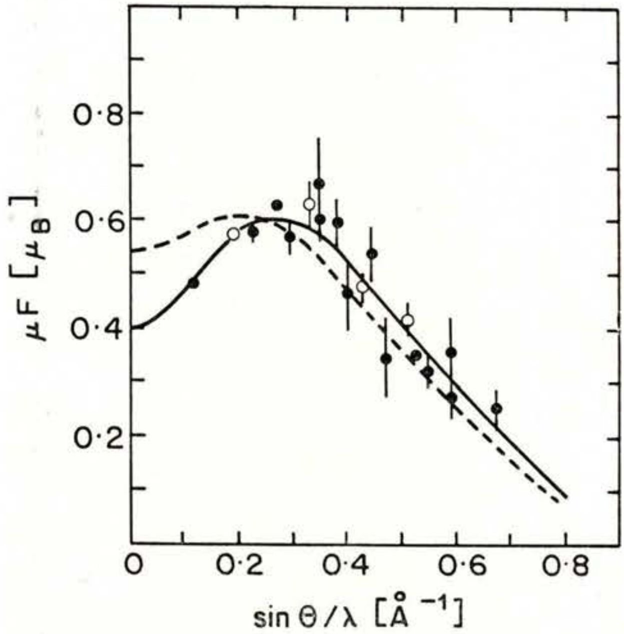

Fig. 11 — The plutonium magnetic scattering in $PuFe_2$. The best fit curve (solid) requires a C_2 value of 6.0 (see text) [16]. The dashed curve corresponds to the value of $C_2 = 3.8$ found in PuSb.

Pu^{3+} is nominally $5f^5$ in which there is strong cancellation of the L and S components of moment in the $J = 5/2$ ground state manifold. The cancellation leads to small g-factors, small magnetic moments and unusual form factors with maxima at $\sin\Theta/\lambda > 0$. Figure 9 shows the magnetic amplitudes in PuSb [15] compared to the here Φ is the azimuthal angle of the scattering vector out of the plane perpendicular to the magnetization and $C_2 = (2-g)/g$, where g is the Landé splitting factor. In Figure 9 the dashed curve corresponds to values of $C_2 = 3.80(7)$, $\Delta C_2 = 1.30(15)$ and $\mu = 0.745(20)\mu B$.

In $PuFe_2$, which has the cubic Laves phase structure, the moment values are found [16] to be:

$$\mu_{Pu} = 0.45(5) \quad \mu_{Fe} = 1.47\ \mu B$$

Figure 10 shows that the **k** dependence of the iron form factor is the same as that for the element, if the latter is normalised to 1.73 μB. Figure 11 shows that the plutonium scattering, which is again a maximum away from $\sin\Theta/\lambda = 0$, does not, however, correspond to that found in PuSb. The best fit curve shown as solid in Figure 11 requires the unrealistically high value of 6.0 for C_2 in equation 7.1. No crystal field level within the $J = 5/2$ manifold can predict so large a value for C_2 and the $J = 7/2$ excited state is at too high an energy to produce mixing. The authors conclude that the explanation may lie in the hybridization of the Pu 5f wavefunctions with the 3d functions on Fe, leading to a reduction in the orbital moment of the Pu.

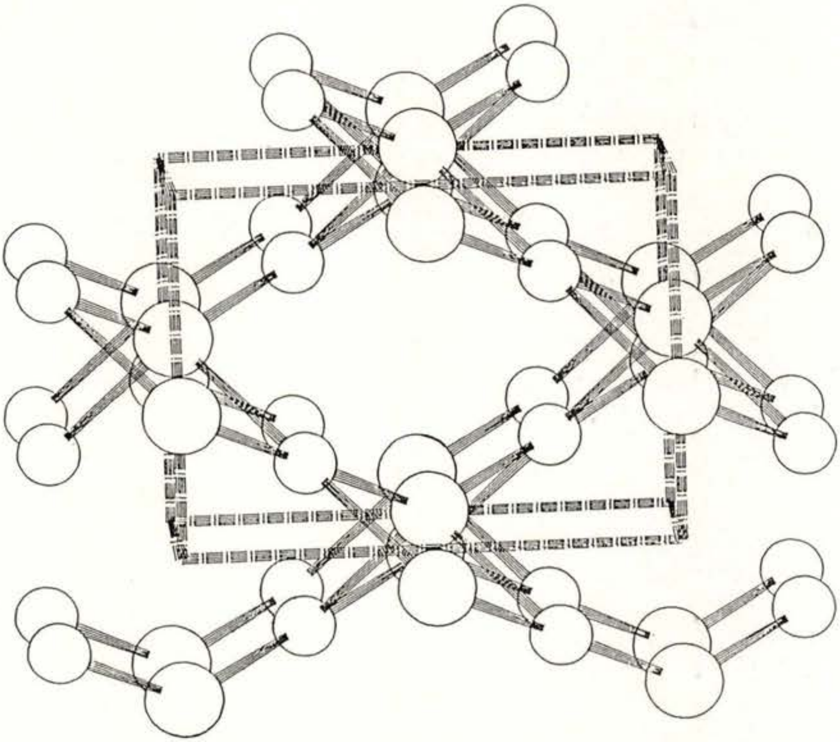

Fig. 12 — The crystal structure of CuO showing the square-planar coordination of Cu by 0.

The third plutonium compound, PuTe, is a paramagnet whose form factor [17] corresponds quite closely to an $L = 0$, spin-only ($C_2 = 0$) situation. In this case, the authors suggest that it is preferable to consider PuTe as a band system, rather like an actinide metal, in which the orbital moment is almost entirely quenched.

Further discussion of the degree of magnetic moment localization in these plutonium compounds is contained in a recent paper [18] and forms part of a poster at this conference [19].

8 — AN UNPOLARIZED BEAM STUDY

Copper oxide provides a topical example of a magnetic structure determination from unpolarized beam data which has,

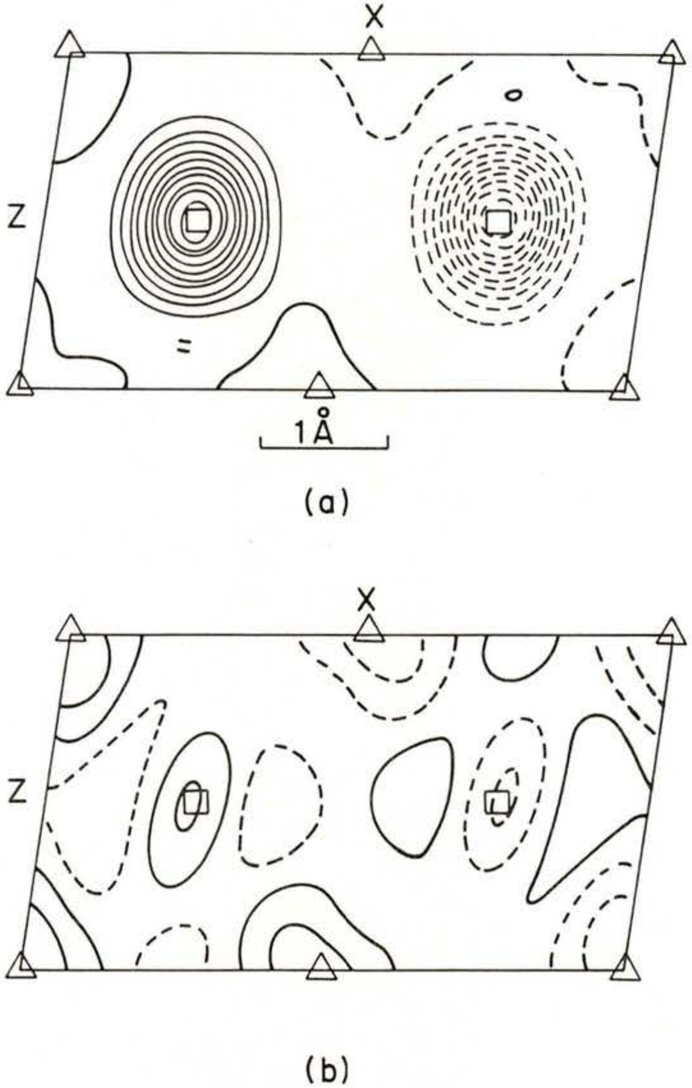

Fig. 13 — CuO [010] Fourier projections of (a) the observed magnetization and (b) the difference density after subtraction of the best fit spherical density on Cu [20]. The positions of the Cu atoms are marked by open squares and those of the oxygens by open triangles. Positive density contours are solid and negative ones are dashed.

nevertheless, allowed some conclusions to be drawn about the orbital occupation of the Cu^{2+} ions, which have square-planar coordination in the monoclinic structure as shown in Figure 12. The antiferromagnetic propagation vector is ($\frac{1}{2}$ 0 $-\frac{1}{2}$) at temperatures below the incommensurate-commensurate phase transition at 213 K. Although the Cu moment is low, 0.65(3) μB parallel to [010], the single crystal integrated magnetic intensities were sufficient to show that there is significant aspherical magnetization density [20]. This was modelled by a multipole expansion which was limited to the terms in Y_{00}, Y_{20} and Y_{22}, since the data did not extend far enough in **k** to define fourth order terms. The multipole coefficients are consistent with equal occupation of $d_{x^2-y^2}$ and d_{xz} orbitals which is perhaps surprising, since the accepted model for Cu^{2+} in an orthorhombic environment is one in which the E_g hole states are lower with a single hole in a $d_{x^2-y^2}$ orbital pointing towards the ligands (z is perpendicular to the plane of the orbitals). Two further parameters were needed to define the total magnetization:

(*a*) a Y_{00} 2p term to describe 0.14(4) μB on the oxygen atoms directed parallel to the majority spin on its Cu neighbours

(*b*) a 9 % radial expansion of the Cu^{2+} free ion form factor.

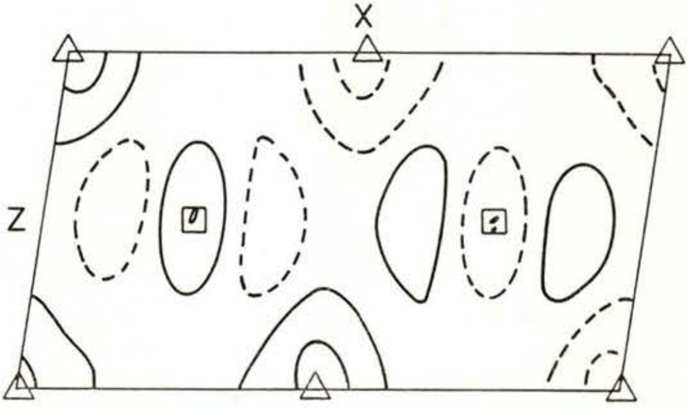

Fig. 14 — [010] Fourier projection of the aspherical magnetization density calculated for the multipole model of CuO [20]. The conventions are the same as for Figure 13.

The latter figure is comparable with the 7 % expansion found in $CuCl_2 . 2D_2O$ [21]. Figure 13 shows (a) the [010] Fourier projections of the observed magnetization and (b) the difference density from a spherical moment distribution solely on the Cu ions. Figure 13(b) is very similar to Figure 14 which shows the aspherical contributions calculated from the best fit multipole model.

9 — GENERAL POLARIZATION ANALYSIS

Magnetic structure determination from intensity data which average over the initial and final neutron polarization states must appeal to the agreement between observed and calculated intensities to define the directions of the moments within the magnetic unit cell. However, neutron polarization is always retained in any single scattering process and its direction

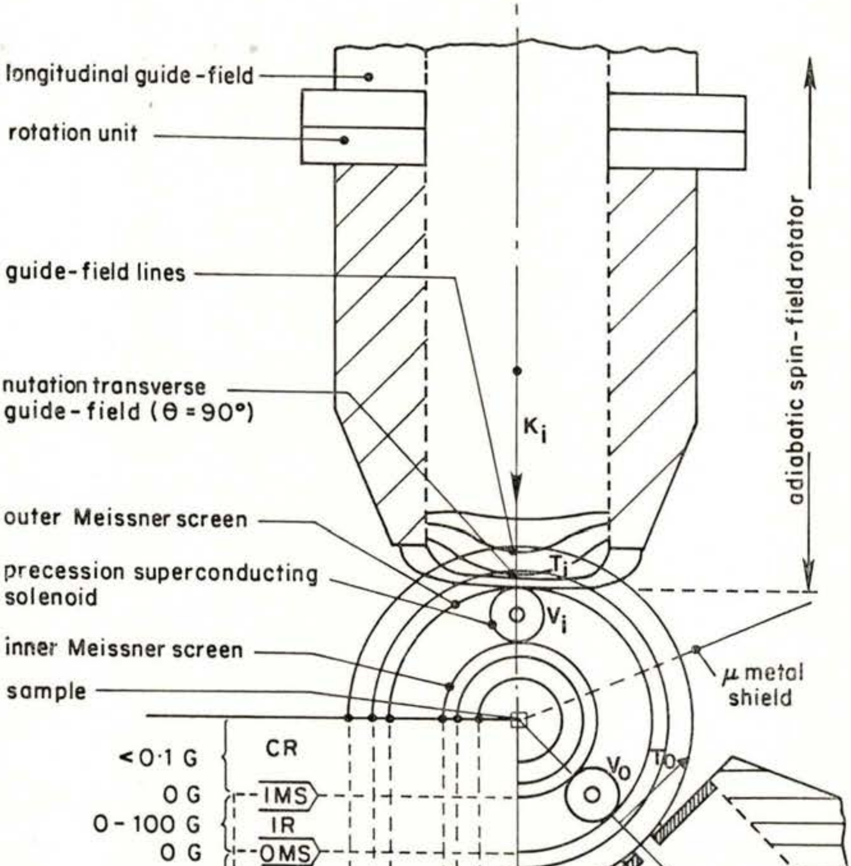

Fig. 15 — Schematic plan, in the horizontal plane of scattering, of the CRYOPAD apparatus for general polarization analysis [25].

is rotated by any components of magnetization in the scatter which are not parallel to its initial direction. The theory has been fully developed by Blume [22]. Ideally, all three components of both the initial and final neutron polarization should be defined in a complete polarization analysis experiment which can provide direct information about the orientation, as well as the magnitude, of atomic moments. Until quite recently, general polarization analys has only been routinely applied in transmission studies of domain structure and kinetics [23]; in most scattering experiments only a single component of the scattered polarization has been analyzed as in the experimental arrangement of Moon, Riste and Koehler [24].

Figure 15 illustrates the major features of a new device due to Tasset [25]; the CROPAD allows complete control over the direction of the initial neutron polarization and enables all components of the final polarization to be determined. It makes use of an inner and an outer, coaxial, Meissner screen (IMS and OMS, respectively) in the form of long vertical test tubes. The plane of scattering is then divided radially into three regions: the central region (CR), an annular intermediate region (IR) and the outer region (OR). Both screens are cooled below their superconducting transition temperature in a zero-field region. The specimen is mounted on the axis of the screens in a variable temperature insert constructed entirely of non-magnetic materials.

The incident and scattered neutron beams pass through adiabatic spin-field rotators (ASFR) which are outside the cryostat. These control the angle of the magnetic guide field Θ to the vertical in the plane perpendicular to the neutron flight path: a polarized beam entering the first ASFR leaves it with its polarization set at this nutation angle. The annular space between the OMS and the IMS houses two vertical superconducting solenoids. The incident and scattered neutron beams each pass diametrically through one of the solenoids: the solenoid current can then be adjusted so that the neutron polarization precesses by an angle Φ at a constant nutation angle Θ about the vertical axis of the coil.

The CRYOPAD has already been used to determine the absolute magnetic configuration of the magnetic moments in Cr_2O_3 [25] and initial estimates suggest that it is capable of determining the direction of initial and final polarizations to a precision of some 1°. It is likely to prove invaluable in the precise determination of non-collinear magnetization densities.

REFERENCES

[1] Oxford Series on Neutron Scattering in Condensed Matter No. 1. «Polarized Neutrons» Williams, W. G., Oxfird University Press (1988).

[2] LOVESEY, S. W., Portgal. Phys. **19**, 81 (1988).

[3] VRTIS, M. L., LOONG, C.-K., HINKS, D. G., STASSIS, C. and ARTHUR, J., J. Appl. Phys., **61**, 3174 (1987).

[4] STASSIS, C., ARTHUR, J., MAJKRZAK, C. F., AXE, J. D., BATLOGG, B., REMEIKA, J., FISK, Z., SMITH, J. L. and EDELSTEIN, A. S., Phys. Rev., **B34**, 4382 (1986).

[5] STASSIS, C., AXE, J. D., MAJKRZAK, C. F., BATLOGG, B. and REMEIKA, J., J. Appl. Phys., **57**, 3087 (1985).

[6] NOHL, H. and ANDERSON, O. K., Proc. Conf. on Transition Metals, Leeds, IOP Conf. Ser., **55**, 61 (1980).

[7] BROWN, P. J., ZIEBECK, K. R. A., SIMON, A. and SÄGEBATH, M., J. Chem. Soc. Dalton Trans., 111 (1988).

[8] NATHANS, R., ALPERIN, H. A., PICKART, S. J. and BROWN, P. J., J. Appl. Phys., **34**, 1182 (1963).

[9] DE ALMEIDA, M. J. M. and BROWN, P. J., J. Phys., **C21**, 1111 (1988).

[10] FENDER, B. E. F., FIGGIS, B. N. and FORSYTH, J. B., Proc. Roy. Soc. London, **A404**, 139 (1986).

[11] FENDER, B. E. F., FIGGIS, B. N., FORSYTH, J. B., REYNOLDS, P. A. and STEVENS, E., Proc. Roy. Soc. London, **A404**, 127 (1986).

[12] DEETH, R., FIGGS, B. N., FORSYTH, J. B., KUCHARSKI, E. S. and REYNOLDS, P. A., Submited to Proc. Roy. Soc. (London), 1988.

[13] LANDER, G. H., BROWN, P. J., SPIRLET, M. R., REBIZANT, J., KANELLAKOPULOS, B. and KLENZE, R., J. Chem. Phys., **83**, 5988 (1985).

[14] LANDER, G. H., Portgal. Phys. **19** (1988), in press.

[15] LANDER, G. H., DELAPALME, A., BROWN, P. J., SPIRLET, J. C., REBIZANT, J. and VOGT, O., J. Appl. Phys., **57**, 3748 (1985).

[16] WULFF, M., LANDER, G. H., REBIZANT, J., SPIRLET, J. C., LEBECH, B., BROHOLM, C. and BROWN, P. J., Phys. Rev., **B37**, 5577 (1988).

[17] LANDER, G. H., REBIZANT, J., SPIRLET, J. C., DELAPALME, A., BROWN, P. J., VOGT, O. and MATTENBERGER, K., Physica B (in Press) (1988).

[18] LANDER, G. H., WULFF, M., REBIZANT, J., SPIRLET, J. C., BROWN, P. J. and VOGT, O., J. Appl. Phys., **63**, 3601 (1988).

[19] LANDER, G. H. and WULFF, M., Portgal. Phys. **19** (1988), in press.

[20] FORSYTH, J. B., BROWN, P. J. and WANKLYN, B. M., J. Phys., **C21**, 2917 (1988).

[21] UMEBAYASHI, H., FRAZER, B. C., COX, D. E. and SHIRANE, G., Phys. Rev., **167**, 519 (1968).

[22] BLUME, M., Phys. Rev., **130**, 1760 (1963).

[23] RECKVELDT, M. Th., J. de Physique, **32**, C579 (1971).

[24] MOON, R. M., RISTE, T. and KOEHLER, W., Phys. Rev., **181**, 920 (1969).

[25] TASSET, F., BROWN, P. J. and FORSYTH, J. B., J. Appl. Phys., **63**, 3606 (1988).

THE COMPANIONSHIP OF NEUTRON AND PHOTON MAGNETIC SCATTERING IN CONDENSED MATTER RESEARCH

STEPHEN W. LOVESEY
Rutherford Appleton Laboratory, Oxfordshire, UK

ABSTRACT — The application of magnetic neutron scattering began in earnest in the 50's with numerous diffraction studies. Inelastic studies were much more demanding in view of the modest neutron flux available in reactor beams. At about the same time, the theoretical physicists Gell-Mann, Goldberger and Low verified that in photon scattering from electrons there is a spin-dependent, relativistic correction to the Thomson (charge) amplitude. The exploitation of this weak addition to charge scattering was hampered by the relatively low photon flux from laboratory X-ray sources. But some years later, de Bergevin and Brunel used such a source for magnetic photon scattering experiments. The advent of synchrotron sources opens the way for magnetic photon diffraction experiments on a routine basis, although inelastic magnetic scattering remains a challenge.

In view of continuing developments at synchrotron sources, and the proposed construction of advanced sources, it is timely to compare and contrast the basic ingredients of magnetic neutron and photon scattering processes. The paper surveys the two processes, using a common language. Cross sections for diffraction of photons by magnetic materials are discussed, together with polarisation induced interference terms. An expression for the photon amplitude that includes inelastic and resonance processes is provided. This provides a basis for a discussion of X-ray resonance exchange scattering.

Invited Talk presented at Sagamore IX, Portugal (1988).

1 — PROLOGUE

Magnetic photon scattering is a burgeoning topic in condensed matter research fuelled by the development of synchrotron radiation sources and instrumentation. The recent spate of work began in 1985. Prior to this date, de Bergevin and Brunel reported seminal studies which used laboratory X-ray and synchrotron sources (references are contained in their review [1]). Their work was inspired by theoretical studies dating back to 1954; the reader is referred to [2] for a complete exposition of the relevant quantum electrodynamics.

By contrast, magnetic neutron scattering is firmly established. Magnetic diffraction and spectroscopic studies are made routinely with reactor and advanced spallation neutron sources.

Magnetic neutron and photon scattering processes engage the same atomic quantities, namely the spin and current (orbital) densities [1, 3-6]. An aim of this paper is to express the theory for the interpretation of magnetic neutron and photon scattering in a common language. We will draw on the theoretical framework established for neutron scattering [6]. For completeness, we include also a brief discussion of electrostatic interactions in neutron scattering.

Very recently, theoretical and experimental work on X-ray resonance exchange scattering has been reported [7, 8, 15]. We will be chiefly concerned here with magnetic photon diffraction, with relatively few comments about inelastic and resonance processes. However, the appropriate scattering amplitude, and its reduction to the form which describes diffraction experiments, is provided in an appendix.

Neutrons are weakly scattered by bulk samples. The scattering occurs chiefly through interactions with nuclei and unpaired electrons. In the case of neutron-electron scattering, the dominant (magnetic) process has an amplitude which is comparable to that observed for the nuclear process, i. e. of order 10^{-12} cm. The neutron scattering technique is therefore a gentle probe of matter that provides information, on an atomic scale, on nuclear and electronic properties. A limitation on its usefulness is the weakness of neutron beams available from reactor and spallation sources; an intensity on the target sample of 10^9 neutrons/cm^2 sec is about the best that can be achieved today.

The photon interaction with matter, described by quantum electrodynamics, is dominated by electron charge coupling. Scattering experiments, which often involve non-linear effects, provide a wealth of electronic information including, of course, surface properties. Magnetic photon scattering is a relativistic effect, and smaller than charge (Thomson) scattering by a factor equal to the ratio of the incident photon energy to the electron rest mass (511 keV). The theory of magnetic photon scattering discussed in this paper is based on a perturbative calculation of the photon amplitude, reviewed in an appendix, which is valid when this ratio is much less than unity.

Synchrotron sources provide intense photon beams, e. g. a factor 10^6 improvement on rotating anode sources. The new facilities under construction at Argonne National Laboratory and ESRF, Grenoble, will provide beams with intensities better by a further two or more orders of magnitude. In the context of neutron scattering, such an increase in intensity would totally revolutionise the utility of the technique in condensed matter and materials research.

To help orientate subsequent discussions we recall now the Thomson cross section for scattering from an electron. The formula can be deduced from a classical picture, in which light radiated by a forced harmonic oscillator corresponds to elastic scattering of incident radiation, or the extreme non-relativistic limit of the Klein-Nishina formula [2]. Let Θ be the angle through which light is scattered, and denote the classical electron radius by $r_e = 0.282 \; 10^{-12}$ cm. With this notation, the formula for Thomson scattering from an electron into an element of solid angle $d\Omega$ is,

$$\frac{d\sigma}{d\Omega} = \frac{1}{2} r_e^2 \, (1 + \cos^2\Theta).$$

Natural units for magnetic neutron and photon diffraction amplitudes are $r_o = \gamma r_e$ and $g r_e$, respectively, where $\gamma = -1.91$ is the neutron gyromagnetic ratio and g is the ratio of the incident photon energy to the electron rest mass.

2 — PHOTON SCATTERING AMPLITUDE

We record the amplitude for charge and magnetic photon scattering. The magnetic contribution is derived as a perturbation to the charge process, and hence g is assumed to be much less than unity. The reader is referred to [9, 10] for a convincing derivation of the result presented below. Because the derivation is quite complicated, at least at first sight, we abstract key parts in an appendix.

First, let us define some notation. The incident photon wave vector and frequency are denoted by $\mathbf{q}$ and ω, respectively. A prime is used to label the quantities for a secondary photon and $\mathbf{k} = \mathbf{q} - \mathbf{q}'$. The dimensionless parameter $g = \hbar\omega/m_e c^2$.

The microscopic electron densities that occur in the photon amplitude are those for charge, spin and current. Let $\mathbf{R}$, $\mathbf{s}$ and $\mathbf{p}$ denote the position, spin and momentum operators for an electron. It is the spatial Fourier transforms of the densities that actually enter the photon amplitude. Using the definitions,

$$n(k) = \sum_j \exp(i\mathbf{k} \,.\, \mathbf{R}_j), \qquad (2.1)$$

$$\mathbf{S}(k) = \sum_j \exp(i\mathbf{k} \,.\, \mathbf{R}_j)\mathbf{s}_j, \qquad (2.2)$$

and

$$\mathbf{L}(k) = (2/i\hbar k^2) \times \times \sum_j \exp(i\mathbf{k} \,.\, \mathbf{R}_j)\ (\mathbf{k} \times \mathbf{p}_j), \qquad (2.3)$$

the photon amplitude for diffraction is [9, 10]

$$r_e \{ n(k)\, \mathbf{e}' \,.\, \mathbf{e} - ig[\mathbf{S}(k) \,.\, \mathbf{B} - 2 \sin^2(\frac{1}{2}\,\Theta)\mathbf{L}(k) \,.\, \mathbf{A}] \}. \qquad (2.4)$$

Here, the first term is the Thomson contribution and the second, prefaced by the small parameter g, is the magnetic amplitude. The quantities $\mathbf{A}$ and $\mathbf{B}$ depend on the photon polarisations in the initial and secondary states, $\mathbf{e}$ and $\mathbf{e}'$ respectively, and explicit formulae are provided in an appendix, together with results appropriate for inelastic magnetic scattering.

If the Fourier transforms of the microscopic densities are purely real, the cross section, proportional to the absolute square of (2.4), is the sum of the squares of the charge and magnetic amplitudes. The magnetic contribution, being of order g^2, is a small correction to the charge scattering. It has been observed in materials with magnetic superlattice structures (antiferromagnets and spiral phases) for which charge and magnetic Bragg peaks are quite separate in reciprocal space [1, 14].

The charge density n(k) will be a complex quantity for a non-centrosymmetric crystal structure, as will spin and current densities. Anomalous scattering also makes n(k) complex, so even for a centrosymmetric structure there can be an interference between charge and magnetic scattering. If we write $n = n' + in''$ the cross section is [1, 4]

$$\frac{d\sigma}{d\Omega} = \left(\frac{d\sigma}{d\Omega}\right)_T + + r_e^2\,(-g)\,n''\{\mathbf{S}(k)\ (1 + \cos\Theta) + + \mathbf{L}(k)\cos\Theta(1 - \cos\Theta)\} \,.\, (\hat{\mathbf{q}} \times \hat{\mathbf{q}}'), \qquad (2.5)$$

in which $\hat{\mathbf{q}}$ and $\hat{\mathbf{q}}'$ are unit vectors, and

$$\left(\frac{d\sigma}{d\Omega}\right)_T = \frac{1}{2}\, r_e^2\, |\, n(k)\, |^2\, (1 + \cos^2\Theta), \qquad (2.6)$$

is Thomson's formula for an atom. The interference term is not only linear in g, but it can be manipulated with an external field to generate difference data. In consequence, such an interference term provides data for the magnetic amplitude together with its sign [1]. Alternatively, the polarisation of incident and secondary photon beams can be used to discriminate magnetic from charge scattering. This topic is the subject of the next section.

We conclude this section by providing the cross section for the scattering of unpolarised photons. From (2.4) it can be shown that, for real charge, spin and current densities, the diffraction cross-section is,

$$\frac{d\sigma}{d\Omega} = \left(\frac{d\sigma}{d\Omega}\right)_T + (g r_e \sin^2 \frac{1}{2}\Theta)^2 [\{\mathbf{S}(k) \cdot (\hat{\mathbf{q}} - \hat{\mathbf{q}}')\}^2 + \{(\mathbf{S}(k) + \mathbf{L}(k)) \cdot (\hat{\mathbf{q}} + \hat{\mathbf{q}}')\}^2 + \{\mathbf{h} \cdot \mathbf{L}(k) \sin\Theta\}^2 + \{\mathbf{h} \cdot [\mathbf{L}(k) \sin\Theta + 2\mathbf{S}(k) \cot \frac{1}{2}\Theta]\}^2], \qquad (2.7)$$

where $\mathbf{h} = -(\mathbf{q} \times \mathbf{q}')/q^2 \sin\Theta$ is a unit vector perpendicular to the plane of scattering. The magnetic contribution in (2.7) is of order g^2, as expected. It is proportional to $\sin^4(\Theta/2)$, and hence decreases rapidly with decreasing scattering vector k. The spin contribution in (2.5) is proportional to $\sin\Theta$ near the forward direction, and hence decreases more slowly than the corresponding term in (2.7). The densities $\mathbf{S}(k)$ and $\mathbf{L}(k)$, evaluated for magnetic ions, vanish in the limit $k \to \infty$. We conclude that the magnetic contribution to the diffraction cross section is significant over a limited range of k. Finally, note that magnetic scattering in (2.7) occurs both in and perpendicular to the plane of scattering. The polarisation induced interference, considered in the next section, vanishes if the spin and current densities are aligned perpendicular to the plane.

3 — PHOTON POLARISATION EFFECTS

Formalisms for handling polarisation effects in scattering experiments are well documented [2, 11] and the applications to neutron and photon experiments have recently been reviewed [4, 6]. In view of this situation, we will simply exhibit the results of immediate interest.

A circular polarisation in the incident photon beam creates an interference between the charge and magnetic amplitudes, which is in general finite at Bragg positions common to the chemical and magnetic reciprocal lattices, e. g. ferromagnets. Reversing or switching on and off the polarisation then affords a very convenient method of extracting the magnetic amplitude. Moreover, the secondary polarisations for charge and magnetic scattering are different, so this parameter provides a handle for discrimination. When coincident charge and magnetic Bragg reflections are analysed, as in the present and anomalous scattering cases, it is advantageous to select peaks for which the charge structure factor is small, since then the relative effect of the magnetic contribution is optimised.

Let P_2 be the Stokes parameter for circular polarisation; the probability of right-hand polarisation is $(1 + P_2)/2$, and that for left-hand polarisation is $(1 - P_2)/2$. The diffraction cross-section derived from (2.4) is,

$$\frac{d\sigma}{d\Omega} = \left(\frac{d\sigma}{d\Omega}\right)_T + (-g) r_e^2 P_2 n(k) (1 - \cos\Theta) \times [\mathbf{S}(k) \cdot (\hat{\mathbf{q}} \cos\Theta + \hat{\mathbf{q}}') + \cos^2(\frac{1}{2}\Theta) \mathbf{L}(k) \cdot (\hat{\mathbf{q}} + \hat{\mathbf{q}}')]. \qquad (3.1)$$

Here, it is assumed that only circular polarisation is present in the incident beam, and the magnetic term of order g^2 is omitted on the grounds that it is negligible compared to the interference term, given $g << 1$.

To be specific, consider a geometry in which the spin and current densities are aligned together in the plane of scattering, and make an angle β with $\mathbf{q}$. In this

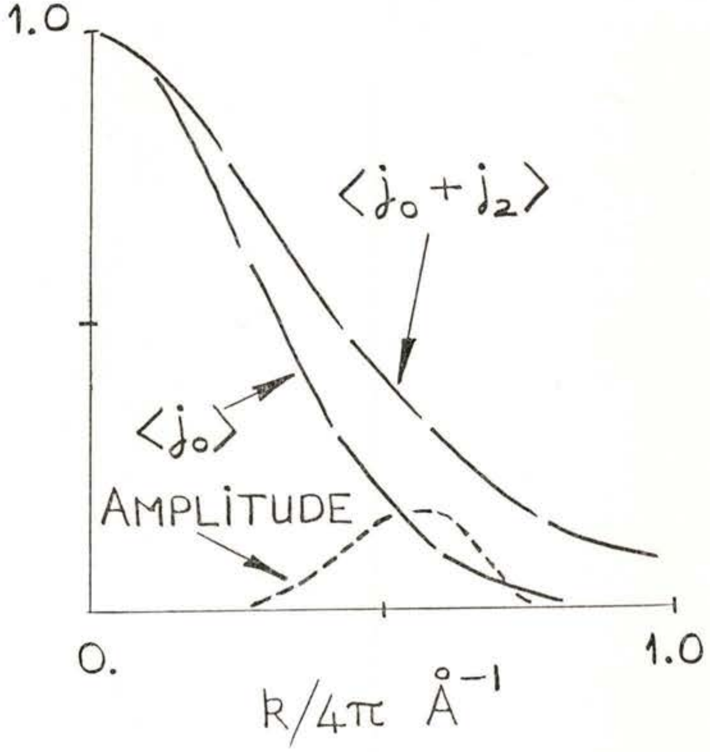

Fig. 1 — The quantity defined in (3.6) is plotted for 10 keV photons. Radial integrals are appropriate for Pr^{3+}, and values of $n(k)/56$ are used, i. e. the X-ray form factor is normalized to unity. The radial integrals $< j_0 >$ and $< j_0 > + < j_2 >$, which occur in the dipole approximation for spin and current densities, are included for completeness.

occur in the dipole approximation for spin and current densities, are included for completeness.

occur in the dipole approximation for spin and current densities, are included for completeness.

occur in the dipole approximation for spin and current densities, are included for completeness.

occur in the dipole approximation for spin and current densities, are included for completeness.

occur in the dipole approximation for spin and current densities, are included for completeness.

occur in the dipole approximation for spin and current densities,

This vanishes in the forward direction and for large scattering vectors. A study of (3.3) at angles Θ, β for which (3.2) is zero shows that an orbital-only scattering experiment is entirely feasible, although L(k) will be observed over just a small range of k values, as illustrated in Figure 1.

It is useful to examine the form of the interference term in (3.1) obtained when the dipole approximation is employed for **S**(k) and **L**(k), which is a reasonable approach to take for modest values of k. Applied to the case of an ion with total angular momentum **J** the dipole approximation gives the estimates [6]

$$\mathbf{S}(k) \equiv \frac{1}{2}\, g_s < j_0(k) > \mathbf{J},$$

$$\mathbf{L}(k) \equiv g_L < j_0(k) + j_2(k) > \mathbf{J}, \tag{3.4}$$

$$\mathbf{S}(k) + \mathbf{L}(k) \equiv \{ < j_0(k) > + (2 - g_0) < j_2(k) > \} \, \mathbf{J},$$

in which g_0 is the Landé factor, and

$$< j_n(k) > = \int dr \; r^2 \; f^2(r) \; j_n(kr), \tag{3.5}$$

where f(r) is the radial wave function and j_n is a spherical Bessel function of order n. Note that the magnetic amplitude is not proportional to the magnetic moment of the ion ($g_0 J/2$) in the limit of small k, which is another distinction in magnetic neutron and photon scattering.

If we use the dipole approximation for L(k) in (3.3) the wave vector dependence of orbital-only scattering is contained in the expression

$$2n(k) \{ \sin\Theta \sin \frac{1}{2} \Theta \}^2 \cos\beta < j_0 + j_2 >. \tag{3.6}$$

This quantity is plotted in Figure 1 for Pr^{3+} using $q = 5.07 Å^{-1}$ (10 keV photons), and $\beta = \tan^{-1} (2/\tan\Theta)$ for which (3.2) is zero. From Figure 1 we see that the orbital-only term is significant over a rather small range of wave vectors.

We conclude this section with the expression for the Stokes circular polarisation parameter of the secondary beam P'_2 obtained for unpolarised incident photons. The result is

$$\left(\frac{d\sigma}{d\Omega} \right)_T P'_2 = - r_e^2 \, g \, n(k) \, (1 - \cos\Theta) \times \times \{ \mathbf{S}(k) \, . \, (\hat{\mathbf{q}} + \hat{\mathbf{q}}' \cos\Theta) + + \cos^2 (\frac{1}{2} \Theta) \, \mathbf{L}(k) \, . \, (\hat{\mathbf{q}} + \hat{\mathbf{q}}') \}. \tag{3.7}$$

As in the cross section, the spin and current contributions in (3.7) are distinguished by geometric factors.

4 — NEUTRON SCATTERING

Our discussion of the theory of neutron scattering will be relatively brief because it has been recently reviewed. The neutron scattering amplitude is dominated by the magnetic and nuclear contributions, which are of a similar magnitude. Let $r_0 = -1.91 \, r_e$, and represent the neutron spin operator by $\underline{\sigma}/2$. With this notation, the magnetic and nuclear amplitudes are, respectively,

$$\frac{1}{2} \, r_0 \, \underline{\sigma} \, . \, \{ \mathbf{k} \times ([2\mathbf{S}(k) + \mathbf{L}(k)] \times \mathbf{k}) \} / k^2, \tag{4.1}$$

and

$$\sum_l \exp(i\mathbf{k} \, . \, \mathbf{l}) \; \{ a_l + \frac{1}{2} \; b_l \; \underline{\sigma} \; \mathbf{I}_l \}, \tag{4.2}$$

in which **I** is the nuclear spin, a_l and b_l are energy independent parameters and the sum runs over all nuclei in the target sample. The magnetic amplitude is proportional to the spatial Fourier transform of the magnetic moment density, and it is not possible to measure just the spin or current components.

In some experiments, including those aimed at high precision magnetic amplitude determinations using polarised neutrons, it is necessary to add the electrostatic correction to (4.1), even though it is a factor $(m_e/m) \sim 10^{-3}$ smaller. The amplitude due to an electrostatic field **E** is

$$\left(\frac{-r_0\, m_e}{4\pi\, m}\right)\frac{1}{e}\int d\mathbf{r}\ \exp(i\mathbf{k}\,.\,\mathbf{r})\ \{(\mathbf{q}\times\underline{\sigma}) + \frac{1}{2}\,\underline{\nabla}\ \}\,.\,\mathbf{E}(r)\,. \qquad (4.3)$$

The first term in the integrand, which contains the neutron spin, was derived by Schwinger, and the second term was derived later by Foldy. When the electric field is derived from the nuclear and electron charge distributions the amplitude (4.3) reduces to,

$$\left(\frac{r_0\, m_e}{2\, m}\right)\{i\underline{\sigma}\,.\,\mathbf{h}\cot\left(\frac{1}{2}\,\theta\right) - 1\}\ \{Z - n(k)\}, \qquad (4.4)$$

which vanishes in a forward scattering configuration since $n(0) = Z$ the number of electrons. Other points to note about the result (4.4) are that, the expression is valid for elastic scattering, **h** is a unit vector, defined following (2.7), perpendicular to the plane of scattering, and the amplitude depends on **q** and **q′**, through **h**, and not just **k** as in all other neutron amplitudes.

Let us turn now to a consideration of polarisation induced effects in the cross section. We assume that the nuclear spins are randomly orientated, and begin with magnetic and nuclear amplitudes, which is usually the case of interest. Note that, for an unpolarised neutron beam, the observed cross section is the sum of magnetic and nuclear cross sections, and no interference effects are present. If the magnetic ions are either parallel or antiparallel to a single direction, a polarisation of the incident beam induces only an interference between the magnetic and nuclear amplitudes. This effect is the basis of experiments designed to measure the magnetic moment density of metals and compounds, since it provides the required signal sensitivity, through changes in the polarisation, and the sign of the magnetisation; see the article in this volume by J. B. Forsyth. For more complicated magnetic structures, such as a helical configuration, polarisation induces a purely magnetic term, in addition to magnetic and nuclear interference scattering.

Turning now to modifications introduced by the electrostatic interaction, interference with the magnetic and nuclear amplitudes occurs even for unpolarised neutrons; the magnetic and Schwinger, and the nuclear and Foldy amplitudes interfere. These terms are of minimal practical interest because the absence of polarisation dependence deprives them of signal sensivity.

The sensitivity required to measure the electrostatic amplitude is provided by incident beam polarisation. In this instance, there is interference with both magnetic and nuclear amplitudes; the nuclear amplitude interferes with the Schwinger term, and the magnetic amplitude interferes with both the Schwinger and Foldy terms. Let F_e F_m and F_n denote the electrostatic, magnetic and nuclear amplitudes, respectively. For a simple magnetic structure, with moments parallel or antiparallel to a single direction defined by the unit vector $\hat{\eta}$, the polarisation dependent interference terms in the cross section are,

$$\left(\frac{\mathrm{m_e\,r_0}}{\mathrm{m}}\right)\{\mathrm{r_0}\,\hat{\eta}\cdot\left[\frac{2\,\mathbf{q}\,(\hat{\mathbf{k}}\,.\,\mathbf{P})}{\mathrm{k}}-\mathbf{P}\right]$$
$$\mathrm{Re}\,.\,(\mathrm{F_m\,F_e^*})\,+$$
$$+\cot\left(\frac{1}{2}\,\Theta\right)\mathbf{P}\,.\,\mathbf{h}\ \mathrm{Im}\,.\,(\mathrm{F_n\,F_e^*})\}. \quad (4.5)$$

Observe that the electrostatic-nuclear contribution is asymmetric, i. e. the cross-section differs for scattering to the right and to the left of the incident beam.

5 — DISCUSSION

Magnetic photon scattering has an edge on its neutron counterpart in as much that the spin and current amplitudes can be measured separately. Moreover, photon scattering provides very good wave vector resolution [14], and the foreseeable improvements in the intensity of photon beams is far larger than that possible with neutron sources.

Our presentation of magnetic photon scattering has focused on the interpretation of diffraction experiments. However, inelastic photon scattering described within the impulse approximation possesses the same basic features. An introduction to inelastic magnetic photon scattering is provided in [4, 5] together with references to more detailed treatments.

The photon amplitude reported in Section 2, and more fully discussed in an appendix, is correct to first-order in $\mathrm{g} = \hbar\omega/\mathrm{m_e}\ {}^2$. Hence, our expressions for magnetic interference contributions are complete to leading order. An analysis of the cross section to order g^2 requires the computation of the amplitude to the same order. This analysis will be required for the interpretation of experiments using energetic photons for which the condition $\mathrm{g} \ll 1$ is not satisfied.

Resonance processes are not covered by the formalism used in the main text, and a separate approach is really required; see appendix to this paper and [7, 15]. The basic difference arises in the term that is proportional to the current density in diffraction experiments. This term is the appropriate limiting form of a contribution in the perturbation expansion for the photon amplitude that has a structure akin to the Kramers-Heisenberg expression cf. (A3). When relativistic effects are included the matrix elements in this expression include both the dipole and spin operators. Near a resonance, when reduction to the form quoted in Section 2 is no longer valid, magnetisation-sensitive resonance processes occur. The sensitivity to the magnetisation arises from exchange interactions between core and unoccupied levels, in which the transition proceeds through the electron current (dipole) operator. At present, there is no solid evidence in favour of transitions created by the relativistic spin-dependent operator, a candidate which has been advocated [12] and invoked [13].

The information that can be extracted from the interpretation of such X-ray resonance processes refers to an instantaneous picture of the electrons, because it is a relatively fast process. In this respect, the information supplements that derived from the frequency and wave vector response function measured in magnetic neutron scattering experiments, i. e. the total scattering, given by the integral of the responses over frequency, is measured. Of course, a resonance effect is large, compared to magnetic contributions considered in the main text, when the width of the resonance is small enough to justify the interpretation in terms of an instantaneous picture of electron behaviour.

I am grateful to M. J. Cooper, J. B. Forsyth and G. T. Trammell for discussions and correspondence.

APPENDIX

We provide an expression for the photon scattering amplitude that describes elastic and inelastic events to an accuracy $g = \hbar\omega/m_e c^2$. This amplitude generates in the corresponding cross section the leading-order expression for charge-magnetic interference processes. It also generates the leading-order expression for the magnetic cross section observed at purely magnetic Bragg reflections. A term of order g^2 in the cross section is missed at mixed charge and magnetic reflections. Our expression can be derived from a thorough treatment of the amplitude to order g^2 [10], which is the expression required for a complete discussion of the magnetic cross section. Later work [12] outlines a semiclassical approach to order g suitable for quasielastic events; the principal results derived in [12] are found in the more complete treatment [10].

Let the initial electronic state, an eigenstate of the non-relativistic Hamiltonian H_0, have energy E. it is convenient to introduce a current operator **J** that depends on the momentum, position and spin variables, namely,

$$\mathbf{J}(\mathbf{q}) = \sum_j (\mathbf{P}_j + i\hbar \mathbf{S}_j \times \mathbf{q}) \exp(i\mathbf{q} \cdot \mathbf{R}_j). \tag{A1}$$

for which

$$\{\mathbf{J}(\mathbf{q}) \cdot \mathbf{e}\}^+ = \mathbf{J}(-\mathbf{q}) \cdot \mathbf{e}$$

The desired expression for the amplitude is,

$$\begin{aligned} r_e \{ n(k)\mathbf{e}' \cdot \mathbf{e} - \frac{i}{2} g(1 + \frac{\omega'}{\omega}) \mathbf{S}(k) \cdot \mathbf{e}' \times \mathbf{e} \} + \\ + \left(\frac{r_e}{m_e}\right) \{ \mathbf{J}(-\mathbf{q}') \cdot \mathbf{e}'(E + \\ + \hbar\omega - H_0)^{-1} \mathbf{J}^+ (-\mathbf{q}) \cdot \mathbf{e} \\ + \mathbf{J}(\mathbf{q}) \cdot \mathbf{e}\,(E - \hbar\omega' - H_0)^{-1} \mathbf{J}^+ (\mathbf{q}') \cdot \mathbf{e}' \}. \end{aligned} \tag{A2}$$

The amplitude has the dimension of length, and it is accompanied by the conservation of energy $E + \hbar\omega = E' + \hbar\omega'$.

Resonant processes arise in the second set of terms in (A2). An appropriate expression is obtained by inserting a complete set of states between **J** and $\mathbf{J}^+$. Consider, for example, the first term and label intermediate states by α. Using,

$$H_0 \mid \alpha > = E_\alpha \mid \alpha >$$

and

$$\sum_\alpha \mid \alpha > < \alpha \mid = 1,$$

the term in question becomes

$$\left(\frac{r_e}{m_e}\right) \sum_\alpha (\mathbf{J}(-\mathbf{q}') \cdot \mathbf{e}' \mid \alpha > < \alpha \mid \mathbf{J}^+(-\mathbf{q}) \cdot \mathbf{e}) / (E + \hbar\omega - E_\alpha + i\Gamma_\alpha/2). \tag{A3}$$

In this expression, an imaginary component has been included in the energy denominator to describe the level width. The analysis of resonant magnetisation-sensitive X-ray scattering presented by Hannon and Trammell [7] is based on (A3), using the momentum component of **J** (A1).

Far away from resonances, where the resolvent operators in (A2) can be safely expanded in $1/\omega$ and $1/\omega'$, the amplitude reduces to

$$\begin{aligned} r_e \{ n(k)\ \mathbf{e}' \cdot \mathbf{e} - ig\, [\mathbf{S}(k) \cdot \mathbf{B} + \\ \left(\frac{i}{\hbar q^2}\right) \sum_j \exp(i\mathbf{k} \cdot \mathbf{R}_j) \\ (\mathbf{q} - \frac{\omega}{\omega'} \mathbf{q}') \times \mathbf{P}_j \cdot \mathbf{e}' \times \mathbf{e}] \}, \end{aligned} \tag{A4}$$

in which

$$
\begin{aligned}
{}_{\omega}\mathbf{B} = {} & \frac{1}{2}\,(\omega + \omega')\,\mathbf{e}' \times \mathbf{e} \, + \\
& \omega'\,(\hat{\mathbf{q}}\,.\,\mathbf{e})\,\hat{\mathbf{q}}' \times \mathbf{e}' - \omega\,(\hat{\mathbf{q}}\,.\,\mathbf{e}')\,\hat{\mathbf{q}} \times \mathbf{e} \\
& - \frac{1}{2}\,(\omega + \omega')\,(\hat{\mathbf{q}}' \times \mathbf{e}') \times \hat{\mathbf{q}} \times \mathbf{e}). \qquad \text{(A5)}
\end{aligned}
$$

For the special case of diffraction $\omega = \omega'$, we obtain the result (2.4) with $\mathbf{A} = \mathbf{e}' \times \mathbf{e}$ and $\mathbf{B}$ from (A5).

REFERENCES

[1] DE BERGEVIN, F. and BRUNEL, M., in Structure and Dynamics of Molecular Systems II, page 69, R. Dandel *et al.* (eds.) published by D. Reidel Co. (1986).

[2] LANDAU, L. D. and LIFTSHITZ, E. M., Quantum Electrodynamics, Pergamon Press (1982).

[3] COOPER, M. J., Physique, **48**, Colloque C9 Supple, No. 12 (1987).

[4] LOVESEY, S. W., J. Phys., **C20**, 5625 (1987).

[5] BALCAR, E. and LOVESEY, S. W., Theory of Magnetic Neutron and Photon Scattering, Oxford University Press (1989).

[6] LOVESEY, S. W., Theory of Neutron Scattering from Condensed Matter, Vol. 2, 3rd impression Oxford University Press (1987).

[7] HANNON, J. P. and TRAMMELL, G. T., Phys. Rev. Lett, **61**, 1245 (1988).

[8] GIBBS, D., HARSHMANN, D. R., ISAACS, E. D., MCWHAN, D. B., MILS, D. and VETTIER, C., Phys. Rev. Lett, **61**, 1241 (1988).

[9] BHATT, G., GROTCH, H., KAZES, E. and OWEN, D. A., Phys. Rev., **A28**, 2195 (1983).

[10] GROTCH, H., KAZES, E., BHATT, G. and OWEN, D. A., Phys. Rev., **A2**, 243 (1983).

[11] MCMASTER, W. H., Rev. Mod. Phys., **33**, 8 (1961).

[12] BLUME, M., J. Appl. Phys., **57**, 3618 (1985).

[13] NAMIKAWA, K. *et al.*, J. Phys. Soc. Japan, **54**, 4099 (1985).

[14] BOHR, J. *et al.*, Physica, **B159**, 93 (1989).

[15] LOVESEY, S. W., Nature, **335**, 673 (1988).

NEW FRONTIERS IN MOMENTUM DENSITIES

S. Manninen

University of Helsinki, Department of Physics, 00170 Helsinki 17, Finland

ABSTRACT — A review of the present state and the near future in momentum density studies is given. The main target is inelastic photon scattering, including the wide range of new techniques due to the potential use of synchrotron radiation and also different ways to utilize coincidence counting. Electron scattering spectroscopy and angular correlation of positron annihilation are considered to some extent.

1 — INTRODUCTION

After the renaissance of momentum density studies beginning in the middle of 1960's, this field of physics partly lost its interest in 1980's. The main reason was the relatively low resolution of solid state detectors used in photon scattering experiments. Although the alternative techniques like electron Compton scattering, positron annihilation and (e, 2e) scattering did not suffer the same problem, they had a limited use because of the sample requirements. The basic theory and the experimental technique in each of these methods has been covered by recent reviews [1-3].

During the last few years several new approaches have brought momentum density studies back to the front line. These include (i) the use of focusing crystal optics to improve both the resolution and the intensity allowing measurements also at relatively high photon energies produced by the insertion devices of a synchrotron, (ii) studies of the momentum distributions of «magnetic» electrons using circularly polarized synchrotron radiation and (iii) photon-photon or photon-electron coincidence measurements which make it possible to separate particular electron shell contributions from the total spectrum of inelastic scattering. The present state of art and also the future prospects of these new techniques are reviewed. Also some attention has been paid to the possibilities to apply some of these techniques in a small scale laboratory.

2 — THE BASIC METHODS TO DETERMINE MOMENTUM DENSITIES

In order to understand the present development in the momentum density research, a brief summary of each basic method is first given.

2.1 — *Compton Scattering*

In a typical Compton scattering experiment monoenergetic photons either from an X-ray tube or from a gamma-ray source are scattered through a fixed angle and the scattered energy spectrum is analyzed using a solid state detector or a crystal analyzer. Providing that the transferred energy is large compared with the electron binding energy one can assume that the final electron state is a plane wave and the scattering takes place in a constant potential. In this so-called impulse approximation (IA) the scattering cross section is proportional to a quantity called Compton profile [1]

$$J(p_z) = \int\int_{p_x p_y} n(\mathbf{p})\, dp_x\, dp_y \qquad (1)$$

where $n(\mathbf{p})$ is the electron momentum density. Comparison between theory and experiment is usually done in terms of the Compton profile, not momentum density, which can be calculated by differentiating Eq. (1).

Some general comments, typical to Compton scattering are:

- Due to the relatively weak cross section of the interaction between the electromagnetic field and the electron, the intensity can be a problem especially if an X-ray tube and a crystal analyzer are used.
- The resolution is only modest if a solid state detector is used (not better than 0.4 a.u. of momentum) and even in the case of a conventional crystal analyzer it is about 0.1-0.2 a.u. [1].
- The multiple photon scattering is a problem which should be handled with a special care. It is always preferable to use as thin samples as possible [1].
- The relation between the measured cross section and the Compton profile is not straightforward especially at higher energies [4].

2.2 — *Electron Compton Scattering*

Compared with photon Compton scattering the use of a monoenergetic electron beam offers some advantages:

- The cross section of electron-electron scattering is significantly larger than in photon-electron scattering.
- The energy of the scattered electron can be measured very accurately; it is easy to have a momentum resolution of 0.01 a.u..

On the other hand it is really difficult to measure any other samples than gaseous ones, which is a serious limitation of this method.

Using an approximation similar to the IA in the case of photon Compton scattering (it is called binary-encounter approximation), the measured cross-section can be expressed in terms of the Compton profile

$$J(p_z) = 2\pi \int_{p_z}^{\infty} n(p)\, p\, dp \qquad (2)$$

This result looks slightly different compared with Eq. (1), because it includes the spherical average of the momentum density (this is due to the use of gaseous samples).

2.3 — *Positron Annihilation*

When a positron interacts with a solid it is thermalized well before it annihilates with an electron by the emission of two photons. The motion of the target electron makes the angle between the two photons to deviate from the angle of 180 degrees. The measurement of the angular correlation spectrum gives therefore information about the electron momentum distribution.

If the interaction between the positron and electron is neglected and the positron wave function does not depend on **r**, the measured cross section is proportional to the Compton profile given by Eq. (1).

The resolution in a positron annihilation measurement is of the order of 0.05 a.u. which is good enough for Fermi surface studies, for example. Additionally the annihilation process prefers outer electrons which usually are the interesting ones and it does not depend on the atomic number of the sample material. On the other hand positrons are effectively trapped into lattice defects which makes it necessary to take a great care in the sample preparation. Also the approximations involved in using Eq. (1) should be carefully studied in each case.

3 — NEW FRONTIERS

3.1 — *General trends*

All three basic methods described shortly in Chapter 2 include several deficiencies concerning the information obtained from the measured data:

- A great part of the information is lost because not all the properties of the particles or quanta involved in the scattering event are measured. These include the energy and the momentum of the Compton electron/target electron in photon scattering/electron scattering and the energies of the annihilation photons.
- The measured cross section is a one-dimensional projection or spherical average of the electron momentum distribution. Although it is possible to make a three-dimensional construction of n(**p**) based on one-dimensional projections, this requires a long set of measurements on a single crystal.
- The contribution of the «non-interesting» electrons is always present in photon and electron Compton scattering and although it is small in positron annihilation, it gives some uncertainty to the absolute cross section measurements.
- More information would be obtained if polarized photon or particle beam were used.
- The resolution of the conventional photon Compton scattering should be better to be compatible with that of electron scattering or positron annihilation methods.

3.2 — *(e, 2e)-spectroscopy*

Already about 15 years ago an Australian group presented a method to observe both the scattered electron and the target electron in coincidence [5]. This technique makes it possible to obtain more information about the target electron properties and additionally to separate different electron shell contributions. The coincidence counting makes, of course, the observed intensity quite small and the resolution is somewhat worse than in conventional electron Compton scattering but in any case this method has turned out to be very potential in atomic and molecular electron momentum studies. The relation between the measured cross section and the theoretically obtained quantities is more complicated due to the coincidence technique but it seems to be well understood by now [2]. A beautiful demonstration of the potential of this technique is a recent study on xenon [6] where the 5p subshell contributions have been measured separately and the importance of the relativistic treatment can be easily seen. Despite of the merits of this method, there still is only one laboratory using it.

3.3 — *2-dimensional Angular Correlation of Positron Annihilation Radiation*

In the conventional positron annihilation technique a narrow slit in front of the detector is used to pick up a particular momentum component (so-called long slit geometry). More than ten years ago Berko and co-workers [7] presented an idea to measure the angular distribution of the annihilation quanta simultaneously using a set of scintillation counters. Since then this idea has been adopted in several laboratories with a variety of detectors including position sensitive detectors and solid state detectors. Using this technique it is possible to make a few measurements on a single crystal in different crystallographic directions and use data to reconstruct the 3-dimensional momentum density. The reconstruction can be done either using spherical harmonics, Fourier transforms, Fourier-Hankel transforms or methods taken from X-ray tomography [8]. It has been turned out that only a few orientations are required to make a surprisingly accurate reconstruction.

The use of polarized positrons make it possible to study electron spin density in momentum space. This was already demonstrated more than ten years ago with 1D-annihilation technique but very recently a 2D-apparatus has been applied to study the momentum density of electrons in ferromagnetic iron [9]. Partially polarized positron beam can be obtained from a Na-22 source. Polarized positrons annihilate prefentially with conduction electrons with opposite polarization. Therefore in a magnetized ferromagnetic crystal in which the number and distribution of electrons are different for electrons with their spins parallel or antiparallel to the magnetization this difference can be studied by polarized positrons. This is so because the reverse of the magnetic field direction only reverses the electron spin polarization, not that of the positron beam [9]. Compared with the circularly polarized photon scattering technique, described later, positron annihilation measurements give better resolution but on the other hand photon-electron scattering is better understood theoretically.

3.4 — *Improvements in Inelastic Photon Scattering*

The recent development in synchrotrons dedicated to produce radiation has done a real revolution in inelastic photon scattering experiments. The resolution which has a long time been the weakest point compared with the competing methods is no longer a problem because the high flux makes it possible to use crystal analyzers to measure the scattered energy spectrum. Additionally the possibility to vary the degree of the beam polarization gives new challenges to measure, for example, the momentum distributions of conduction electrons in magnetic materials. Also the coincidence technique becomes possible, one can take the coincidence between the scattered photon and either the Compton electron or the fluorescence photon which makes it possible to study particular electron shells.

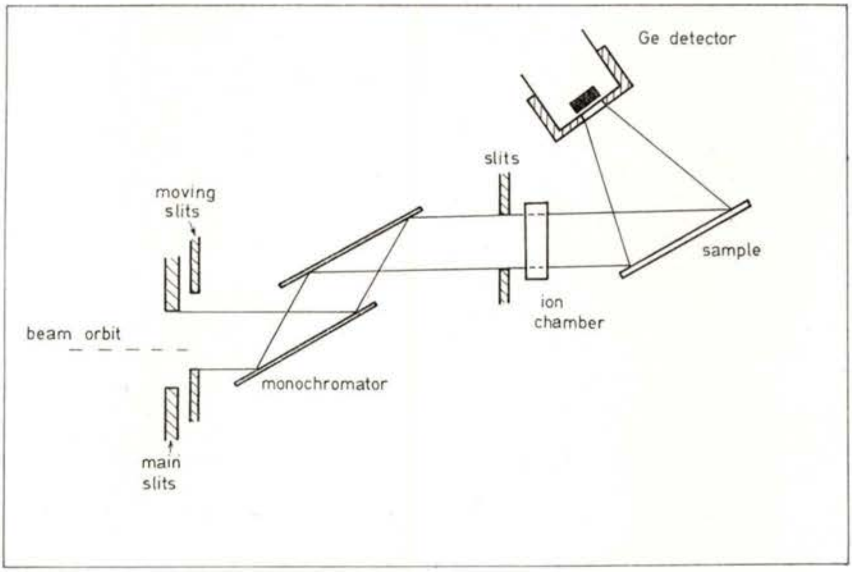

Fig. 1 — A schematic lay-out of the magnetic Compton scattering experiment.

3.4.1 — Momentum Densities of Conduction Electrons in Ferromagnetic Materials

It is well known [10] that the electromagnetic field-electron interaction treated relativistically produces in the first order an imaginary spin-dependent term in the scattering cross section. A real contribution can be obtained, however, if the polarization factor in the cross section is imaginary, i. e. incident radiation is circularly polarized. This possibility has been previously applied by Sakai and Ono [11] using a gamma-ray source but the small intensity makes this type of experiment time consuming.

A more effective alternative is to benefit from synchrotron radiation properties, i. e. out of the orbital plane there are both parallel and perpendicular polarization components present and the radiation is at least partially circularly polarized. The group in Warwick University (UK) has successfully studied ferromagnetic 3d transition metals using the technique shown in Figure 1 [12]. Although the degree of circular polarization increases by going more above (or below) the beam orbit the rapid decrease of the flux forces some compromize to be made.

The other choice to produce circularly polarized radiation is to use quarter wave plates which now seem to work also at higher X-ray energies [13].

If linearly or circularly polarized incident beam is used and the state of polarization of the scattered beam is measured, more information can be obtained. This kind of measurements are now possible offering an interesting task in the future.

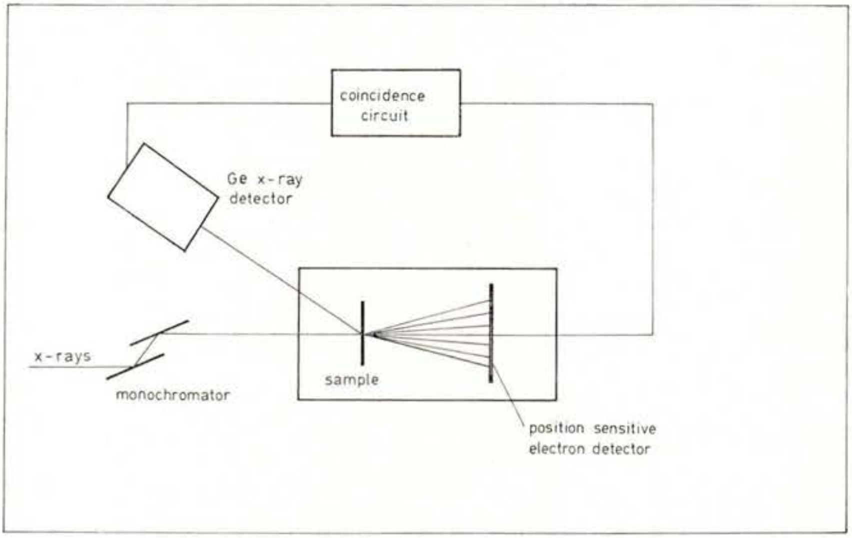

Fig. 2 — A schematic lay-out of the photon-electron coincidence spectrometer.

3.4.2 — Compton Scattering with Electron Analysis

In conventional Compton scattering only the energy and the momentum of the scattered photon are measured. This means (see Eq. (1)) that the measured cross section is an integral of the three-dimensional momentum density over the energy states. However, if the Compton electron is also detected in coincidence with the scattered photon the integration is avoided and the desired volume element in momentum space can be studied.

The experimental arrangement is shown schematically in Figure 2 [14]. It is designed to be operating in the new European synchrotron (ESRF), although in principle it can be tested using a high intensity gamma ray source. High source flux, short wavelength and thin samples are required to produce and detect sufficient number of electrons. A synchrotron source is therefore a natural choice. In an experiment the scattered photon is detected using a solid state detector and two orthogonal components of the recoil electron momentum are measured in coincidence with the photon using a two-dimensional position sensitive electron detector.

3.4.3 — High Resolution Compton Scattering Spectroscopy

The resolution of a crystal spectrometer is at least one order of magnitude better than that of a solid state detector at X-ray energies. However, they have not been used for momentum density studies until very recently mainly because the conventional X-ray sources did not produce fluxes high enough to make step by step energy scanning worthwile. The rapid development of focusing crystal optics, largely due to the synchrotron instrumentation, is now replacing the energy dispersive technique in momentum density studies.

There have already been some operating crystal spectrometers in 1980's used to study momentum densities. One of those is located at LURE synchrotron laboratory (Orsay, France) and it is based on a transmission analyzing crystal and a position sensitive counter [15]. The other choice has been a focusing curved crystal spectrometer and a conventional X-ray tube, simultaneously build in Finland and in Germany [16]. They all have roughly the same momentum resolution (0.15 a.u.) and they are designed to work at energies not much larger than 10 keV. An example of the performance of the conventional X-ray tube spectrometer is shown in Figure 3 in which the Compton profile of boron is shown [17]. The K-edge can be seen on the low energy side of the profile and the fine structure is related to the density of unoccupied electron states above the Fermi energy. In this energy region impulse approximation is not valid, although it predicts the general behaviour quite well. This kind of technique can be used alternatively with EXAFS (Extended X-ray Absorption Fine Structure), especially in the case when the absorption

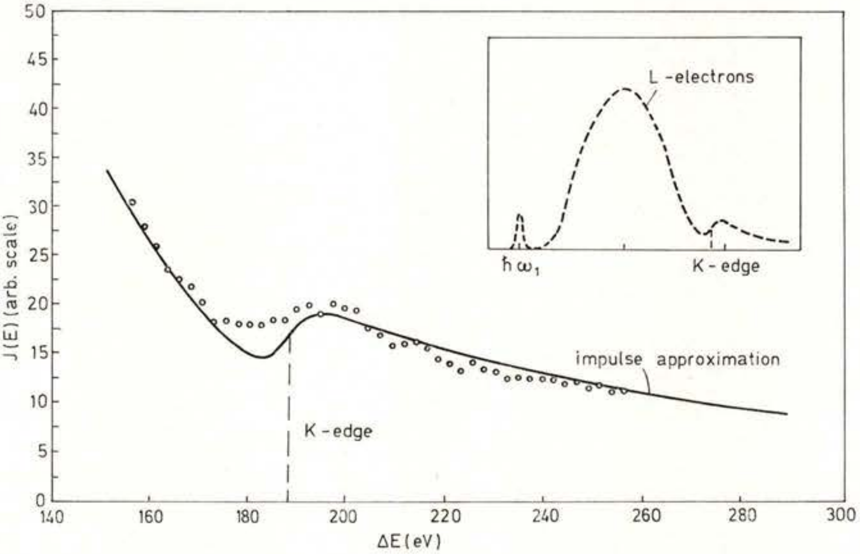

Fig. 3 — The Compton profile of boron measured using curved crystal spectrometer [17]. The energy range close to the B K-edge is shown including the theory based on the impulse approximation convoluted with the experimental resolution. The inset shows the whole spectrum.

edge occurs at low energies. In Compton scattering one can use much higher primary energies, for example in the case of Figure 3, 8 keV instead of about 200 eV required by EXAFS measurements in this case.

At present there are already beam line designs at DESY (Hamburg, Germany) and at KEK (Tsukuba, Japan) which have at least 0.1 a.u. momentum resolution at 30 keV. This is often enough but not as good as in electron scattering or positron annihilation.

The plan for ESRF which will be located at Grenoble, France, will include a Compton scattering beam line having 25 eV resolution at 50 keV. This means about 0.02 a.u. momentum resolution. A schematic design (the final version might be different) can be seen in Figure 4 [18]. Because of the focusing optics small single crystals can also be studied.

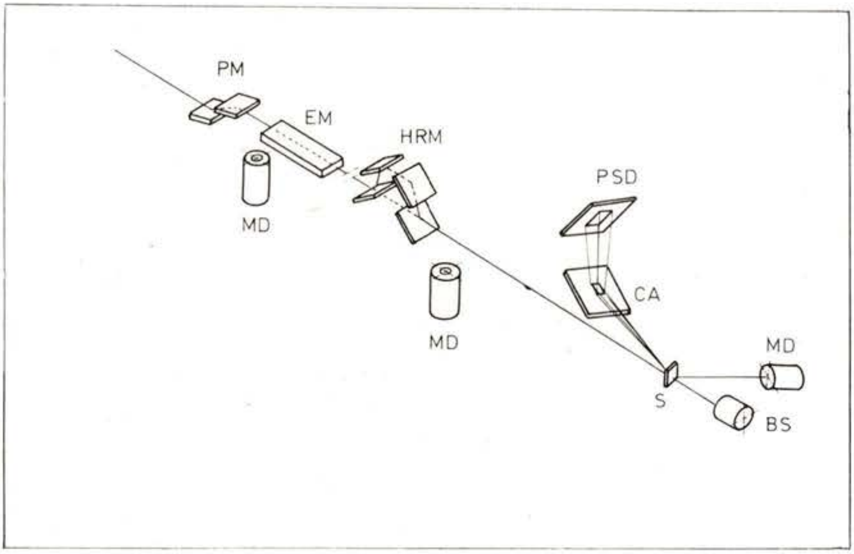

Fig. 4 — The plan for high resolution Compton scattering spectrometer [18]. It consists of primary monochromator (PM), elliptical mirror (EM), high resolution monochromator (HRM), sample (S), crystal analyser (CA), position sensitive detector (PSD), monitor detectors (MD) and beam stop (BS).

3.4.4 — Inelastic Coincidence Spectroscopy

A particular electron shell contribution to the total Compton profile can be also obtained in photon spectroscopy using coincidence technique. Two detectors, one measuring the scattered photon and the other X-ray fluorescence arising from the transition to the vacant electron state left by the Compton electron are required. A schematic lay-out of the apparatus is shown in Figure 5. Both gamma ray sources [19] and synchrotron radiation [20] have been recently applied to study K-shell spectra of some 3d transition metals. This turns out to be one of those rare cases where conventional radiation sources can beat synchrotrons. This is due to the time structure of the electron beam in a synchrotron. In order to pick up the true coincidences from the chance ones (fluorescence and scattered photon, although detected simultaneously, do not belong to the same scattering event) one has to make a measurement in which there is a time offset from the coincidence window. In a synchrotron this cannot be done within the time of one pulse but the next one should be used. This limits the time resolution and lowers the true/chance coincidence ratio.

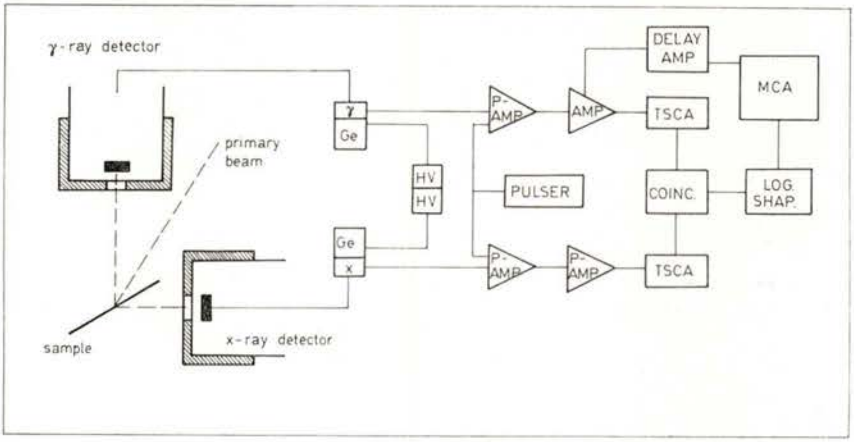

Fig. 5 — A schematic lay-out of the gamma ray — X-ray coincidence spectrometer.

Gamma ray sources used so far also have serious limitations. In order to have a well-collimated beam which is necessary to define the scattering vector properly one has to use very small solid angles. Most of the photons emitted by the source are therefore lost and the coincidence counting rate is very low. A promising improvement which is under construction in our laboratory is to use a high voltage (160 kV) X-ray generator, W-tube and a monochromator to produce an intensive W-K_{α_1} beam (see figure 6). It has roughly the same energy than Am gamma rays used so far in these experiments but using focusing geometry it can be collimated into a small focus at a sample site. In addition to coincidence experiments this apparatus can also be used in conventional Compton scattering to study small single crystals which has not been possible so far due to the non-focusing gamma-ray geometry.

3.3.5 — Conclusions

Although the general trend in the future of momentum density studies is certainly based on the large scale machines, there is also space left in small scale laboratories. In addition to the coincidence studies and high energy X-ray sources mentioned earlier conventional Compton scattering can also be used in those cases where the momentum resolution is not a crucial question. Systems like ionic crystals, for example, can be effectively studied using a modest resolution spectrometer. This is demonstrated in Figure 7 in which the electron momentum anisotropy is shown in the case of NaF and CaO [21]. The merits and dismerits of both theories can be easily seen and the improvement of the resolution hardly makes any difference in conclusions.

Finally it should be mentioned that the present high flux sources make it possible to achieved statistical accuracy which in many experiments is much better than the accuracy of approximations used in data processing (impulse approximation, ignorance of other scattering contributions etc.). One possible way to check the quality of the experiment is to perform it in an absolute scale. This kind of measurement is very rare and from this point of view is really worthwile doing.

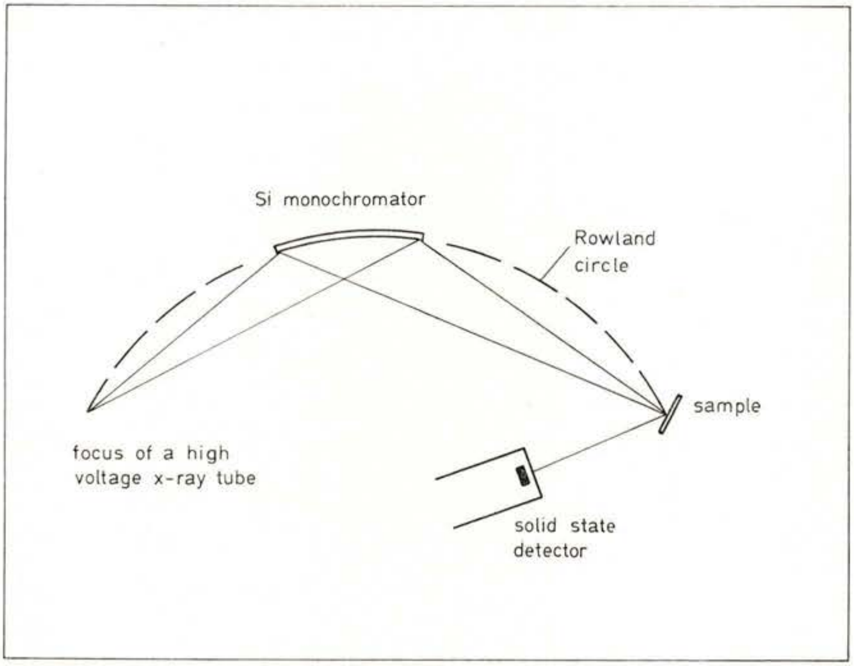

Fig. 6 — A plan for a focusing X-ray spectrometer based on a high voltage tungsten tube.

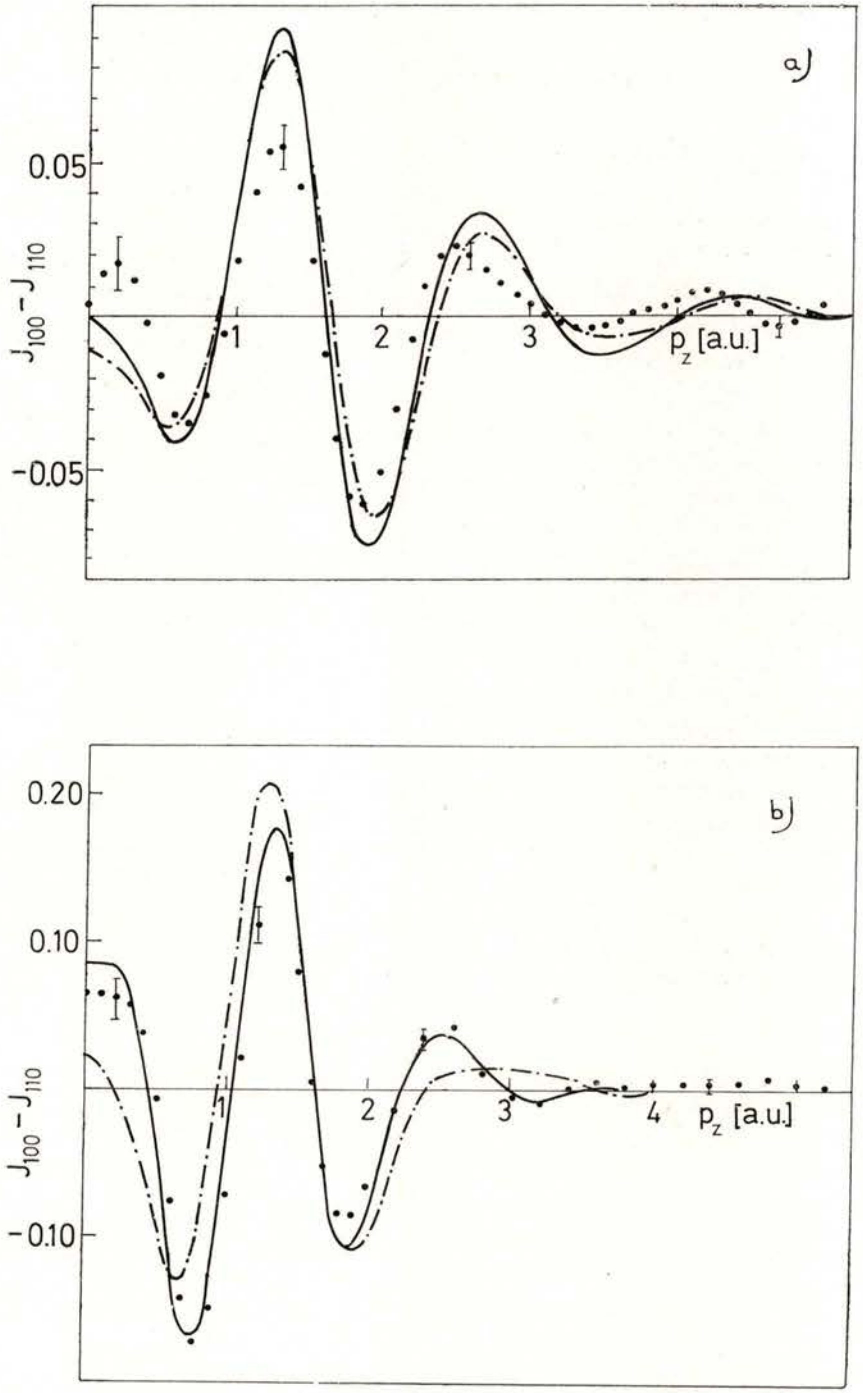

Fig. 7 — The electron momentum anisotropy in a) NaF, b) CaO crystals [21]. The solid line corresponds APW calculation and the dashed line LCAO method. Both theories have been convoluted with the experimental resolution.

REFERENCES

[1] COOPER, M. J., Rep. Prog. Phys., **48**, 415 (1985).

[2] MCCARTHY, I. E. and WEIGOLD, E., Phys. Rep., **27C**, 275 (1976).

[3] BERKO, S. in Compton Scattering (ed. B. G. Williams), McGraw-Hill, London (1977).

[4] RIBBERFORS, R., Phys. Rev., **B12**, 2067 and 3136 (1975).

[5] WEIGOLD, E., HOOD, S. T. and TEUBNER, P. J. O., Phys. Rev. Lett., **30**, 475 (1973).

[6] COOK, J. P. D., MITROY, J. and WEIGOLD, E., Phys. Rev. Lett., **52**, 1116 (1984).

[7] BERKO, S. and MADER, J. J., Appl. Phys., **5**, 287 (1975).

[8] PECORA, L. M., EHRLICH, A. C., MANUEL, A. A., SINGH, A. K., PETER, M. and SINGRU, R. M., Phys. Rev., **B37**, 6772 (1988).

[9] GENOUD, P., SINGH, A. K., MANUEL, A. A., JARLBORG, T., WALKER, E., PETER, M. and WELLER, M., J. Phys. F., **18**, 1933 (1988).

[10] PLATZMAN, P. M. and TZOAR, N., Phys. Rev., **B2**, 3556 (1970). LOVESEY, S. W., J. Phys., **C20**, 5625 (1987).

[11] SAKAI, N. and ONO, K., Phys. Rev. Lett., **37**, 351 (1976).

[12] COOPER, M. J., LAUNDY, D., CARDWELL, D. A., TIMMS, D. N., HOLT, R. S. and CLARK, G., Phys. Rev., **B34**, 5984 (1986).

[13] GOLOVCHENKO, J. A., KINCAID, B. M., LEVESQUE, R. A., MEIXNER, A. E. and KAPLAN, D. R., Phys. Rev. Lett., **57**, 202 (1986).

[14] ESRF Foundation Phase Report, Chapter V, (1987).

[15] LOUPIAS, G. and PETIAU, J., J. Physique, **41**, 265 (1980).

[16] SUORTTI, P., PATTISON, P. and WEYRICH, W., J. Appl. Cryst., **19**, 336 and 343 (1986).
PATTISON, P., SUORTTI, P. and WEYRICH, W., J. Appl. Cryst., **19**, 353 (1986).
SUORTTI, P., ETELÄNIEMI, V., HÄMÄLÄINEN, K. and MANNINEN, S., J. Physique, **C9**, 831 (1987).

[17] MANNINEN, S., ETELÄNIEMI, V. and SUORTTI, P., Phys. Rev. Lett., **61**, 2815 (1988).

[18] European Synchrotron Radiation Facility (eds. B. Buras and S. Tazzari) Chapter 6 (1984).

[19] NAMIKAWA, K. and HOSOYA, S., Phys. Rev. Lett., **53**, 1606 (1984).
MANNINEN, S., Phys. Rev. Lett., **57**, 1500 (1986).
MANNINEN, S., HÄMÄLÄINEN, K., PAAKKARI, T. and SUORTTI, P., J. Physique, **C9**, 831 (1987).

[20] MARCHETTI, V. and FRANK, C., Phys. Rev. Lett., **59**, 1557 (1987).

[21] J. REDINGER, R. PODLOUCKY, S. MANNINEN, T. PITKÄNEN and O. AIKALA, Acta Cryst. **45**, 478 (1989).

NEW FRONTIERS IN EXPERIMENTAL CHARGE DENSITY STUDIES

JOCHEN R. SCHNEIDER

Hamburger Synchrotron Strahlungslabor HASYLAB, Deutsches Elektronen-Synchrotron DESY,
Notkestr. 85, D - 2000 Hamburg 52, FRG

ABSTRACT — Recent developments in experimental charge density studies in inorganic materials are described with emphasis on the use of synchrotron radiation and the possibilities of combining data taken with neutrons from spallation sources on time-of-flight diffractometers with those obtained from short wavelength X-ray diffraction experiments performed on the same sample. In addition Be is discussed as an example of successful interplay between theory and various experimental techniques. Finally new developments in the treatment of extinction are presented.

INTRODUCTION

In the present paper no attempt is made to review the experimental charge density work performed over the last three years. Instead a limited number of examples will be discussed which deal with some of the more problematic aspects in charge density studies. The subjects are: measurement of weak reflections with synchrotron radiation to complement standard X-ray data sets; propagation of solid state effects to high order reflections; combination of diffraction experiments with spallation source neutrons and short wavelength X-rays performed on the same sample, and new developments in the treatment of extinction.

Synchrotron radiation data from Cuprite, Cu_2O, and Corundum, α - Al_2O_3

In their charge density study of Cuprite, Cu_2O, Restori and Schwarzenbach [1] show that standard deformation-density refinements lead to unsatisfactory results, since 3/8 of the structure factors are too small to be measured with X-rays from sealed tubes. Progress should be expected from the use of synchroton radiation because of its high intensity and extremely good collimation, provided problems due to the instability of the synchrotron source, both in space and time, can be overcome. In order to access the accuracy that can be obtained with synchrotron radiation, Kirfel and Eichhorn [2] collected data from two well determined reference structures: Cuprite, Cu_2O, [1] and Corundum, α-Al_2O_3, [3]. They used the 5-circle diffractometer installed at HASYLAB in Hamburg which is described by Kupcik et al. [4].

Fig. 1 shows the layout of the diffractometer. After modifications of both electrical and mechanical functions a STOE 4-circle diffractometer has been mounted on a fifth circle with the intention to rotate the whole diffractometer around the primary beam. The monochromator consists of two flat Germanium (111) single crystals each separately movable and the following specifications for the exit beam are met: the beam position is independent of wavelength which can be varied in the range of 0.3 to 2.2 Å. The energy resolution at 12.4 keV is 4×10^{-4}, the angular divergence of the monochromatic beam is 3.6 sec. of arc, higher harmonics are efficiently suppressed. A combined polarization/intensity real time monitor of the type described by Smend et al. [5] has been installed between the monochromator and the diffractometer.

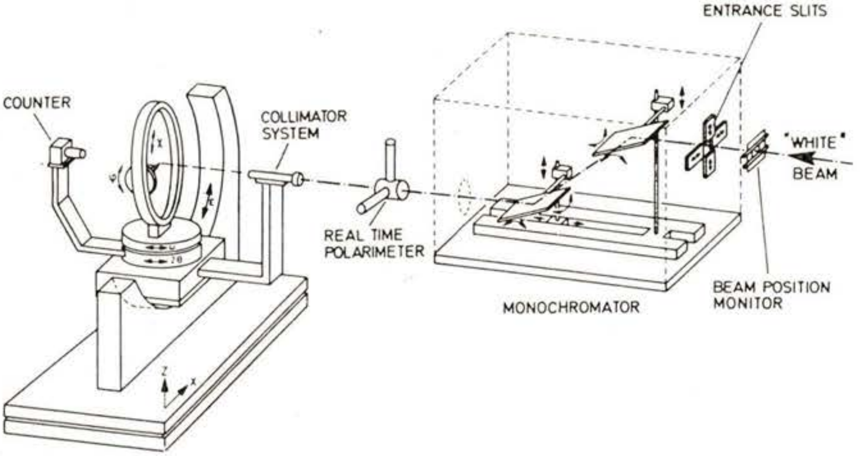

Fig. 1 — Layout of the 5-circle diffractometer for Synchrotron radiation in the wavelength range from 0.3 to 2.2 Å installed at DESY-HASYLAB in Hamburg, FRG [4].

Kirfel and Eichhorn [2] showed that X-ray structure amplitudes of excellent quality can be obtained with synchrotron radiation, after proper attention is given to data collection strategies and to data reduction procedures. From comparison with the data from a sealed X-ray tube [1, 3] they concluded, that little can be gained by measuring strong reflections, however, the improvement due to the use of synchrotron radiation is very pronounced for the weaker or even «forbidden» reflections. The second statement is supported by Fig. 2, which shows a comparison between calculated and observed structure factors deduced from synchrotron radiation or sealed X-ray tube data [3], respectively, via multipole refinements. Whereas the X-ray data scatter over a wide range, a nearly 1 to 1 correspondence is observed for the synchrotron data.

Effect of valence electron hybridization on high order structure factors in Beryllium metal

Since the X-ray study by Brown in 1972 [6] charge density studies on Be metal have attracted a lot of interest, both in theory and in experimental work. By combining neutron [7], γ-ray [8] and X-ray diffraction data [9], Hansen and Larsen calculated in 1984 for the first time what might be called a parameter-free deformation density of Be metal, which confirms that the bonding goes through the tetrahedral holes of the hexagonal closed-packed structure. The experimental data are in very good agreement with ab initio HF-SCF-LCAO [10] and pseudopotential calculations [11]. The

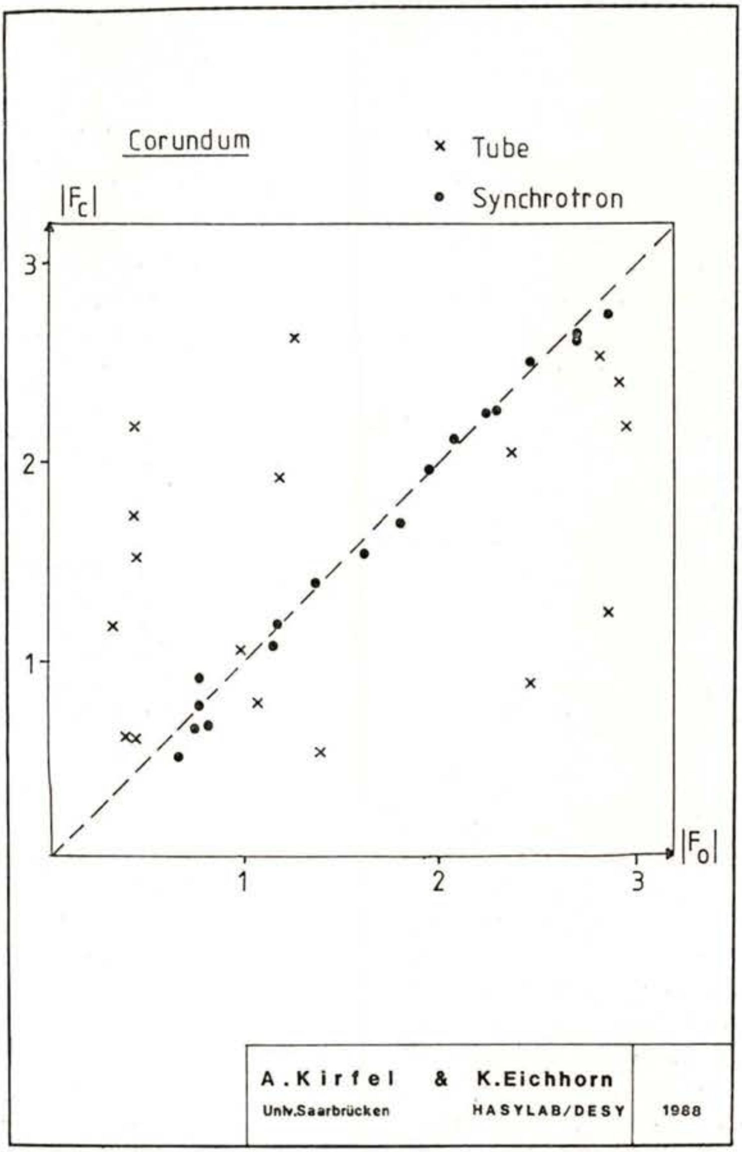

Fig. 2 — Comparison between calculated and observed structure factors of α-Al_2O_3 deduced from synchrotron radiation [2] or sealed X-ray tube data [3], respectively.

earlier X-ray data [6], which were measured on an absolute scale, do not agree with the results of the more recent measurements [8, 9]. Besides a scale factor problem the greatest discrepancy is observed for the 002 reflection. On the other hand an early augmented-plane-wave (APW) calculation performed within the muffin-tin approximation to the crystal potential by Inoue and Yamashita [12] agreed rather well with Brown's data. The results of this APW calculation have been reproduced by Redinger et al. [13].

More recently Blaha and Schwarz [14] did a self-consistent all-electron full potential linearised-augmented-plane-wave (LAPW) calculation of the structural and electronic properties of Be, using the local density approximation (LDA) for the exchange and correlation energy functional. Their structure factors are in very good agreement with the γ-ray data on absolute scale [8] as well as with the recent X-ray data [9]. Therefore the difference in the calculated 002 structure factor is due to the muffin-tin approximation, the agreement between the muffin-tin APW calculations and the 1972 X-ray data is accidental, most probably due to extinction effects in the experimental data which had been considered negligible at the time.

Pindor et al. [15] performed self-consistent LAPW calculations for the charge density of metallic Be again within the LDA. The overall agreement with the γ-ray structure factors [8] is good, and it is argued that the remaining discrepancies are due to the inadequacy of the LDA and, for some reflections, in neglecting the non-sphericity of the core charge density.

The γ-ray data of Be [8] have been taken by using low-intensity 0.03 Å radiation from ^{198}Au sources which necessitated quite long measuring times. In order to improve on this Hansen et al. [16] employed a second γ-ray diffractometer using 0.12 Å radiation from a ^{153}Sm source [17]. This intermediate wavelength should be quite useful for scattering systems with light atoms where intensities at 0.03 Å are too low, but where extinction is still a problem with X-ray measurements. The sample used in this γ-ray study was an almost cubic single crystal of Be; it is the larger crystal used by Larsen et al. [7] for their neutron diffraction measurement, but subsequently etched to dimensions $1.70 \times 1.90 \times 2.16$ mm. During a period of 36 days, 500 rocking curves were measured, corresponding to 37 symmetry-independent reflections with $\sin(\Theta)/\lambda \leqslant 0.85$ Å^{-1} and 14 reflections were observed above this limit. The 0.03 Å γ-ray diffraction data which were measured on an absolute scale [8] have been used to scale the 0.12 Å data and to correct them for extinction. The extinction correction for the 002 structure factor (the strongest reflection) amounts to 3.4 %. It has been impossible to obtain a reliable estimate for extinction using only the 0.12 Å data, because one cannot separate the effect of valence electron density deformation from extinction.

Fig. 3 shows the differences between Be crystal and free-atom form factors as a function of scattering angle. In view of the size of the random errors estimated for the experimental data (between 0.5 and 1 %), the three theories are in satisfactory agreement with each other, and with experiment, especially for the first three reflections (100, 002 and 101). At higher orders, structure factors are only available from the two pseudopotential calculations [11, 18]. In spite of the large scatter, the experimental values above $\sin(\Theta)/\lambda = 0.6$ Å^{-1} tend to be lower than the free-atom form factors. This has also been found in earlier studies and was interpreted as due to a core expansion. A high order refinement along the lines suggested by Coppens et al. [19] yielded a 1 % linear expansion, implying a 2 % decrease of the kinetic energy of the core electrons, i. e. by about 7.5 eV. On the other hand, based on careful Hartree-Fock band structure calculations, Dovesi et al. [20] have shown that the change in kinetic energy of the core electrons (the 1s orbital) compared with the free atom amounts to only 1.5 eV. Blaha et al. [14] also examined the possibility of a core expansion by comparing free-atom and crystalline form factors, both derived in the local density approximation. They find a core expansion of about 0.1-0.3 %, which is too small to be detected experimentally. These results suggest that the major source of the low values observed for the form factors at high scattering angles resides in modifications of the valence electron distribution in the solid.

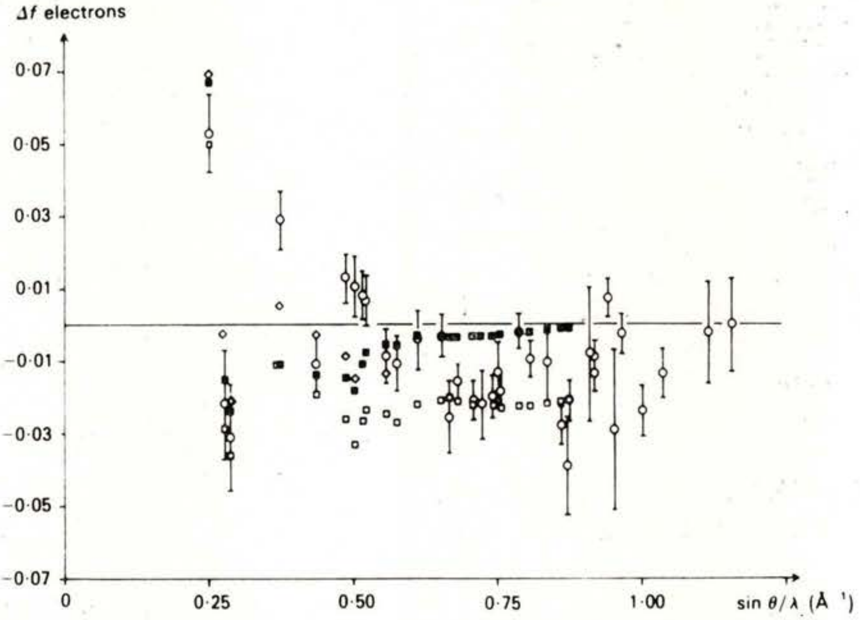

Fig. 3 — Differences between Be-crystal and free-atom form factors as a function of momentum transfer sin(Θ)/λ. Theoretical data: ◇ ◇ ◇ Pindor et al. [15], □ □ □ von Barth et al. [18], ■ ■ ■ Chou et al. [11]. ○ ○ ○ experimental γ-ray diffraction data [16].

We believe that the right explanation of the effect has been given by von Barth and Pedroza [18]. With a pseudopotential approach they reproduced the observed trend of the form factors quite accurately, although they made no effort to take into account the effects of the crystal field on the core electron density, but they corrected for the non-orthogonality of the pseudo-valence wave functions with respect to the core. The condition of orthogonality between core and valence states leads to a core-like cusp in the valence density of the s-like states (for the atom as well as for the solid), which is absent in the p-like states. In the solid von Barth et al. [18] find only about 0.6 electrons per atom in valence s states, whereas the atom which is subtracted (as in commonly done) has two electrons in the 2s orbital. Because of this promotion of electrons from 2s to mainly 2p states in the solid, one observes lower form factor values for the crystal than for the atom. A comparison of the results of Chou et al. [11], who have added to their form factors the Hartree-Fock core contribution calculated by Dovesi et al. [10], with those of von Barth et al. [18] in Fig. 3 shows that the orthogonalization effect dominates above 0.6 Å^{-1}.

A combined spallation source neutron and γ - ray diffraction study of MnF_2 at 15 and 300 K

The advantages and disadvantages of a combination of neutron and X-ray scattering experiments in charge density studies have been discussed extensively in the literature [21]. Neglecting magnetic effects neutrons interact with the nuclei of the atoms and provide unbiased information on the positional and temperature parameters of the investigated crystal. X-rays interact with the electrons and the results of both type of measurements have been interpreted in terms of X-n maps. In neutron scattering experiments one needs crystals much larger in size than what can be handled in X-ray diffraction experiments, i. e. two different samples are needed which may be different with respect to extinction and stoichiometry. Therefore positional and thermal parameters have often been deduced from high order X-ray refinements.

As an example we would like to refer to a bonding study of TiC and TiN by Dunand et al. [22], the results of which have been compared with ab initio solid state calculations by Blaha et al. [23]. The experiment was performed with Ag-Kα radiation. Severe anisotropic extinction affected the intense low-order reflections. Inhomogeneity in the mosaic spread and domain size produced small but significant differences between reflection and antireflection for the same plane of diffraction. These effects have been modeled and refined together with a scale factor, isotropic thermal parameters, a population parameter of the non-metal site, the amplitude of metal-atom static displacements around non-metal vacancies, and an atomic model which includes occupancy factors of the separate orbital contributions of the valence electrons combined with linear expansion-contraction parameters [19]. Very good agreement between model and experimental data has been obtained.

On the other hand, the charge density study on Be metal, discussed above, is considered as an example where the combination of X-ray and neutron scattering is decisive. X-n maps calculated from X-ray data taken at a small, and from neutron data taken at a large crystal, agreed with those were the X-ray structure factors have been measured with 0.12 Å γ-radiation on the neutron sample. Be is light and may be considered as an extreme example. In the following we shall discuss a combined neutron and gamma-ray diffraction study at a large MnF_2 single crystal, approximately 3.7 mm in diameter.

MnF_2 has a rutile type structure (tetragonal space group $P4_2/mnm$). Two parameters, the axial ratio c/a and the free parameter x of the anion position, define the geometry. A strong change in the optical linear birefringence takes place in the fluorides of transition metals when antiferromagnetic ordering occurs [24, 25]. The possible origin of this effect has been somewhat controversial [26]. The magnetic birefringence may be attributed to magnetostrictive distortions or to purely electronic contributions giving rise to a spin-dependent polarizability. Jauch et al. [27] suggested that the fluorine position parameter could show a small shift of the order 5×10^{-4} as a result of exchange interaction, which would be sufficient to account for the temperature dependence of the birefringence. In order to test this suggestion accurate determinations of the positional parameter x were undertaken both at room temperature and at 11 K, where the magnetic ordering is complete ($T_N = 67$ K), using 412 keV γ-radiation [28].

Because of intensity problems only 27 Bragg reflections have been measured, each on an absolute scale. The strongest reflections which were most sensitive to the positional parameter, and which were not affected by extinction, have been selected. The percentage error in the integrated intensities due to counting statistics ranges from 0.4 % to 1 %. The data were refined on a model with anisotropic temperature factors. Fukamachi's atomic scattering factors for Mn^{2+} and F^- were used [29]. The analysis of the γ-ray data provides a shift in the x parameter of $\delta x = x(11\,K) - x(300\,K) = -(52 \pm 9) \cdot 10^{-5}$, from which a change in the birefringence was calculated which is in excellent agreement with the experimental value.

In order to assess the degree of accuracy that can be achieved at present with single crystal time-of-flight (TOF) neutron diffraction, extensive data sets have been taken at 300 and 15 K on MnF_2 at IPNS in Argonne, U.S.A., and compared with the results of a complete γ-ray diffraction study performed on the same sample, a sphere of 3.7 mm diameter [30]. Table 1 summarizes the results of the refinements with the room temperature data and Table 2 those obtained with the low temperature data. In addition Table 1 shows the results of the refinement of X-ray data by Alte da Veiga et al. [31].

At room temperature the values of the fluorine positional parameters from TOF neutrons and γ-rays are virtually identical. Although the neutron data are less precise then the γ-ray data, the standard deviation of the neutron x parameter is considerably smaller than the corresponding γ-ray value. This is due to the difference between the scattering powers of the two atomic species for the two kinds of radiation. A small but significant difference between the neutron and the γ-ray parameter is observed at low temperature. In view of the very good agreement at room temperature it seems unlikely that the difference is due to systematic experimental error. This effect can be attributed to the non-coincidence of the centre of the electronic charge distribution and the nucleus in the antiferromagnetic state. At low temperature the overall agreement between neutron and γ-ray temperature parameters is good. At room temperature the neutron values are consistently smaller which is attributed to thermal diffuse scattering included in the neutron diffraction peaks. The γ-ray data were corrected for TDS though the corrections were small because of the narrowness of the diffraction profiles. More sophisticated models are presently developed with the aim to localize

TABLE 1 — Results of the refinement of neutron time-of-flight, γ-ray and X-ray data taken at a MnF_2 single crystal at room temperature.

	TOF	G	X
Mn U_{11} (Å^2)	0.00796(8)	0.00981(6)	0.0096(2)
U_{33}	0.00558(16)	0.00687(6)	0.0071(2)
U_{12}	− 0.00155(6)	− 0.00153(11)	− 0.0019(5)
F U_{11}	0.01433(8)	0.01564(13)	0.0155(4)
U_{33}	0.00931(14)	0.00995(18)	0.0102(4)
U_{12}	− 0.00755(5)	− 0.00742(18)	− 0.0079(3)
x	0.30491(3)	0.30492(8)	0.3050(2)
wR (F^2)	0.067	0.021	*
No. of unique reflections	448	294	76
			* wR(F) = 0.01

TOF = parameters obtained from TOF neutron data [30].
G = parameters obtained from γ-ray data [30].
X = parameters obtained from X-ray data [31].

a significant change in the charge density due to magnetic ordering.

In the neutron TOF diffraction experiments the used wavelength range is from 0.6 to 3.6 Å and extinction will be important, especially because of the high quality of the large MnF_2 single crystal. High resolution double-crystal γ-ray rocking curves [32] showed a full width at half maximum of 10.5 ± 1 sec. of arc. If y is the ratio between the measured integrated reflecting power and the value calculated from kinematical theory, the data set can be characterized as following: 0.5 % of the reflections are in the range $0 \leqslant y \leqslant 0.2$, 2.5 % in the range $0.2 \leqslant y \leqslant 0.4$, 12 % in $0.4 \leqslant y \leqslant 0.6$, 36 % in $0.6 \leqslant y \leqslant 0.8$ and 49 % of the measured reflections in the range $0.8 \leqslant y \leqslant 1$. Various extinction models have been investigated:

1. Isotropic type I formalism of Zachariasen [33] (extinction dominated by mosaic spread).
2. Becker & Coppens type I extinction with a Lorentzian mosaic distribution [34, 35].
3. Becker & Coppens type I extinction with a Gaussian mosaic distribution.
4. Becker & Coppens type II extinction (particle size dominated).
5. Anisotropic type I Zachariasen correction [36].
6. Random elastic deformation model of Kulda [37].

Refinements were done on the complete data sets and on data sets where the most extinguished reflections were excluded. As a function of the cut-off in y a significant variation in the goodness-of-fit parameter is observed indicating some failure of all models in the case of extreme extinction. The final refinements were therefore confined to data with $y \geqslant 0.4$. The best fit was obtained with models 1 (and 5) and 2. The corresponding residuals are lower than those with the other models and, more important, it is only for these models that the thermal parameters remain constant as the data set is reduced. The improvement of fit produced by introducing an anisotropic extinction correction is hardly significant. In addition, the anisotropy of the extinction has no effect on the anisotropy of the thermal parameters. It is thus concluded that the extinction is isotropic within the experimental accuracy, which is in line with the weak variation of the FWHM of the high resolution γ-ray rocking curves measured for different crystal orientations. The overall agreement between the observed and fitted mosaic spread is excellent. From this we conclude that in the present case the extinction parameters represent a real physical situation and are not only adjustment parameters. The fact that model 1 and 2 are equally satisfactory initially seemed surprising since model 1 is considered to give reliable results for small extinction only ($y \geqslant 0.8$). It is, however, not fortuitous since in the angular range of 30° to 60°, covered by the neutron TOF diffractometer, the expressions for y are virtually the same for both models.

New developments in the treatment of extinction

Zachariasen's 1967 paper on extinction [33] is considered as a landmark and stimulated a lot of progress in the field. The theory by Becker & Coppens [38] has been proven successful in many applications, the discussion on the underlying physical principles continues. As an example people have been puzzled by the fact that the assumption of a Lorentzian mosaic

TABLE 2 — Results of the refinement of neutron time-of-flight, γ-ray and X-ray data taken at a MnF_2 single crystal at low temperature.

	TOF	G
Mn U_{11} (Å^2)	0.00258(7)	0.00247(8)
U_{33}	0.00180(14)	0.00197(8)
U_{12}	−0.00037(5)	−0.00046(14)
F U_{11}	0.00566(6)	0.00513(10)
U_{33}	0.00399(13)	0.00337(15)
U_{12}	−0.00253(2)	−0.00187(14)
x	0.30480(2)	0.30442(8)
wR (F^2)	0.059	312
No. of unique reflections	309	0.022

TOF = parameters obtained from TOF neutron data (T = 15 K) [30].
G = parameters obtained from γ-ray data (T = 11 K) [30].

distribution leads to a better agreement between measured and calculated structure factors, although a Gaussian is the more likely distribution. From modeling the thickness dependence of the integrated reflecting power measured with 0.0392 Å γ-radiation in annealed silicon crystals Schneider et al. [39] concluded that the physically unrealistic Lorentzian mosaic distribution models the effect of primary extinction in an extinction theory based on the energy-transfer model. Recently Sabine [40] analyzed the various extinction theories based on Darwin's intensity transfer equations and found that Lorentzian or Fresnellian functions for the coupling constant can be used to describe primary extinction while secondary extinction requires a Gaussian, rectangular or triangular function.

In a series of papers [38, 41] Kulda describes an extinction theory which does not make use of the mosaic model. His random elastic deformation (RED) model is based on a stochastic sequence of elastically deformed domains, which allows a more adequate treatment of primary extinction by direct use of dynamical diffraction theory. Secondary extinction is treated in the conventional way by solving the intensity coupling equations.

Kato developed a statistical dynamical diffraction theory [42-44] which covers the full transition from dynamical to kinematical diffraction behavior as a function of two correlation parameters, τ and E, the first one describing short range and the second one describing long range correlation. The integrated reflecting power is calculated as the sum of a coherent, an incoherent and a mixed term:

$$R = R_{coh} + R_{mix} + R_{incoh} .$$

In the limit of an ideally perfect crystal ($E = 1$) one gets $R = R_{coh}$, which is equal to the value R_{dyn} calculated from classical dynamical diffraction theory. For an ideally imperfect single crystal the coherent and mixed terms vanish and one gets the result which is usually determined from kinematical diffraction theory.

Fig. 4 shows the integrated reflecting power measured in transmission with 0.0392 γ-radiation at reflection 220 of a highly perfect Si single crystal as a function of the parameter A, which is the ratio of sample thickness and extinction length $t_{ext} = 0.216$ mm, in the present case. The effective sample thickness has been varied by tilting the crystal around the scattering vector [45]. The experimental data are very well reproduced using the 220 structure factor as determined from X-ray Pendellösung measurements [46].

In order to check the statistical dynamical diffraction theories samples with a homogeneous distribution of defects are needed. Czochralski grown dislocation free Si single crystals contain typically 20 ppm oxygen atoms which, at higher temperatures, diffuse through the lattice to produce small agglomerates which grow into precipitate particles of silica (SiO_2). A series of samples have been studied by means of neutron small angle scattering [47]. For a crystal containing 7.4×10^{17} oxygen atoms per cm^3 and annealed for 72 hours at 750°C one finds $4 \cdot 3 \cdot 10^{12}$ cm^{-3} cuboidal precipitates, $280 \cdot 280 \cdot 22$ Å^3 in dimension, their habit plane is $\{100\}$. These precipitates will create a long range strain field and the resulting Huang diffuse scattering has been observed with high resolution γ-ray diffractometry in the same sample [48]. Pendellösung oscillations have been measured with 0.0392 Å γ-radiation in this material;

the result is shown in Fig. 5 [49]. The observed Pendellösung oscillations show the period expected from dynamical diffraction theory for a perfect crystal, however, the experimental data are about 50 % higher than the average value of the integrated reflecting power expected for a perfect crystal. The data are well described by the expression

$$R_{theor} = R_{dyn}(A) + CDIFF \cdot A,$$

where CDIFF is a fitting constant. This result suggests that the weak diffuse scattering caused by the SiO_2-precipitates is superimposed on the Pendellösung oscillations characteristic of a perfect crystal; no interaction between coherent and incoherent scattering is observed.

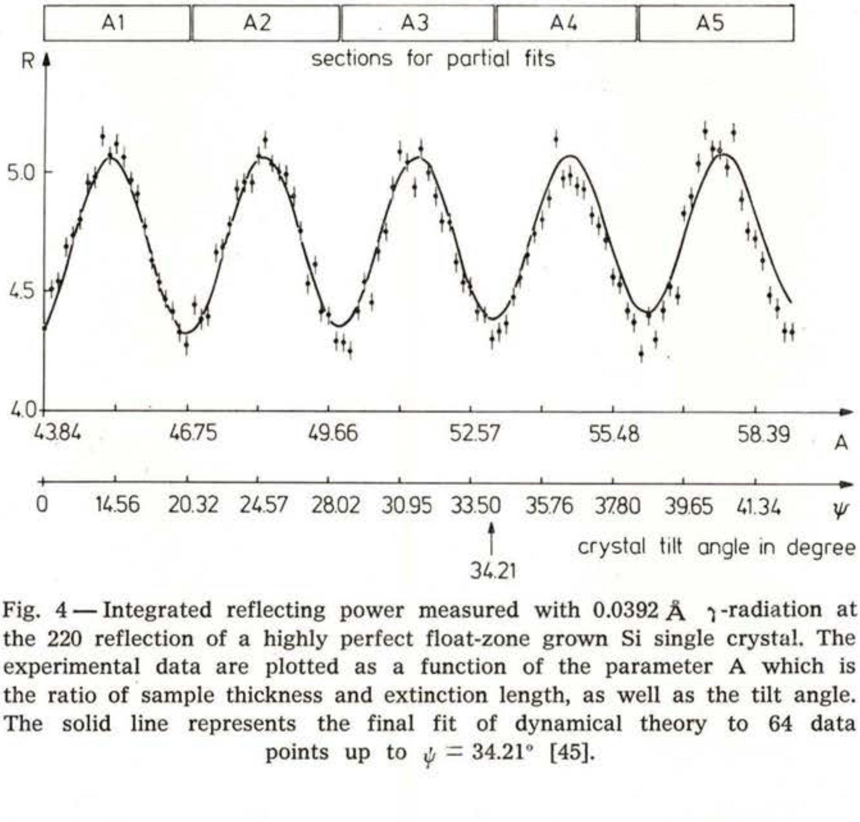

Fig. 4 — Integrated reflecting power measured with 0.0392 Å γ-radiation at the 220 reflection of a highly perfect float-zone grown Si single crystal. The experimental data are plotted as a function of the parameter A which is the ratio of sample thickness and extinction length, as well as the tilt angle. The solid line represents the final fit of dynamical theory to 64 data points up to $\psi = 34.21°$ [45].

The same data have been fitted to Kato's statistical dynamical diffraction theory and the result is shown in Fig. 6. The fit is satisfying, although a systematic deviation is clearly visible, the theoretical curve being too steep. The two parameters τ/Λ, $\Lambda = \pi \cdot t_{ext}$ and E are highly correlated in the present case and τ/Λ was fixed to a value of 1.0. The value $E = 0.99957(2)$ obtained from the fit is very close to 1 and indicates that the deviation of the sample from a perfect crystal is somehow very small. It certainly is premature to consider the observed discrepancy between experiment and theory as a shortcoming of the latter. Rather, one should consider that the experiment may deal with a very special case. The average value of the dynamical reflecting power is reached after penetration into the crystal of approximately 0.1 mm, whereas the diffuse scattering is from the whole crystal, 10 mm thick.

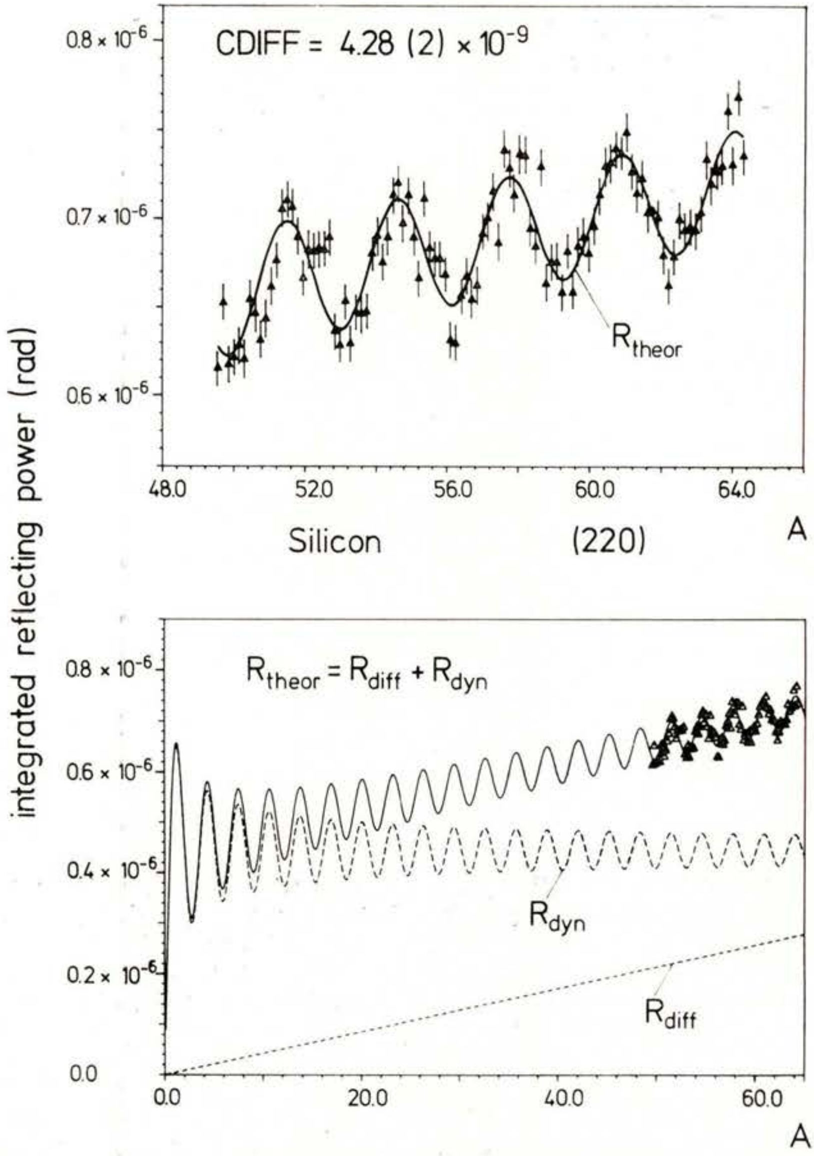

Fig. 5 — Pendellösung intensity beats measured with 0.0392 Å γ-radiation in a Czochralki grown Si crystal containing 7.7×10^{17} cm^{-3} oxygen atoms after annealing for 70 hours at 770°C. Comparison is made with the result from dynamical theory, R_{dyn}, and its superposition with a scattering term, R_{diff}, proportional to the parameter $A = T/t_{ext}$ and thus the sample thickness.

Therefore the diffuse scattering is strongly enhanced compared to the Bragg scattering, which may explain the fact that a simple superposition of dynamical and diffuse scattering gives a better fit than the application of Kato's theory.

Al Hadad and Becker [50] introduced corrections to Kato's original solution which

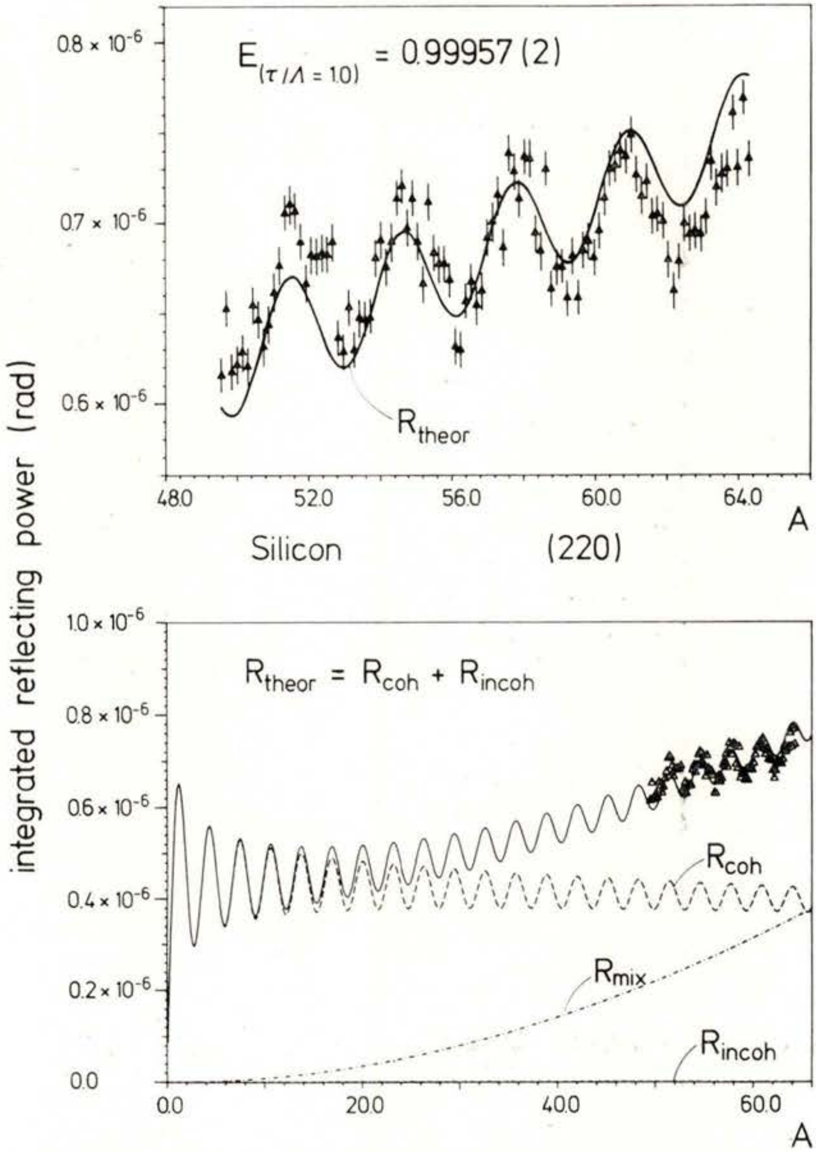

Fig. 6 — Comparison of the experimental data shown in Fig. 5 with the best fit of Kato's statistical dynamical theory. E is the parameter describing long range correlation. The parameter $\mathcal{T}$, describing short range correlation, was fixed to a value equal the Pendellösung length

$\Lambda = \pi \cdot t_{ext}$. The parameter $A = T/t_{ext}$.

have a significant effect, even in the case of crystals with a high degree of long range perfection. The authors apply their expressions to experimental measurements on parallel plates of Si with different dislocation densities by Olekhnovich et al. [51]. The modified theory reproduces the observations quite well.

In order to make further progress in the development of extinction theories, i. e. to improve our understanding of the diffraction process in imperfect single crystals, the new theories have to be probed against experimental data obtained on samples with well characterized, homogeneously distributed defects. The defect structure created in Czochralski grown Si single crystals by annealing them at temperatures between 750 and 1300°C appears to be most suitable for such studies. In a first step γ-ray diffraction studies can probe the basic concepts of the statistical dynamical theories of the kind introduced by Kato, because absorption is very weak, anomalous dispersion does not occur, and due to the small Bragg angles of typically 1° the diffraction geometry is quasi one-dimensional, polarization effects can be neglected. Next neutron diffraction experiments should be performed on the same samples using various wavelengths because absorption, anomalous dispersion and polarization effects are againeither weak or non-existant, but the full range of Bragg angles occurs and those aspects in the theories dealing with boundary conditions related to the scattering geometry can be tested. In a third step diffraction experiments with synchrotron radiation should be performed, always on the same material. Here one can tune the wavelength such that the importance of absorption, anomalous dispersion and polarization effects increases. In this context one should mention that for the first time diffraction experiments with 145 keV synchrotron radiation have been performed at CHESS in Cornell, USA, recently [52]. Annealed Si crystals have been investigated and it became clear that experiments of that type can be performed with wavelengths as short as 0.05 Å. As a by-product of extinction studies along these lines one can also develop materials very well suited for X-ray optical devices, i. e. via a special annealing process the Si crystal was internally deformed in such a way, that the FWHM of the diffraction pattern for 145 keV photons increased from approximately 0.2 to 8 sec. of arc, a plateau of maximum reflectivity was observed, 4 sec. of arc wide [53].

Thanks are due to Prof. A. Kirfel for kindly providing the synchrotron radiation diffraction data prior to publication.

REFERENCES

[1] RESTORI, R. and SCHWARZENBACH, D., Acta Cryst. B, **42**, 201 (1986).

[2] KIRFEL, A. and EICHHORN, K., private communication. Address: DESY-HAYSLAB, Notkestr. 85, D-2000 Hamburg 52, FRG.

[3] LEWIS, J., SCHWARZENBACH, D. and FLACK, H. D., Acta Cryst A, **38**, 733 (1982).

[4] KUPCIK, V., WENDESCHUH-JOSTIES, W., WOLF, A. and WULF, R., Nucl. Instr. and Meth. in Phys. Res. A, **246**, 624 (1986).

[5] SMEND, F., SCHAUPP, D., CZERWINSKI, H., MILHOUSE, A. H. and SCHENK-STRAUSS, H., Nucl. Instr. and Meth. in Phys. Res. A, **241**, 290 (1985).

[6] BROWN, P. J., Phil. Mag., **26**, 1377 (1972).

[7] LARSEN, F. K., LEHMANN, M. S. and MERISALO, M., Acta Cryst. A, **36**, 159 (1980).

[8] HANSEN, N. K., SCHNEIDER, J. R. and LARSEN, F. K., Phys. Rev. B, **29**, 917 (1984).

[9] LARSEN, F. K. and HANSEN, N. K., Acta Cryst. B, **40**, 169 (1984).

[10] DOVESI, R., PISANI, C., RICCA, F. and ROETTI, C., Phys. Rev. B, **25**, 3731 (1982).

[11] CHOU, M. Y., LAM, P. K. and COHEN, M. L., Phys. Rev. B, **28**, 4179 (1983).

[12] INOUE, S. T. and YAMASHITA, J., J. Phys. Soc. Japan, **35**, 677 (1973).

[13] REDINGER, J., SCHWARZ, K., HANSEN, N. K., BAUER, G. E. W. and SCHNEIDER, J. R., Hahn-Meitner-Institut, Berlin, Report HMI **B412**, 79 (1984).

[14] BLAHA, P. and SCHWARZ, K., J. Phys. F, **17**, 899 (1987).

[15] PINDOR, A. J., VOSKO, S. H. and UMRIGAR, C. J., J. Phys. F, **16**, 1207 (1986).

[16] HANSEN, N. K., SCHNEIDER, J. R., YELON, W. B. and PEARSON, W. H., Acta Cryst. A, **43**, 763 (1987).

[17] ALKIRE, R. W. and YELON, W. B., J. Appl. Cryst., **14**, 362 (1981).

[18] BARTH, U. von, and PEDROZA, A. C., Phys. Scr., **32**, 353 (1985).

[19] COPPENS, P., GURU ROW, T. N., LEUNG, P., STEVENS, E. D., BECKER, P. and YANG, Y. W., Acta Cryst. A, **35**, 63 (1979).

[20] DOVESI, R., ANGONOA, G. and CAUSA, M., Phil. Mag. B, **45**, 601 (1982).

[21] COPPENS, P., in: Neutron Diffraction p. 71 (H. Dachs, ed.). Berlin-Heidelberg-New York: Springer 1978.

[22] DUNAND, A., FLACK, H. D. and YVON, K., Phys. Rev. B, **31**, 2299 (1985).

[23] BLAHA, P., REDINGER, J. and SCHWARZ, K., Phys. Rev. B, **31**, 2316 (1985).

[24] BOROVIK-ROMANOV, A. S., KREINES, N. M., PANKOW, A. A. and TALALAEV, M. A., Sov. Phys. — JETP, **37**, 890 (1973).

[25] JAHN, I. R., Phys. Stat. Sol. (b), **57**, 681 (1973).

[26] BOROVIK-ROMANOV, A. S., KREINES, N. M. and Paces, J., Sov. Phys. — JETP, **50**, 1198 (1979).

[27] JAUCH, W. and DACHS, H., Solid State Commun., **14**, 657 (1974).

[28] JAUCH, W., SCHNEIDER, J. R. and DACHS, H., Solid State Commun., **48**, 907 (1983).

[29] FUKAMACHI, T., Tech. Rep. ISSP, Ser. B., No. 12 (1971).

[30] JAUCH, W., SCHULTZ, A. J. and SCHNEIDER, J. R., J. Appl. Cryst., **21**, 975 (1989).

[31] ALTE DA VEIGA, L. M., ANDRADE, L. R. and GONSCHOREK, W., Z. Kristallogr., **160**, 171 (1982).

[32] SCHNEIDER, J. R. and GRAF, H. A., J. of Cryst. Growth, **74**, 191 (1986).

[33] ZACHARIASEN, W. H., Acta Cryst., **23**, 558 (1967).

[34] BECKER, P. and COPPENS, P., Acta Cryst. A, **30**, 129 (1974), ibid. **30**, 148 (1974).

[35] BECKER, P. and COPPENS, P., Acta Cryst. A, **31**, 417 (1975).

[36] COPPENS, P. and HAMILTON, W. C., Acta Cryst. A, **26**, 71 (1970).

[37] KULDA, J., Acta Cryst. A, **43**, 167 (1987).

[38] BECKER, P., Acta Cryst. A, **33**, 243 (1977).

[39] SCHNEIDER, J. R., GONÇALVES, O. D. and GRAF, H. A., Acta Cryst. A, **44**, 461 (1988).

[40] SABINE, T. M., Acta Cryst. A, **44**, 368 (1988).

[41] KULDA, J., Acta Cryst. A, **44**, 283 (1988), ibid. **44**, 368 (1988).

[42] KATO, N., Acta Cryst. A, **32**, 453 (1976); ibid. **32**, 458 (1976).

[43] KATO, N., Acta Cryst. A, **35**, 9 (1979).

[44] KATO, N., Acta Cryst. A, **36**, 770 (1980).

[45] GRAF, H. A. and SCHNEIDER, J. R., Phys. Rev. B, **34**, 8629 (1986).

[46] ALDRED, P. J. E. and HART, M., Proc. R. Soc. London, Ser. A, **332**, 223 (1973), ibid. **332**, 239 (1973).

[47] MESSOLORAS, S., STEWART, R. J., SCHNEIDER, J. R. and ZULEHNER, W., Semiconductor Sci. Technol., **4**, 340 (1989).

[48] SCHNEIDER, J. R., NAGASAWA, H., JAUCH, W. and ZULEHNER, W., to be published.

[49] SCHNEIDER, J. R., GONÇALVES, O. D., ROLLASON, A. J., BONSE, U., LAUER, J. and ZULEHNER, W., Nucl. Inst. Meth. in Phys. Res. B, **29**, 661 (1988).

[50] AL HADAD, M. and BECKER, P., Acta Cryst. A, **44**, 262 (1988).

[51] OLEKHNOVICH, N. M., KARPEI, A. L. OLEKHNOVICH, A. I. and PUZENKOVA, L. D., Acta Cryst. A, **39**, 116 (1983).

[52] SIDDONS, D. P., HASTINGS, J. B., SCHNEIDER, J. R. and BERMAN, L. E., Proceedings of the Synchrotron Radiation Instrumentation Conference SRI-88, Tsukuba, Japan 29.8-2.9.88, Rev. Sci. Instr., **60**, 2398 (1989).

[53] SCHNEIDER, J. R., NAGASAWA, H., BERMAN, L. E., HASTINGS, J. B., SIDDONS, D. P. and ZULEHNER, W., Nucl. Instr. and Meth. in Phys. Res., A, **276**, 636 (1989).

INELASTIC SCATTERING OF SYNCHROTRON RADIATION

W. SCHÜLKE
Institute of Physics, University of Dortmund,
D-4600 Dortmund 50, Fed. Rep. of Germany

ABSTRACT — With respect to the fundamental information which can be obtained by means of Inelastic X-ray Scattering Spectroscopy (IXSS), three different experimental demands can be distinguished; (i) the Compton scattering regime, where IXSS yields information about electron distribution in momentum space, (ii) the regime of electron excitation, where the long and short range correlation connected with excitations in a many electron system can be followed up, and (iii) the regime of collective ion excitation, where IXSS with very high energy resolution makes feasible the measurement of phonon dispersion.

The fundamentals of these three regimes of IXSS, the corresponding synchrotron experiments and their results are reviewed. Finally two peculiarities of IXSS with Synchrotron radiation are stressed: (i) Coherent inelastic scattering which yield information about nondiagonal elements of the density matrix in momentum space and nondiagonal elements of the reciprocal dielectric matrix, respectively, (ii) magnetic inelastic scattering.

1 – INTRODUCTION

Inelastic X-ray Scattering Spectroscopy (IXSS) provides the most direct access to correlated motion of electrons in many particle systems and may therefore contribute to the solution of actual problems of solid state physics which are connected with the adequate description of quasi-particle properties beyond approximations commonly in use. In principle, this potentiality of IXSS is well known since the late thirties. But only the advent of strong sources of Synchrotron radiation in the photon energy range from 5 keV to 20 keV has made possible inelastic scattering experiments on condensed matter systems with better than 1 eV resolution and a high signal to noise ratio. Thus very accurate information about the dynamic structure factor $S(\mathbf{q}, \omega)$ of the scattering electron system becomes available for a wide range of energy ($\hbar\omega$) — and momentum ($\mathbf{q}$) — transfer opening insight into both long-range and short-range correlation and into the elementary excitations connected with these correlations in an inhomogeneous many electron system.

Besides some fundamentals of IXSS, which are presented in section 2, sections 3-5 are devoted to the three types of inelastic X-ray scattering experiments, which has to be distinguished with respect to the correlation in time and space one is looking at. Moreover in section 6-7 two peculiarities of IXSS experiments are stressed which became possible as a consequence of the unique properties of Synchrotron radiation: Inelastic scattering utilizing Bloch-type initial photon states (coherent inelastic scattering), and inelastic scattering of circularly polarized X-rays (spin selective inelastic scattering).

2 – FUNDAMENTALS

A typical IXSS-experiment measures the double differential scattering cross section $d^2\sigma/(d\Omega\, d\omega)$ by using a monochromatic and well collimated primary beam, by fixing experimentally a certain solid angle element $d\Omega$ of the scattered radiation and by energy analyzing the scattered radiation. Thus the transferred energy $\hbar\omega$ and the transferred momentum $\hbar\mathbf{q}$ are well defined for one data point of an experimental spectrum, which, in all cases mentioned here, is a constant $\mathbf{q}$-scan.

The double differential scattering cross section can be separated into two pieces

$$\frac{d^2\sigma}{d\Omega\, d\omega} = \left(\frac{d\sigma}{d\Omega}\right)_0 S(\mathbf{q}, \omega) \qquad (1)$$

where the dynamic structure factor $S(\mathbf{q}, \omega)$ reflects properties of the scattering sample in the absence of the perturbing probe, since the scattering process is governed by the weak coupling determined by the Thomson scattering cross section, $(d\sigma/d\Omega)_0$, so that it can be treated in lowest order Born approximation.

By taking into account only terms of the system Hamiltonian which are quadratic in the vector potential of the photon field (non resonant case) one gets in lowest order perturbation theory for the dynamic structure factor

$$S(\mathbf{q}, \omega) = \sum_f |<f| \sum_j e^{i\mathbf{q}\cdot\mathbf{r}_j} |i>|^2 \times \delta(E_f - E_i - \hbar\omega) \qquad (2)$$

where $|i>$ and $|f>$ are the initial and the final state of the scattering system respectively. E_i and E_f are the corresponding energies. The position $\mathbf{r}_j$ of the j-th electron of the system determines the scattering phase $\exp(i\,\mathbf{q}\cdot\mathbf{r}_j)$.

Following van Hove [1], one can utilize the Heisenberg representation of the time dependence of the scattering phase operator $\exp(i\,\mathbf{q}\cdot\mathbf{r}_j)$, ending up with an expression for $S(\mathbf{q}, \omega)$, which does not contain explicitely the final states

$$S(\mathbf{q}, \omega) = \frac{1}{2\pi}\int dt\; e^{-i\omega t} \times <i| \sum_{jj'} e^{-i\mathbf{q}\cdot\mathbf{r}_{j'}(t)}\, e^{i\mathbf{q}\cdot\mathbf{r}_j(o)} |i>. \qquad (3)$$

By introducing the two-particle density function

$$n_2(\mathbf{r}', \mathbf{r}, t) \equiv\; <i| \sum_{jj'} \delta(\mathbf{r}' - \mathbf{r}_j(o)) \times \delta(\mathbf{r}' + \mathbf{r} - \mathbf{r}_{j'}(t)) |i>, \qquad (4)$$

one gets equ. (3) in the following form:

$$S(\mathbf{q}, \omega) = \frac{1}{2\pi}\iiint dt\; e^{-i\omega t} \times n_2(\mathbf{r}', \mathbf{r}, t)\; e^{-i\mathbf{q}\cdot\mathbf{r}}\, d\mathbf{r}\, d\mathbf{r}'. \qquad (5)$$

$n_2(\mathbf{r}', \mathbf{r}, t)$ is, in the classical limit, the probability density of finding an electron at time $t = o$ at $\mathbf{r}'$, and (the same or another) electron at time t' at $\mathbf{r}' + \mathbf{r}$. Equation (5) reveals best the information about the correlated electron motion which is provided by the measurement of $S(\mathbf{q}, \omega)$: The dynamic structure factor is the Fourier transform in time and space ($\mathbf{r}$) of the two particle density function, more precisely, the dynamic structure factor is the Fourier transform. Thus, for instance, the relationship between the quasiperiodicity of correlation distances as found in the collective motion of many electron systems and the frequency of this motion (plasmon dispersion) can be studied.

What type of correlated motion one is looking at with a concrete experiment, depends on the relation between the momentum transfer, q, and the interparticle distance, a, on the one hand, between the measured energy transfer $\hbar\omega$ and characteristic energies of the scattering system on the other hand.

Therefore, one has to distinguish between three types of IXSS-experiments:

i Compton scattering regime:

If $\hbar\omega >>$ characteristic energies of the electron system (Fermi energy, binding energy) and if $2\pi/q < a$, one is observing (within the classical limit) the correlation between the position of the same particle at very small time intervals. This means that information is obtained about the momenta of single particles (momentum distribution), where one has to guarantee, by choosing $\hbar\omega$, that the time interval $2\pi/\omega$ is short enough to prevent the remaining system to become rearranged (impulse approximation [2]).

ii Regime of electron excitations

If $\hbar\omega \approx$ characteristic excitation energies of the electron system (plasmon energy) and if $2\pi/q \gtrsim a$, one is observing the correlated motion of different particles connected both with individual and collective excitations of the system.

iii Regime of collective ion excitation

If an energy transfer $\hbar\omega$ can be experimentally resolved, which is comparable with the excitation energy of the collective motion of the ion cores (phonons), and if $2\pi/q \approx$ interatomic distance, one gets, within the limits of the adiabatic approximation, information about the correlated motion of the ion cores (phonons, collective excitations in amorphous and liquid matter).

In principle, the dynamic structure factor can also be measured by means of inelastic electron scattering, where the double differential scattering cross section is given by

$$\frac{d^2\sigma}{d\Omega\, d\omega} = \left(\frac{d\sigma}{d\Omega}\right)_R S(\mathbf{q}, \omega), \qquad (6)$$

where the Rutherford scattering cross section

$$\left(\frac{d\sigma}{d\Omega}\right)_R = \frac{4\, e^4\, m^2}{\hbar^2\, q^4} \qquad (7)$$

is by many orders of magnitude larger (for small q) than the Thomson cross section and depends strongly on q, so that nearly forward scattering is extremely accentuated. The differences between photon and electron scattering makes both methods complementary.

The advantages of IXSS compared with inelastic electron scattering is the unlimited range of momentum transfer q, the small amount of multiple scattering and the true bulk information, whereas the advantages of inelastic electron scattering over IXSS are the access to the limit $q \approx o$, the surface sensitivity and the unlimited range of the atomic number Z of the scattering sample.

3 – COMPTON SCATTERING REGIME

In sect. 2 it was stated, that within the limits of the impulse approximation [2] ($\hbar\omega > E_c$ (E_c = characteristic energies of the scattering system), and $2\pi/q << a$ (a = interparticle distance)), the measurement of the double differential scattering cross section provides information about the momentum density distribution $n(\mathbf{p})$ of the electrons. By means of a rigorous calculation one obtains the following relation:

$$\frac{d^2\sigma}{d\Omega\, d\omega} = \left(\frac{d\sigma}{d\Omega}\right)_o \frac{1}{(2\pi)^3} \int d\mathbf{p}\; n(\mathbf{p}) \times \delta\left(\omega - \frac{\hbar q^2}{2m} - \frac{\mathbf{p}\cdot\mathbf{q}}{m}\right). \qquad (8)$$

A constant **q**-scan yields direct information about projections of the electron momentum density $n(\mathbf{p})$ on the scattering vector **q** (see the argument of the δ-function in equ. (8)). The measurement of a larger number of those projections with different directions of **q** makes feasible the reconstruction of the complete three dimensional momentum density $n(\mathbf{p})$ [3], [4].

A most recent review of Compton scattering experiments has been given by Cooper [5]. Till now most of the Compton experiments, that keep a certain standard with respect to statistical accuracy, have been performed by using γ-ray sources and solid state detectors for energy analysis. The limited energy resolution of this technique enables a momentum space resolution not better than 0.45 a. u.

Only the advent of strong sources of Synchrotron radiation in the energy range from 30-50 keV makes feasible crystal dispersive techniques for the energy analysis of the scattered radiation. The better energy resolution of these techniques leads to a momentum space resolution of about 0.1 a. u. together with a statistical accuracy, that might keep the standard of more than 5×10^6 counts in the whole Compton profile for atomic numbers $Z < 20$.

Experiments of this kind have been performed by G. Loupias at LURE [6] (but only with a primary energy of 10 keV), by a group at the Photon Factory in Japan [7], [8], [9] and are in preparation at HASYLAB, Hamburg [10], [11].

A typical set-up of those Compton experiments with Synchrotron radiation is shown in Fig. 1. The white Synchrotron light is monochromatized and focused onto the scattering sample. The energy analysis is performed by means of a Cauchois type analyzer in connection with a position sensitive detector placed at the Rowland circle.

Whereas the Japanese group till now has only reproduced well known Compton profile anisotropies of Si [8], the LURE group has tackeled two real physical problems.

By comparing the measured Compton profiles of Be [12] with a local density-functional calculation done by Chou et al. [13], Loupias et al. found the exchange correlation correction [14] of the local density results of Chou not well represented by the homogeneous electron gas correction as proposed by Rennert [15]. This statement is in agreement with findings of Bauer and Schneider on Cu [16].

The measurement of Compton profiles of graphite and Li-intercalated graphite (LiC_6) [17] has shown that neither the rigid band model for the states of electrons donated by Li nor a nearly free electron behaviour could account for the profile differences between graphite and LiC_6. A more sophisticated band structure calculation of the corresponding Compton profiles [18] could reproduce the profile differences quite well and has related them to the special shape of the LiC_6-Fermi surface.

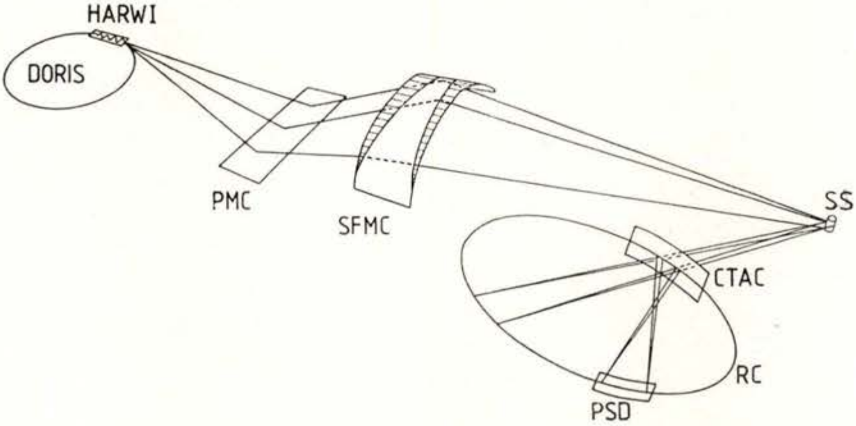

Fig. 1 — Experimental set-up of the Compton spectrometer at the HARWI-beamline of HASYLAB

PMC = plane monochromator crystal
SFMC = sagittal focusing monochromator crystal
SS = scattering sample
CTAC = Cauchois type analyzer crystal
PSD = position sensitive detector
RC = Rowland circle

4 – REGIME OF ELECTRON EXCITATIONS

It was established in sect. 2 that under experimental conditions, where both the transferred energy is comparable with the energy of electron excitations and the reciprocal transferred momentum, $2\pi/q$, is comparable with the mean electron distance, the measurement of the energy distribution of inelastically scattered X-ray photons provides a very detailed picture of correlated motion in the scattering electron system, as given in equ. (5). It is very common in solid state physics to represent the interparticle correlation of an electron system by a response function, Im $\varepsilon^{-1}(\mathbf{q}, \omega)$, rather than in terms of the two-particle density function, where $\varepsilon^{-1}(\mathbf{q}, \omega)$ is the reciprocal dielectric function (if one wants to include local field effects, $\varepsilon^{-1}(\mathbf{q}, \omega)$ has to be replaced by $[\varepsilon^{-1}(\mathbf{q}, \omega)]_{00}$, the 0-0-term of the inverse dielectric matrix [19]).

Rewriting equ. (5) in terms of the dielectric response function, one ends up with

$$S(\mathbf{q},\omega) = (-\hbar\, q^2/4\pi^2 e^2 \rho)\ \mathrm{Im}\ \varepsilon^{-1}(\mathbf{q},\omega) \tag{9}$$

where ρ is the electron density.

If one neglects local field effects $\mathrm{Im}\ \varepsilon^{-1}(\mathbf{q},\omega)$ is simply connected with the dielectric function

$$\varepsilon(\mathbf{q},\omega) \equiv \varepsilon_1(\mathbf{q},\omega) + i\,\varepsilon_2(\mathbf{q},\omega) \tag{10}$$

via

$$\mathrm{Im}\ \varepsilon^{-1}(\mathbf{q},\omega) = -\varepsilon_2(\mathbf{q},\omega)/(\varepsilon_1^2(\mathbf{q}\cdot\omega) + \varepsilon_2^2(\mathbf{q},\omega)) \tag{11}$$

The collective excitations of the system are represented by peaks of the response function $\mathrm{Im}\ \varepsilon^{-1}(\mathbf{q},\omega)$ as due to zeros of $\varepsilon_1(\mathbf{q},\omega)$ at positions of (nearly)-zeros of $\varepsilon_2(\mathbf{q},\omega)$ (plasmon poles).

Within the limits of the random phase approximation $\varepsilon_2(\mathbf{q},\omega)$, the imaginary part of the dielectric function, is directly related to the individual excitations of electrons. Written in terms of a Bloch-type one electron representation of the system, this relation reads as follows:

$$\begin{aligned}\varepsilon_2(\mathbf{q},\omega) = -\frac{4\pi^2 e^2}{q^2} \sum_{\substack{\mathbf{k}',l'\\ \mathbf{k},l}} |\langle \mathbf{k}',l'|\,e^{i\mathbf{q}\cdot\mathbf{r}}\,|\mathbf{k},l\rangle|^2 \\ \times [f_0(\mathbf{k}',l') - f_0(\mathbf{k},l)] \\ \times \delta(\hbar\omega + E(\mathbf{k},l) - E(\mathbf{k}'l')),\end{aligned} \tag{12}$$

where $\mathbf{k}$ is the Bloch wave vector, l the band index, $E(\mathbf{k},l)$ the energy and $f_0(\mathbf{k},l)$ the occupation number of the Bloch state. Thus ε_2 reflects the joint density of states (JDOS) via the δ-function, weighted by the squared matrix element, which connects occupied with nonoccupied one-electron states and can produce symmetry projections of the JDOS.

According to equ. (12) $\varepsilon_2(\mathbf{q},\omega)$ may also describe transitions from core states into unoccupied states above the Fermi level. In this case $\varepsilon_2(\mathbf{q},\omega)$ should exhibit an edge like structure at $\hbar\omega = E_B$, where E_B is the binding energy of the core electrons. Since in this case $\varepsilon_1(\mathbf{q},\omega) \approx 1$, this edge-like structure is also found in $\mathrm{Im}\ \varepsilon^{-1}(\mathbf{q},\omega)$, and because of equ. (9) also in $d^2\sigma/(d\Omega\, d\omega)$. Furthermore, if $q\,a \ll 1$ (a-core-radius) the dipole approximation of the matrix element in equ. (12)

$$\langle \mathbf{k}',l'|\,e^{i\mathbf{q}\cdot\mathbf{r}}\,|\mathbf{k},l\rangle \approx \mathbf{q}\cdot\langle \mathbf{k}',l'|\,\mathbf{r}\,|\mathbf{k},l\rangle \tag{13}$$

is justified, so that the edge structure of $d^2\sigma/(d\Omega\, d\omega)$ should be identical with the edge structure in corresponding X-ray absorption spectra [20]. Then $\mathbf{q}$ in IXSS plays the same role as the electric field vector in absorption spectroscopy.

By utilizing the f-sum rule

$$\int_0^\infty S(\mathbf{q},\omega)\,\omega\, d\omega = \hbar\, q^2/2m \tag{14}$$

one can measure $d^2\sigma/(d\Omega\, d\omega)$ and therewith also $\mathrm{Im}\ \varepsilon^{-1}(\mathbf{q},\omega)$ on an absolute scale, so that also $\varepsilon_1(\mathbf{q},\omega)$ and $\varepsilon_2(\mathbf{q},\omega)$ can be extracted directly from the experimental data by means of Kramers-Kronig-transformation [21]. Thus a very direct comparison between IXSS results and band structure calculations becomes feasible.

When IXSS experiments are performed using conventional X-ray sources, the energy resolution is limited by the natural line width of the characteristic radiation, the statistical accuracy is poor because of the relative low flux compared with

Synchrotron sources and the signal to noise ratio is low due to the contamination of the spectra with bremsstrahlung. A review of the state of art of conventional technique has been given by Platzman [22, 23].

We have started IXSS experiments with Synchrotron radiation at HASYLAB, Hamburg in 1983 by using an experimental set-up [24], which is shown in Fig. 2. An energy resolution of better than 1 eV and signal to noise ratio of better than 300 in the case of Li could be achieved.

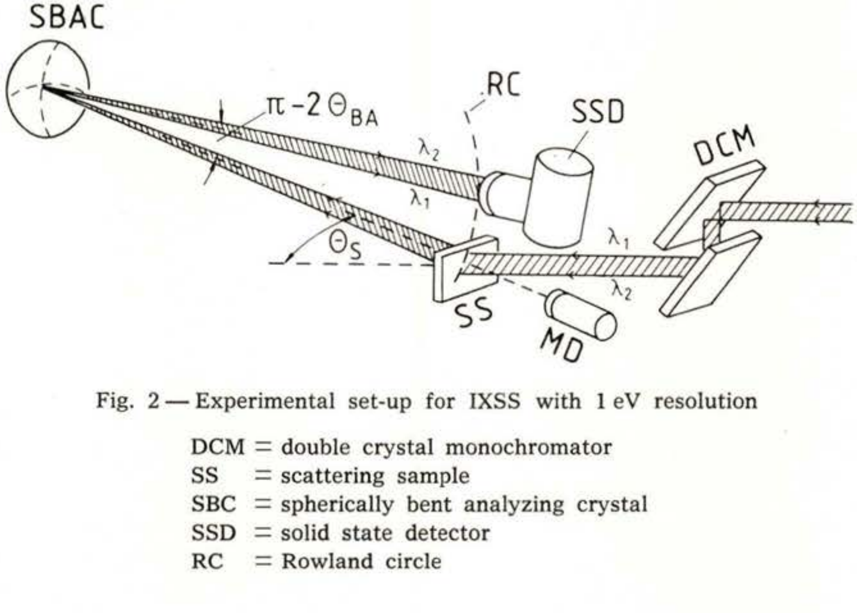

Fig. 2 — Experimental set-up for IXSS with 1 eV resolution

DCM = double crystal monochromator
SS = scattering sample
SBC = spherically bent analyzing crystal
SSD = solid state detector
RC = Rowland circle

The white Synchrotron beam is monochromatized by means of a fixed exit double crystal monochromator. The scattering sample is positioned at the Rowland circle of a spherically bent Si crystal so that the Bragg angle is near $\pi/2$, which guarantees a high energy resolution for the inelastically scattered beam. The constant-**q** spectra (scattered intensity as a function of ω) are obtained in so called inverse geometry, that means by changing the primary energy and by keeping fixed the passband of the analyzer.

Additionally one can choose the Bragg angle of the monochromator such that the energy distribution, which is generated at the sample position along the Rowland circle due to the vertical divergency of the Synchrotron beam, is Bragg reflected simultaneously by the analyzer. As a consequence, the transmitted passband ΔE_t is much larger than the energy width ΔE_r which determines the energy resolution of the experiment, so that the transmitted intensity can be increased by more than a factor 5 without sacrificing resolution (dispersion compensation [25]).

Using this experimental set-up the dynamical structure-factor $S(\mathbf{q}, \omega)$ has been measured on Li [26, 27], Be [28, 29], graphite [21], and Li-intercalated graphite (LiC) [30] for a wide range of q (0.3 a. u. $< q < 2.0$) and including also the core excitation spectra which have been discussed separately [31, 32, 33].

The most important physical conclusion which could be drawn from these measurements can be summarized as follows:

In the intermediate range of q, that is the range of q, where plasmons are no longer well defined elementary excitations ($q > q_c$; q_c = cutoff wave vector), but where q is not large enough to follow only the movement of individual electrons (Compton regime), the dynamic structure factor $S(\mathbf{q}, \omega)$ of electrons in Li and Be is not well represented by the random phase approximation of a homogeneous electron gas. The overall shape of the experimental $S(\mathbf{q}, \omega)$'s could be brought in agreement with calculated ones, if both correlation effects via a static local field correction [34, 35] and lifetime effects in a scheme, first proposed by Rahman and Vignale [36], were taken into account [27, 28, 29].

The dynamic structure factor $S(\mathbf{q}, \omega)$ of Li and especially of Be exhibit a very rich fine structure, which depends strongly on the q-direction. Most of this fine structure could be attributed to excitation gaps due to energy gaps of the excited states across zone boundaries in the extended zone scheme [27, 28, 29] as already proposed by Foo and Hopfield [37] and thoroughly discussed by Sturm and Oliveira [38]. It has been shown [29] that the dispersion of this fine structure can be used to get data about the dispersion of occupied energy bands. In the case of Be [28] the existence of a new collective mode above q_c the so called zone boundary collective state [37], could be clearly demonstrated by additional zeros of $\varepsilon_1(\mathbf{q}, \omega)$, as deduced by Kramers-Kronig transformation. Part of the fine structure of $S(\mathbf{q}, \omega)$ found in Li and Be could not be attributed to excitation gaps on a single zone boundary perpendicular to **q**. Nevertheless, also this part of the fine structure exhibits a certain dependence on q-orientation, at least for Be, so that the following question must be left unsolved: Is the fine structure also present in the homogeneous electron liquid, as first deduced by Platzman and Eisenberger [39], or is it the result of cooperative action of more than one zone boundary, as discussed by the author [29].

The measurements of $S(\mathbf{q}, \omega)$ of graphite, above all those with $\mathbf{q}$ // c-axis, together with the Kramers-Kronig-analysis of the results have provided interesting information about the graphite band structure [21]. The first time $\varepsilon_2(\mathbf{q}, \omega)$ could be derived for $\mathbf{q}$ // c-axis and for a large range of q. By utilizing dipole selection rules and the q-dependence of the transition matrix element of equ. 12, transition from occupied π-states into the so called interlayer states of graphite, as predicted by Posternak et al. [40], could clearly be identified. Thus a very direct access to the interlayer states is opened, which are of large importance for the understanding of intercalation. The measurements of $S(\mathbf{q}, \omega)$ on Li-intercalated graphite (LiC_6) [30] have supported the above statement by showing a 2 eV-shift of the interlayer state with respect to the occupied π- and σ-states upon intercalation.

The measurements of the K-edge structure of Li, Be, graphite and LiC_6 in the $S(\mathbf{q}, \omega)$-spectra for $q \cdot a < 1$ (a = core radius) have revealed a very near resemblance of these spectra with corresponding absorption spectra [31]. Discussing these results it was stressed [32, 33] that the unique possibility, to obtain K-edge spectra of *low*-Z elements using *high* energy X-rays in the 20-50 keV region, could be exploited, whenever these spectra are demanded from samples in special environments, where the application of soft X-rays or electrons is impossible.

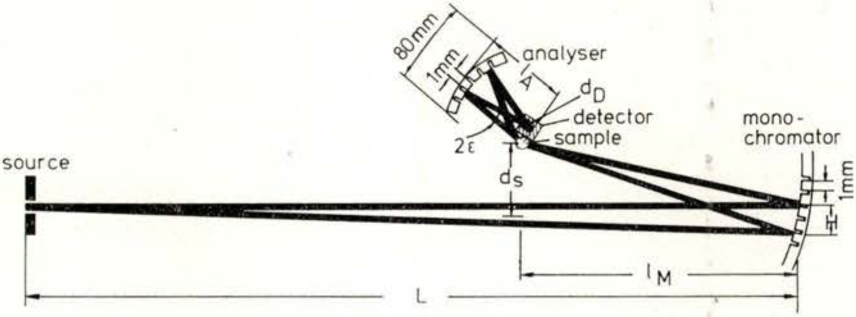

Fig. 3 — Experimental set-up for IXSS with 10 meV resolution [43]

5 – REGIME OF ION EXCITATION

As stated in section 2, also the access to collective ion-excitation (phonons) could be opened by means of inelastic X-ray scattering, provided the energy resolution could reach the meV-range. It has been shown [41] that in this case the dynamic structure factor can be calculated as follows by making use of the adiabatic approximation:

$$S(\mathbf{q},\omega) = \frac{1}{2\pi}\int dt\, \epsilon^{-i\omega t} \times <I|\sum_{ll'} f_{l'}\, e^{-i\mathbf{q}\cdot\mathbf{R}_{l'}(t)}\, f_l\, e^{i\mathbf{q}\cdot\mathbf{R}_l(o)}|I>, \tag{15}$$

where R_l is the position vector of the l-th ion core with form factor f_l and $|I>$ denotes the ground state of the ion system. By analogy with corresponding expressions for inelastic neutron scattering, one will find peaks of $S(\mathbf{q},\omega)$ in constant q-scans for $\mathbf{q} = \mathbf{Q} + \mathbf{g}$ at the phonon energies $\hbar\omega(\mathbf{Q})$, where $\mathbf{Q}$ is the phonon wave vector and $\mathbf{g}$ a reciprocal lattice vector.

Fujii et al. [42] and Dorner and Peisl [43] have first stressed the fact that inelastic X-ray scattering with 10 meV energy resolution should become feasible when using Synchrotron radiation.

The first who have realized this kind of ambitious experiment were Burkel et al. [44] following the proposal of ref. 43 by using an experimental set-up which is sketched in Fig. 3:

White Synchrotron radiation is nearly back-Bragg reflected and focused onto the sample by means of a spherically bent Si crystal, the surface of which has to be facetted in order to prevent elastic strains from bending which would destroy the high energy resolution obtained by a Bragg angle very near to $\pi/2$. The scattered radiation is energy analyzed by means of a spherically bent Si crystal machined in the same manner as the monochromator. The energy analysis is performed by scanning a temperature difference between monochromator and analyzer, so that the difference in the lattice spacing shifts the passband transmitted by the monochromator (inverse geometry).

This set up has stood the test by measuring for the first time a phonon dispersion curve (Be) by inelastic X-ray scattering [45].

The advantage of ultra high resolution IXSS over inelastic neutron scattering is both the decoupling of energy- and momentum transfer with IXSS, so that high excitations connected with small momentum transfer can be investigated, and the possibility to focus the monochromatic beam onto small samples.

6 – COHERENT INELASTIC SCATTERING

As shown in section 3, IXSS in the Compton scattering regime yields information about the momentum density of electrons with equal weight at every position of the crystal unit cell. In the language of quantum mechanics, averaging over position space means that only diagonal elements of the momentum space one-particle density matrix are involved in conventional Compton scattering.

The same is true with IXSS in the regime of electron excitations. It was shown in section 2 that also the information about the two- particle density function $n_2(\mathbf{r}', \mathbf{r}, t)$ is position space averaged with respect to the coordinate $\mathbf{r}'$ of the reference particle. In the language of the theory of dielectric response this means that only information about diagonal elements of the reciprocal dielectric matrix can be obtained by means of conventional IXSS.

But it has been pointed out by the author that for both, the Compton regime [46, 47] and the regime of electron excitation [48], a certain element of position space selectivity can be brought into play by using a standing wave field

$$E(\mathbf{r}) = A e^{i \mathbf{K}_0 \cdot \mathbf{r}} + B e^{i\varphi} e^{i(\mathbf{K}_0 + \mathbf{g}) \cdot \mathbf{r}} \tag{16}$$

as initial photon state of an inelastic scattering experiment, where $\mathbf{K}_0$ is the wave vector of the incident wave.

Such a standing wave field can be produced within the scattering sample by bringing the sample into Bragg-position with respect to one reciprocal lattice vector **g**. As predicted by the dynamical theory of X-ray diffraction [49], the phase factor $\exp(i\varphi)$ in equ. (16) is determined by the exact angular position within the Bragg reflection range, the width of which is of the order of a few seconds of arc.

With a standing wave field as initial photon state the double differential scattering cross section gets an additional interference term and reads as follows

$$\frac{d^2\sigma}{d\Omega\, d\omega} = \left(\frac{d\sigma}{d\Omega}\right)_0 \left\{ S(\mathbf{q}, \omega) + 2\cos\varphi \times \frac{AB}{A^2 + B^2}\, S(\mathbf{q}, \mathbf{g}, \omega) \right\} \tag{17}$$

where

$$S(\mathbf{q}, \mathbf{g}, \omega) = \iiint dt\; e^{-i\omega t}\, n_2(\mathbf{r}', \mathbf{r}, t) \times e^{-i\mathbf{q} \cdot \mathbf{r}}\, e^{-i\mathbf{g} \cdot \mathbf{r}'}\, d\mathbf{r}\, d\mathbf{r}'. \tag{18}$$

This means that the interference term contains information about the **g**-th Fourier component of n_2 with respect to the reference particle coordinate $\mathbf{r}'$, rather than the $\mathbf{r}'$-space average (see equ. (5)).

This additional information can be expressed in terms of nondiagonal elements of the momentum space density matrix $\Gamma(\mathbf{p}+\mathbf{g},\mathbf{p})$ for the Compton scattering regime (impulse approximation),

$$S(\mathbf{q},\mathbf{g},\omega)=\int d\mathbf{p}\;\Gamma(\mathbf{p}+\mathbf{g},\mathbf{p})\times\delta\left(\omega-\frac{\hbar q^2}{2m}-\frac{\mathbf{p}\cdot\mathbf{q}}{m}\right),\qquad(19)$$

proposed $\Gamma(\mathbf{p}+\mathbf{g},\mathbf{p})$ is real and both plane wave components of the standing wave field form the same angle with the scattered wave. (For more details see [50]).

For the regime of electron excitations the additional information of the interference term of equ. (17) can be expressed in terms of nondiagonal elements of the inverse dielectric function $\varepsilon^{-1}(\mathbf{q},\mathbf{q}+\mathbf{g},\omega)$

$$S(\mathbf{q},\mathbf{g},\omega)=-\frac{\hbar\, q^2}{4\pi^2 e^2\rho}\,\mathrm{Im}\;\varepsilon^{-1}(\mathbf{q},\mathbf{q}+\mathbf{g},\omega).\qquad(20)$$

Coherent inelastic scattering experiments in the Compton scattering regime have been performed by using Synchrotron radiation by Golovchenko et al. [51] and by means of conventional X-ray technique by Schülke et al. [47, 52]. Experiments in the regime of electron excitations are underway [53].

In all cases the scattering sample is the second crystal of a non-dispersive double crystal setting. For the Compton measurements the scattered radiation was analysed by a solid state detector, so that the results are poor with respect to momentum space resolution. The coherent scattering experiments in the regime of electron excitations were done using crystal dispersive analysis [53].

7 – MAGNETIC INELASTIC SCATTERING

Since magnetic X-ray scattering is reviewed separately at this conference [54] magnetic inelastic scattering should be mentioned here very briefly.

It was first pointed out by Platzman and Tzoar [55] that one can extract information about magnetic properties of matter from inelastic scattering by making use of the fact that the scattering amplitude M_j is composed of the Thomson scattering amplitude $r_0 A$ (in the sections 1-6 only this part of the scattering amplitude was considered) and a much weaker magnetic scattering amplitude $i\, r_0\, \mathbf{D}\cdot\underline{\sigma}_j$, So that

$$M_j = r_0\,(A + i\,\mathbf{D}\cdot\underline{\sigma}_j),\qquad(21)$$

where $\mathbf{D}$ is a complex expression containing polarization- and wave-vectors of the incident and scattered beam, respectively, and $\underline{\sigma}_j$ is the spin vector of the j-th electron. r_0 is the classical electron radius. Equ. (21) applies to systems where only the interaction of the photons with the spin induced magnetic moment has to be taken into account and where the orbital magnetic moment can be neglected. It is important that A is of order one but $|\mathbf{D}|$ is of order $\hbar\omega_1/mc^2$, where $\hbar\omega_1$ is the primary photon energy. Furthermore, it is decisive for the magnetic scattering experiments that $\mathbf{D}$ is real for linear polarized incident photons but complex for a circularly polarized incident wave.

Writing the double differential cross section in a form analogous to equ. (2):

$$\frac{d^2\sigma}{d\Omega\, d\omega}=\sum_f \left|<f\left|\sum_j M_j\, e^{i\mathbf{q}\cdot\mathbf{r}_j}\right|i>\right|^2\times\;\delta\; E_f-E_i-\hbar\,\omega),\qquad(22)$$

one sees that, besides the Thomson scattering term which is proportional to A^2, the interference term between Thomson and magnetic scattering can be of importance, whereas the squared magnetic scattering amplitude can be neglected, since $\hbar\,\omega_1/mc^2$ is between $10^{-1} - 10^{-2}$.

But this interference term has only real values if **D** is complex, that means, if the incident wave is circularly polarized.

Some experiments with circularly polarized Synchrotron radiation have already been performed, where this interference term is utilized in the Compton scattering regime in order to get information about spin densities in momentum space [56-62].

But it should be mentioned that this kind of experiments could also be rather informative when done in the regime of electron excitation. Including the interference term between Thomson and magnetic scattering one obtains the following expression for the double differential scattering cross section

$$\frac{d^2\sigma}{d\Omega\, d\omega} = r_0^2 A^2 \{S\downarrow(\mathbf{q},\omega) + S\uparrow(\mathbf{q},\omega)\} + 2\,\mathrm{Im}\,(A^* D_z)\,\{S\uparrow(\mathbf{q},\omega) - S\downarrow(\mathbf{q},\omega)\} \tag{23}$$

where ↑ and ↓ means spin up and spin down, respectively. Thus valuable information about electronic excitations of electrons with unpaired spins could be obtained.

Funded by the German Federal Minister of Research and Technology under Contract No. 05 334 AX B2.

REFERENCES

[1] VAN HOVE, L., Phys. Rev. **95**, 249 (1954).

[2] EISENBERGER, P. and P. M. PLATZMAN, Phys. Rev. **A2**, 415 (1970).

[3] MIJNARENDS, P., «Compton scattering», edited by B. Williams, 1977, New York, Mc Graw Hill, pp. 323-345.

[4] HANSEN, N. K., «Reconstruction of the EMD from a set of directional Compton profiles», Hahn-Meitner-Institute, Berlin, Rep. HMI B 342, 1980.

[5] COOPER, M. J., Rep. Prog. Phys. **48**, 415 (1985).

[6] LOUPIAS, G. and J. PETIAU, J. Phys. (Paris) **41**, 265 (1980).

[7] ITOH, F., M. SAKURAI, N. SUZUKI, K. SUZUKI, N. SHIOTANI, N. SAKAI, H. FUJIMAKI, H. KAWATA, Y. AMEMIYA and M. ANDO, Photon Factory Activity Report, 1986, p. 277.

[8] ITOH, F., M. SAKURAI, N. SUZUKI, K. SUZUKI, N. SHIOTANI, N. SAKAI, H. FUJIMAKI, H. KAWATA, Y. AMEMIYA and M. ANDO, Photon Factory Activity Report, 1987, p. 324.

[9] ITOH, F., M. SAKURAI, T. SUGAWA, K. SUZUKI, N. SHIOTANI, N. SAKAI, O. MAO, H. KAWATA, Y. AMEMIYA and M. ANDO (to be published in this Volume of Portugaliae Physica, Poster of Sagamore XI, «High resolution Compton...»).

[10] SCHMITZ, J. R., H. SCHULTE-SCHREPPING and W. SCHÜLKE, HASYLAB Jahresbericht, 1987, p. 355.

[11] SCHMITZ, J. R., H. SCHULTE-SCHREPPING and W. SCHÜLKE (to be published in this Volume of Portugaliae Physica, Poster of Sagamore IX, «The Compton-Spectrometer at the HARWI-beamline...»).

[12] LOUPIAS, G., J. PETIAU, A. ISSOLAK and M. SCHNEIDER, Phys. Stat. Sol. (b) **102**, 79 (1980).

[13] CHOU, M. Y., P. K. LAM and M. L. COHEN, Phys. Rev. **B28**, 1696 (1983).

[14] LAM, L. and P. M. PLATZMAN, Phys. Rev. **B9**, 5122 (1974).

[15] RENNERT, P., Phys. Stat. Sol. (b) **105**, 567 (1981).

[16] BAUER, G. E. W. and J. R. SCHNEIDER, Phys. Rev. **B31**, 681 (1985).

[17] LOUPIAS, G., J. CHOMILIER and D. GUÉRARD, Solid State Commun. **55**, 299 (1985).

[18] CHOU, M. Y., M. L. COHEN and St. G. LOUIE, Phys. Rev. **B33**, 6619 (1986).

[19] WISER, N., Phys. Rev. **129**, 62 (1963).

[20] MIZUNO, Y. and Y. OHMURA, J. Phys. Soc. Japan **22**, 445 (1967).

[21] SCHÜLKE, W., U. BONSE, H. NAGASAWA, A. KAPROLAT and A. BERTHOLD, Phys. Rev. **B38**, 2112 (1988).

[22] PLATZMAN, P. M., «Elementary Excitations in Solids, Molecules and Atoms», edited by J. T. Devrese, A. B. Kunz and T. C. Collins, Plenum Press, London and New York, 1974, p. 31.

[23] PLATZMAN, P. M., Japan. J. Appl. Phys. **17** (Suppl. 17-2), 56 (1978).

[24] SCHÜLKE, W. and H. NAGASAWA, Nucl. Instr. and Meth. **222**, 203 (1984).

[25] SCHÜLKE, W., Nucl. Instr. and Meth. **A246**, 491 (1986).

[26] SCHÜLKE, W., H. NAGASAWA and S. MOURIKIS, Phys. Rev. Lett. **52**, 2065 (1984).

[27] SCHÜLKE, W., H. NAGASAWA, S. MOURIKIS and P. LANZKI, Phys. Rev. **B33**, 6744 (1986).

[28] SCHÜLKE, W., U. BONSE, H. NAGASAWA, S. MOURIKIS and A. KAPROLAT, Phys. Rev. Lett. **59**, 1361 (1987).

[29] SCHÜLKE, W., H. NAGASAWA, S. MOURIKIS and A. KAPROLAT, Phys. Rev. **B40**, 12215 (1989).

[30] SCHÜLKE, W., A. BERTHOLD, A. KAPROLAT and H. J. GÜNTHERODT, Phys. Rev. Lett. **60**, 2217 (1988).

[31] NAGASAWA, H., S. MOURIKIS and W. SCHÜLKE, J. Phys. Soc. Jpn. **58**, 710 (1989).

[32] SCHÜLKE, W. and H. NAGASAWA, Acta Cryst. **A43**, C262 (1987).

[33] SCHÜLKE, W., «Proceedings of the Workshop on Applications of High Energy X-Ray Scattering at the ESRF», edited by A. K. Freund, ESRF, 1988, p. 208.

[34] HUBBARD, J., Proc. R. Soc. London, Ser. **A243**, 336 (1957).

[35] ICHIMARU, S. and K. UTSUMI, Phys. Rev. **B24**, 7385 (1981).

[36] RAHMAN, S. and G. VIGNALE, Phys. Rev. **B30**, 6951 (1984).

[37] FOO, E.-NI and J. J. HOPFIELD, Phys. Rev. **173**, 635 (1968).

[38] STURM, K. and L. E. OLIVEIRA, Phys. Rev. **B30**, 4351 (1984).

[39] PLATZMAN, P. M. and P. EISENBERGER, Phys. Rev. Lett. **33**, 152 (1974).

[40] POSTERNAK, M. A. BALDERESCHI, A. J. FREEMAN, E. WIMMER and M. WEINERT, Phys. Rev. Lett. **50**, 761 (1983).

[41] SCHÜLKE, W., «Handbook of Synchrotron Radiation», Vol. 3, edited by D. Moncton and G. Brown, North-Holland, Amsterdam, in preparation.

[42] FUJII, Y., J. B. HASTINGS, S. C. ULC, and D. E. MONCTON, SSRL Activity Report, 1982, p. VIII-95.

[43] DORNER, B. and J. PEISL, Nucl. Instr. Meth. **208**, 587 (1983).

[44] BURKEL, E., J. PEISL and B. DORNER, Europhys. Lett. **3**, 957 (1987).

[45] DORNER, B., E. BURKEL, TH. ILLINI and J. PEISL, Z. Phys. **B69**, 179 (1987).

[46] SCHÜLKE, W., Phys. Lett. **A83a**, 451 (1981).

[47] SCHÜLKE, W. and S. MOURIKIS, Acta Cryst. **A42**, 86 (1986).

[48] SCHÜLKE, W., Solid State Commun. **43**, 863 (1982).

[49] LAUE, M. VON, «Röntgenstrahl-Interferenzen», Frankfurt/Main, Akademische Verlagsgesellschaft, 1960.

[50] SCHÜLKE, W. (to be published in this Volume of Portugaliae Physica, lecture at Pre-Sagamore Workshop.
«Experimental Methods to Obtain Nondiagonal...».

[51] GOLOVCHENKO, J. A., D. R. KAPLAN, B. KINCAID, R. LEVESQUE, A. MEIXNER, M. P. ROBBINS and J. FELSTEINER, Phys. Rev. Lett. **46**, 1454 (1981).

[52] SCHÜLKE, W., U. BONSE and S. MOURIKIS, Phys. Rev Lett. **47**, 1209 (1981).

[53] KAPROLAT, A. and W. SCHÜLKE, HASYLAB-Jahresbericht 1987, p. 151.

[54] COOPER, M. J. (to be published in this Volume of Portugaliae Physica, Lecture at Sagamore IX, «Magnetic X-ray scattering»).

[55] PLATZMAN, P. M. and N. TZOAR, Phys. Rev. **B2**, 3556 (1970).

[56] HOLT, R. S., D. LAUNDY, D. A. CARDWELL, M. J. COOPER, T. NAYLOR, S. MANNINEN and P. HATTON, Nucl, Instr. Meth. **A243**, 608 (1986).

[57] COOPER, M. J., D. LAUNDY, D. A. CARDWELL, D. N. TIMMS, R. S. HOLT *and* G. CLARK, Phys. Rev. **B34**, 5984 (1986).

[58] GOLOVCHENKO, J. A., B. M. KINCAID, R. A. LEVESQUE, A. E. MEIXNER and D. R. KAPLAN, Phys. Rev. Lett. **57**, 202 (1986).

[59] MILLS, D. N., Phys. Rev. **B36**, 6178 (1987).

[60] MILLS, D. N., Nucl. Instr. Meth., **A266**, 531 (1988).

[61] SAKAI, N., N. SHIOTANI, M. ITOH, F. ITOH, M. SAKURAI, T. SUGAWA, H. KAWATA, Y. AMEMIYA and M. ANDO, Portgal. Phys. **19** (1988), in press.

[62] COLLINS, S. P., D. N. TIMMS, M. J. COOPER, A. BRAHMIA, P. P. KANE, R. S. HOLT and D. LAUNDY (to be published in this Volume of Portugaliae Physica, Poster of Sagamore IX «The Directional Magnetic Compton Profiles of Iron»).

CHARGE DISTRIBUTION, INTERMOLECULAR POTENTIALS AND COMPUTER SIMULATION IN AQUEOUS INORGANIC SYSTEMS

KERSTI HERMANSSON

Department of Chemistry
Uppsala University
Box 531
S-751 21 Uppsala, Sweden

ABSTRACT — An overview of computer simulation methods is given. Simple potentials commonly used in computer modelling of aqueous systems are exemplified, and improvements to the intermolecular pair potentials are discussed in terms of a more detailed description of the charge distribution and the inclusion of non-additive effects.

1 – INTRODUCTION

Since the introduction in 1953 of the Monte Carlo (MC) method by Metropolis et al [1] for a system of hard-sphere particles, and the pioneering Molecular Dynamics (MD) work of Alder and Wainwright in 1957 [2], also on a fluid of hard spheres, the number and variety of systems attacked by computer simulation have increased tremendously. Computer simulation techniques have become invaluable tools in the interpretation of experimental studies of condensed matter and in the prediction of new results. The structure and dynamics of liquid water, solvation of biomolecules, protein folding, the structure of interfaces, crystal growth, melting and phase transitions are just a few examples of the diversity of the method. When experimental data is not available, computer simulation techniques can be used to provide such data, and are therefore also referred to as «computer experiments». (A more fundamental aspect of computer simulations is the application to very simple fluid systems, where they can serve as a check against analytical theories and elucidate basic principles of physics).

The core of a simulation study is the potential model, which represents the interactions in the many-body system. For *long range* interactions, it may be adequate to set the interaction between neutral molecules to zero or treat an ion as a point charge, while at *short range* it is essential to account for the electron distributions of the interacting molecules in a more elaborate way, with repulsive electron overlap and polarization of the electron clouds appropriately reflected in the model. Fig. 1 shows the calculated *re*distribution of the electron density due to the *inter*molecular interaction in a water dimer. There is a complicated electron rearrangement involving a polarization of both molecules. A third molecule approaching would interact with this polarized dimer, rather than with two unperturbed water molecules. If the purpose is to model a «real» system, the potential model has to reproduce not only the dimer interaction energies, but ideally also account for the fact that «all» molecules interact simultaneously with one another. It is evident that there is a close connection between computer simulations and electron densities *via* the interatomic potentials, i. e.

$$\begin{array}{c}\text{electron distributions}\\ \upharpoonleft\!\downharpoonright\\ \text{interatomic potentials}\\ \upharpoonleft\!\downharpoonright\\ \text{computer simulation}\end{array}\qquad(1)$$

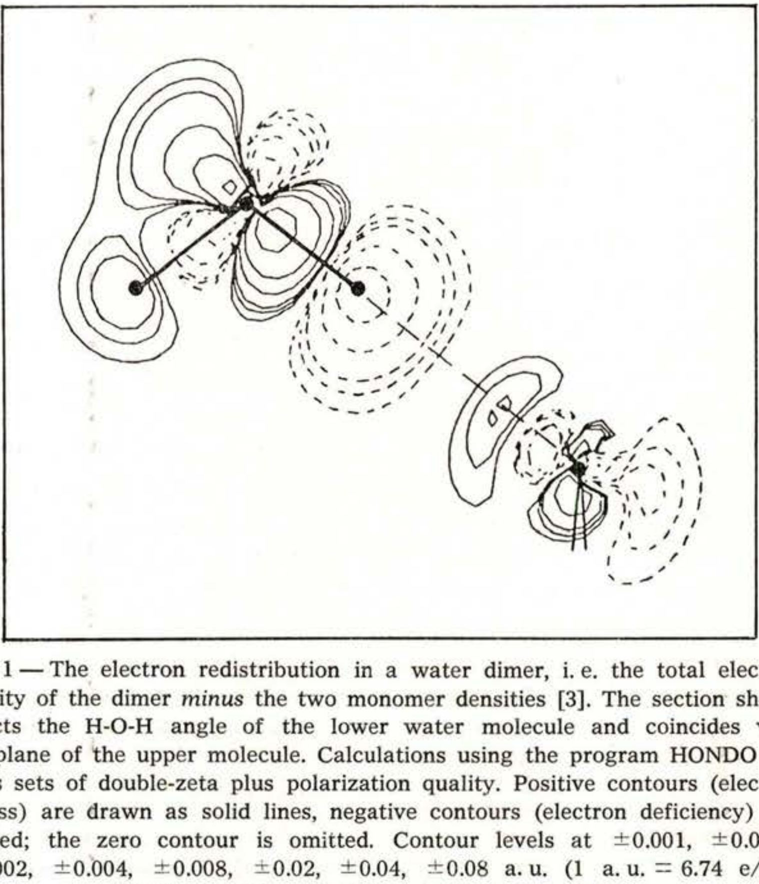

Fig. 1 — The electron redistribution in a water dimer, i. e. the total electron density of the dimer *minus* the two monomer densities [3]. The section shown bisects the H-O-H angle of the lower water molecule and coincides with the plane of the upper molecule. Calculations using the program HONDO [4], basis sets of double-zeta plus polarization quality. Positive contours (electron excess) are drawn as solid lines, negative contours (electron deficiency) are dashed; the zero contour is omitted. Contour levels at ±0.001, ±0.0015, ±0.002, ±0.004, ±0.008, ±0.02, ±0.04, ±0.08 a. u. (1 a. u. $= 6.74$ e/Å^3) (Reproduced by permission of *J. Chem. Phys.*).

Although under continued development, the potential functions currently used in computer simulations, are — for economic reasons — very simple in form.

By means of a few examples, this brief review will illustrate the connection between features of the potential functions used in a simulation and the resulting system properties calculated. This is presented for pure water in Section 3 and for ionic aqueous systems in Section 4. Crystallographers and quantum chemists, with their clear understanding of electron distributions in molecules, could help stimulate the development of more adequate schemes for parameterizing the electron density and assist in devising new potentials for computer modelling. Some examples of existing approaches along these lines are given in Section 5. In Section 2, the basics of computer simulation techniques are discussed.

Many excellent reviews exist for these various areas. Refs. [5-8] are electron density reviews, Refs. [9-10] deal with intermolecular potentials, Ref. [11] with Molecular Mechanics and Refs. [12-18] with MC and MD techniques.

2 – COMPUTER SIMULATION TECHNIQUES

Energy minimization methods, also called *static modelling* or *Molecular Mechanics*, constitute a computational approach with a wide range of applications. The static simulation method with special emphasis on solid state applications has been described by Busing and Matsui [19]. In short, when the forms for the intra- and/or intermolecular potentials have been assumed, the equilibrium structure can be found by adjusting the structural variables so as to minimize the total system energy. Among others, the computer programs MM2 [20], AMBER [21], ECEPP [22] and WMIN [23] (the latter particularly adapted to crystal structures with long-range polar interactions) are being widely used for this purpose.

In statistical mechanics, all physical properties are given as ensemble averages. If the system studied can be described classically, the equilibrium value of some quantity F, is then

$$< F > = \frac{\int F \cdot \exp(-U/kT)\ d\mathbf{r}^N}{\int \exp(-U/kT)\ d\mathbf{r}^N} \qquad (2)$$

where U is the potential energy. For a system of rigid molecules, U is a function of all the molecular positions, $\{\mathbf{r}_I\}$, and orientations, $\{\underset{\sim}{\Omega}_I\}$; i. e. $U = U(\mathbf{r}_1, \underset{\sim}{\Omega}_1; \mathbf{r}_2, \underset{\sim}{\Omega}_2; \ldots; \mathbf{r}_N, \underset{\sim}{\Omega}_N)$. The *Monte Carlo method* is a simple numerical scheme for solving multidimensional integrals, where the integral in (2) would be written as a *sum* over randomly chosen configurations, each contribution to F weighted with the Boltzmann factor. For computer simulations, this 'naive' MC approach is not applicable since, due to large low-density (high-energy) regions in phase space, the convergence would be slow. Instead, in the procedure devised by Metropolis et al. [1], the configurations are already selected with a probability proportional to the Boltzmann factor. They are then weighted evenly in the summation, and $< F >$ is calculated as

$$< F > = \lim_{M \to \infty} 1/M \ \Sigma\ F(\mathbf{r}_1, \underset{\sim}{\Omega}_1; \mathbf{r}_2, \underset{\sim}{\Omega}_2; \ldots; \mathbf{r}_N, \underset{\sim}{\Omega}_N) \qquad (3)$$

where M is the number of MC configurations.

In an MC simulation one is forced to fix certain thermodynamic variables, such as number of particles, system volume, temperature or pressure. The most common choice is that the first three of these are fixed, and the equilibrium quantities calculated in the simulation correspond to those of an NVT (or canonical) ensemble.

In the *Molecular Dynamics* method, one follows the classical trajectories of all members of a collection of N molecules ($N \sim 100$-1000, as in MC simulations) by solving numerically the 3N coupled Newtonian differential equations for translational motion and, for rigid non-linear molecules, 3N coupled Eulerian equations of motion. The time-step is typically of the order of 1 fs. The result is a specific trajectory of this many-body system in phase space. MD simulations are most often carried out under conditions corresponding to the microcanonical ensemble of statistical mechanics, i. e. the total energy E, number of particles N and the volume V are fixed. By the ergodic theorem, the evaluation of average mechanical properties of the system (such as energy, pressure and fluctuation properties) from the trajectory in phase space is equivalent to sampling from a statistical ensemble weighted by the many-body Boltzmann probability distribution. The MD method also permits study of time-dependent properties of individual molecules and of the collective behaviour of the system. CHARMM [24], GROMOS [25] and McMoldyn [26] are examples of MD programs that are being applied widely.

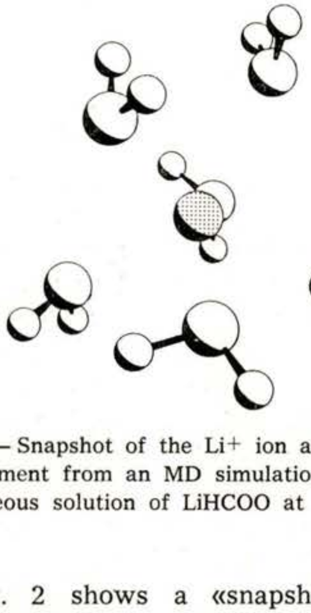

Fig. 2 — Snapshot of the Li+ ion and its nearest environment from an MD simulation of a 0.43 M aqueous solution of LiHCOO at 300K [27].

Fig. 2 shows a «snapshot» of the nearest environment around a lithium ion in a 20 ps MD simulation of a 0.43 M aqueous solution of LiHCOO [27] at 300 K. It should be borne in mind that the significance of one such snapshot is small. Only when averages are taken over many molecules and many time-steps (or configurations in MC) do the results become meaningful. Fig. 3 shows the atom-atom *radial distribution functions*, g(*r*), for the Li-OW and Li-HW distances in this LiHCOO (aq) system. g(*r*) gives the probability density of finding a pair of atoms a distance *r* apart, relative to the probability expected for a completely random distribution at the same density. In a liquid, the particles are uncorrelated for large intermolecular distances, and $g(r) \rightarrow 1$ as $r \rightarrow \infty$.

The *coordination number*, or hydration number, for the Li^+ ion in Fig. 2 is defined as

$$n_{Li^+}(r) = 4\pi\rho_{OW} \int_0^{\text{cut-off}} r^2 g_{Li\text{-}OW}(r)\,dr \tag{4}$$

where ρ_{OW} is the number density of water oxygen atoms. The *n*(*r*) curve for the Li-OW g(*r*) curve in Fig. 3 shows a well pronounced plateau, corresponding to a hydration number of 6, for cut-off values between 2.6 and 3.3 Å, e. g. for a cut-off close to the first minimum in the g(*r*) curve.

Many experimental methods probe *time correlation functions*, which are related to some property of the individual molecules or to a collective property of the system as a whole, such as density fluctuations. Both kinds can be studied by the MD technique. For example, the average motion of individual molecules is readily studied in terms of the translational *velocity autocorrelation function*, which is defined as

$$\phi(t) = <\mathbf{v}(0) \cdot \mathbf{v}(t)>/<\mathbf{v}(0)^2> \quad (5)$$

where $\mathbf{v}$ is the center-of-mass velocity of a given molecule at time t and the averages are taken over time origins and molecules. The molecular *mean-square displacement* and *self-diffusion coefficient* are also readily calculated. The fourier transform of (5) yields the *power spectrum* of the frequencies of the motions of the system particles and is closely related to the experimental IR and Raman spectra.

Approximations

In simulations, one is usually interested in modelling a physical system of macroscopic size, i. e. for ~10^{23} particles, for a long time and with realistic potentials which take the mutual interaction between all N particles into account. Unfortunately, due to computer (and human!) time limitations, various approximations and restrictions have to be introduced. Some of the more important are listed below (only *a* and *b* are directly concerned with the interplay between electron distribution and computer simulation, i. e. the topic of this review, while *d*, in particular, is more concerned with limitations within the

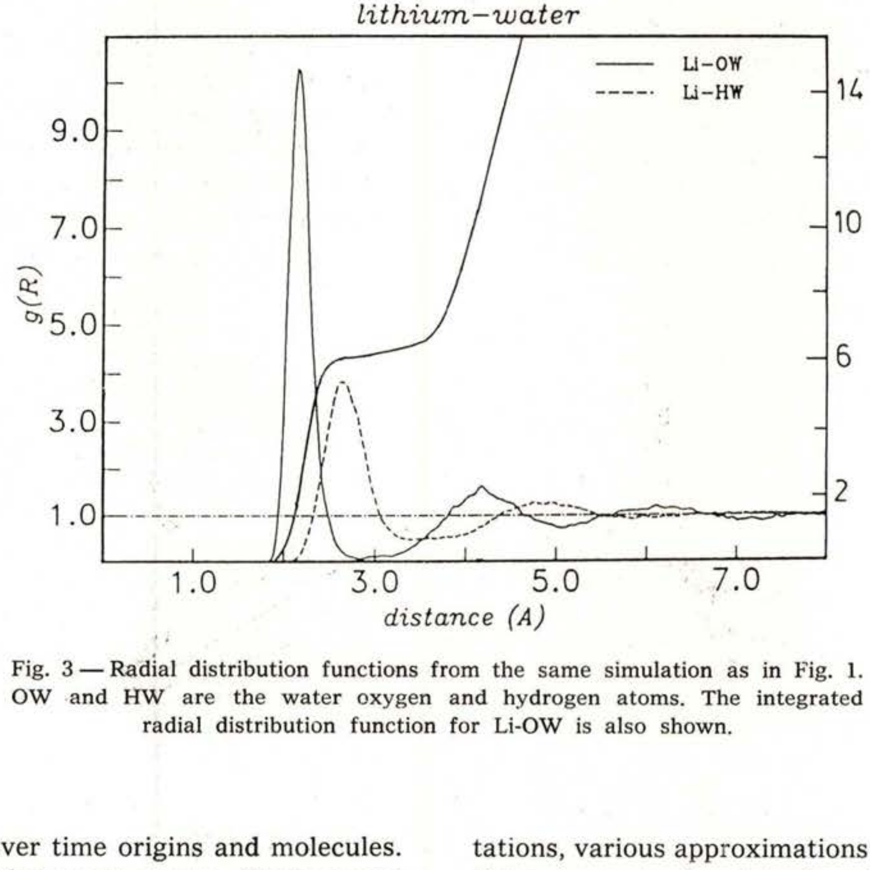

Fig. 3 — Radial distribution functions from the same simulation as in Fig. 1. OW and HW are the water oxygen and hydrogen atoms. The integrated radial distribution function for Li-OW is also shown.

simulation procedures themselves). In the following discussion, the system particles will usually be referred to as molecules.

a) *Pair-wise additive potentials*

As stressed above, the interaction energy for a system is a complicated function of the molecular positions and orientations. Most commonly, the particles are assumed to interact via pair-wise additive potentials, i. e. the total potential energy is approximated by a sum over all different *pairs* of particles:

$$U(\mathbf{r}_1, \underset{\sim}{\Omega}_1; \mathbf{r}_2, \underset{\sim}{\Omega}_2; \ldots; \mathbf{r}_N, \underset{\sim}{\Omega}_N) = \\ = \sum_{I} \sum_{J>I} U(\mathbf{r}_I, \underset{\sim}{\Omega}_I; \mathbf{r}_J, \underset{\sim}{\Omega}_J) \qquad (6)$$

The pair potentials can be either (*i*) *true pair potentials*, i. e. derived from quantum-mechanical calculations on isolated dimers, or (*ii*) *effective pair potentials* with non-additive terms included in an average way. All effective pair potentials are based, in one way or another, on empirical data for their parameterization.

b) *Functional form*

Whether true or effective pair potentials are being used, it is necessary for each dimer interaction to have a simple functional form (there are $O(N^2)$ interactions to be evaluated for each time-step or configuration!). Most commonly, the molecule-molecule pair interaction is expressed

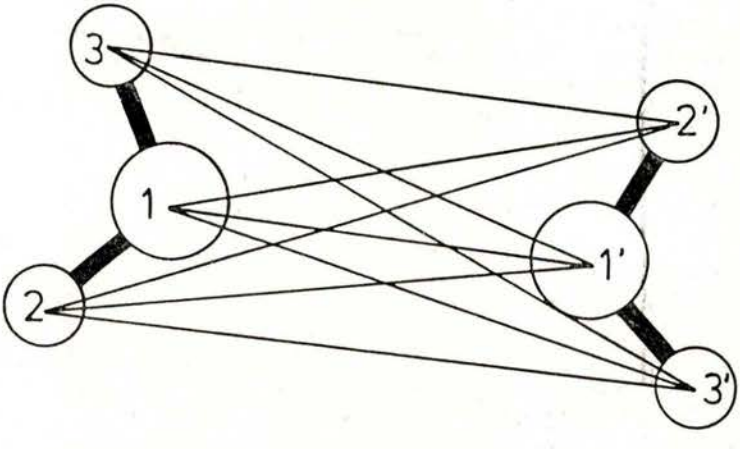

$$U(H_2O-H_2O) = \sum_{\substack{\text{sites i on} \\ \text{molecule} \\ \text{I}}} \; \sum_{\substack{\text{sites j on} \\ \text{molecule} \\ \text{J}}} u_{ij}(r_{ij})$$

$$\text{where } u_{ij}(r_{ij}) = \frac{q_i q_j}{r_{ij}} - \frac{A}{r_{ij}^{6}} + \frac{B}{r_{ij}^{12}}$$

Fig. 4 — Schematic picture of a typical pair-additive potential for a dimer.

as a sum (again) of interactions between a small number of sites on each molecule; each interaction being a function of site-site distance only. The interaction sites are often, but not always, centered on the nuclei in the real molecule, so as to represent some basic features of the molecular shape. An example is given in Fig. 4, which shows a «typical» pair potential for water.

In the case of true pair potentials, the potential is usually derived by fitting a set of analytical functions to quantum-mechanical energies calculated for a large number of geometric configurations. If the charges are also being fitted, caution should be exercised in attaching a physical significance to the values obtained. In the case of effective pair potentials, the functional form is usually selected to contain an electrostatic part, an attractive term for the London-dispersion forces and a short-range repulsive part for the electron overlap. A «standard» form for the latter two is the Lennard-Jones type potential, i. e.

$$u_{ij}(r_{ij}) = 4\varepsilon_{ij}\left[\left(\frac{\sigma}{r_{ij}}\right)^{12} - \left(\frac{\sigma}{r_{ij}}\right)^{6}\right] \quad (7)$$

(or an exponential analogue for the r-12 term), where ε_{ij} and σ_{ij} represent the well-depth and the zero energy intercept, respectively.

The *intra*molecular potential functions commonly employed in static and dynamic modelling of non-rigid large molecules (e. g. proteins) are quite different in form, consisting of sums of terms for bond stretching, angle bending, torsional angles, non-bonded van der Waals contacts, etc.

c) *Molecular rigidity*

The majority of simulations performed for small non-biological molecules treat the molecules as rigid. Flexible molecules have been modelled as collections of atoms interacting with the other atoms in the same molecule via an intramolecular potential (central force models) [28, 29]. Here, there are only translational equations of motion to solve for each atom in the system. Performing an MD simulation using such a model is very time-consuming, however, since the time-step used has to be selected considerably shorter than when only slower rigid-body motions are present. Other methods based on constraint dynamics [30] have been used especially for long-chain organic molecules to fix certain bond lengths and angles

d) *System size, simulation time*

A typical simulation system of small molecules consists of 100-1000 particles. In order to make such a small system «quasi-infinite» and avoid disturbing boundary effects, *periodic boundary conditions* are usually introduced, meaning that the system is surrounded in all three dimensions by identical images, related to the original «central simulation box» by translations. If a molecule leaves the central box through one face, it automatically reappears at the opposite face. This is illustrated in two dimensions in Fig. 5.

The limited time span of an MD simulation (typically of the order of 10 to 100 ps) puts a severe restriction on the type of dynamical phenomenon possible to study by MD. The time span (or, for

MC, the number of configurations) naturally also affects the statistical error in the macroscopic quantities calculated.

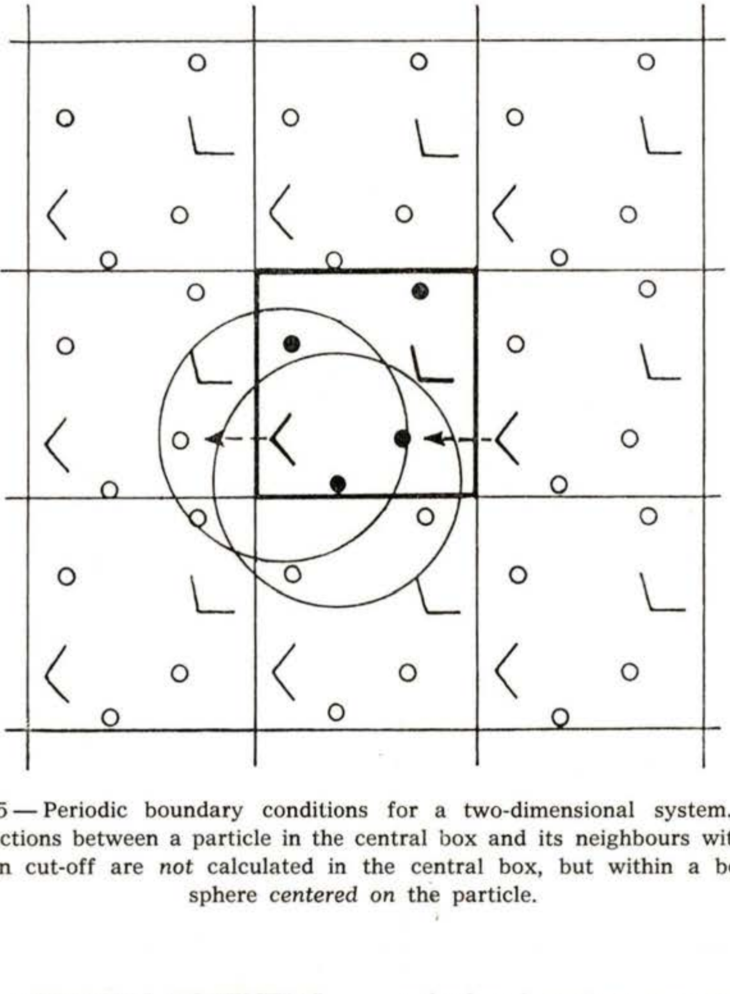

Fig. 5 — Periodic boundary conditions for a two-dimensional system. The interactions between a particle in the central box and its neighbours within a certain cut-off are *not* calculated in the central box, but within a box or sphere *centered on* the particle.

3 – RELATIONS BETWEEN POTENTIAL MODEL AND SIMULATED PROPERTIES IN PURE WATER

Using the water dimer as an example, this section is devoted to the interplay between potential model and the calculated properties of the condensed bulk water system. First, the characteristics of some well-known water dimer potentials are summarized. Their application to computer simulation studies of liquid water is then discussed. As will be seen, the resulting calculated system properties are affected by the limitations inherent in the pair potentials employed, most notably (as discussed in Section 2): *a*) total neglect or inappropriate treatment of many-molecule interactions, and *b*) a description of the continuous charge distribution in terms of a small set of discrete point charges with a superposed repulsive function for the short-range electron overlap. The first approximation will be discussed in some detail here. Examples will be given of quantum-mechanical studies of these effects, and of computer simulations which involve many-body forces, and potential models which explicitly take polarization into account. Improvements to the second approximation are discussed in Section 5.

The water dimer potential

Finney, Quinn and Baum [31] have made an extensive and excellent review of various aspects of the potential surface for the water dimer.

The number of existing water-water potentials is large. The models are often referred to by cryptic, but well established, abbreviations, e. g. BNS [32], ST2 [33], EPEN/2 [34], MCY [35], CF [28], TIP4P [36], PE [37], SPC [38], etc. Among the ones listed here, only the MCY potential of Matsouka, Clementi and Yoshimine is a pure dimer potential, derived from fitting analytical functions to CI energies calculated for many different dimer geometries. The other models should be classified rather as effective pair potentials. The number of point charges in each H_2O

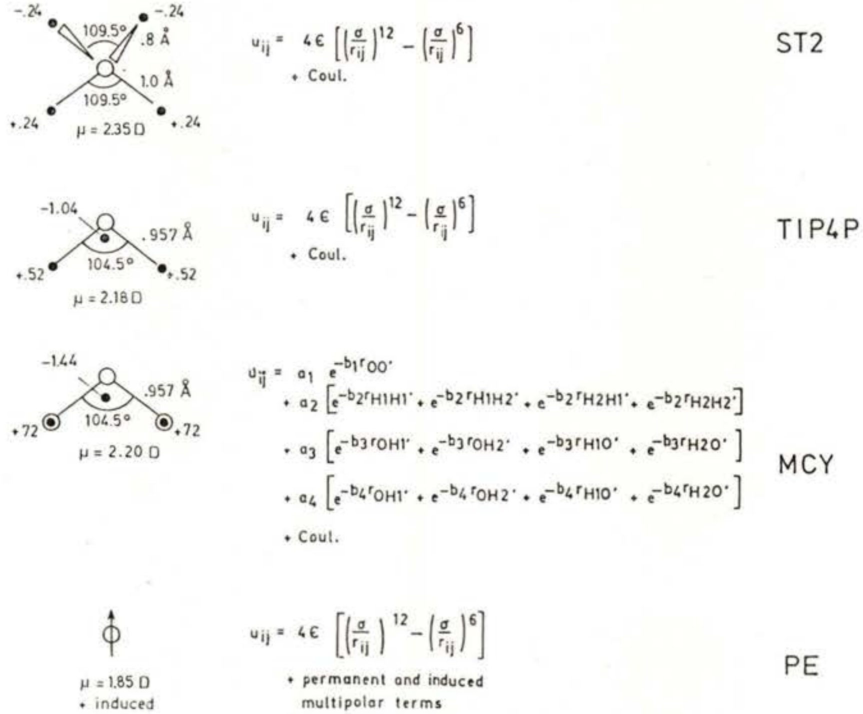

Fig. 6 — Schematic picture of the features of some water-water potentials. The charged sites are represented by dots, and the non-Coulombic sites by a circle.

molecule varies between 3 and 7 for the eight models above, and the number of non-Coulombic interaction sites between 1 and 3. The central force model (CF) describes flexible water molecules, while the others are rigid. A few of these potentials are shown in Fig. 6. Note that the Lennard-Jones parameters, σ and ε, are different in the different models. The TIP4P potential is perhaps the best water-water potential within the series of TIPS (Transferable Intermolecular Potential Functions) designed by Jorgensen et al. to give simple, effective pair potentials for fluid simulations. The PE (Polarizable Electropole) model will be discussed further below.

TABLE 1 — Some equilibrium dimer properties of different water models. r is the O...O distance. θ is defined for the $H_2O(1)$-$H_2O(3)$ pair in Fig. 9, i. e. it is the angle between the bisector of the H-bond accepting water molecule and the O...O direction. References in the text. (The experimental values are taken from Ref. [39]).

Model	ΔE (kJ/mol)	r (Å)	θ (°)
BNS	28.8	2.76	55
ST2	28.6	2.85	52
MCY	24.6	2.87	37
CF	28.0	2.87	61
TIP4P	26.1	2.75	46
PE	20.9	3.00	52
SPC	27.6	2.76	27
Experiment	22.6(± 8)	2.98	59

Table 1 is a list of some equilibrium dimer properties of different water models. For some of these models, the potential energy curves have been plotted in the review by Finney et al. [31], and discussed in detail there.

Singh and Kollmann [40] have taken an interesting approach in constructing a dimer potential based on the Morokuma energy component analysis. Each of the dispersion, polarization, charge transfer and excharge repulsion + mixing + electrostatic energy terms was fitted to an analytical expression. The resulting functional form is unfortunately quite elaborate.

Liquid water and ice

Reviews by Reimers et al. [39], Jorgensen et al. [36], and Beveridge et al. [41], as well as that of Finney et al. [31], compare several models used in MC and MD simulations of pure water with respect to various system properties. I will focus here on the radial distribution function as an example.

Liquid water has an experimental oxygen-oxygen pair correlation function that is qualitatively different form inert gas liquids and shows a distinct second peak at relatively short r values due to hydrogen bonding [42] (Fig. 7). Simulation using different theoretical models, however, gives $g(r)$ curves of varied appearance. Some examples are given in Fig. 7. Finney et al. [31] have compared various models with respect to this curve. The *form* of the computed curve is found to be generally correct for most of the effective pair potentials, although «the *relative heights* of the first two peaks are in significant disagreement with experiment». Except for the ST2 and CF models, all first peak maxima occur at slightly too low an r value. Some of the models give too low a first minimum, indicating that the first-neighbour shell is here too orientationally structured. All models, except

ST2, underestimate the depth of the second minimum, indicating that longer-range correlations are inadequately accounted for. Finney et al. also discuss in detail the g(*r*) curves arising from different quantum-mechanical potentials, both from SCF and CI calculations. In particular, two different parameterizations based on the same CI points, the MCY potential [35] and the Bounds potential [45], are compared in detail, the first giving a water-like g(r) (Fig. 7), the second a much less structured curve. Finney et al. conclude that «the computed structure is *highly* sensitive to *details* in the potential function».

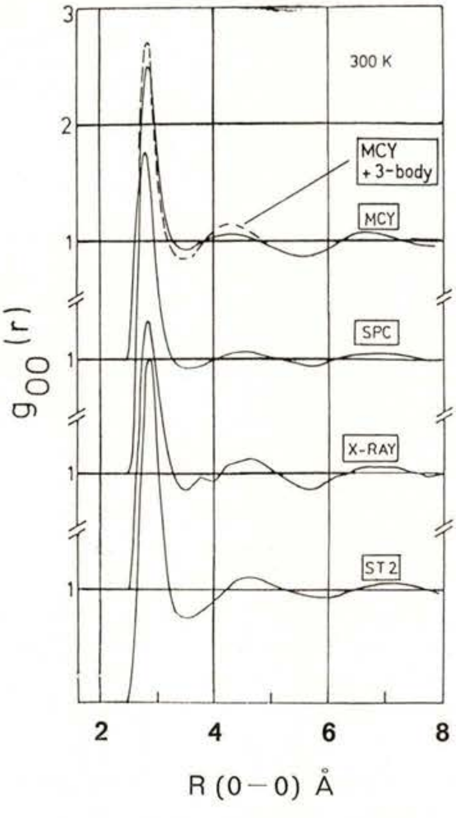

Fig. 7 — O-O radial distribution functions from experiment [42] and simulation. Redrawn from Postma [43] with permission from the author. The «MCY + 3-body» curve is redrawn from Ref. [44] by permission of *J. Chem. Phys.*

Morse and Rice [46] compared several 2-body water pair potentials (BNS, ST2, MCY and others) and examined their ability to reproduce the structures and properties of different proton-ordered ices. They conclude that, despite leading to an underestimate of all the ice densities by ~20 %, the MCY potential succeeds the best in reproducing the experimental hydrogen-bond schemes and the O ... O angles. Several simulation studies on small ice crystallites and on bulk ice can be found in Ref. [47].

Many-body interactions

The effective water potentials, designed for use in many-particle systems such as liquid water or aqueous solutions, include many-particle interactions (= «*many-body effects*» = *non-additivity effects*) only in an average manner. Quantum-mechanical calculations have proven to be a useful tool for the evaluation of the magnitudes of many-body effects in small water clusters.

Following Hankins, Moskowitz and Stillinger [48], the 3-body contribution to the interaction energy of a molecular triplet (ijk) is defined as the difference between the total interaction energy and the sum of the pair interaction energies, i. e.

$$\Delta^3 E\,(ijk) = \Delta E\,(ijk) - [\Delta E\,(ij) + \Delta E\,(ik) + \Delta E\,(jk)] \qquad (8)$$

where

$$\Delta E\,(ij) = E\,(ij) - [E\,(i) + E\,(j)] \qquad (9)$$

and

$$\Delta E\,(ijk) = E\,(ijk) - [E\,(i) + E\,(j) + E\,(k)] \qquad (10)$$

The non-additive energy components for two different water triplets have been calculated according to (8)-(10), using the program HONDO [4] and basis sets of double-zeta plus polarization quality. These are shown in Fig. 8. All oxygen-oxygen distances were set to 2.90 Å. The 3-body contribution to the complex in *a*, i. e. $\Delta^3E/\Delta E$, is 3 %, while it is 16 % in *b*. Several other *ab initio* studies on water triplets (see, for example, Refs. [49-51]) have shown the 3-body energy to be up to 15 % of the total interaction energy for certain triplets.

Many-body contributions to the energies, forces, electron densities, dipole moments and Mulliken charges for a water molecule bound in a tetrahedral environment have been calculated by *ab initio* SCF methods for an $(H_2O)_5$ complex (and two $\oplus_2 \ominus_2 \cdot H_2O$ complexes) by Hermansson [3]. The definition of 2- and 3-body contributions to the deformation density is completely analogous to equations (8)-(10) above. Non-additive effects in the *energies*, can to a large extent, be explained on the basis of the *electron redistribution* for the *pair* interactions (cf. Fig. 1), while non-additive effects in the electron rearrangement were found to be small. 4- and 5-body corrections to all the pentamer properties calculated were found to be small. This is illustrated in Fig. 9.

Model calculations of the type discussed here, performed for small clusters or crystal-like fragments, constitute a helpful tool for evaluating the importance of many-body effects on different properties. Their final effect on thermodynamic quantities, and on overall structural and dynamic properties in a real many-body system should be evaluated by computer simulation techniques, however.

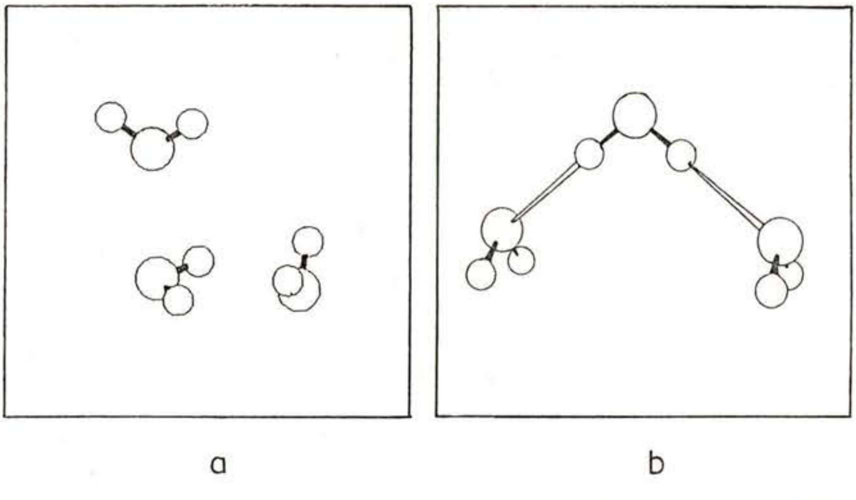

Fig. 8 — Two water triplets discussed in the text. All O-O distances are 2.90 Å.

Clementi and coworkers improved their 2-body quantum-mechanical potential by introducing 3-body corrections. Starting from the MCY pair potential, Clementi and

Corungiu [52] have first calculated the 3-body corrections for a large number of triplets in different geometrical arrangements; then made a fit to a proposed analytical form, and finally applied this new potential in MC (Detrich, Corungiu and Clementi [53]) and MD (Wojcik and Clementi [54]) simulations of liquid water. The resulting g(*r*) curve from the MD simulation is shown in Fig. 7. Briefly, the addition of 3-body effects makes the liquid more structured and agreement with experiment has improved. Other properties calculated with the 3-body potential, such as the internal energy and the decay of the orientational correlation functions, also agree better with experiment, while for some others, e. g. the self-diffusion coefficient, the agreement is worse [54].

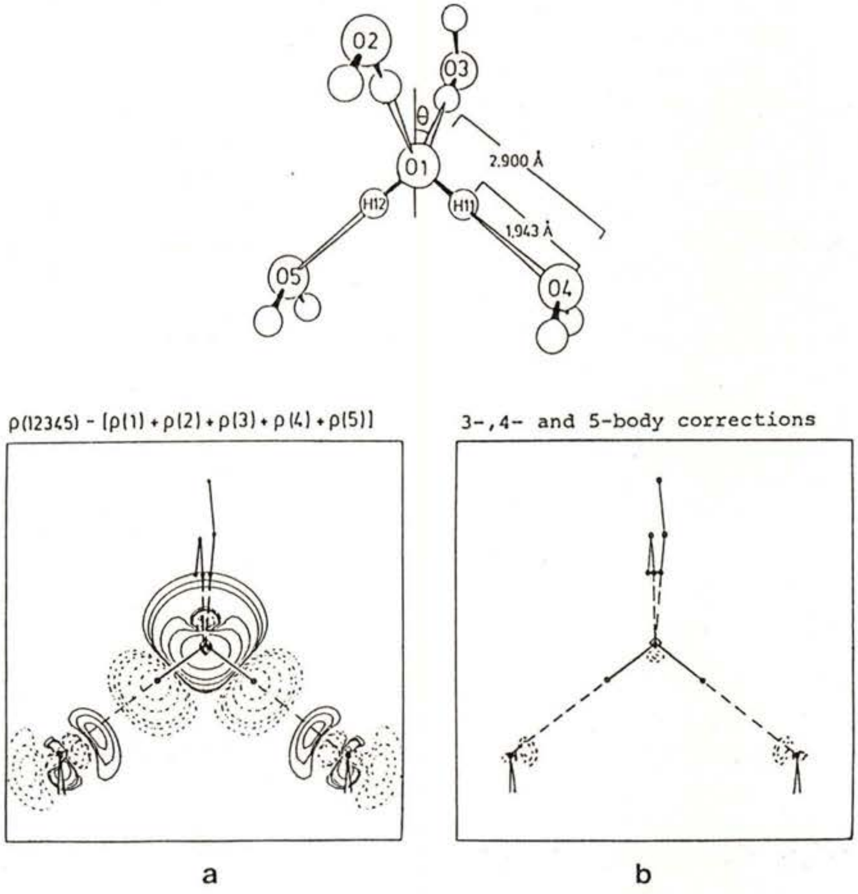

Fig. 9 — Difference electron density distribution for the water pentamer shown in the figure. The total difference is shown in *a*, and the non-additive part in *b* (see text for definitions). Same contour intervals as in Fig. 1. The angle θ is referred to in Table 1. (Redrawn by permission of *J. Chem. Phys.*).

Yoon, Morokuma and Davidson [50] have investigated different contributions to the lattice energy for ice by means of *ab initio*-calculated energies (a refit of the MCY (CI) potential points was done, including Hartree-Fock energies for additional dimer geometries; also various trimer energies were calculated). They found the 3-body contribution to the lattice energy per water molecule in two ordered models of the ice Ih structure to be 9 % and 19 %, respectively. They also evaluated the effect on the lattice energy of relaxing the internal water geometry and found a lowering of another 2 % for both structures.

Polarizable water models

Some water models involve a quite different approach to non-additivity effects. The many-body part of the potential is *not* obtained by fitting to *ab initio* calculated triplet energies, *nor* is it treated in an average way as in the case of effective pair potentials; instead, the non-additivity terms are accounted for in a detailed way by introducing the concept of polarizability.

The characteristics of the PE model [37] is as follows (cf. Fig. 6). The electrostatic interaction between non-overlapping molecules can be expressed in terms of the moments of the charge distributions of these molecules. In the PE model, the field strength, **E**, at any given molecule is calculated from the point charges and permanent and induced dipole (and higher) moments of all the surrounding molecules. The molecule is thus polarized, resulting in a new dipole moment $\underline{\mu} = \underline{\mu}^0 + \Delta\underline{\mu}$, where $\Delta\underline{\mu} = \alpha \cdot \mathbf{E}$. Here, α is the isotropic dipole polarizability, and $\underline{\mu}^0$ the experimental dipole moment of a free water molecule (1.85 D). The calculation of new dipole moments is carried out for each molecule. New field strengths are calculated, and the process is repeated until some desired accuracy is attained. The method can in principle be applied at any desired level of multipolar expansion of the charge distribution. The resulting water dipole moments from MC simulations of liquid water and ice Ih were calculated by Finney and Goodfellow [55] and found to lie in the range 2.1-2.9 D for water (with an average value of 2.5 D) and 2.5-3.2 D for ice. (It could here be interesting to point out that also the flexible--molecule models, although through a totally different approach, allow for changes in the molecular dipole moment. Lie and Clementi [29] found water dipole moments in the range 2.17 to 2.43 D in their bulk water simulation using an «MCY + intramolecular» potential, compared to 2.19 D for the rigid MCY water molecule).

Gellatly, Quinn, Barnes and Finney [56] evaluated the 3- and 4-body contributions to the total energy of liquid water within the PE model by selecting representative 3- and 4-molecule clusters from a room--temperature Monte Carlo simulation. They found that, despite the larger number of quartets compared to triplets, the steric restrictions in the choice of connected 4-body clusters, as well as the small magnitude and variable sign of the 4-body energies, would make the 4-body effects on the total energy negligible.

The philosophies behind the polarizability models of Campbell and Mezei [57] and of Lybrand and Kollmann [58] are similar to that of the PE model.

Several attempts have been made to incorporate polarizability into an existing model. Berendsen and van der Velde [59] introduced a polarization term in conjunction with the ST2 model. Polarization was added to the CF model by Stillinger and David [60].

4 – RELATIONS BETWEEN POTENTIAL MODEL AND SIMULATED PROPERTIES IN ION-WATER SYSTEMS

An important area of application of computer simulation is concerned with ion-water interactions, in inorganic and biological systems, in liquid and solid states. The water-water and water-ion potentials that have been used are of the same general form as those discussed in Section 3. Some examples are given below of computer simulations of inorganic, aqueous ionic solutions and crystals. The possibility of model improvement due to the inclusion of many-body effects is discussed. Possible model improvement in terms of better descriptions of the charge distribution is discussed in Section 5.

Computer simulation of aqueous electrolyte solutions

A large number of MC and MD simulations on aqueous ionic solutions (especially with alkali, alkaline earth or halides ions) have been undertaken (see Refs. [61-68, 27]). Heinzinger [69] and Bopp [70] have recently reviewed the field, with special emphasis on results obtained with the CF model (flexible water molecules).

Fig. 10 is included to point out (once more) the sensitivity of properties of the calculated system to details in the interaction potentials. The figure shows the probability distribution of the angle θ for water molecules in the first hydration shell around Na^+ and Cl^- in two MD simulations using different potential functions. There is still a lot of discussion both among experimentalists and theoreticians concerning the orientation of the water molecules around even «simple» monoatomic ions.

The power spectrum of the hindered translations of Li^+ (cf. Eqn. (6)) has been calculated from the simulation referred to in Figs. 1 and 2 (Fig. 11). The Li^+ ion is found to «rattle around» in its cage of six water neighbours with a frequency of ~450 cm^{-1}, i. e. in close agreement with the value found experimentally for Li^+ ions in crystalline hydrates. This simulation was done using true pair-additive potentials from quantum-mechanical SCF calculations. Practically all simulations on ionic aqueous solutions published so far have used effective or true pair-additive potentials. Some exceptions exist and are discussed below.

Ion-water interactions in the solid state

The field of Lattice Dynamics and MD studies of molecular crystals has been reviewed by Righini [71]. Klein [72] and Catlow [73] have reviewed other areas of solid state simulations. Several useful review papers are also found in a volume edited by Catlow and Mackrodt [74].

Many simulations have previously been performed of ionic crystals, but none of ionic crystalline hydrates. The presence of ionic interactions, hydrogen bonding and van der Waals interactions makes an ionic crystalline hydrate a relatively complex system, and most interesting from a theoretical point of view. We are currently studying the interactions, dynamics and hydration / dehydration aspects in the $LiHCOO \cdot H_2O$ - $LiHCOO$ system by means of static and dynamic modelling. Some preliminary results from this work will be given here as an example of a solid-state application of simulation techniques.

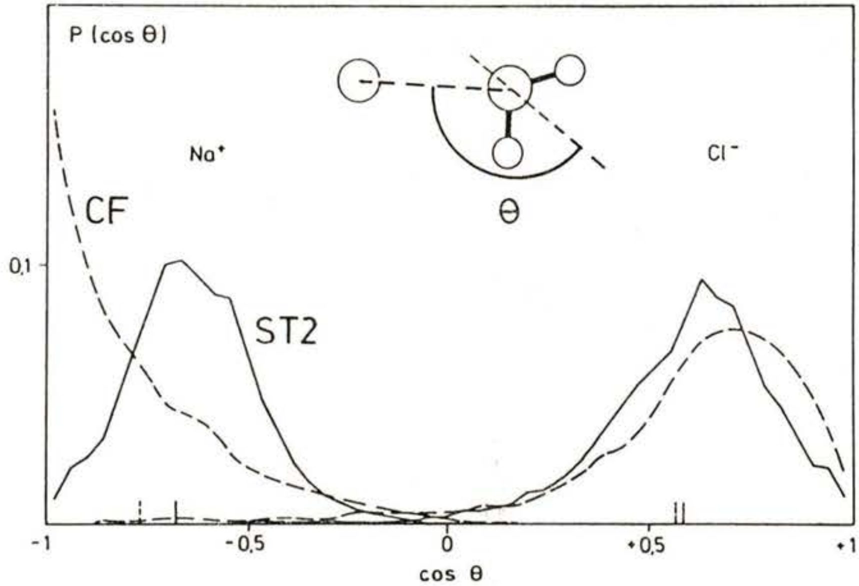

Fig. 10 — The cosθ distribution for water molecules around a Na^+ and Cl^- ion in a 2.2 M solution, using two different potentials [69]. (Redrawn by permission of *Physica*).

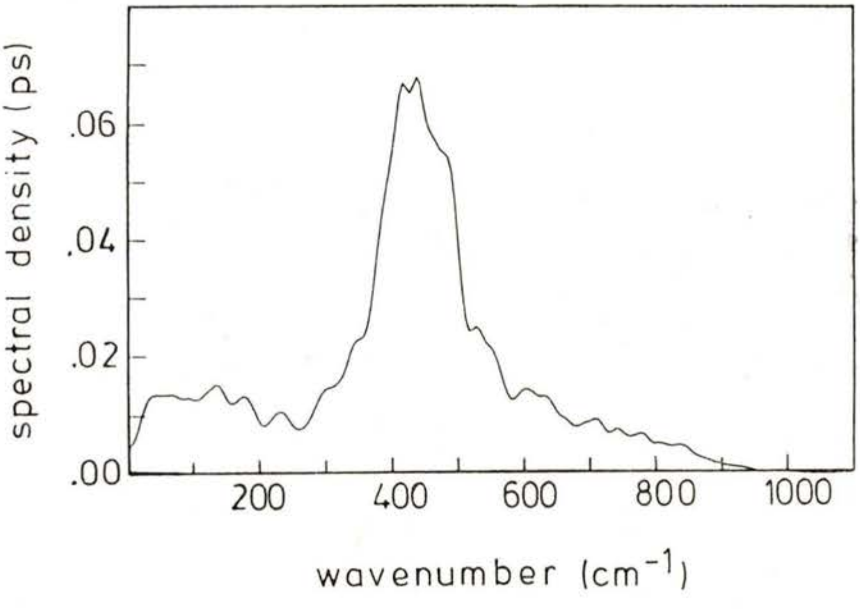

Fig. 11 — The spectral density for Li^+ translations from the same simulation as in Fig. 1.

Effective pair-additive potentials for $LiHCOO \cdot H_2O$ crystal were derived [75] by fitting a set of analytical functions (essentially Lennard-Jones + electrostatic) to the experimental crystal structure of the monohydrate [76], using rigid molecules and the program WMIN [23]. The model potential retains all essential structural features of the real crystal. When applied to the crystal structure of anhydrous LiHCOO [77], which is quite different from the monohydrate, these same potentials were able to reproduce the new structure equally satisfactorily.

Constant pressure MD simulations according to the method of Parrinello and Rahman [78] have been performed for the monohydrate structure at several temperatures between 51 and 660K, using the potentials described, a simulation box with 96 particles of each kind (Li^+, $HCOO^-$, H_2O) and periodic boundary conditions. Two examples will be given from the preliminary analysis of the MD data. Table 2 show the atomic *r.m.s.* displacements from the room-temperature MD simulation and from neutron diffraction. The overall agreement is quite good. Even the derived anisotropic displacement parameters (not given here) correctly reproduce, for example, the larger thermal motion of the

TABLE 2 — Atomic *r.m.s.* displacements (in Å) in $LiHCOO \cdot H_2O$ at 315K.

	MD	Neutron diffraction
Li	0.175	0.185
C	0.171	0.171
O1	0.196	0.189
O2	0.183	0.179
H	0.268	0.272
OW	0.201	0.177
HW1	0.213	0.207
HW2	0.245	0.219

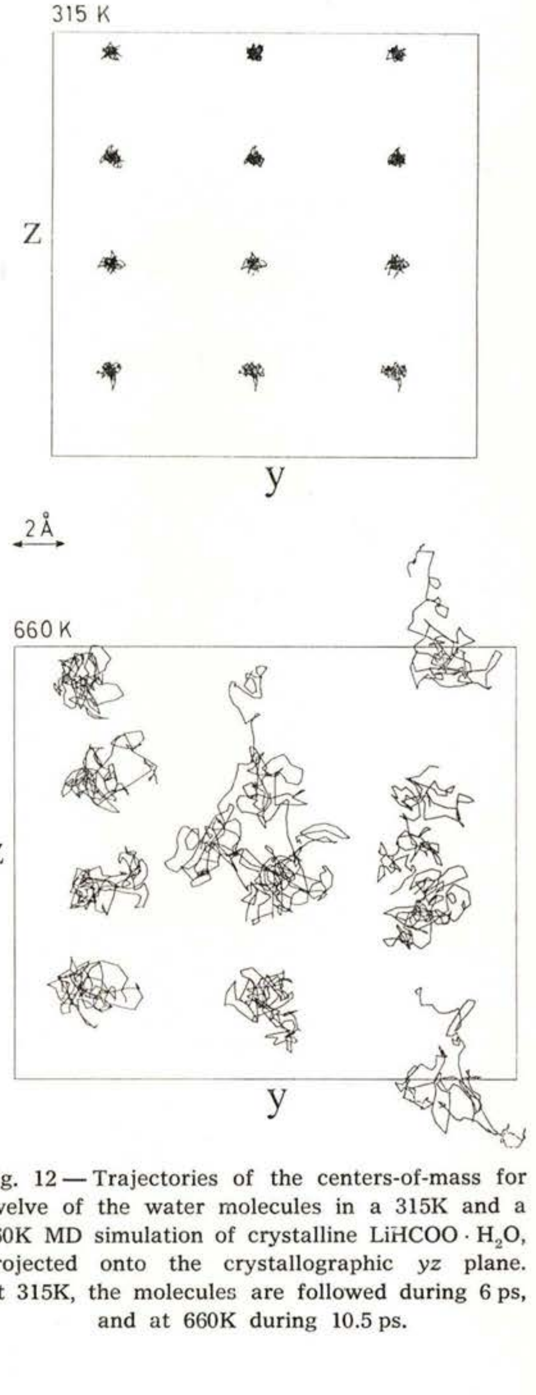

Fig. 12 — Trajectories of the centers-of-mass for twelve of the water molecules in a 315K and a 660K MD simulation of crystalline $LiHCOO \cdot H_2O$, projected onto the crystallographic *yz* plane. At 315K, the molecules are followed during 6 ps, and at 660K during 10.5 ps.

formate atoms perpendicular to the sheets formed by the formate and lithium ions. The interpretation of this agreement is not so clear cut, however, since internal motion such as out-of-plane C-H bending is not allowed in the rigid model.

Fig. 12 shows the trajectories of 12 of the water molecules in the simulation box during 3 ps, at 315K and 660K. At 315K, the molecules «rattle around» their equilibrium positions throughout the simulation (in fact, in a highly harmonic fashion). At the higher temperature, the lithium and formate ions (not shown here) remain close to their equilibrium positions, while some of the water molecules start to diffuse.

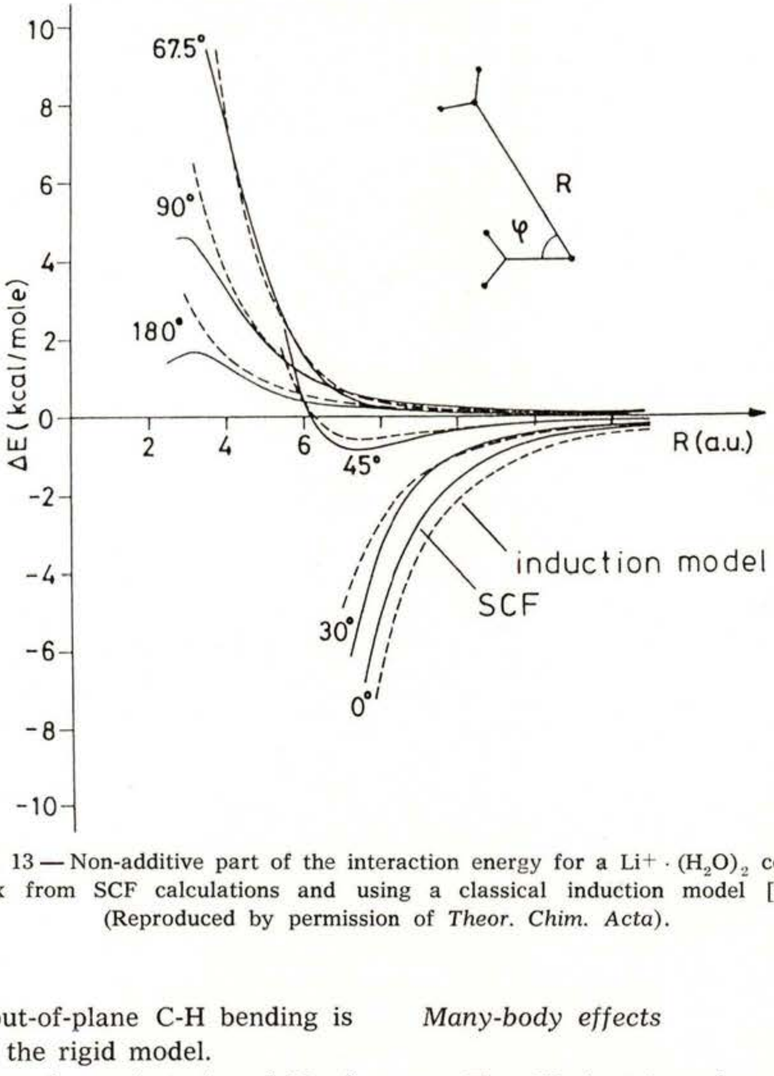

Fig. 13 — Non-additive part of the interaction energy for a $Li^+ \cdot (H_2O)_2$ complex from SCF calculations and using a classical induction model [79]. (Reproduced by permission of *Theor. Chim. Acta*).

Many-body effects

Fig. 13 is taken from the work of Clementi, Kistenmacher, Kolos and Romano [79] and shows the non-additive part of the interaction energy for a $Li^+ (H_2O)_2$ complex as a function of the second water molecule for fixed positions of the Li^+ ion and the first water molecule. The *ab initio* curves in Fig. 13 thus show $\Delta^3E(ijk)$ as defined in Eqns. (8)-(10), with i, j and k representing Li^+, $H_2O(1)$ and $H_2O(2)$. The dashed curves show the non-additive contribution calculated from *classical induction* theory, assuming anisotropic bond polarizabilities for the water molecule. The study by Clementi et al. shows that (*i*) non-additivity is subtantial for this complex, (*ii*) for long and intermediate ion-water distances, the *ab initio* values are well reproduced by the simple induction theory, and (*iii*) experimentally determined ΔH values for a series of (H_2O) $(n = 1\text{-}6)$ complexes are well reproduced if induction is incorporated into the model.

For ion-water complexes, the non-additivity is generally substantial and larger than for water n-mers (cf. Refs. [79-90]). Probst [90] has evaluated the non-additivity contribution to the interaction energy for symmetric Na^+, Mg^{2+} and Al^{3+} aquo complexes with up to six water molecules. The resulting values are listed in Table 3, expressed as ΔE(non-add.)/ΔE (in per cent), where, ΔE (non-add.) contains all 3-, 4-, 5- etc. body contributions; ΔE is the total interaction energy. The non-additivity is seen to be as large as 27 % for the Al^{3+} hexamer, and 17 % for the Mg^{2+} hexamer.

TABLE 3 — Non-additivity contributions (in *per cent*) to the interaction energy for aquo complexes of Na^+, Mg^{2+} and Al^{3+} [90].

n	Na^+	Mg^{2+}	Al^{3+}
1			
2	1.8 %	3.3	6.0
3	3.6	6.8	12.3
4	5.9	10.1	17.3
6	9.7	16.6	27.1

Perez, Lee and Prohofsky [86] performed energy minimization calculations (by using MD calculations while gradually lowering the temperature) for hydrated Na^+ microclusters of 1-6 water molecules, using the PE model. The experimental gas-phase ion-hydration enthalpies were much improved compared to two-body models, and a geometrical analysis showed the minimum energy configuration for the hexaaqua complex to be non-octahedral. Lybrand and Kollmann [58] have constructed ion-water potentials including polarizability terms and applied these in energy minimizations of ion-water clusters (Na^+, K^+, Mg^{2+}, Cl^- with up to 6 H_2O). They found an «excellent agreement» with experimental gas-phase hydration enthalpies. Immersion of these hydrated ions in a bath of ~200 water molecules and allowing further restricted relaxation gave estimates of solvation enthalpies in «good overall agreement» with experiment. The use of these potentials in MC or MD simulations will enable a more critical evaluation of their ability to simulate bulk liquid structure (cf. «note added in proof»).

5 — CHARGE DISTRIBUTION AND THE POTENTIAL MODEL

Some shortcomings of the potential models used in simulations of pure water and ionic aqueous systems were discussed in Sections 3 and 4. Two approximations were pointed out: the neglect of many-body effects and a description of the continuous charge distribution in terms of a few charge centers. The first approximation was discussed in Section 3 for water and in Section 4 for ion-water systems. I shall here focus on possible improvements to the second approximation. The examples given will not be restricted to aqueous systems.

Though not directly within the context of computer simulation, a number of schemes have been put forward to obtain charges and higher multipoles from (quantum-mechanical or experimental) electron distributions. Some are listed in Table 4.

TABLE 4 — Some schemes for the parameterization of ρ (r).

	Parameterization of ρ (r)	
1.	Mulliken charges	[91]
2.	Bader charges	[93]
3.	Multipole-consistent charges	
	Brobjer & Murrell	[95]
	Thole & van Duijnen	[96]
4.	Distributed multipoles	
	Kurki-Suonio	[97]
	Hirshfeld least-squares	[98]
	stockholder	[102]
	Stewart	[99]
	Hansen & Coppens	[100]
	Stone	[103]
5.	'Fuzzy boundary' and other integration schemes	[104, 105]
6.	Electrostatic potential-derived charges	[107]

The limitations of charges derived from a Mulliken population analysis [91] of quantum-mechanical wave functions are well-known. Alternative schemes have been devised, such as the population analysis based on occupation numbers of «modified atomic orbitals» by Ehrhardt and Ahlrichs [92]. These authors also review some of the predecessors to their method. Bader [93] defines an «atom in a molecule» as a disjoint region in real space, which is bounded by a surface through which the flux of the gradient of the charge density is zero, and which contains a single «nuclear attractor». The description of this subspace and its properties are obtained through the application of Schwinger's action principle [94]. Brobjer and Murrell [95] and Thole and van Duijnen [96] devised different procedures for obtaining a small set of distributed point charges which correctly reproduces the multipole moments of the total charge distribution to a desired level. Kurki-Suonio [97], Hirshfeld [98], Stewart [99] and Hansen and Coppens [100] (see also Ref. [101]) have derived distributed multipoles from experimental electron distributions. Their approaches are slightly different, but share the essential idea of expanding the total density into spherical and non-spherical components, whose occupancy coefficients are included in the least-squares refinement. Hirshfeld [102] has also introduced the 'stockholder recipe', by which the *deformation density* at a point in space is divided between the nearby atoms in proportions described by the corresponding *unperturbed atomic densities*. Stone [103] has derived a method to obtain multipole-consistent distributed multipoles from quantum-mechanical *ab initio* wave functions. Various integration schemes (e. g. the 'fuzzy boundary' scheme) for the partitioning of real space into reasonable atomic fragments have been discussed (and practiced) by Moss and Coppens [104], and Coppens and Stevens [105]. Maslen and Spackman [106] have given a detailed account of similarities, differences and physical interpretation of the atomic charges from Bader's and Hirshfeld's partitioning schemes. A general review on the subject of space partitioning of electron densities is given by Becker [107].

Cox and Williams [108] have extended the work of Momeny [109] and determined atomic charges by fitting the model electrostatic potential in a shell outside the molecular van der Waals radius to the potential calculated directly from the quantum-mechanical wave functions.

Electrostatic interactions in the majority of *static and dynamic modelling studies*, however, have been accounted for by a small number of *distributed point charges:* usually Mulliken charges, effective charges or charges obtained from a fit to quantum-mechanical energies. Only a few of the more elaborate models in Table 4 have been applied to computer modelling; some examples are given here. Starting from Hartree-Fock molecular wavefunctions, Hirshfeld and Mirsky [110] performed lattice-energy calculations for three crystal structures (C_2H_2, CO_2 and C_2N_2) with the electrostatic energy calculated at three levels of sofistication: (*i*) replacing each molecule by a point quadrupole at its center of symmetry, (*ii*) placing a point charge at each nucleus (the values chosen to reproduce the calculated molecular quadrupole moment), and, the most elaborate, (*iii*) decomposition into atomic fragments according to the stockholder recipe of Hirshfeld. They found large differences in the lattice energies, which were up to 60 % larger for the third model. Berkovitch-Yellin and Leiserowitz have used Hirshfeld's 'least--squares charges' and 'stockholder charges' from X-ray data in crystal packing calculations of amides [111] and other systems. Berkovitch-Yellin et al. [112] and Berkovitch-Yellin [113] also used such charges in calculations of the habits of organic crystals. Moss and Feil [114] and Feil and Moss [115] derived the electrostatic 'in-crystal' potential of the pyrazine molecule from a Hirshfeld type deformation refinement, and investigated the importance of the electrostatic interaction in determining the crystal structure.

MD simulations for the orientationally disordered phase I of solid KCN have been performed by Klein and McDonald [116], who concluded that an interionic potential incorporating «a realistic model of the CN^- charge distribution» was able to account semi-quantitatively for a wide range of properties of this crystal, as opposed to previous simulations, where only one effective quadrupole moment had been used to model the anisotropy of the electrostatic interaction. The construction of the new potentials was guided by the distributed multipole analysis made by Stone (cf. above) for the CN^- ion [117].

Some guidelines for the improvement of the *non-electrostatic* part of interaction potentials have also been suggested. In their review of water dimer potentials, Finney et al. [31] concluded that most of the effective pair potentials with three point charges and one non-Coulombic interaction site display too strong an 0 ... 0 attraction, while the orientational dependence is too weak. They discuss possible improvements with respect to the functional form of the potentials and conclude that the addition of explicit H-H repulsion terms may be an important modification.

The constant pressure MD [78], which allows the unit cell volume and shape to change, has been particularly important in discriminating between different models, allowing the study of phase transitions to take place and showing the importance of thermal motion for the stability of the calculated crystal structure. A large number of Lattice Dynamics and Molecular Dynamics simulations have been performed for molecular crystals of small molecules, such as CH_4, N_2, Cl_2, CS_2, CSe_2 (cf. the review by Righini [71] and references therein). In many cases the potential functions applied have been Lennard-Jones atom-atom potentials with no electrostatic interaction or with a simple quadrupolar interaction. Many different parameterizations have been attempted and many different physical properties calculated. Righini [71] concludes that such simple models are inadequate; higher-order terms in the multipole expansion play an important role in the stability and dynamics of these crystals, and the form of the non-electrostatic terms also requires special attention. Solid Cl_2 is an interesting example. The experimental structure cannot be reproduced by traditional isotropic atom-atom pair potentials, even if quadrupole-quadrupole interaction is included. Price and Stone [118] and Burgos et al. [119], using different formalisms showed that by inclusion of anisotropy in the lone-pair electron density, the model potential succeeds to describe the experimental structures very accurately. Price and Stone [118] make use of Stevens' [120] experimental electron density maps in discussing the physical validity of their anisotropic potential model. Finney et al. [31] suggest that a similar modification of the water-water potential, allowing for the anisotropy of the repulsive core around the oxygen lone-pair region, may lead to an improvement in the agreement between experimental and calculated properties for liquid water.

Further developments along these lines, or more sophisticated approaches, could prove most rewarding.

6 — CONCLUSIONS

In this paper, I have briefly reviewed the methods used in computer simulations of condensed matter, and the results obtainable with these techniques. I have concentrated on the use of realistic pair potentials and have given an overview of some models that are widely used for aqueous systems. Quantum-chemical and experimental methods to investigate electron densities have already proved to be most valuable in studying basic chemical and physical principles. It should be feasible to make more use of these densities for the construction of improved intermolecular potentials, accounting for the continuous electron distribution in a more detailed way than is being done at present, and by a more adequate modelling of the polarization mechanisms occurring in real systems. I believe that such developments will further increase the power and applicability of simulation methods.

Note added in proof:

Rullmann and van Duijnen [121] recently published a new polarizable water model which resembles the PE model but also exhibits some important differences. The potential was applied in Monte Carlo calculations of liquid water and calculations of hydration and protonation energies of amines. Ahlstr et al. [122] investigated the effect of adding a point polarizability to an SPC like rigid water molecule in MD simulations, and found an 'increased structure' and slower dynamic properties as compared to the original SPC model. MD simulations for aqueous ionic systems using potentials beyond the pair-additive model have been performed for $BeCl_2$ (aq) by Probst et al. [123]. They found the hydration number to decrease from 6 to 4 on including non-additivity effects. Curtiss et al. [124, 125] have calculated many-body contributions for $Fe^{2+}(H_2O)_n$ and $Fe^{3+}(H_2O)_n$ clusters from ab initio methods. They also compared MD results using true ab initio pair potentials and effective 2-body potentials.

REFERENCES

[1] METROPOLIS, N., ROSENBLUTH, A. W., ROSENBLUTH, M. N., TELLER, A. H. and TELLER, E., J. Chem. Phys. **21** (1953).

[2] ALDER, B. J. and WAINWRIGHT, T. E., J. Chem. Phys **27**, 1208 (1957).

[3] HERMANSSON, K., J. Chem. Phys. **89**, 2149 (1988).

[4] DUPUIS, M., RYS, J. and KING, H. F., J. Chem, Phys. **65**, 111 (1976); DUPUIS, M., WATTS, J. D., VILLAR, H. O. and HURST, G. J. B., Hondo-Version 7.0, IBM Research Report, KGN-169 (January 18, 1988).

[5] BADER, R. F. W., «Molecular Charge Distributions — Their Display and Use», In: *International review of Science, Physical Chemistry Series Two* (ed. Buckingham, A. D.). London: Butterworth (1975).

[6] *Electron and Magnetization Densities in Molecules and Crystals, NATO Advanced Study Institutes Series,* Series B, Vol. **48**. Ed.: Becker, P. Plenum Press: New York, London (1980).

[7] Isr. J. Chem., **16**, Guest editor: Hirshfeld, F. Jerusalem: The Weizmann Science Press of Israel (1977).

[8] COPPENS, P. and HALL, M. B., *Electron Distributions and the Chemical Bond,* Eds., New York: Plenum (1982).

[9] *Interatomic Interactions: From Diatomics to Biopolymers.* Pullman, B. (Ed.), New York: John Wiley and Sons (1978).

[10] RAZNAKIEVICH, H. and ORVILLE-THOMAS, W. J. (Eds.), *Molecular Interactions,* Volumes **1**, **2**, **3**. New York: John Wiley and Sons (1980).

[11] BURKERT, U. and ALLINGER, N. L., *Molecular Mechanics, ACS Monograph* **177**, (Caserio, M. C., Series Editor). American Chemical Society (1982).

[12] VALLEAU, J. P. and WHITTINGTON, S. G., In: *Modern Theoretical Chemistry,* Vol. **5** (Berne, B. J., ed.), p. 137, Plenum Press, New York (1977).

[13] KUSHICK, J. and BERNE, B. J. (Eds.), *Modern Theoretical Chemistry:* Part B, Vol. **6**, Plenum Press, New York (1977).

[14] LYKOS, P. (Ed.), *Computer Modelling of Matter, ACS Symposium Series,* No. **86**, ACS, Washington, D. C. (1978).

[15] WOOD, D. W., In: *Water — a Comprehensive Treatise,* Franks, F. (ed.), Vol. **6**, Plenum Press, New York (1979).

[16] HEERMAN, D. W., *Computer Simulation Methods in Theoretical Physics,* Springer-Verlag. Berlin, Heidelberg (1986).

[17] ALLEN, M. P. and TILDESLEY, D. J., *Computer Simulation of Liquids,* Oxford University Press. Oxford, New York (1987).

[18] CICCOTTI, G., FRENKEL, D. and MACDONALD, I. R., *Simulations of Liquids and Solids. Molecular Dynamics and Monte Carlo Methods in Statistical Mechanics.* North-Holland Personal Library (1988).

[19] BUSING, W. R. and MATSUI, M., Acta Cryst., **A40**, 532 (1984).

[20] ALLINGER, N. L., J. Am. Chem. Soc. **99**, 8127 (1977).

[21] AMBER: Assisted model building with energy refinement. A general program for modelling molecules and their interactions. P. K. Weiner and P. A. Kollman, J. Comp. Chem. **2**, 287 (1981).

[22] ECEPP: MOMANY, F. A., MCGUIRE, R. F., BURGESS, A. W. and SCHERAGA, H. A., J. Phys. Chem. **79**, 2361 (1975); NEMETHY, G., POTTLE, M. S. and SCHERAGA, H. A., J. Phys. Chem. **87**, 1883 (1983).

[23] WMIN: BUSING, W. R., WMIN Report ORNL-5747, Oak Ridge National Laboratory, Oak Ridge, TN (1981).

[24] CHARMM: a program for macromolecular energy, minimization and dynamics calculations. BROOKS, B. R. BRUCCOLERI, R. E., OLAFSON, B. D., STATES, D. J., SWAMINATHAN, S. and KARPLUS, M., J. Comput. Chem. **4**, 187 (1983).

[25] GROMOS: Groningen Molecular Simulation System, VAN GUNSTEREN et al., University of Groningen. Unpublished.

[26] McMOLDYN: Computer Simulation Package for Liquids and Solids with Polar Interactions. A. LAAKSONEN and E. CLEMENTI, Comp. Phys. **42**, 271 (1986).

[27] HERMANSSON, K., LIE, G. C. and CLEMENTI, E. IBM Technical Report, DSD, KGN-54 (1986); *ibid.* KGN-73 (1986).

[28] LEMBERG, H. L. and STILLINGER, F. H., J. Chem. Phys. **62**, 1677 (1975).

[29] LIE, G. C. and CLEMENTI, E., Phys. Rev. **A33**, 2679 (1986).

[30] RYCKAERT, J. P., CICCOTTI, G. and BERENDSEN, H. J. C., J. Comp. Phys. **23**, 327 (1977).

[31] FINNEY, J. L., QUINN, J. E. and BAUM, J. O., In: *Water Science Reviews*, Vol. **1**. (Franks, F., ed.) p. 93. Cambridge University Press (1985).

[32] BEN-NAIM, A. and STILLINGER, F. H., In: *Structure and Transport Processes in Water and Aqueous Solution* (Horne, R. A., ed.), p. 295. Wiley-Interscience: New York (1972).

[33] STILLINGER, F. H. and RAHMAN, A., J. Chem. Phys. **60**, 1545 (1974).

[34] SHIPMAN, L. L. and SCHERAGA, H. A., J. Phys. Chem. **78**, 909 (1974).

[35] MATSOUKA, O., CLEMENTI, E. and YOSHIMINE, M., J. Chem. Phys. **64**, 1351 (1976).

[36] JORGENSEN, W. L., CHANDRASEKHAR, J. MADURA, J. D., IMPEY, R. W. and KLEIN, M. L., J. Chem. Phys. **79**, 926 (1983).

[37] BARNES, P., FINNEY, J. L., NICHOLAS, J. D. and QUINN, J. E., Nature, **282**, 459 (1979); BARNES, P., In: *Progress in Liquid Physics* (Croxton, C. A., ed.), Chap. 9. Wiley-Interscience (1983).

[38] BERENDSEN, H. J. C., POSTMA, J. P. M., VAN GUNSTEREN, W. F. and HERMANS, J. In: *Intermolecular Forces*, p. 131. (Pullman, B., ed.). Reidel: Dordrecht (1981).

[39] REIMERS, J. R., WATTS, R. O. and KLEIN, M. L., Chem. Physics **64**, 95 (1982).

[40] SINGH, U. C. and KOLLMAN, P. A., J. Chem. Phys. **83**, 4033 (1985).

[41] BEVERIDGE, D. L., MEZEI, M., MEHROTRA, P. K., MARCHESE, F. T., RAVI-SHANKER, G., VASU, T. and SWAMINATHAN, S., In: *Molecular Based Study and Prediction of Fluid Properties* (Haile, S. M. and Mansouri, G. A., Eds.), Advances in Chemistry, ACS (1983).

[42] NARTEN, A. H., J. Chem. Phys. **56**, 5681 (1972).

[43] POSTMA, J. P. M.: A Molecular Dynamics Study of Water. Ph. D. thesis. University of Groningen (1985).

[44] WOJCIK, M. C. and CLEMENTI, E., J. Chem. Phys. **84**, 5970 (1986).

[45] BOUNDS, D. G., Chem. Phys. Lett. **96**, 604 (1983).

[46] MORSE, M. D. and RICE, S. A., J. Chem. Phys. **76**, 650 (1982).

[47] J. Phys. Chem. **87** (1983). Procedings from the 6th International Symposium on the Physics and Chemistry of Ice, Univ. of Missouri-Rolla, Aug. 2-6, 1982.

[48] HANKINS, D., MOSKOWITZ, J. W. and STILLINGER, F. H., J. Chem. Phys. **53**, 4544 (1970); J. Chem. Phys. **59**, 995 (1973).

[49] CLEMENTI, E., KOLOS, W., LIE, G. C. and RANGHINO, G., Int. J. Quantum Chem. **17**, 377 (1980).

[50] YOON, B. J., MOROKUMA, K. and DAVIDSON, E. R., J. Chem. Phys. **83**, 1223 (1985).

[51] KIM, K. S., DUPUIS, M., LIE, G. C. and CLEMENTI, E., Chem. Phys. Lett. **131**, 451 (1986).

[52] CLEMENTI, E. and CORONGIU, G., Int. J. Quantum Chem.: Quantum Biology Symposium **10**, 31 (1983).

[53] DETRICH, J., CORONGIU, G. and CLEMENTI, E., Int. J. Quantum Chem.: Quantum Chemistry Symposium **18**, 701 (1984).

[54] WOJCIK, M. C. and CLEMENTI, E., J. Chem. Phys. **85**, 3544 (1986); J. Chem. Phys. **85**, 6085 (1986).

[55] FINNEY, J. L. and GOODFELLOW, M. In: *Structure and Dynamics: Nucleic Acids and Proteins* (Clementi, E. and Sarma, R. H., Eds.), New York: Adenine Press (1983).

[56] GELLATLY, J. B., QUINN, J. E., BARNES, P. and FINNEY, J. L., Mol. Phys. **59**, 949 (1983).

[57] CAMPBELL, E. S. and MEZEI, M., J. Chem. Phys. **67**, 2338 (1977).

[58] LYBRAND, T. P. and KOLLMAN, P. A., J. Chem. Phys. **83**, 2923 (1985).

[59] BERENDSEN, H. J. C. and VAN DER VELDE, G. A. In: *Report of CECAM Workshop on Molecular Dynamics and Monte Carlo Simu-*

lations on Water (Berendsen, H. J. C., ed.), p. 63. CECAM: Paris (1972).

[60] STILLINGER, F. H. and DAVID, C. W. J. Chem. Phys. **69**, 1473 (1978).

[61] IMPEY, R. W., MADDEN, P. A. and MCDONALD, I. R., J. Phys. Chem. **87**, 5071 (1983).

[62] MEZEI, M. and BEVERIDGE, D. L., J. Chem. Phys. **74**, 6902 (1981).

[63] CLEMENTI, E. and BARSOTTI, R., Chem. Phys. Lett. **59**, 21 (1978).

[64] CHANDRASEKHAR, J., SPELLMEYER, D. C. and JORGENSEN, W. L., J. Amer. Chem. Soc. **106**, 903 (1984).

[65] ENGSTRÖM, S., JÖNSSON, B. and IMPEY, R. W., J. Chem. Phys. **80**, 5481 (1984).

[66] BOUNDS, D. J., Mol. Phys. **54**, 1335 (1985).

[67] BOPP, P., JANCSO, G. and HEINZINGER, K., Chem. Phys. Letters **98**, 129 (1983).

[68] PROBST, M. M., BOPP, P., HEINZINGER, K. and RODE, B. M. Chem. Phys. Letters **106**, 317 (1984).

[69] HEINZINGER, K., Physica **131B**, 195 (1985).

[70] BOPP, P., Pure and Appl. Chem. **59**, 1071 (1987).

[71] RIGHINI, R., Physica **131B**, 234 (1985).

[72] KLEIN, M. L., Ann. Rev. Phys. Chem. **36**, 525 (1985).

[73] CATLOW, C. R. A.: Computational Techniques and Simulation of Crystal Sctructures, In: *Solid-State Chemistry Techniques*, p. 231. (Cheetham, A. K. and Day, P., Eds.). Clarendon Press, Oxford (1987).

[74] *Computer Simulation of Condensed Matter.* Preceedings of the NATO Advanced Research Workshop at East Anglia, UK, 22-27 July 1984. (Catlow, C. R. A. and Mackrodt, W. C., Eds.). Physica **131 B+C**, Nos. 1-3 (1985).

[75] WOJCIK, M. and HERMANSSON, K., Acta Chem. Scand. **A41**, 562 (1987).

[76] TELLGREN, R., RAMANUJAM, P. S. and LIMINGA, R., Ferroelectrics **6**, 191 (1974).

[77] KANSIKAS, J. and HERMANSSON, K., Acta Cryst. **C45**, 187 (1989).

[78] PARRINELLO, M. and RAHMAN, A., Phys. Rev. Letters **45**, 1196 (1980).

[79] CLEMENTI, E., KISTENMACHER, H., KOLOS, W. and ROMANO, S., Theor. Chim. Acta **55**, 257 (1980).

[80] KOLLMAN, P. A. and KUNTZ, I. D., J. Amer. Chem. Soc. **94**, 9236 (1972); J. Amer. Chem. Soc. **96**, 766 (1974).

[81] H. KISTENMACHER, H. POPKIE and CLEMENTI, E., J. Chem. Phys. **61**, 799 (1974).

[82] KRESS, J. W., CLEMENTI, E., KOZAK, J. J. and SCHWARZ, M. E., J. Chem. Phys. **63**, 3907 (1975).

[83] SCHUSTER, P., JAKUBETZ, W. and MARIUS, W., *Topics in Current Chemistry* **60**, 1. Berlin: Springer-Verlag (1975).

[84] ORTEGA-BLAKE, I., NOVARO, O., LES, A. and RYBAK, S., J. Chem. Phys. **76**, 5405 (1982).

[85] HABITZ, P., BAGUS, P., SIEGBAHN, P. and CLEMENTI, E., Int. J. Quantum Chem. Vol. **XXIII**, 1803 (1983).

[86] PEREZ, P., LIE, W. K. and PROHOFSKY, W. K., J. Chem. Phys. **79**, 388 (1983).

[87] MATHERS, T. L. and KESTNER, N. R., Int. J. Quantum Chem.: Quantum Chem. Symposium **19**, 297 (1986).

[88] HERMANSSON, K., Acta Chem. Scand. **A41**, 513 (1987).

[89] HASHIMOTO, K., YODA, N. and IWATA, S., Chem. Physics **116**, 193 (1987).

[90] PROBST, M. M., Chem. Phys. Lett. **137**, 229 (1987).

[91] MULLIKEN, R. S., J. Chem. Phys. **23**, 1833 (1955).

[92] EHRHARDT, C. and AHLRICHS, R., Theor. Chim. Acta **68**, 231 (1985).

[93] BADER, R. F. W., NGUYEN-DANG, T. T. and TAL, Y., J. Chem. Phys. **70**, 4316 (1979); BADER, R. F. W., ANDERSON, S. G. and DUKE, A. J., J. Amer. Chem. Soc. **101**, 1389 (1979).

[94] SCHWINGER, J., Phys. Rev. **82**, 914 (1951).

[95] BROBJER, J. T. and MURRELL, J. N., J. Chem. Soc., Faraday Trans. 2, **78**, 1853 (1982); ibid. **79**, 1455 (1983).

[96] THOLE, B. T. and VAN DUIJNEN, P. Th., Theor. Chim. Acta (Berl.) **63**, 209 (1983).

[97] KURKI-SUONIO, K., Acta Cryst. **A24**, 379 (1968); Isr. J. Chem. **16**, 132 (1977).

[98] HIRSHFELD, F. L., Acta Cryst. **B27**, 769 (1971).

[99] STEWART, R. F., J. Chem. Phys. **51**, 4569 (1969); STEWART, R. F., In: *Electron and Magnetization Densities in Molecules and Crystals*, NATO Advanced Study Institutes Series, Series B, Vol. **48**, 405. Ed.: Becker, P. Plenum Press: New York, London (1980).

[100] HANSEN, N. K. and COPPENS, P., Acta Cryst. **A34**, 909 (1978).

[101] COPPENS, P., GURU ROW, T. N., LEUNG, P., STEVENS, E. D., BECKER, P. J. and YANG, Y. W., Acta Cryst. **A35**, 63 (1979).

[102] HIRSHFELD, F. L., Theor. Chim. Acta **44**, 129 (1977); Isr. J. Chem. **16**, 198 (1977).

[103] STONE, A. J., Chem. Phys. Lett **83**, 233 (1981).

[104] MOSS, G. and COPPENS, P., Chem. Phys. Lett. **75**, 298 (1980).

[105] COPPENS, P. and STEVENS, E. D., In: *Electron and Magnetization Densities in Molecules and Crystals*, NATO Advanced Study Institutes Series, Series B, Vol. **48**, 447 (Becker, P., ed.). Plenum Press: New York, London (1980).

[106] MASLEN, E. N. and SPACKMAN, M. A., Aust. J. Phys. **38**, 273 (1985).

[107] BECKER, P., In: *Electron and Magnetization Densities in Molecules and Crystals*, NATO Advanced Study Institutes Series, Series B, Vol. **48**, 375 (Becker, P., ed.) Plenum Press: New York, London (1980).

[108] COX, S. R. and WILLIAMS, D. E., J. Comp. Chem. **2**, 304 (1981).

[109] MOMANY, F. A., J. Phys. Chem. **82**, 592 ((1978).

[110] HIRSHFELD, F. L. and MIRSKY, K., Acta Cryst. **A35**, 366 (1979).

[111] BERKOVITCH-YELLIN, Z. and LEISEROWITZ, L., J. Amer. Chem. Soc. **102**, 7677 (1980).

[112] BERKOVITCH-YELLIN, Z., VAN MIL, J., ADDADI, L., IDELSON, M., LAHAV, M. and LEISEROWITZ, L., J. Amer. Chem. Soc. **107**, 3111 (1985).

[113] BERKOVITCH-YELLIN, Z., J. Amer. Chem. Soc. **107**, 8239 (1985).

[114] MOSS, G. and FEIL, D., Acta Cryst. **A37**, 414 (1981).

[115] FEIL, D. and MOSS, G., Acta Cryst. **A39**, 14 (1983).

[116] KLEIN, M. L. and MCDONALD, I. R., J. Chem. Phys. **79**, 2333 (1983).

[117] STONE, A. J. (Unpublished work).

[118] PRICE, S. L. and STONE, A. J., Mol. Phys. **47**, 1457 (1982).

[119] BURGOS, E., MURTHY, C. S., RIGHINI, R., Mol. Phys. **47**, 1391 (1982).

[120] STEVENS, E. D., Mol. Phys. **37**, 27 (1979).

[121] RULLMANN, J. A. C. and VAN DUIJNEN, P. TH., Mol. Phys. **63**, 451 (1988).

[122] AHLSTRÖM, P., WALLQVIST, A., ENGSTRÖM, S. and JÖNSSON, B., Mol. Phys. **68**, 563 (1989).

[123] PROBST, M., SPOHR, E. and HEINZINGER, K., Chem. Phys. Lett. **161**, 405 (1989).

[124] CURTISS, L., HALLEY, J. W., HAUTMAN, J. and RAHMAN, A., J. Chem. Phys. **86**, 2319 (1987).

[125] CURTISS, L. A., HALLEY, J. W. and HAUTMAN, J., Chem. Phys. **133**, 89 (1989).

ELECTRONIC STRUCTURE CALCULATIONS OF TRANSITION METALS AND ALLOYS

K. SCHWARZ and P. BLAHA
Technical University Vienna
Getreidemarkt 9/158, A-1060 Vienna Austria

ABSTRACT — The electronic structure of metals and alloys is calculated by the full potential linearized augmented plane wave (LAPW) method using the local spin density approximation (LSDA) for treating exchange and correlation effects. Since no shape approximation is made for either the potential or the charge density, this is presently among the most accurate computational techniques for electonic structure calculations. Using these LSDA energy band calculations, three types of applications are discussed:

i) Charge and spin densities and the related structure factors are the most direct quantities to be compared with experiment.

ii) The electric field gradient (EFG) is a sensitive quantity in solids. Recently it became possible to calculate EFGs in the superionic conductor Li_3N from first principles. Here this method is applied to hexagonal closed packed (hcp) metals from Be to Cd. The EFGs including the sign are calculated without the use of any Sternheimer factor. Although the d-electrons of transition metals lead to an electronic charge density which deviates from spherical symmetry, it is mainly the small admixture of p electrons in the valence charge density which is responsible for the EFG. This result is accomplished by the r^1 form of the wave function near the nucleus.

iii) The Mössbauer isomer shift (IS) is determined by the difference in contact density (electron density at the nucleus) between the material in question and a reference system. Although the contact density is mainly determined by the core or semi-core states, the IS originates mostly from the valence electrons. When an alloy is formed, the volume dependence is a crucial factor for IS. These aspects are illustrated for Fe and the Fe compounds FeAl, FeTi and FeCo.

1 — INTRODUCTION AND LAPW METHOD

The electron density is the key quantity in density functional theory (DFT) which is the basis for most electronic structure calculations in solids [1-2]. Although in principle the DFT is exact, in practice the functional is unknown and thus one is forced to use an approximation. Applications in solid state theory are usually based on the local spin density approximation (LSDA). The DFT in combination with the LSDA simplifies the complicated

Portgal. Phys. — Vol. 19, fasc. 1-2, pp. 159-171, 1988

many-body problem to an effective one-electron picture which contains approximate electronic exchange and correlation effects. In the present work we use the parameterisation by Hedin, Lundqvist and Janak for these correlation potentials [3-4].

In many electronic structure calculations, the DFT and LDA are further simplified by assuming the muffin-tin approximation (MTA) for potential and charge density within the self-consistency iterations. We have chosen the full potential linearized augmented wave (LAPW) method in which we do not make this approximation and thus can fully exploit the LSDA.

In the LAPW method, which is well described in literature, [5] the unit cell is divided into non-overlapping spheres and an interstitial region; in the former the wave functions are expressed in atomic-like functions and in the latter, in plane waves. The charge density (and analogously the potential) is written inside the spheres as a linear combination of radial functions $\rho_{LM}(r)$ times symmetrized lattice harmonics $Y_{LM}(\hat{r})$ and in the interstitial region as a Fourier series:

$$\rho(r) = \begin{cases} \sum_{LM} \rho_{LM}(r)\; Y_{LM}(\hat{r}) & \text{inside sphere} \\ \sum_{K} \rho(K)\; e^{iKr} & \text{interstitial} \end{cases} \qquad (1)$$

LSDA energy band calculations provide the basis for an understanding of the electronic structure, electron densities, chemical bonding or spectra related to densities of states as illustrated for example for transition metal compounds [6]. In this paper three applications are reviewed below: electron and spin densities and related structure factors, electronic field gradients, and Mössbauer isomer shifts.

2 – ELECTRON AND SPIN DENSITIES

By summing the modulus of the wave functions of all the occupied states one obtains the electron densities. In case of a ferromagnet these quantities are obtained for spin-up and spin-down electrons separately and their difference yields the spin density. In the DFT and the LSDA these densities are the essential quantities which are obtained self-consistently.

We show selected examples for hcp metals. Self consistent calculations on hcp Be have shown [7] that the use of a general potential is important. When the potential is assumed to be of muffin-tin form the resulting electron density shows maxima along the c axis and an excess of p_z-like charge (Fig. 1a). The full potential LAPW calculation, however, yields a valence electron density which is almost spherically symmetric around the Be nuclei and very flat in between (Fig. 1b). This result is surprising, since one would expect the MTA to yield a more spherical density. The full potential LAPW results are confirmed by the related structure factors which agree significantly better with experimental data than those of the muffin-tin case, especially for the 002 reflection (see Fig. 6 of [7]).

Next we discuss hcp Ti as one example of a transition metal [8]. Its difference density (Fig. 2) is negative between the two titanium atoms shown in the $(11\bar{2}0)$ plane and is positive in the $[\bar{1}10]$ and $[001]$ direction. In the interstitial region the difference density is small and rather flat. The large anisotropy stems from the d electrons and can be understood on the basis of symmetry decomposed partial densities of states (DOS) (bottom of Fig. 3). Up to the Fermi energy E_F, there is a depletion of the d_{xz}, d_{yz} component with respect to the other two types of d symmetries leading to the clover-leaf shape in the difference density. The p-DOS (top of Fig. 3) shows an anisotropy too, which as it is a very small

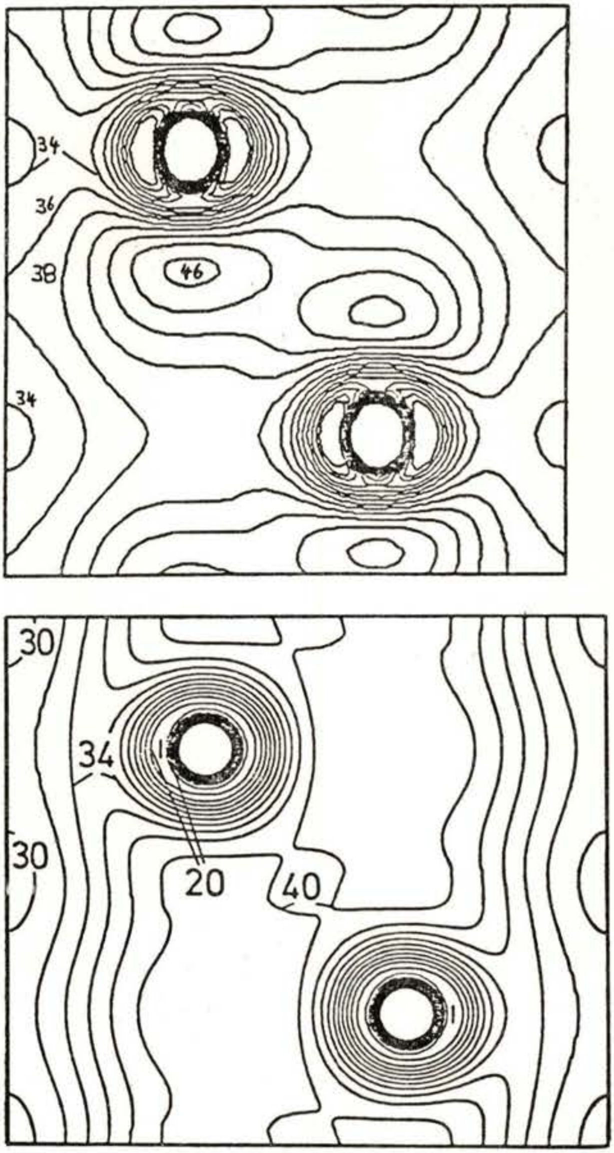

Fig. 1 — Valence electron density of hcp Be in the $(11\bar{2}0)$ plane: In the contour plot units of 0.001 electrons au^{-3} are used (taken from [7]).

a) muffin-tin APW calculation;
b) general potential LAPW calculation.

component cannot be seen in the difference density, but will be important in connection with the electric field gradient [9].

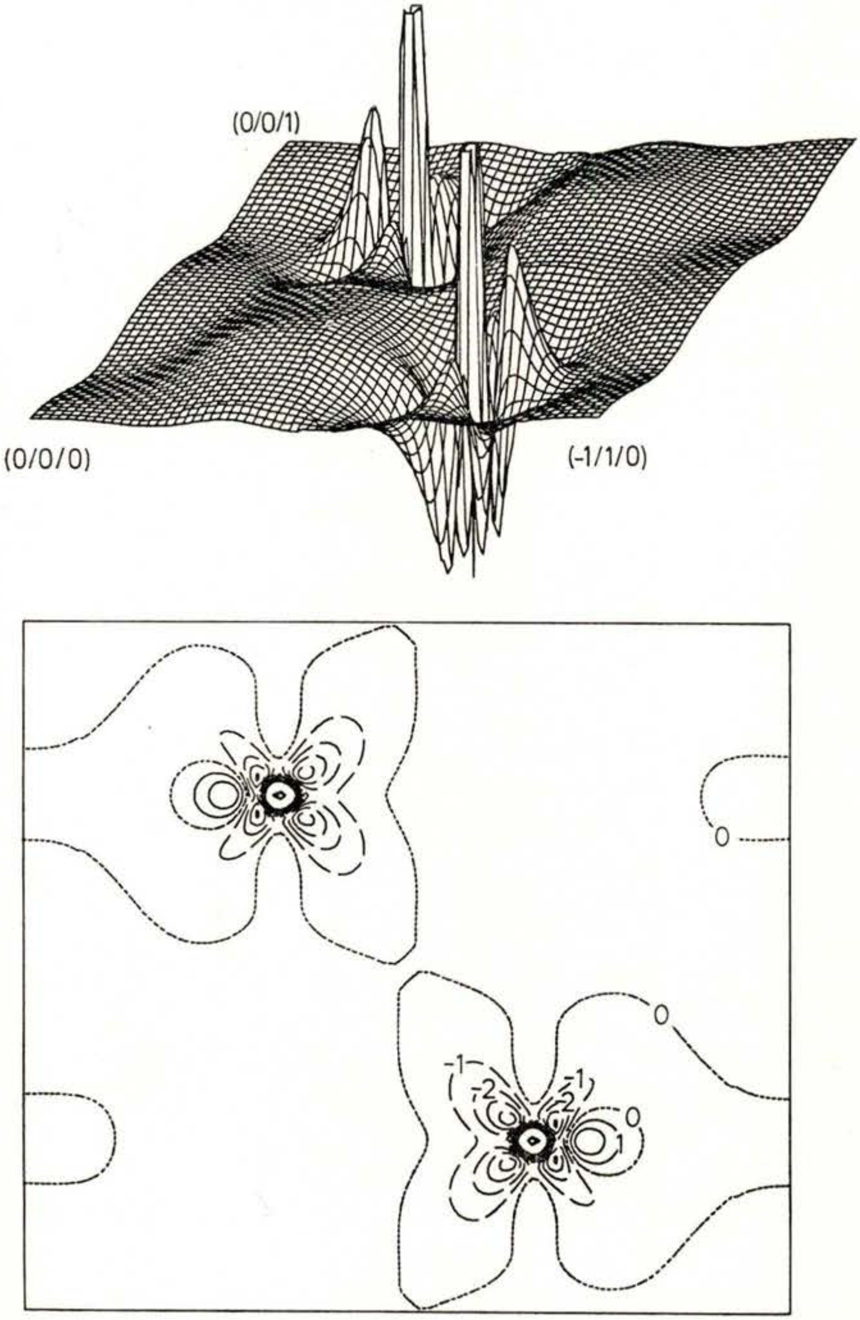

Fig. 2 — Difference electron density (crystaline minus superposed atomic densities) of hcp Ti in the $(11\bar{2}0)$ plane: perspective plot (top) and contour plot (bottom) with units 0.01 electrons au^{-3}.

The Fourier transform of the electron density yields the related structure factors from which the crystalline form factors are deduced. Four representative examples (Co, Mg, Sc and Ti) are summarized in Table 1. In each case the LAPW results and the relative difference with respect to the free atomic Hartree-Fock values [10] are listed. In general the differences are less than 1 percent except for the 011

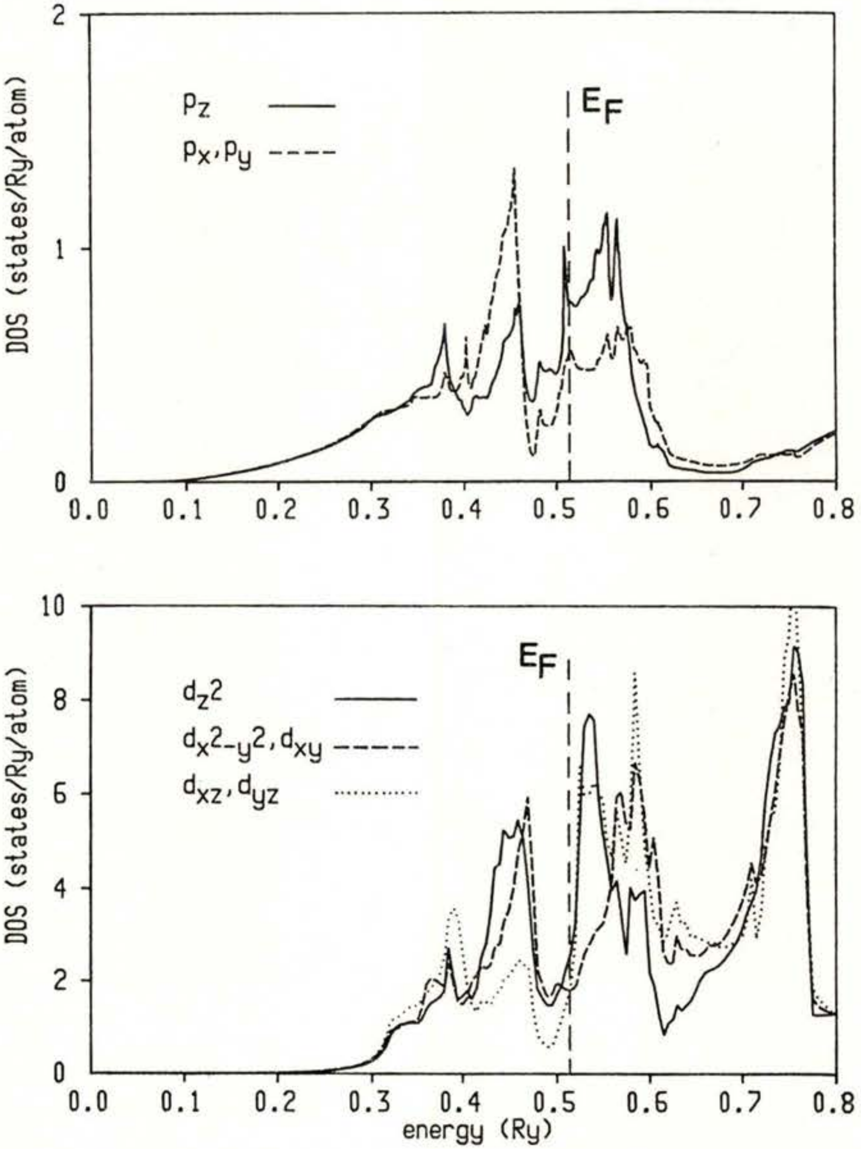

Fig. 3 — Symmetry decomposed p- and d-partial densities of states of hcp Ti.

TABLE 1 — LAPW form factors f of four hcp metals: the deviation with respect to the free atomic Hartree Fock [10] form factors is specified as $\Delta/f = (f^{LAPW} - f^{HF})/f^{HF}$:

K	Cobalt		Magnesium		Scandium		Titanium	
	f	Δ/f	f	Δ/f	f	Δ/f	f	Δ/f
0 0 0	26.999	0.04	11.997	0.09	21.000	0.01	22.000	0.01
0 1 0	19.919	−0.50	8.974	−0.43	15.796	−0.59	16.057	−0.76
0 0 2	19.350	−0.75	8.774	−0.75	15.299	−0.87	15.477	−1.04
0 1 1	18.806	0.91	8.596	−0.93	15.049	−0.83	15.076	−1.84
0 1 2	16.365	−0.95	7.885	−0.48	13.516	−0.02	13.438	−0.26
1 1 0	14.585	−0.69	7.282	−0.37	12.367	−0.02	12.188	−0.23
0 1 3	13.654	−0.56	6.930	−0.35	11.596	−0.13	11.365	−0.11
0 2 0	13.003	−0.61	6.671	−0.37	11.279	0.07	11.034	−0.01
1 1 2	12.831	−0.49	6.595	−0.33	11.091	−0.06	10.819	−0.23
0 2 1	12.646	−0.44	6.516	−0.31	10.991	−0.04	10.726	−0.16
0 0 4	12.320	−0.39	6.372	−0.31	10.622	−0.01	10.379	0.45
0 2 2	11.680	−0.29	6.075	−0.33	10.273	−0.05	9.981	−0.12
0 1 4	11.265	−0.34	5.881	−0.31	9.916	0.13	9.632	0.38
0 2 3	10.431	−0.22	5.448	−0.31	9.373	0.06	9.061	−0.04
1 2 0	10.120	−0.20	5.277	−0.32	9.203	0.07	8.902	−0.03
1 2 1	9.933	−0.18	5.171	−0.31	9.073	0.15	8.783	0.19
1 1 4	9.768	−0.14	5.074	−0.31	8.876	0.07	8.574	0.08
1 1 5	9.446	−0.15	4.881	−0.33	8.691	−0.01	8.385	−0.20
0 2 2	9.431	−0.16	4.874	−0.33	8.620	0.08	8.342	0.36
0 2 4	9.225	−0.05	4.741	−0.32	8.497	0.02	8.204	0.02

reflection of Ti. Therefore hcp Ti would be of special interest for high precision diffraction measurements.

Ferromagnetic hcp Co has been studied by LAPW calculations [8]. The spin density $\rho\uparrow(r) - \rho\downarrow(r)$ is derived from an itinerant electron picture, but shows (Fig. 4) that it is spatially localized around the Co sites. This spin density originates mainly from d electrons and its deviation from spherical symmetry is minor. A small negative spin density occurs in the interstitial region.

3 — ELECTRIC FIELD GRADIENTS (EFGs)

In a system which contains a nucleus with a nuclear-spin quantum number $I \geqslant 1$ at a site with non-cubic point symmetry the interaction between the nuclear quadrupole moment Q and the electric field gradient (EFG) at that atomic site can be measured accurately by various methods [11]. Such experiments are used to characterize surfaces, impurities, and vacancies [12].

Recently the current status of the theory of EFGs was summarized [13]. Often a partitioning into an ionic (lattice) and a valence EFG is made and these quantities are modified by estimated antishielding functions $\gamma(r)$ by Sternheimer antishielding factors γ_∞ whose application is not justified in solids.

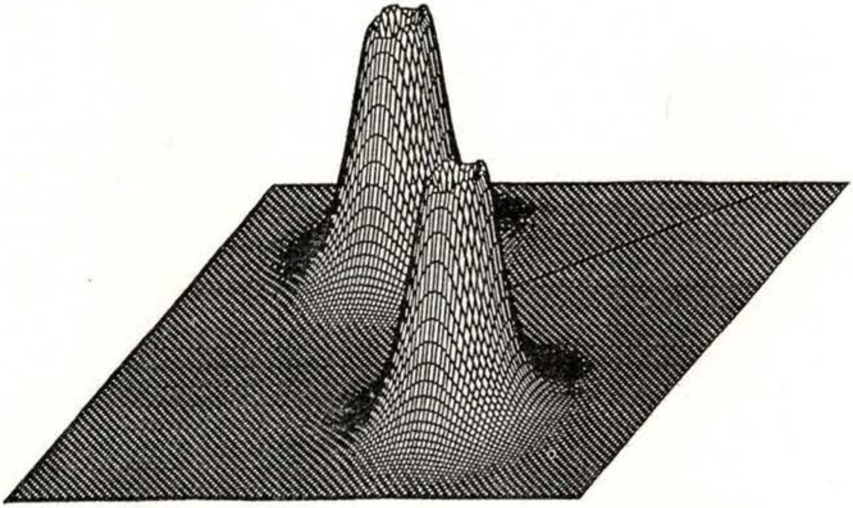

Fig. 4 — Spin density $\rho\uparrow(r) - \rho\downarrow(r)$ of ferromagnetic hcp Co in the $(11\bar{2}0)$ plane.

In 1985 Blaha et al. [14] developed a new method of calculating EFGs based on LSDA band structure calculations and applied it to Li_3N, a superionic conductor. This work was extended to hexagonal closed packed (hcp) Be [7], the other hcp metals [9] and to Cu_2O [15].

The basis for the calculation of the EFG is again the full-potential LAPW methodology. Using the total crystal charge density (including the core electrons) the electrostatic potential is derived by solving Poisson's equation, then the EFG is obtained numerically without further approximations. The key quantity in this scheme is the radial charge density coefficient $\rho_{20}(r)$ of eqn. (1) which can be obtained from the corresponding wavefunctions. The relevant $L = 2$, $M = 0$ component originates only from p-p, d-d and s-d combinations of wavefunctions and thus an analysis according to this decomposition can be used to interprete the origin of the EFG [16].

In a suitable coordinate system the z z-component of the EFG tensor is obtained from the $L = 2$ potential coefficients by:

$$V_{zz} = \sqrt{\frac{5}{4\pi}}\ 2\ V_{20}(0) \qquad (2)$$

The evaluation of the radial potential coefficients $V_{LM}(r)$ for $L = 2$ and $M = 0$ at $r = 0$ consists of three terms [16]; the first is the well-known integral over the charge density $\rho_{20}(r)$ times the $L = 2$ Legendre polynomial divided by r^3, but integrated only over the atomic sphere; we call this contribution the *valence* EFG.

The second and third terms arise from the boundary value problem and from charge density contributions outside the sphere in question and the sum is termed the *lattice* EFG. Since we calculate the EFG from the self-consistent total charge density of the system we do not need to incorporate additional Sternheimer factors or other (arbitrary) corrections.

3.1 — *Results for the insulators Li_3N and Cu_2O*

This new method was first applied to Li_3N, a superionic conductor [14], where EFGs on nitrogen as well as on both lithium sites were measured [17]. A simple point charge model was not able to explain the EFG, but our results using this new method were in very good agreement with the experimental values. In particular the ratio of the EFGs at the two Li sites, which is not affected by an uncertainty in the Q value, gives perfect agreement between theory and experiment, while the point charge model yields a significantly larger ratio, which cannot be altered by a single Sternheimer antishielding factor γ_∞.

Recently [15] we have also applied our method to cuprite Cu_2O, where a previous cluster calculation [18] obtained an EFG at the Cu site in rather good agreement in magnitude compared with the experimental EFG [19]. The cluster approach yields a positive sign in contradiction to a simple point charge model [20]. Although the electronic structure, in particular the depletion of Cu-d charge towards the next nearest oxygen atoms is similar in our LAPW and the cluster calculation, the resulting EFG differs significantly. We obtain a negative sign for the EFG which

TABLE 2 — Experimental (V_{zz}^{exp}) and theoretical (V_{zz}^{th}) EFGs (in 10^{13} esu/cm^3) for hcp elements. The sign of the experimental values is unknown if not given explicitly. In addition, contributions to the total EFG V_{zz}^{th} from the «lattice» and «valence» parts (see text) and further decomposition of V_{zz}^{val} into p-p and d-d contributions are given.

	V_{zz}^{exp}	V_{zz}^{th}	V_{zz}^{latt}	V_{zz}^{val}	V_{zz}^{p-p}	V_{zz}^{d-d}
Be	1.6	− 1.4	+ 1.8	− 3.2	− 3.2	0
Mg	1.8	+ 1.6	− 0.1	+ 1.7	+ 1.7	0
Sc	13	+ 32	− 4	+ 36	+ 40	− 5
Ti	54	+ 69	− 14	+ 83	+ 48	+ 33
Co	− 9.6	− 6.2	+ 1	− 7	− 13	+ 4
Zn	+ 120	+ 125	− 19	+ 144	+ 177	− 32
Y	—	+ 93	− 10	+ 103	+ 106	− 11
Zr	123	+ 143	− 18	+ 161	+ 123	+ 32
Tc	23	− 49	+ 6	− 55	− 70	+ 14
Ru	− 32	− 41	+ 8	− 49	− 75	+ 22
Cd	+ 230	+ 254	− 26	+ 280	+ 322	− 39

originates from the Cu 4p contributions. In the cluster calculation the positive 3d contribution to the EFG dominates the negative 4p contribution, in contrast to our calculation [15].

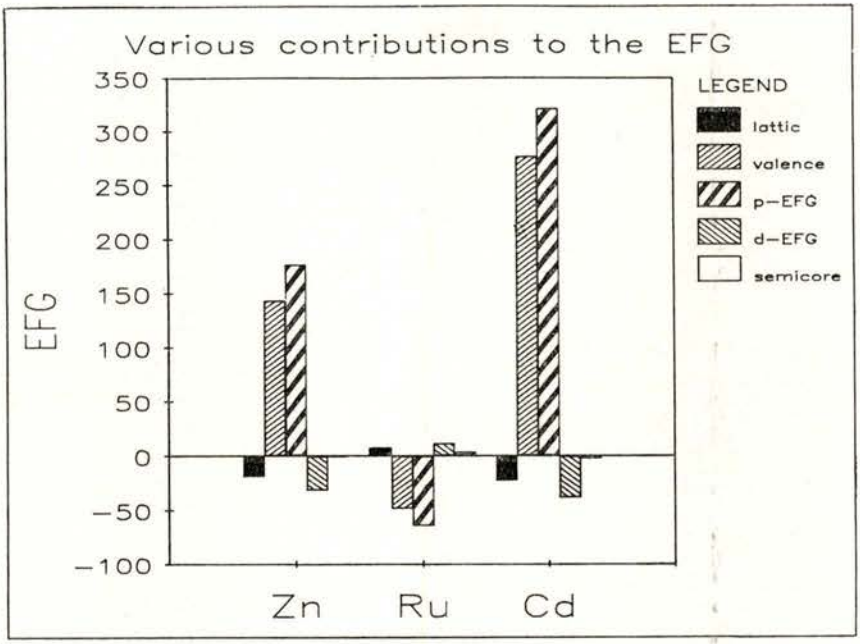

Fig. 5 — Various contributions to the EFG (in 10^{13} esu/cm^3) for Zn, Ru and Cd.

3.2 — *Results for hcp metals*

In Table 2 we list the experimental values and our theoretical results for the EFGs of all hcp metals up to Cd [9]. Except for Sc, the agreement is very good considering that often Q is not known accurately and influences of structure and temperature may increase the experimental uncertainties to about 10 to 20 %. This is the first time that one theory can reproduce the experimental values of the EFGs in *all* hcp metals including the sign wherever it is measured (Co, Zn, Ru, Cd).

In addition, these calculations provide a new understanding of the physics determining the EFG. Previously, the origin of the EFG was unclear even if the calculated values were reasonable. Is it the lattice or the valence contribution? What are the roles of valence and core electrons? We find (Fig. 5) that the valence EFG dominates over the lattice EFG which contributes at most 10-15 % (except for Be). Therefore the EFG originates mainly from the non-spherical charge density inside the atomic sphere. This charge density is built up from the core, the semicore (i. e. 1s for Be; 1s, 2s for Mg; 3s and 3p in the 3d series; and 3d, 4s, 4p in the 4d series) and the valence electrons. Since the contribution from the semicore states is almost negligible, we have neglected the «core polarization» by forcing their charge density to be spherically symmetric.

The non-spherical valence density can be split into p-p and d-d contributions (the mixed s-d term is negligible). To our surprise we found that the EFG is dominated by the p-p term (see Fig. 5 and Table 2). This even holds in the 3d and 4d transition metal series or in cuprite, where the total p population is small while the d charge and its anisotropy is large. The radial dependence of the anisotropic charge density is very important, since the leading term involves a radial integral of $\rho_{20}(r)$ times a factor of $1/r^3$ which strongly enhances the contribution near the nucleus. Effectively the EFG is determined by the region inside the first node of the p-wavefunction with the only exception of Be, where the nodeless 2p orbital is a special case.

The sensitivity of the EFG with respect to the c/a ratio and the small dependence on volume is discussed in detail for Be [7].

4 – MÖSSBAUER ISOMER SHIFTS (IS)

The Mössbauer isomer shift [21] depends on the electronic structure of solids and can be directly related to the charge densities $\rho(0)$ at the nuclei. This spectroscopy is a widely used tool to study effects of chemical bonding in crystalline and amorphous solids. A simple model to explain the IS was introduced by Miedema and van der Woude [22] in terms of electronegativities and the mismatch of the electron densities at the Wigner-Seitz cell boundaries. With a set of empirical parameters, this model is widely applicable and yields correct trends for the IS in Fe intermetallic compounds [23]. In the present work we investigate the IS of Fe and some intermetallic Fe compounds using our LAPW results [24]. In addition we focus on changes of the IS with volume (pressure).

The isomer shift is given by

$$\mathrm{IS} = \alpha\,[\rho_a(0) - \rho_s(0)], \qquad (3)$$

where $\rho_a(0)$ and $\rho_s(0)$ are the electron densities (contact density) at the nuclear sites of the system investigated and the reference system, which in our case is always bcc Fe; the factor α is the nuclear calibration constant, a quantity which depends solely on nuclear properties. This constant is chosen as $\alpha = -0.24\, a_0^3$ mm s^{-1}, a value previously used by Akai et al. [25].

The IS and its pressure dependence of bcc and hcp Fe has been measured by Williamson et al. [26]. The pressure dependence of the IS in bcc Fe was obtained from LAPW calculations at several lattice constants (Fig. 6), while the IS of hcp Fe is calculated only at one particular volume. Table 3 indicates that the IS agree well between theory and experiment including hcp Fe. For bcc Fe we find the slope $\partial \mathrm{IS}/\partial \ln V = 1.3$ mm/s to be compared with the experimental values of 1.33 ± 0.08 and 1.44 ± 0.11 mm/s, at 300K and 82K, respectively.

In order to investigate the origin of the IS, the contact density is partitioned into contributions from the core (1s, 2s), semicore (3s), and valence (4s) states. Although the core electrons dominate the contact density by orders of magnitude, it is generally the valence contribution which determines the IS. The pressure dependence of the IS comes primarily from the valence elctrons, whose contact density $|\psi(0)|^2$ decreases with volume while core and semicore contributions increase slightly. This statement holds for bcc Fe as well as for the intermetallic compounds FeAl and FeTi, which possess very different total IS. In hcp Fe, however, the contribution of the semicore states is about one third that of the valence states Table 3. At the experimental lattice spacing very good agreement with experiment is found. FeAl exhibits a large positive IS, and has the same sign (Table 3). While the valence contribution of hcp Fe fits nicely into the volume trend of bcc Fe, it is the semicore contribution which causes the large difference in the IS between bcc and hcp Fe (taken at the same volume). Nevertheless the main contribution to the IS in hcp Fe comes from the valence states.

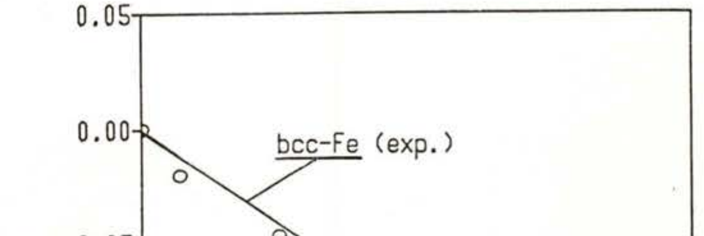

Fig. 6 — IS of bcc and hcp Fe as a function of volume change with respect to the experimental volume. Lines are from a fit through experimental results [26]; theory for bcc Fe (open circles) and for hcp Fe (full circle).

The IS for the 3 intermetallic compounds FeAl, FeTi and FeCo are given in FeTi a smaller negative one, and FeCo shows almost no IS, as is to be expected, since Co is next to Fe in the periodic table. The contributions to the IS of valence, semicore and core states do not show a systematic trend in sign (for FeTi all 3 contributions are negative, but in FeAl and FeCo the core is opposite to the valence and semicore contribution). The volume dependence of the IS is again determined by the valence contributions

TABLE 3 — Experimental and theoretical (decomposed into valence, semicore, and core contributions) isomer shifts (IS in mm/s) of Fe and Fe compounds at experimental lattice constants or at theoretical equilibrium (marked with *) with volume (in au).

	a (au)	Vol/atom	IS_{ex}	IS_{th}	IS_{val}	IS_{sc}	IS_{co}
bcc Fe	5.405	78.95	0.00	0.00	0.00	0.00	0.00
bcc Fe *	5.200	70.30	−0.15 [a]	−0.14	−0.19	0.03	0.02
hcp Fe		70.24	−0.23 [a]	−0.23	−0.18	−0.08	0.03
FeAl	5.496	83.01	0.24 [b]	0.25	0.24	0.04	−0.03
FeAl *	5.313	74.99	—	0.15	0.10	0.07	−0.02
FeTi	5.620	88.75	−0.15 [b]	−0.15	−0.13	−0.02	−0.00
FeTi *	5.473	81.97	—	−0.24	−0.24	0.00	0.00
FeCo	5.317	75.16	0.01 [c]	−0.03	−0.04	0.00	0.01

a) Williamson [26]; *b*) v. d. Kraan [23]; *c*) I. Vincze [27].

which decrease, while those from core and semicore states slightly increase with reduced volume.

We determine the theoretical equilibrium lattice parameters, which are about 2-4 % smaller than experiment. It should be noted that the evaluation of the IS at the theoretical equilibrium yields values in poor agreement with experiment, probably since the theoretical lattice parameters of these 3 compounds deviate from experiment by different percentages.

5 – SUMMARY

We have used the full potential LAPW method to perform self-consistent LSDA band structure calculations for a number of systems. The electron densities obtained in these calculations are used to derive additional quantities. Difference densities are used to show small anisotropies in the electron densities and X-ray structures factors provide a basis for comparison with experiment.

The EFG tensor is obtained numerically from the self consistent charge densities without further approximations. Reliable results are obtained for the two insulators Li_3N and Cu_2O and all hcp metals. Our analysis strongly suggests that the EFG is determined by the aspherical electron density distribution of the valence electrons, predominantly from p-electrons. In cases of heavier elements (i. e. beyond the first row elements with nodeless 2p functions), the aspherical valence charge density close to the nucleus is most important. To obtain this charge distribution reliably both full-potential and all-electron calculations are required.

Another quantity related to electron densities is the Mössbauer IS which is investigated for bcc Fe, hcp Fe, FeAl, FeTi and FeCo. The IS at the Fe nucleus as well as its pressure dependence is in good agreement with experiment. The main contribution to the IS is due to the valence 4s electrons, but a small contribution (of either sign) comes from the core and semicore (3s) states.

This work was supported by the Hochschuljubiläumsstiftung der Stadt Wien. In addition we thank Stephan Turnovsky for his help in generating the structure factors.

REFERENCES

[1] HOHENBERG, P. and KOHN, W., Phys. Rev., **143B**, 864 (1964).

[2] KOHN, W. and SHAM, L. J., Phys. Rev. **140**, A1133 (1965).

[3] HEDIN, L. and LUNDQVIST, S., J. Physique Coll. **33**, C3 73 (1972).

[4] JANAK, J. F., Solid State Commun. **25**, 53 (1978).

[5] BLAHA, P. and SCHWARZ, K., Int. J. Quantum Chem. XXIII, 1535 (1983).

[6] SCHWARZ, K., CRC Critical Rev. Solid State and Mat. Sci. **13**, 211 (1987).

[7] BLAHA, P. and SCHWARZ, K., J. Phys. F: Metal Phys. **17**, 899 (1987).

[8] BLAHA, P., SCHWARZ, K. and DEDERICHS, P. H., Phys. Rev. **B38**, 9368 (1988).

[9] BLAHA, P., SCHWARZ, K. and DEDERICHS, P. H., Phys. **B37**, 2792 (1988).

[10] DOYLE, P. A. and TURNER, P. S., Acta Cryst. **A24**, 390 (1968).

[11] VIANDEN, R., Hyperfine Interactions 15/16, 189 (1983).

[12] WIECHERT, TH. and RECKNAGEL, E., Microscopic Methods in Metals, in Vol. 40 of Topics in Current Physics, edited by U. Gonser (Springer-Verlag, Berlin 1986).

[13] DAS T. P. and SCHMIDT, P. C., Z. Naturforsch. **41a**, 47 (1986).

[14] BLAHA, P. SCHWARZ, K. and HERZIG, P., Phys. Rev. Lett. **54**, 1192 (1985).

[15] BLAHA, P. and SCHWARZ, K., Hyperfine Interactions (in press).

[16] BLAHA, P., SORANTIN, P., AMBROSCH, C. and SCHWARZ, K., Hyperfine Interactions, **51**, 917 (1989).

[17] DIFFERT, K. and MESSER, R., J. Phys. C **13**, 717 (1980).

[18] NAGEL, S., J. Phys. Chem. Solids **46**, 743 (1985).

[19] KUSHIDA, T., BENEDEK, G. B. and BLOEMBERGEN, N., Phys. Rev. **104**, 1364 (1956).

[20] HAFNER, S. S. and NAGEL, S., Phys. Chem. Minerals **9**, 19 (1983).

[21] «Mössbauer Isomer Shifts.», eds. G. K. Shenoy and F. E. Wagner, North Holland, Amsterdam (1978).

[22] MIEDEMA, A. R. and VAN DER WOUDE, F., Physica B **100**, 145 (1980).

[23] VAN DER KRAAN, A. M. and BUSCHOW, K. H. Physica, **138B**, 55 (1986).

[24] BLAHA, P. and SCHWARZ, K., J. Physique Coll. **C8**, 101 (1988).

[25] AKAI, H., BLÜGEL, S., ZELLER, R. and DEDERICHS, P. H., Phys. Rev. Lett. **56**, 2407 (1986).

[26] WILLIAMSON, D. L., BUKSHPAN, S. and INGALLS, R., Phys. Rev. **B6**, 4194 (1972).

[27] VINCZE, I., CAMPBELL, I. A. and MEYER, A. Z., Sol. State Commun. **15**, 1495 (1974).

CHARGE DENSITY IN TRANSITION METALS

MARIA MARGARIDA R. COSTA
Departamento de Física, Universidade de Coimbra
3000 Coimbra, Portugal

The interest of accurate diffraction measurements leading to the experimental determination of charge densities has been repeatedly pointed out: the direct observation of asphericities in electron distributions enables a better understanding of the nature of the bonding in solids.

One of the very first problems the experimentalist is faced with is that of selecting a sample which is suitable for charge density studies.

The criterion introduced by Coppens — the inverse core electron density concentration, $S = V/(\Sigma n^2_{core})^{1/2}$ — may be used as a guide; only if S is large enough is the compound suitable for any charge density maps.

In this sense, as pointed out by Hirshfeld in 1985 [1], the structure should only contain light atoms of the 1st and possibly 2nd row of the periodic table. Although this, in principle, excludes transition metals, success has been obtained in this field [2-4].

The importance of charge and spin density studies in atoms with open d-shells is well known. The d-electrons are relatively localised and hence interact strongly amongst themeselves; such interactions often result in significant departures from the spherical symmetry and lead to an atomic magnetic moment. Therefore, they play an important role in the magnetism of solids.

On the other hand, their wavefunctions are sufficiently spread so that d electrons may also contribute to cohesion in solids. The delocalisation of the magnetisation density reflects the participation of d electrons in chemical bonding.

In materials with d electrons, both the magnetisation density and the charge density can be measured. Although the measurement and interpretation of magnetisation densities is far more complicated than that of charge densities, this dual possibility is an advantage because it enables difficulties inherent to each type of measurement and interpretation to be resolved.

Amongst the wide variety of transition metal compounds, the Laves phases and the rutile structures are particularly suitable for comparison of experimental and theoretical results as will be mentioned now.

LAVES PHASES

The Laves phase compounds, generally with stoichiometric composition AB_2, crystallize in three fundamental structures tipified as C14 ($MgZn_2$), C36 ($MgNi_2$)

Portgal. Phys. — Vol. 19, fasc. 1-2, pp. 173-183, 1988

— with hexagonal unit cells and C15 ($MgCu_2$) — with a cubic unit cell [5]. Most (if not all) atomic positions are fixed by symmetry [Figs. 1a) and b)]; this constitutes an obvious advantage for charge density studies.

These close packing structures can be described in terms of triangular nets of A and B atoms, stacked between a Kagomé net of B atoms [6]. Different possibilities for the stacking of such layers give rise to the three fundamental types of structure, which only differ in the local symmetry of the nearest neighbours A and B.

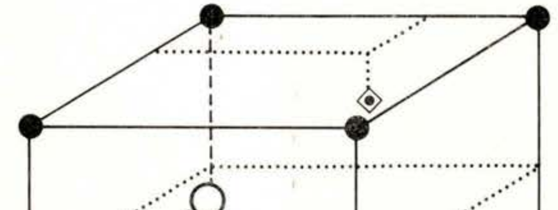

Fig. 1 — Unit cells of two Laves phases

a) $TiFe_2$ — C14 type

● Fe(I) (0, 0, 0); (0, 0, 1/2)
○ Fe(II) (x, x, 1/4); (x, 2x, 1/4); (2x, x, 1/4);
(x, 2x, 3/4); (2x, x, 3/4); (x, x, 3/4)
◈ Ti (1/3, 2/3, z); (2/3, 1/3, z)
(2/3, 1/3, 1/2 + z); (1/3, 2/3, 1/2 − z)

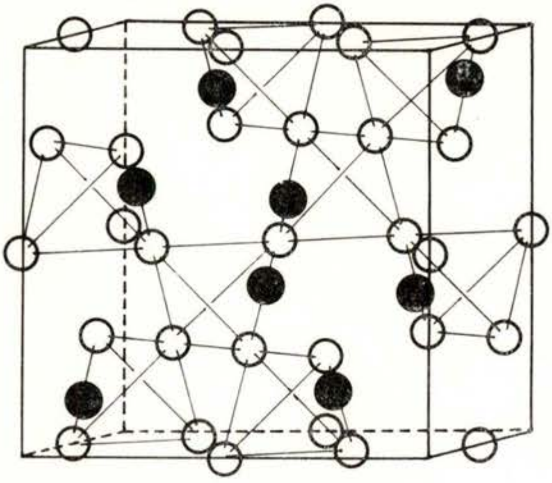

b) $TiCo_2$ — C15 type

○ Co (0, 0, 0); (1/4, 1/4, 1/4)
● Ti (5/8, 5/8, 5/8); (5/8, 7/8, 7/8);
(7/8, 5/8, 7/8); (7/8, 7/8, 7/8)

Laves phases have been regarded as size factor compounds in that the relative sizes of the constituent atoms (taken as their Goldschmidt radii) is, in general, close to the ideal value, $R_A / R_B = 1.225$ wich corresponds to their close packing in the structure.

Several phases are known where such ratio deviates significantly from the ideal value, varying between 1.05 and 1.68.

This has been attributed to changes in the valences of the constituent elements causing adjustments in the atomic volumes so as to preserve the closest possible packing of atoms in the structure.

Values of R_A / R_B favouring the structure of Laves phases often occur when A is a transition metal to the left of Cr in the periodic table and B is an element to the right of this metal, either belonging to the same or to a different series.

When $R_A / R_B < 1.225$ significant contractions are observed in B-B distances — the interatomic distance is smaller than that expected from the known values of the Goldschmidt radii.

It has been found [7, 8] that the observed contraction of B-B distances cannot be attributed only to geometrical factors and appears to depend on the atomic number of the B element, thus on its electronic configuration. If such structural features are attributed to the distribution of the valence electrons, then one should expect significant charge transfer or deformation of the spherical charge density distribution to be observed along B-B directions.

In order to investigate these effects the study of three Laves phases $TiMn_2$, $TiFe_2$ and $TiCo_2$ has been undertaken our Laboratory.

RUTILE STRUCTURES

The rutile structures, well known since 1926 [9], have a simple crystal structure, where the transition metal ion is surrounded by six ligand ions at the corners of a nearly regular octahedron.

This structural simplicity favours the choice of such compounds for an investigation of asphericities in the electron distribution. Moreover, as a consequence of the antiferromagnetic structure adopted by these compounds (Fig. 2a)) a number of magnetic reflections appear at reciprocal space positions where only nuclear scattering should occur if the magnetisation density around the metal ion were spherically symmetric, or had tetragonal symmetry. The small magnetic contributions to these «forbidden» magnetic reflections can be accurately measured with the polarised neutron technique and used to investigate the aspherical part of the magnetisation density.

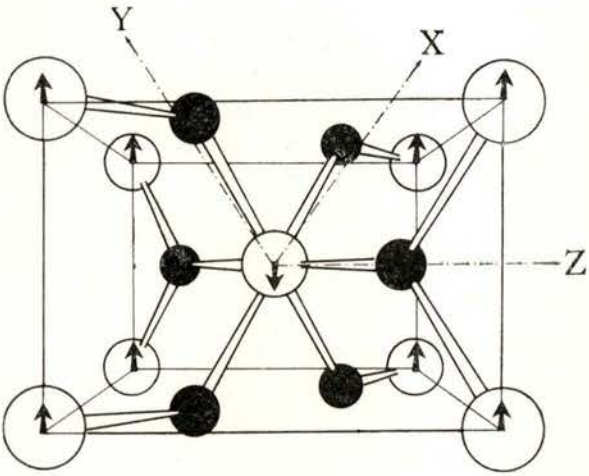

Fig. 2 — Unit cell of an antiferromagnetic rutile structure

○ ligand ion
● transition metal ion

ACCURACY OF EXPERIMENTAL CHARGE DENSITIES

Applying Coppens criterion to the alloys and compounds mentioned above, typical values of 2-4 are obtained for the inverse core electron density concentration. Such small values can be compensated by using sufficient care in optimising the measurements. One therefore should aim at:

(i) improving the counting statistics within the limit of the equipement available;

(ii) carrying out measurements at a high resolution $[S = (2\sin\Theta)/\lambda]$, obviously limited by the wavelength of the radiation used;

(iii) avoiding or minimizing sistematic errors;

(iv) measuring sets of reflection intensities from more than one crystal (selected from the same sample) with different shapes and volúmes; this enables the reproducibility of the data to be tested and the detection of common features on the observed charge densities, which are most likely to be significant;

(v) trying to avoid the uncertainties arising from thermal vibrations by making measurements at low temperature.

All X-ray measurements leading to the results which will be discussed later were carried out on a CAD4 diffractometer, with a graphite plane crystal monochromator and Mo-Kα radiation.

Reflection intensities were measured in ω - 2Θ scans with variable width, basically inferred from a peak profile analysis of several reflections occurring at various Bragg angles. The scan speed for each reflection was established so that a precision better than 2 % was attained in all measurements.

These were carried out inside an Ewald sphere with radius $1.1 - 1.25$ Å^{-1} ($S = 2.2 - 2.5$ Å^{-1}); reflections in all octants were scanned whenever the reflection position was accessible. This enables the extent of absorption and the «efficiency» of the absorption correction to be estimated. The internal agreement between equivalent reflections corrected for absorption (¹) is typically $1.5 - 2.5$ %.

It has been claimed that «weak» reflection intensities ($I < 3\sigma$) should not be neglected. However, in the samples investigated, these reflections have little weight and their number is small, so that they make no significant changes in the refined parameters. Rejection of «weak» reflections after averaging equivalent intensities appears to be more appropriate than if made at earlier stages of the data analysis.

Possible sources of sistematic errors are:

(i) the intensity variation of the main beam during the experiment (typical value: 2 % in 300 h), accounted for by periodically measuring a set of 4-6 standard reflections;

(ii) misorientation of the crystal due to frequent movement of the diffractometer and goniometer axes; this is avoided by checking the orientation of the sample every 120 measurements and automatically reorientating it when the direction of the scattering vector differed by more than 10 % from that derivated from the UB matrix.

(iii) the error arising from asymetric peak profiles; this appeared to be more important when Ag - Kα radiation was used and was accounted for in any case by establishing sufficiently wide limits for the scan width in order to include all the peak.

(¹) A psi-scan absorption correction suggested by North and Phillips [10] was found to be preferable in all cases to the usual path-length dependent correction which relies on an accurate definition of the crystal shape.

REFINEMENT PROCEDURES

A least squares refinement of positional and harmonic anisotropic thermal parameters as well as that of a scale factor is performed using high-order data ($\sin\Theta/\lambda \geqslant 0.6$ Å^{-1}). These reflection intensities are less liable to be affected by extinction and by any deformation of the charge density distribution.

The values of simultaneously refined parameters may be affected by correlations. Their effect on the scale factor should not be neglected, although an error on the scale factor is known to have a much smaller effect in the bond regions than in the vicinity of the atomic positions.

The use of reliable high-order data — which are strongly dependent on thermal vibrations — is expected to lower correlations between different parameters.

The scale factor has also been measured experimentally for several data sets with a probable uncertainty of 4 %, arising mainly from the approximate evaluation of the crystal volume. Nevertheless, the experimental values were found not to differ significantly from those refined with high order data. This confirms that the latter values are not significantly correlated with other parameters.

An empirical extinction parameter g is finally refined with all data by comparing the quantities F_{obs} and $[F_{calc}\,(1 + gI_{calc})^{-1}]$ in a least-squares procedure.

Alternatively, a simultaneous refinement of the mentioned parameters together with those describing the extinction and charge density models may be performed. This will be mentioned again later.

Difference density maps are obtained from Fourier analysis of a set of $(SF_{obs} - F_{calc})$, where SF_{obs} are the observed structure factors on an absolute scale and F_{calc} are the corresponding values derived from the refined parameters and Hartree-Fock scattering factors for the free atom (or ion), corrected for anomalous dispersion [11].

The importance of calculating error maps should be stressed here. These, together with an estimate of the mean error in the unit cell:

$$\overline{\sigma^2(\rho_0)} = \frac{2}{V^2} \sum_{\frac{1}{2}K} \sigma^2(F_0)$$

enables the significance of the observed features on the difference density maps to be evaluated.

MODELISATION OF CHARGE DENSITIES

The interpretation of charge densities (either in real or in reciprocal space) is most conveniently made in terms of a parametric model; a small number of appropriately chosen parameters may then be refined either independently from (or simultaneously with) structural parameters.

The symmetry of the 3d electron distribution, as well as the translational properties of the crystal symmetry, play an important role in simplifying the calculations.

The experimental 3d charge density may be compared with that deduced from a one-electron wavefunction $\psi(\mathbf{r})$ written as a linear combination of 3d atomic orbitals $\varphi_i(\mathbf{r})$:

$$\psi(\mathbf{r}) = \sum_i \varphi_i(\mathbf{r}) \qquad (1)$$

each $\varphi_i(\mathbf{r})$ being the product of a common radial function, R (r), and an angular function which is a linear combination of spherical harmonics:

$$\varphi_i(\mathbf{r}) = R(r) \sum_m Y^l_m(\Theta, \phi) \qquad (2)$$

The 3d electron density may then be expressed as:

$$\rho_d = \sum_i \alpha_i \, |\varphi_i|^2 \qquad (3)$$

However, since the structure factors are the Fourier components of the electron density

$$\rho(\mathbf{r}) = \frac{1}{V} \sum_{\mathbf{K}} F(\mathbf{K}) \exp(i\mathbf{K} \cdot \mathbf{r}) \qquad (4)$$

the comparison of the observed density with a model density may be performed in terms of structure factors, which are the quantities directely observed in the experiment.

Scattering factors for the φ_i can be simply evaluated by making use of the properties of the spherical harmonics, as shown by Schweitzer (1978) [12].

The total scattering factor, f (**K**), is then expressed as a linear combination of contributions from the appropriate d-orbitals:

$$f(\mathbf{K}) = \sum_i \alpha_i \, f_i(\mathbf{K}) \qquad (5)$$

Where α_i represents the fractional occupancy of the d_i orbital; each f_i is expressed is terms of the radial integrals $\langle j_0 \rangle$, $\langle j_2 \rangle$ and $\langle j_4 \rangle$. In order to obtain the corresponding structure factors from (5), only the appropriate geometrical factor and the correction for thermal motion have to be considered.

The five-fold degeneracy of the level L = 2 for 3d electrons in an isolated atom is totally or partially lifted by the local symmetry of the crystal field. This symmetry must be preserved by the combination of atomic orbitals used to calculate the total wavefunction $\psi(\mathbf{r})$, (1).

In the case of rutile structures the crystalline environment of the transition metal ion is such that the ligand ions occupy the corners of a slightly deformed octahedron. The symmetry of the crystal field is therefore orthorhombic. The five 3d orbitals referred to the axes in Fig. 2 have the following angular wavefunctions:

$$e_{g_1} - d^2_z;\; e_{g_2} - d_{x^2-y^2};\; t_{2g_1} - d_{xy};$$
$$t_{2g_2} - d_{xz};\; t_{2g_3} - d_{yz}$$

The latter two are degenerate owing to symmetry requirements.

In Laves phases the local symmetry is different for distinct atomic positions. For two of them, the point group symmetry is trigonal: the d-atomic orbitals split into one singlet, A_{g_1}, and two doubly degenerate, E_{g_1} and E_{g_2}, with wavefunctions:

$$E_{g_1} \begin{cases} d_{xy} \\ d_{yz} \end{cases} \qquad E_{g_2} \begin{cases} d_{xy} \\ d_{x^2-y^2} \end{cases} \qquad A_{1g} - d_{z^2}$$

The charge density observed in the difference maps represents the Fourier transform of the differences between the observed structure factors and those calculated for a spherical electron distribution (ΔF_{hkl}).

Therefore, only the aspherical contributions to the scattering factor, $\langle j_2 \rangle$ and $\langle j_4 \rangle$, have to be considered to calculate the «aspherical» structure factors, F^{asph}_{hkl}.

The parameters α_i — appropriately constrained by symmetry and normalisation — are then least-squares refined by comparison of the ΔF_{hkl} with the corresponding F^{asph}_{hkl}.

Alternatively, the charge density may be described in terms of a superposition of atomic densities each of which is a series expansion in real spherical harmonics (multipole functions):

$$\rho(\mathbf{r}) = P_c \, \rho_{core} + P_v \, \rho_v \, \chi'^3 \, (\chi', r) + \\ + \Sigma \, R_l \, (\chi'' \, r) \sum_{m=0}^{l} P_{lm} \pm$$

where P_c, P_v and $P_{lm} \pm$ are the population coefficients; the total number of electrons associated with one atom is $P_c + P_v + P_{00}$, the core and valence densities, ρ_c and ρ_v, are calculated from Hartree-Fock wavefunctions and the radial extent of ρ_v is governed by the adjustable parameter χ'. [13].

Based on this description a set of structure factors may be calculated and compared with the experimental observations.

Thermal and position parameters, a scale factor, extinction parameters (domain size an mosaic spread) as well as the populations of the multipoles allowed by symmetry are then refined simultaneously, using all the observed data, and the least-squares program MOLLY. The number of electrons outside an argon core may also be refined for each atom.

GENERAL FEATURES OF DIFFERENCE DENSITIES

Result thus obtained for rutile structures and Laves phases will be summarized and illustrated with a few examples.

In order to avoid overinterpretation of the available data, only those features

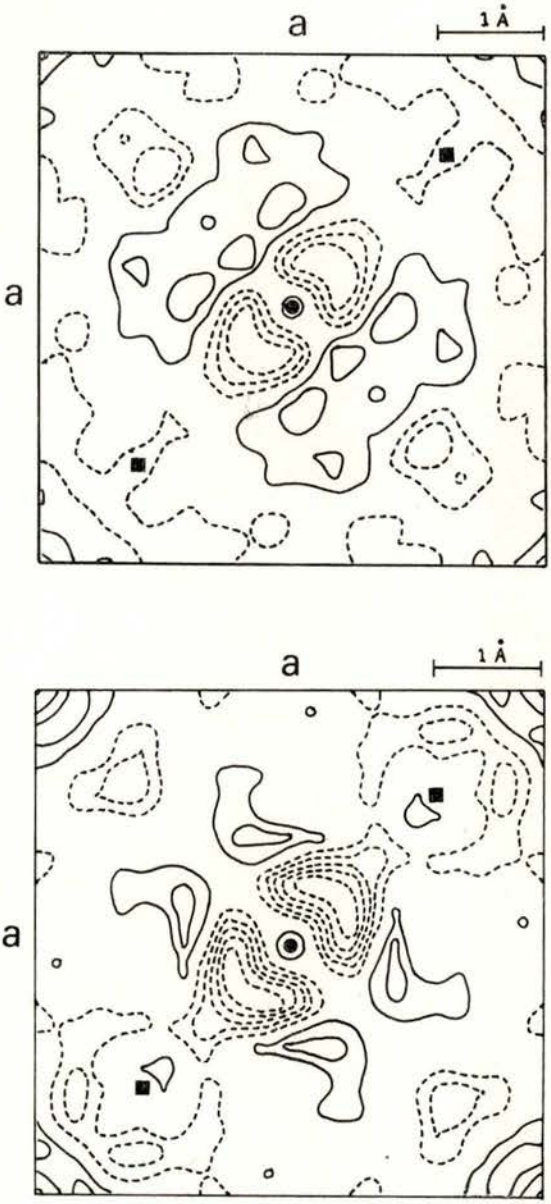

Fig. 3 a), b) — Fourier difference maps for two crystals of FeF_2. Contours at 0.1 e$\mathrm{\AA}^{-3}$. Section [001] of the unit cell. Broken lines represent negative contours.

● Fe atoms ■ F atoms

which are consistently observed in charge densities from more than one crystal of the same material are assumed to evidence a «real» effect. In all cases mentioned, complete data are available from measurements (either preliminary or published) made in our Laboratory, although only a limited number of representative examples have been selected.

a) *Rutile structures*

The main feature observed on all difference maps is a negative density along the metal-ligand bond, corresponding to a depletion of charge density in that region; this can be seen on Figs. 3 a) and 3 b) for two different crystals of FeF_2 [14], as well as on Figs. 4, 5 and 6 a), for NiF_2, VF_2 and MnF_2.

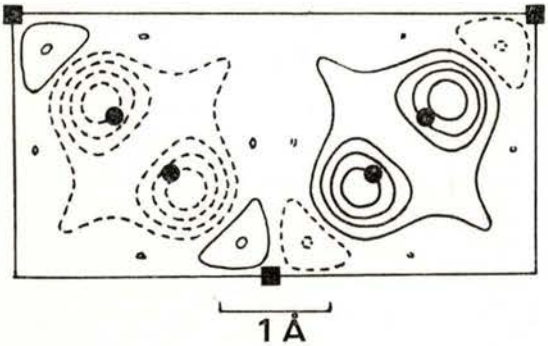

Fig. 3 c) — Fourier projection of the covalent magnetisation density in FeF_2. Projection down [001]. Contours at $0.015\,\mu_B\,\text{Å}^2$. Broken lines represent negative contours.

The results of magnetisation density measurements are also presented in terms of difference density maps for FeF_2 [15] and MnF_2 [16] in Figs. 3 c) and 6 b). Both

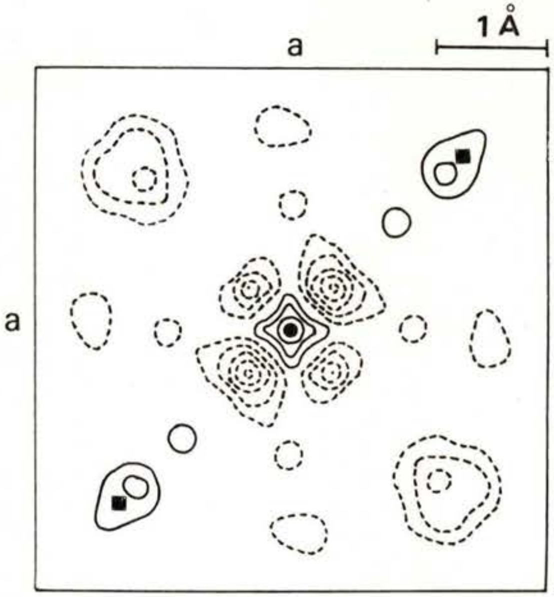

Fig. 4 — Fourier difference map for NiF_2. Section [001] of the unit cell. Contours at 0.2 $e\text{Å}^{-3}$. Broken lines represent negative contours.

● Ni atoms ■ F atoms

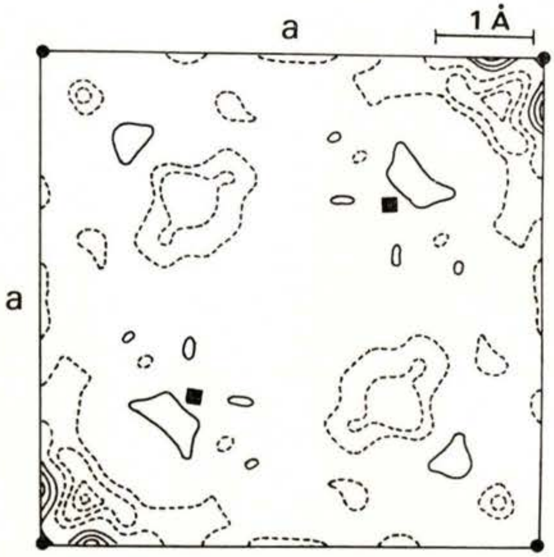

Fig. 5 — Fourier difference map for VF_2. Section [001] of the unit cell. Contour at 0.17 $e\text{Å}^{-3}$. Broken lines represent negative contours.

● V atoms ■ F atoms

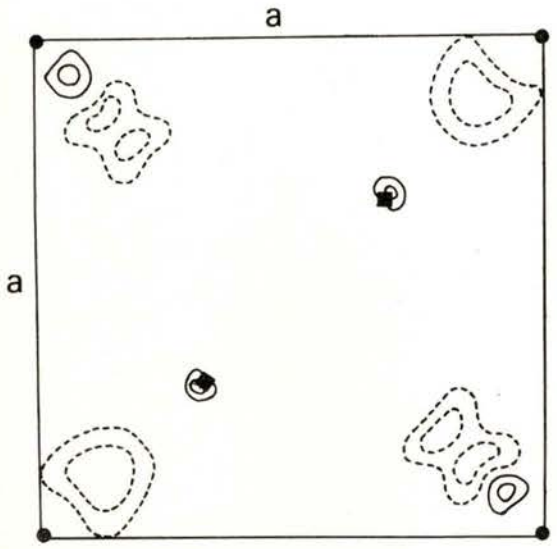

Fig. 6 a) — Fourier difference map for MnF_2. Section [001] of the unit cell. Contours at 0.1 e$Å^{-3}$. Broken lines represent negative contours.

● Mn atoms ■ F atoms

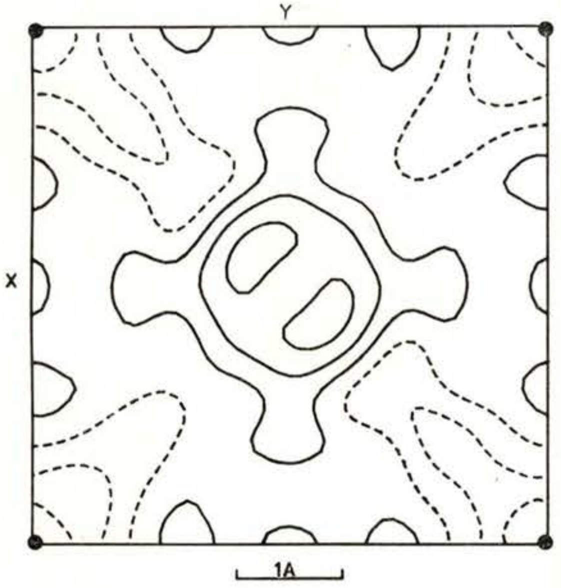

Fig. 6 b) — Fourier difference map for the magnetisation density in MnF_2. Projection down [001]. Contours at 0.02 μ_B $Å^{-2}$. Broken lines represent negative contours

● Mn atoms ■ F atoms

evidence a covalent transfer of magnetisation from the magnetic ion to the ligand. Bearing in mind the electronic structure of the 3d shell in Mn^{2+} and Fe^{2+}, it appears that this loss of magnetisation density is compatible with the observed depletion of charge density (in the viccinity of the fluorine ion) along the bond direction.

Such depletion is also compatible with the values obtained for the occupancy of the d_{z^2} orbital (Table 1) the quantum axis ZZ′ being chosen along the metal-ligand direction. These show a common tendency to be lower than the value that would correspond to spherical symmetry (30 %). In some cases, the deviation is hardly significant as should be expected from the low R-factors for the spherical refinement (typically 1 %).

TABLE 1 — Occupancy of the dz^2 orgital of the transition metal ion for different rutile structures. The two values mentioned for FeF_2 refer to different crystals selected from the same sample.

	VF_2	MnF_2	FeF_2	NiF_2
d_{z^2}	0.10(8)	0.12(3)	0.20(2) 0.19(3)	0.15(2) 0.17(3)

b) *Laves phases*

Two features are consistently observed in hexagonal Laves phases:

(i) on the (00.1) at $z = \frac{1}{4}$ section containing a triangle of Mn (Fe) atoms (Fig. 1 a), positive contours along the metal-metal directions and a negative density inside the triangle formed by such lines are observed (Fig. 7 a). This suggests a preference of the 3d elctrons for directions joining two nearest neighbours Mn or Fe, leaving a depletion along the lines bissecting the angles formed by the sides of each triangle.

(ii) Negative density along the c-axis direction between two nearest Ti atoms (Fig. 7 b); this can be interpreted as a «contraction» of the associated 3d charge density along these directions.

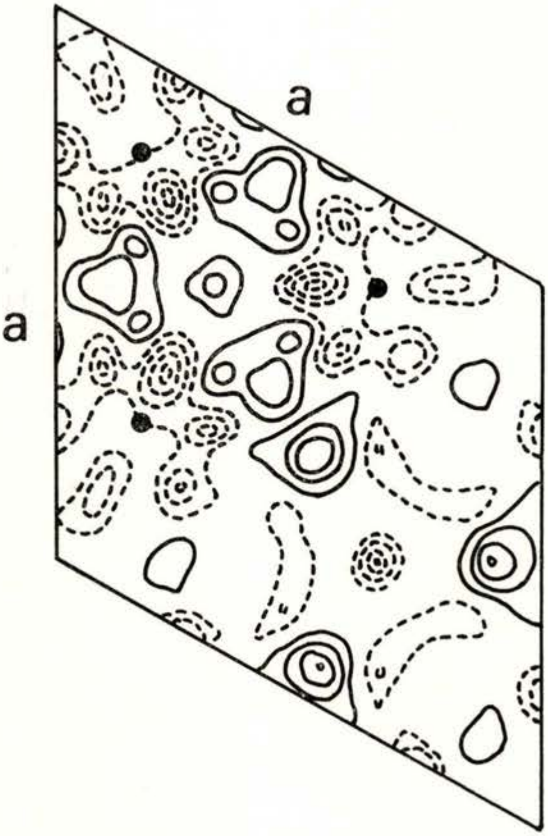

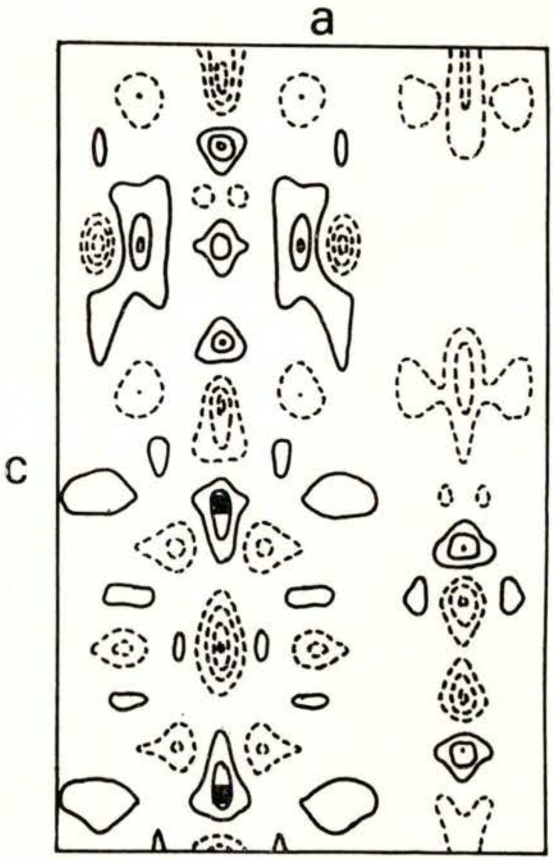

b) Section [10.0] of the unit cell at x = 1/3

Fig. 7 — Fourier difference map for $TiFe_2$. Contours at 0.1 $e\text{Å}^{-3}$. Broken lines represent negative contours

a) Section [00.1] of the unit cell at z = 1/4

REFERENCES

[1] HIRSHFELD, F. L. (1985) — J. of Mol. Struct. **130**, 125.

[2] WEISS, R. J. and MAZZONE, G. (1981) — J. Appl. Cryst. **14**, 401.

[3] IWATA, M. and SAITO, Y. (1973) — Acta Cryst. **B29**, 822.

[4] REES, B. and COPPENS, P. (1973) — Acta Cryst. **B29**, 2516.

[5] LAVES, F. and WITTE, H. (1936) — Metallwirt. Metallwiss. Metalltech. **15**, 840.

[6] SINHA, A. K. (1972) — Progress in Materials Science **15**, 93.

[7] BERRY, R. L. and RAYNOR, G. N. (1953) — Acta Cryst. **6**, 178.

[8] COSTA, M. M. R. and ALMEIDA, M. J. M. (1986) — Portgal. Phys. **17**, n.^{os} 3, 4, 173.

[9] FERRARI, A. (1926) — Rend. Accad. Lincei, III, 6, 224.

[10] NORTH, A. C. T., PHILLIPS, D. C. and MATHEWS, F. S. (1968) — Acta Cryst. **A24**, 351.

[11] International Tables for Crystallography, vol. IV.

[12] SCHWEITZER, J. (1980) — Electron and Magnetisation Densities in Molecules and Crystals-Nato Advanced Study Institute Series (ed. P. Becker), Plenum Press.

[13] HANSEN, N. K. and COPPENS, P. (1978) — Acta Cryst. **A34**, 909.

[14] ALMEIDA, M. J. M. and COSTA, M. M. R. (1988) — Acta Cryst. **B45**, 549.

[15] ALMEIDA, M. J. M. and BROWN, P. J. (1988) — J. Phys. C, **21**, 1111.

[16] COSTA, M. M. R. and BROWN, P. J. (1988) — Physica B, 156-157, 329.

Composição, Impressão e Acabamento
na
Imprensa Portuguesa • Rua Formosa, 108-116 • 4000 PORTO

SOCIEDADE PORTUGUESA DE FÍSICA
AV. REPÚBLICA 37-4.º, 1000 LISBOA, PORTUGAL

PORTUGALIAE PHYSICA publishes articles or research notes with original results in theoretical, experimental or applied physics; invited review articles may also be included.

Manuscripts, with an abstract, may be written in English or French; they should be typewritten with two spaces and in duplicate. Figures or photographs must be presented in separate sheets and be suitable for reproduction with eventual reduction in size; captions should make the figures intelligible without reference to the text. Authors are requested to comply with the accepted codes concerning references.

There is no page charge. Author(s) will get 50 free reprints (without covers); these are to be shared among all the authors of the article. Authors interested in more reprints should say so when sending their manuscripts; quotations shall be sent with the proofs.

Subscription rates for volume 19:

3.600 Escudos (US$24) — individuals
9.000 Escudos (US$60) — libraries

PORTUGALIAE PHYSICA may also be sent on an exchange basis; we wellcome all suggestions to such effect.

All mail to be addressed to

PORTUGALIAE PHYSICA

C/O LABORATÓRIO DE FÍSICA, FACULDADE DE CIÊNCIAS
PRAÇA GOMES TEIXEIRA
4000 PORTO PORTUGAL

PORTUGALIAE PHYSICA

VOL. 19 · NUMB 1/2 · 1988

CONTENTS

ISSN 0048-4903

POPYA4 19 (1/2) 1-183 (1988)